Versatile Multi-faceted Bimetallic Catalysts for Benzylic C–H Oxidation

by

Thomas Nicolaas Ran

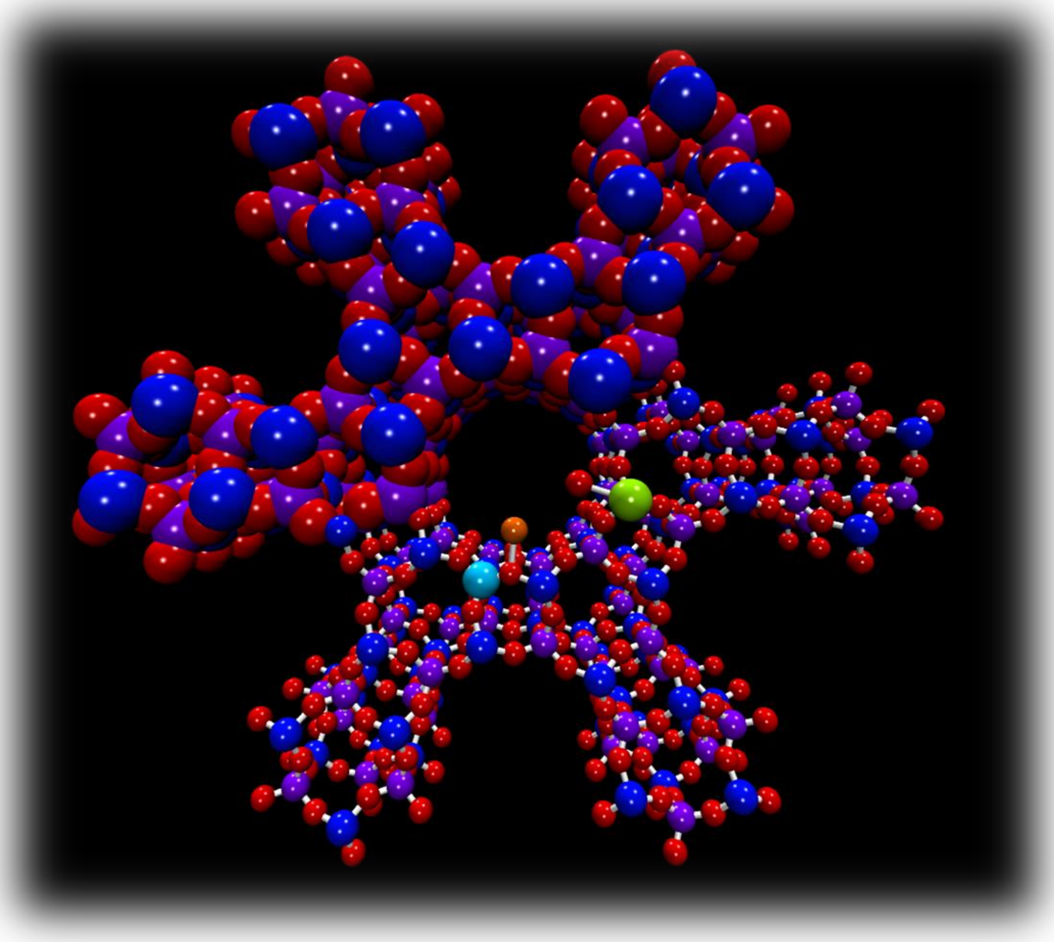

Supervisors: David C. Harrowven, Robert Raja

Advisor: Ramon Rios Torres

This page has been intentionally left blank.

This page has been intentionally left blank.

UNIVERSITY OF SOUTHAMPTON

ABSTRACT

FACULTY OF NATURAL ENVIRONMENTAL SCIENCES

Chemistry

Thesis for the degree of Doctor of Philosophy

Versatile Multi-faceted Bimetallic Catalysts for Benzylic C–H Oxidation

Thomas Nicolaas Ran

In this thesis, the development of a new methodology for the C–H oxidation of a variety of organic substrates using a bimetallic vanadium-titanium molecular sieve, VTi AlPO-5, is presented. Preliminary studies using model substrate propylbenzene were conducted to elucidate trends in catalytic activity by varying a wide array of reaction and catalyst parameters. Following that is a series of studies documenting the uses of VTi AlPO-5 in the oxidation of other substrates, in which different types of reactivity were probed. The catalyst is highly active and capable of redox- as well as acid catalysis due to the inclusion of its vanadium and titanium centres, the combination of which has been found to be capable of effecting two-step syntheses in the same pot, or enhancing selectivity to very high levels in several reactions. The physicochemical nature of the material as well as spectroscopic investigation of the V and Ti centres in the catalyst has been investigated using a variety of techniques. This data, combined with the catalytic data obtained during reactions, led to the proposal of structures for the metal ions and a preliminary reaction mechanism.

Front page picture: impression of vanadium-titanium AlPO-5.

This page has been intentionally left blank.

This page has been intentionally left blank.

Contents

ABSTRACT iii

Contents i

Acknowledgements v

Definitions and abbreviations ix

DECLARATION OF AUTHORSHIP xi

1. Introduction 1

- 1.1 Principles of catalysis 1
- 1.2 Porous materials 4
- 1.3 Zeolites and zeotypes 5
- 1.4 Single-site catalysis and catalyst design strategies 14
- 1.5 C–H oxyfunctionalisation 19
- 1.6 Catalysis using AlPOs 26
  - 1.6.1 Vanadium AlPOs 30
  - 1.6.2 Titanium AlPOs 33
  - 1.6.3 Multimetallic AlPOs 37
- 1.7 Aims and objectives 40

2. Experimental methods 43

- 2.1 Catalysis 43
- 2.2 Catalyst design and synthesis 44
  - 2.2.1 Nature of the catalyst 44
  - 2.2.2 Synthesis of the catalysts 46
- 2.3 Analytical methods 57
  - 2.3.1 Analysis of catalysis products 57
    - 2.3.1.1 Nuclear magnetic resonance (NMR) spectroscopy 58
    - 2.3.1.2 Gas chromatography (GC) 61
    - 2.3.1.3 Mass spectrometry (MS) 63
    - 2.3.1.4 Infrared (IR) spectroscopy 65
  - 2.3.2 Analysis of catalyst batches 66
    - 2.3.2.1 Powder X-ray diffraction (PXRD) 66
    - 2.3.2.2 Inductively coupled plasma optical emission spectroscopy (ICP-OES) 69
    - 2.3.2.3 Brunauer-Emmett-Teller (BET) surface area techniques 71
    - 2.3.2.4 Scanning electron microscopy (SEM) 75

2.3.2.5 Energy dispersive X-ray (EDX) spectroscopy 77
2.3.2.6 Ultraviolet-visible (UV-Vis) spectroscopy 78
2.3.2.7 Solid-state nuclear magnetic resonance (SSNMR) spectroscopy 82
2.3.2.8 X-ray photoelectron spectroscopy (XPS) 85
2.3.2.9 Electron paramagnetic resonance (EPR) spectroscopy 89
3. Oxidation of propylbenzene **93**
3.1 Aims and objectives 93
3.2 Background 93
3.3 Results & Discussion 97
3.3.1 Screening tests 97
3.3.2 Reaction trends 103
3.3.3 Catalyst recyclability 115
3.4 Conclusions 124
4. Substrate scope and new opportunities **127**
4.1 Tetralin oxidation 127
4.1.1 Introduction 127
4.1.2 Results and discussion 134
4.2 Oxidation of indan 137
4.2.1 Introduction 137
4.2.2 Results and discussion 139
4.3 Oxidation of methylbenzenes 140
4.3.1 Introduction 140
4.3.2 Results & discussion 146
4.4 Heterocycle oxidation 151
4.4.1 Introduction 151
4.4.2 Results & discussion 153
5. Analysis of catalysts **157**
5.1 Physicochemical characteristics 157
5.1.1 Physical appearance 157
5.2 Spectroscopic analysis 178
5.3 Discussion 196
6. Summary & conclusions **203**
7. Future work **210**
8. Experimental details **211**
8.1 General methods 211

8.2 General procedure for the oxidation of propylbenzene 212
8.3 General procedure for the oxidation of tetralin 213
8.4 General procedure for the catalytic oxidation of indan 214
8.5 General procedure for the oxidation of toluene 214
8.6 Oxidation of *o*-xylene 215
8.7 Oxidation of *p*-xylene 216
8.8 Oxidation of mesitylene 216
8.9 Oxidation of durene 217
8.10 Oxidation of indoline 217
8.11 Oxidation of tetrahydroquinoline 218
8.12 General procedure for the synthesis of VTi AlPO-5 219
8.13 General procedure for the synthesis of non-VTi AlPO-5 (bi- and monometallic) 219
8.14 Procedure for recycling study 1 220
8.15 Procedure for recycling study 2 220
8.16 Procedure for recycling study 3 221
8.17 Procedure for recycling study 4 221
8.18 Hot-filtration study 221
8.19 Leaching study 222
8.20 Synthesis of APB 222
9. Appendix 223
9.1 Calibration of GC response factors 223
9.2 Formulae used for reaction analysis 230
  9.2.1 GC determination of moles of compound 230
  9.2.2 NMR determination of moles of compound 230
  9.2.3 Determination of conversion, selectivity, yield and mass balance 230
9.3 Titration procedure for TBHP 231
9.4 Determination of crystallite size 232
9.5 Powder diffractograms of V-heterometal series 232
9.6 Compound spectra and chromatograms 233
  9.6.1 Propylbenzene 233
  9.6.2 Tetralin 237
  9.6.3 Indan 239
  9.6.4 Toluene 241
  9.6.5 *o*-Xylene 244
  9.6.6 *p*-Xylene 247
  9.6.7 Mesitylene 250
  9.6.8 Durene 253

9.6.9 Indoline 256
9.6.10 Tetrahydroquinoline 258
9.6.11 Tetrahydroisoquinoline 260
9.6.12 Dihydrobenzofuran 262
Bibliography 265

Acknowledgements

I have many people to thank for this, so let's get started.

I would like to sincerely thank my supervisors Prof. David C. Harrowven and Prof. Robert Raja for their invaluable support and guidance regarding my *Ph. D.* as well as the EPSRC and the INTERREG AI-CHEM Channel scheme for a limited amount of funding. See the (rather ugly) logos below to acknowledge this fact (hey, it's in my contract somewhere, don't blame me).

Furthermore I would like to thank Dr Neil Wells (NMR), Dr Mark Light (XRD), Alistair Clark (SEM), Julie Herniman (MS), Stuart Elliott (EPR) and Prof. Marina Carravetta (SSNMR) for their help with the characterisation of my compounds and materials.

And then there are those that helped me endure the work while I was here and make life liveable. From the Harrowven group, past and present: "Sunny" Sun Wei, Faisal Almalki, Dharyl "Grumpy" Wilson, "Becca" Matters, Emma "Emski" Packard, Marc "MRad" Radigois, Jean-Baptiste "JB" Vendeville, David Skinner, Will Nesbit, Fiona "Fifi" Gunn, Paul "P-man" Murgues, Zeshan "Zee" Yousuf, Mubina Mohamed, Theo Gonçalves, and Lawrence "Cookie" Searle, and especially Majdouline "Maggie Dou" Roudias; we've been through so much together over the years... Thank you all so much, your warm friendship and daily companionship has truly helped me through this PhD. Furthermore students past and present, in particular my own project students, Adam Paul, and Jordan Horsford, both of whom were involved with my project and lent a helping, if sometimes slightly unsteady, hand. It was great fun working with you, guys! Also, of course, from the Raja group, past and present: Stephanie "Chappers" Chapman, "foetus" William Webb, Arran "Norverner" Gill, Cameron "Cam" Ross, Davide "Italian Stallion" Ansovini, Danni Sun, Sivan van Aswegen, William Mothersole, Chris "Hindee" Hinde, Agnieszka Dzielendziak (see, I can spell it properly!), Chris "GC" Pamouktsis, David Xuereb, Mary Cholerton, and students past and present; thank you for all the great times we had together and for your love and support! If only I could have shared an office and lab with you all every day as well… And, especially, Matthew Potter and Stephanie "Big Steve" Newland for their endless patience, loyal and warm friendship, and for more or less teaching me everything I know about inorganic chemistry. Genuinely, guys, I couldn't have done it without you. Shout-out to Matt's amazing wife Em of course, I’m really going to miss you! Matt, you take good care of her! Thanks everyone, I couldn’t have done it without you and your constant support and love (and banter!) But not you, Becky. You don’t get any thanks from me at all.

Then there are my very good friends from the home front who supported me throughout the whole bloody thing and who cheered me up every time I went back home, including; Bas “Beperkt” Reijers, Jurian “Jur” Biesheuvel, Rienk “Rienkieboy” Sybrandi, Amanda “’Mandaatje” Maurits, William Koppelaar, Koen Smit, Cadet Soldier 3rd class Marcel Tubben, Marcella “Marslaatje” van der Poel, Marieke van Dijk, Nathalie Olivier, Just Hovens Greve, Arthur Nieuwland, and my friends and former colleagues from the BKG group; Peter Spannring, Manuel “Manueltje” Basauri, Ties Korstanje, Emma Folkertsma, Suresh Raju, Yuxing Huang, Sohail Anjam, Peter Hausoul, “Vitaaltje” Yazierski, Eric Derrah, and from Leo’s group, Jacco “Zjacco” Hoekstra. Your support all the way from the home front, and even over here, has meant more to me than you can know.

Thanks also to Kyle “The Dee Arr” Carter (also for the artwork!), Ben “dirty dirty physicist” Parkes, Ande “Andy” Oey, Teemu “Wands” Soikkeli, Karol “bastard focker” McGonigle, and Brad “Bradders” Bradford, I mean Critchlow, for long-distance support outside of working hours!

Massive thanks go to my amazing and loving family, including but most definitely not limited to, Jan Ran, Joke Pikaar, Carolien Greep, Eddy Leerkotte, Mathijs Ran, Simon Ran, Eva Ran, and Casper Leerkotte, who kept me motivated through it all and who were always there for me, no matter what, as well as for financial support. Without their never-ending love and mental support I would never have made it this far, and would surely have lost my mind by now — thanks so much for everything, everyone!

And of course, Tim Goodridge; thanks for everything, thanks for the amazing company and all the great moments we shared. You helped me through and cheered me up in even the darkest days and hours. Thanks for putting up with me all this time.

france (manche channel) england
interreg
European Regional Development Fund
The European Union, investing in your future
Fonds européen de développement régional
L'union Européenne investit dans votre avenir
CHem CHannel

This page has been intentionally left blank.

This page has been intentionally left blank.

Definitions and abbreviations

1P1P	1-phenyl-1-propanol
acac	acetylacetonate
ACP	acetophenone
AFI	AlPO-5 (IZA code)
AIBN	azobisisobutyronitrile
AlPO	aluminophosphate
APB	acetyl peroxyborate
Ar	aryl
BDE	bond dissociation energy
BE	binding energy
BET	Brunauer-Emmett-Teller
BHT	butylated hydroxytoluene
bmim	1-butyl-3-methylimidazolium
BTSP	bis(trimethylsiloxy)phosphine
Bu	butyl
CAM	ceric ammonium molybdate
cat.	catalyst
CHP	cumene hydroperoxide
CI	chemical ionisation
Cp	cyclopentadienyl
Cy	cyclohexyl
DCE	1,2-dichloroethane
DCM	dichloromethane
DDQ	2,3-dichloro-5,6-dicyanobenzoquinone
DMSO	dimethyl sulfoxide
DNPH	dinitrophenyl hydrazine
DRS	diffuse reflectance spectroscopy
EB	ethylbenzene
EBHP	ethylbenzene hydroperoxide
EDX	energy-dispersive X-ray (spectroscopy)
EI	electron ionisation
EM	electron microscopy
EPR	electron paramagnetic resonance
equiv.	equivalents
ESEEM	electron spin echo envelope modulation
ESI	electron spray ionisation
Et	ethyl
EXAFS	extended X-ray absorption fine structure
FID	flame ionisation detector
FTIR	Fourier-transform infrared (spectroscopy)
FWHM	full width at half maximum
GC	gas chromatography
GCMS	gas chromatography-mass spectrometry
HYSCORE	hyperfine sublevel correlation
ICP-OES	inductively-coupled plasma optical emission spectrometry
i-Pr	isopropyl
IR	infrared (spectroscopy)
IZA	International Zeolite Association
KE	kinetic energy
KIE	kinetic isotope effect
MALDI	matrix-assisted laser desorption/ionisation
MAS	magic-angle spinning
MBA	methyl benzyl alcohol
Me	methyl
MFI	ZSM-5 (IZA code)
MS	mass spectrometry
MTO	methanol-to-olefins
NADPH	nicotinamide adenine dinucleotide phosphate
NHPI	N-hydroxyphthalimide
NHTPPI	N-hydroxy-3,4,5,6-tetraphenylphthalimide
NMR	nuclear magnetic resonance
ODH	Oxidative dehydrogenation
PAA	per(oxy)acetic acid
Pc	Phthalocyanine
PDMS	Polydimethylsiloxane
PET	polyethylene terephthalate
Ph	phenyl
PO	propylene oxide
PP	1-propiophenone
Pr	propyl
PXRD	powder X-ray diffraction
py	pyridine
RF	response factor
RT	room temperature
SAPO	silicon AlPO
SAXS	small-angle X-ray scattering
SDA	structure-directing agent
SEM	scanning electron microscopy
SET	single-electron transfer
SM	styrene monomer
SSNMR	solid-state NMR
TAPO	titanium AlPO
TBA	*tert*-butyl alcohol
t-Bu	*tert*-butyl
TBHP	*tert*-butyl hydroperoxide
TEDDI	tomographic energy dispersive diffraction imaging
THP	tetralin hydroperoxide
TLC	thin-layer chromatography
TOF	turnover frequency
TON	turnover number
UV-Vis	ultraviolet-visible (spectroscopy)
VAPO	vanadium AlPO
VPO	vanadyl phosphate
VPP	vanadyl pyrophosphate
vtc-XES	valence-to-core X-ray emission spectroscopy
WAXS	wide-angle X-ray scattering
XANES	X-ray absorption near-edge structure
XAS	X-ray absorption spectroscopy
XPS	X-ray photoelectron spectroscopy
XRD	X-ray diffraction

DECLARATION OF AUTHORSHIP

I, Thomas Nicolaas Ran

declare that this thesis and the work presented in it are my own and has been generated by me as the result of my own original research.

VERSATILE MULTI-FACETED BIMETALLIC CATALYSTS FOR THE C–H OXIDATION OF HIGH-VALUE COMPOUNDS

I confirm that:

1. This work was done wholly or mainly while in candidature for a research degree at this University;
2. Where any part of this thesis has previously been submitted for a degree or any other qualification at this University or any other institution, this has been clearly stated;
3. Where I have consulted the published work of others, this is always clearly attributed;
4. Where I have quoted from the work of others, the source is always given;
5. With the exception of such quotations, this thesis is entirely my own work;
6. I have acknowledged all main sources of help;
7. Where the thesis is based on work done by myself jointly with others, I have made clear exactly what was done by others and what I have contributed myself.

Signed:

....

Date:

....

This page has been intentionally left blank.

This page has been intentionally left blank.

1. Introduction

1.1 Principles of catalysis

The term “catalysis” or “catalytic power” was coined in 1836 by the Swedish scientist J. J. Berzelius, who described catalysis as “a new power to produce chemical activity belonging to both inorganic and organic nature” which allows “substances … to awaken affinities that are asleep at this temperature.”[1,2] In other words, Berzelius recognised that catalysts were able to effect transformations at a lower temperature than was possible without them.

Since that time, catalysis has attracted an enormous amount of research. As a result, our understanding of the principles and workings of catalysis has increased hugely. The IUPAC Gold Book describes a catalyst as “a substance that increases the rate of a reaction without modifying the overall standard Gibbs energy change in the reaction.”[3] Essentially, the pathway from the starting material to the product is modified to proceed via lower-energy transition states, such that the activation energy of the overall reaction is reduced (illustrated schematically in Figure 1). The lower energy states are provided by the reactants / reagents adsorbing on or interacting with the catalyst, which stabilises reaction intermediates. As the “free” reactants / reagents do not experience such stabilisation, more energy is required to initiate the reaction. This leads to an increase in the rate of the reaction compared to the uncatalysed reaction at the same temperature.

1. Introduction

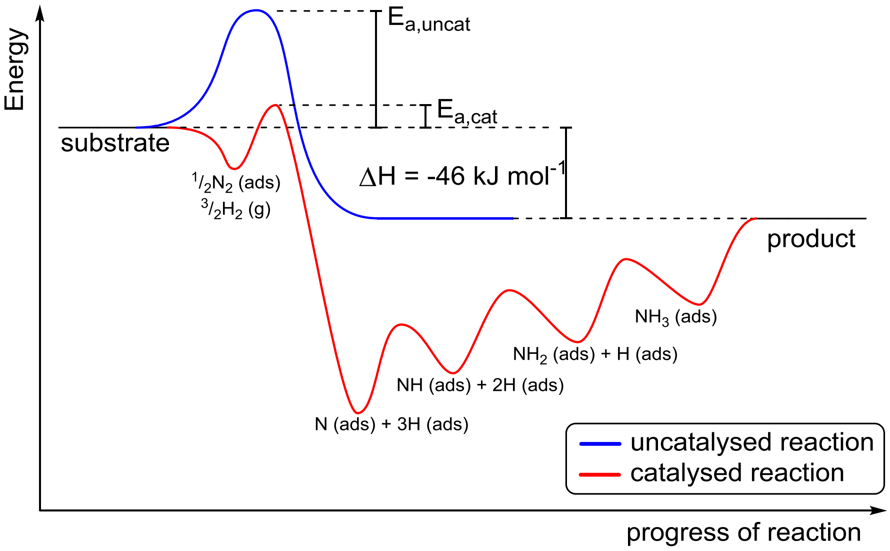

Figure 1: Schematic representation of the Haber process (synthesis of ammonia) as an uncatalysed (blue) and catalysed (red) version of the reaction. The catalytic pathway proceeds via lower-energy transition states which means the activation energy of the catalysed reaction $E_{a,cat}$ *is considerably lower than the activation energy of the uncatalysed reaction* $E_{a,uncat}$.

Catalysis can be divided into two main types; homogeneous, in which the reaction involves only one phase, and heterogeneous, in which two or more phases are involved in the reaction, typically a solid and a gas or liquid.[3,4] Advantages of the former are (generally) higher activity and/or selectivity at milder conditions, while the latter are usually more practicable due to ease of separation and recovery.[5] It is the latter category we are focusing on in this research project.

There are several ways in which a solid, heterogeneous catalyst can effect chemical transformations. The main mechanisms are displayed below (Scheme 1).

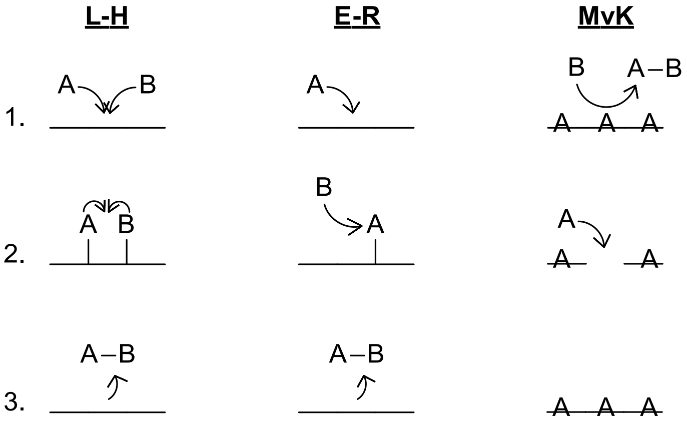

Scheme 1: Schematic representation of the Langmuir-Hinshelwood (left, "L-H"), Eley-Rideal (middle, "E-R") and Mars-Van Krevelen (right, "MvK") reaction mechanisms.

By far the most commonly occurring, the Langmuir-Hinshelwood mechanism involves the adsorption of two separate atoms or molecules, A and B, on the surface of the catalyst and a subsequent reaction between them that liberates the product AB. In this model, the rate of the reaction is dependent on the rate of adsorption of both species, providing this is the rate-limiting step. The rate of reaction is also influenced by factors such as pressure, reactant dispersion and adsorbed reactant stoichiometry. An example of a reaction proceeding via a Langmuir-Hinshelwood mechanism is the oxidation of CO to CO_2 using O_2 over Pt.

By contrast, the Eley-Rideal mechanism involves adsorption of only one species A on the surface of the catalyst. This activates it towards reaction with another species B which “scavenges” it off the surface of the catalyst, liberating the product AB. This mechanism is kinetically distinct from the Langmuir-Hinshelwood mechanism as the rate of reaction is dependent on the rate of adsorption of only one species. Factors that influence reaction rate further include pressure of the reactant gas and coverage of the adsorbed species.

A third mechanism is the Mars-Van Krevelen mechanism. This mechanism, described by D. W. van Krevelen and P. Mars in 1954, was observed in a reaction in which a vanadium oxide catalyst promoted the oxidation of benzene and several polycyclic aromatic substrates.[6] It was found that the oxygen used in the reaction was actually oxygen from the lattice of the catalyst, which subsequently got replenished by atmospheric oxygen to regenerate the active oxygen site, without the loss of framework integrity (Scheme 2). Similarly, McKay *et al.* showed it was possible to incorporate nitrogen from the framework of a Co_3Mo_3N catalyst during the synthesis of ammonia.[7]

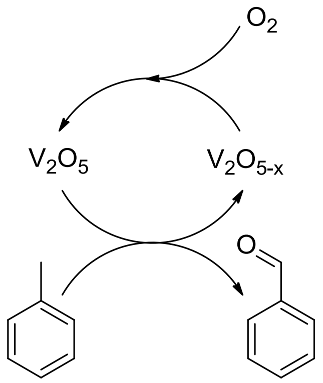

Scheme 2: Schematic representation of the Mars-Van Krevelen reaction illustrating the incorporation of lattice oxygen into the product and subsequent replenishment of the active oxygen sites by atmospheric oxygen.[7]

1.2 Porous materials

There are many types of solid catalyst or solid support in use today in catalysis, both amorphous and structurally defined. Many of both types are also designed to be porous in nature, as porosity intrinsically increases surface area and carries with it the potential for increased activity. Porous materials functionalised with catalytically active sites can allow for high reactivity as well as easy separation, the latter being a trait inherent to heterogeneous catalysts.

In a chemical context, a porous material is associated with one of several classes depending on the size of the pore aperture. The IUPAC defines three types of porosity: microporous (pore size smaller than 20 Å), mesoporous (pore size between 20 Å and 500 Å) and macroporous (pore size bigger than 500 Å).[3] Additionally, systems with different types of porosity, for example a framework including both micropores and mesopores, are generally referred to as hierarchically porous materials.

Examples of macroporous materials include low-surface catalyst bed supports in which the pore sizes are sometimes so large that they are visible to the naked eye, and can be mechanically drilled or punched out rather than having to use a molecular templating agent. They are generally designed to let large amounts of molecules through at the same time.

Mesoporous materials include a wide variety of silicas such as the Mobil Composition of Matter (MCM) series of materials, of which MCM-41 and MCM-48 are the most well-known (Figure 2). They are usually engineered to let larger molecules through, or larger volumes of small molecules. They can additionally be functionalised with various metals or moieties by different techniques such as grafting and tethering.

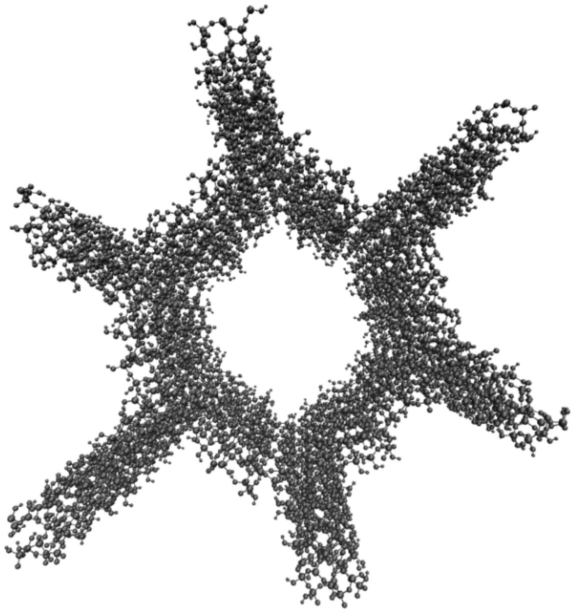

Figure 2: Structure of MCM-41.

Microporous materials have pore apertures similar in size to small molecules. A well-known example of an amorphous microporous material is activated charcoal (also known as activated carbon), which has many uses including the purification of water and for the treatment of ingested poisons. Well-ordered microporous materials with a defined pore size have the ability to separate molecules on a molecular level,[8] and as such porous materials with pores of molecular dimensions are generally referred to as "molecular sieves", a term coined by J. W. McBain in 1932 in his book *The Sorption of Gases and Vapours by Solids*.[9] They are used in laboratories and chemical plants to sterilise gases by filtration, and as desiccants by trapping water. TS-1, a titanium-based microporous material, is a well-known and industrially applied catalyst that has many applications.[8,10,11]

1.3 Zeolites and zeotypes

A prominent class of microporous materials is zeolites, named after the ancient Greek words ζέω "to boil" and λίθος "stone": their discoverer, Axel Cronstedt, found in 1756 that heating these naturally occurring minerals liberated large amounts of steam which came from the water adsorbed in the pores (Figure 3). Zeolites are highly-ordered aluminosilicates with a variable amount of aluminium substituting silicon in the framework (Figure 3). This amount of aluminium is generally expressed as an Si:Al ratio which can range from anywhere below 1:0 to 1:1. This ratio has to be below 1:0 as a complete lack of aluminium would mean the structure is not an aluminosilicate and therefore not strictly speaking a zeolite, and above 1:1 as a value less than this would mean Al–O–Al bonds would be present which is not allowed for two aluminium tetrahedra. As proposed by Löwenstein, such structures are unfavourable due to the electrostatic repulsion of the neighbouring aluminium cations.[12]

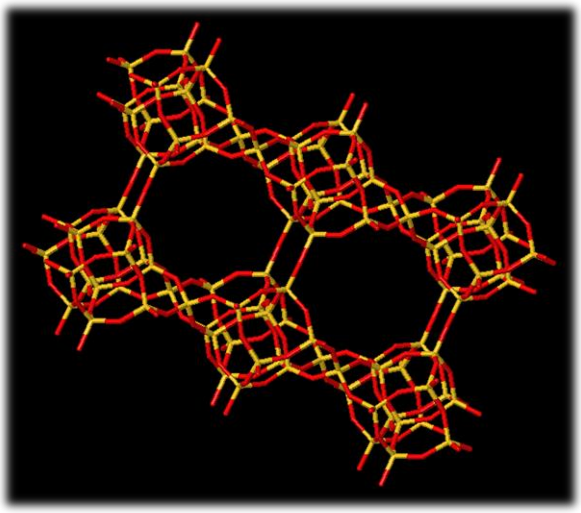

Figure 3: Representation of zeolite framework STI, to which stilbite, the mineral that the Swedish mineralogist Cronstedt observed liberates large amounts of steam when heated, belongs. Aluminium and silicon are depicted in yellow, oxygen in red.[13]

Although the earliest work on zeolites was performed using natural materials, the discovery of some 20 synthetic zeolites by Breck *et al.* at Union Carbide Corporation (UCC) in the late 1940s and early 1950s[14] caused a breakthrough that eventually led to their large-scale adoption in industry.[15] That this discovery was far from trivial is illustrated by the revenue this field generates, as molecular sieves currently encompass a multi-gigadollar industry.[16]

The earliest zeolites to be used for adsorptive and catalytic purposes, zeolite A and zeolite X,[15] discovered by Milton *et al.* and patented in 1959,[17] were aluminium-rich. Over time however, frameworks and materials of gradually higher degrees of siliceousness (*i.e.* Si:Al ratio *ca.* 2–5[16]) were discovered during the 1960s,[15] such as zeolite Y by Breck *et al.*[18] and the large-pore Zeolon by Sand,[19] both of which were also adopted for industrial application. Based on an attempt to obtain materials with higher acidity and greater thermal stability than previously known zeolites, Breck's zeolite Y played a monumental role in the catalytic conversion of hydrocarbons.[16] Other intermediate-silica zeolites, such as mordenite, zeolite L, erionite, chabazite, clinoptilolite and zeolite Ω, were also synthesised.[16] Subsequent research led to the development of hydrophobic, high-silica zeolites, such as the important pentasil family. Synthesised by workers at Mobil Oil Corporation, these were reported in the late 1960s and early 1970s,[15] such as zeolite Beta by Wadlinger and co-workers in 1967[20] and ZSM-5 by Argauer and Landolt in 1972.[21] Ever since their inception, these materials have played an important role in shape-selective catalysis.[16]

Incorporation of ever-increasing amounts of silicon eventually led to the synthesis of compounds with no aluminium in the framework at all, composed purely of silicon and oxygen. In 1975, Grose and Flanigen, again at UCC, synthesised the well-known material silicalite, a purely siliceous form of ZSM-5.[22] Silicalite-2, a similar analogue of ZSM-11 but with only straight channels (as opposed to straight and interconnected ones present in silicalite-1), soon followed. The extensive amount of research put into the topic and exploration of zeolites with varying Si:Al ratios, as well as different structures, thermal stabilities, acidity, hydrophobicity/hydrophilicity, and ion-exchange capability, has been said to "greatly facilitate the applications of zeolites and stimulated industrial processes."[16] Zeolites applied in industry, both synthetic and natural, include zeolites A, X, Y, L, Ω, Zeolon, mordenite, chabazite, erionite, and clinoptilolite. Their main applications can be divided into catalysis, separation and ion-exchange. A number of these applications are shown in Scheme 3.

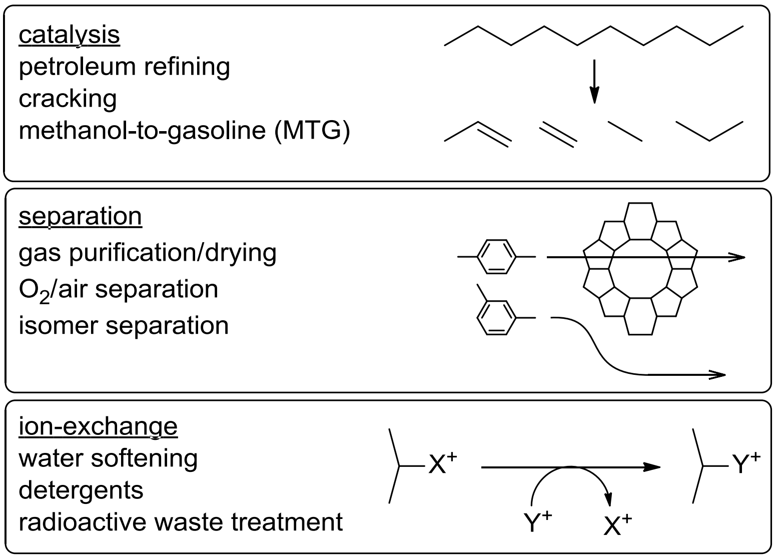
catalysis
petroleum refining
cracking
methanol-to-gasoline (MTG)
separation
gas purification/drying
O2/air separation
isomer separation
ion-exchange
water softening
detergents
radioactive waste treatment
X+
Y+
Y+
X+

Scheme 3: Outline of major industrial applications of zeolites.

In the petrochemical and oil refining industries in particular zeolites have achieved notable use as solid acid catalysts for the alkylation of hydrocarbons as their use circumvents the waste and handling problems inherent to reagents like sulfuric and hydrofluoric acids, aluminium trichloride *etc.* Moreover, compared to amorphous aluminosilicates, the crystalline zeolites require milder reaction conditions, lower capital investment and often have greater flexibility.[8]

A major consequence of the presence of aluminium in the framework of aluminosilicates is the presence of a net charge. This is because the substitution of an Si^{4+} site for an Al^{3+} site results in a negative net charge on the framework. This net charge attracts cations which compensate for this charge. These cations can be flexibly exchanged, giving zeolites their ion-exchange capability. As silicates lack this framework charge, they are not capable of ion-exchange (Scheme 4).

The same group at UCC that was responsible for the synthesis of pure-silicon frameworks would later achieve another milestone in the field during their investigation of frameworks and molecular sieves that were not based on silicon at all. In 1982, Wilson, Lok and Flanigen synthesised the first family of framework oxides that were completely silicon-free.[23] This comprised of *ca.* twenty structures made up of alternating tetrahedral AlO_4 and PO_4 units, with the overall chemical formula of $AlPO_4$, called aluminophosphates (Scheme 4). The nomenclature for these structures is "AlPO-*n*" with the number *n* being used to differentiate between the different structures (Figure 4). Most of these structures were novel, but three (AlPO-17, AlPO-20, and AlPO-24) were isostructural with known zeolites[23] (erionite (IZA structure code ERI), sodalite (SOD) and analcime (ANA) respectively), albeit made up of different atoms. Such structures are known as zeotypes, to distinguish them from their aluminosilicate zeolite cousins. Particular attention, both then and in the years to follow, was paid to structure number 5 (*i.e.* AlPO-5, IZA structure code AFI), which was a novel structure with no known natural zeolite analogue, but whose structure corresponded to "net no. 81" hypothesised by J. V. Smith several years prior.[24]

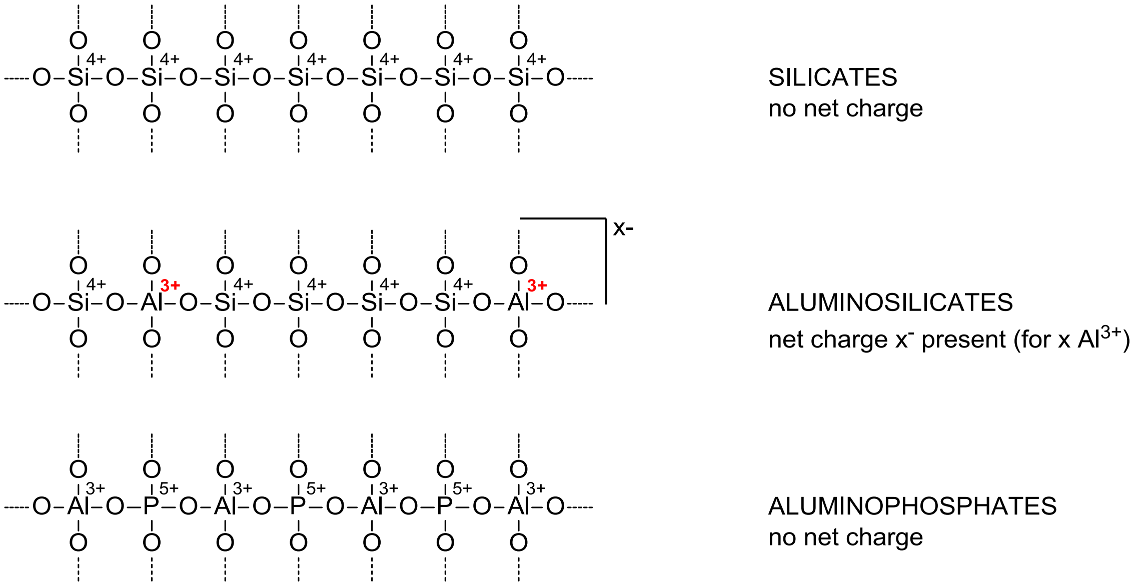
4+
3+
5+
x-
SILICATES
no net charge
ALUMINOSILICATES
net charge x⁻ present (for x Al³⁺)
ALUMINOPHOSPHATES
no net charge

Scheme 4: Schematic representation of silicates (top), aluminosilicates (middle) and aluminophosphates (bottom).

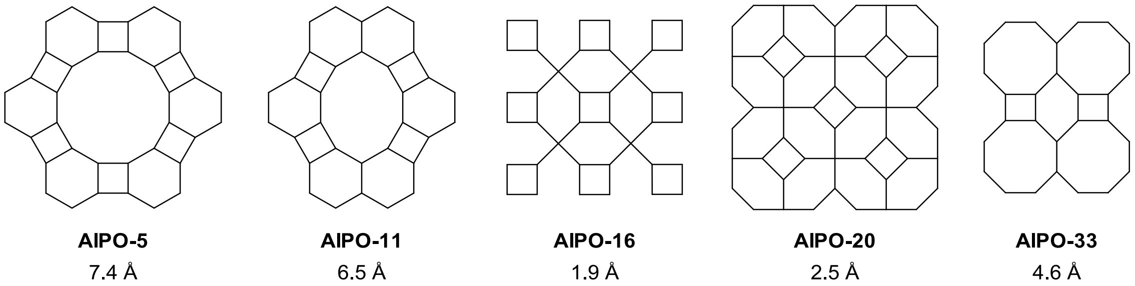
AlPO-5
7.4 Å
AlPO-11
6.5 Å
AlPO-16
1.9 Å
AlPO-20
2.5 Å
AlPO-33
4.6 Å

Figure 4: 2D-view of some of the aluminophosphate frameworks discovered by Wilson et al.[23] Pore sizes are noted below the structure, measured in Å.

Whereas the siliceous networks of silicates consisted solely of Si^{4+} tetrahedra, aluminophosphates substitute these for Al^{3+} and P^{5+} tetrahedra. Due to the strict alternation of these two sites, no charge imbalance is present when Al^{3+} and P^{5+} substitute for Si^{4+}, and an inherently neutral network is obtained.[23] This means that the frameworks have very low acidity or other ion-exchange capabilities.[15] AlPOs possess a mild hydrophilicity,[25,26] and can be synthesised by using a specific organic template, generally alkylated amines or alkylammonium cations.[23] This strategy of using an organic template to effect structure specificity during synthesis was developed during the 1960s by scientists at Mobil for the fabrication of their high-silica zeolites.[16]

It was reported by Wilson *et al.* in their initial study that the newly introduced synthetic aluminophosphates had widely different specificities with respect to the organic templates. For example, AlPO-5 was formed by as many as 23 different templates, while AlPO-20 was formed by just one.[23] Template specificities also show great variation with some templates giving specific structures, while others can direct the formation of multiple frameworks (more than ten in the case of Pr_2NH!).[26]

The project culminated in the successful incorporation of yet other metals as dopants in the structure, as reported by Flanigen *et al.*[15] This is considered to be another major development in the field of porous materials, as their functionalisation with metal ions allows for a potentially vast amount of active frameworks to be synthesised.[16,26] The first element to be included was silicon ("SAPOs"),[27] and by 1986, a total of thirteen elements were recorded to be successfully incorporated into the structure (Table 1).[15] Subsequently, researchers have reported the incorporation of other metals, such as V and Cr, and even combinations of metals.[28]

AlPO-*n*	IZA code	ring size	dopants
5	AFI	12	Si, Co, Fe, Mg, Mn, Zn, Be, Ga, Ge, Li, Ti
31	ATO	12	Si, Co, Fe, Mg, Mn, Zn
36	ATS	12	Co, Mg, Mn, Zn, Be, Ga
37	FAU	12	Si
40	AFR	12	Si
46	AFS	12	Co, Fe, Mg, Mn, Zn
11	AEL	10	Co, Fe, Mg, Mn, Zn, As, Be, Ti
41	AFO	10	Si, B
14	AFN	8	Mg, Zn
17	ERI	8	Si, Co, Fe, Mg, Ga, Ge
18	AEI	8	As, Ga, Ge, Ti
34	CHA	8	Si, Co, Fe, Mg, Mn, Zn, Be, Li, As, B, Ge, Ga, Ti
35	LEV	8	As, B, Ge, Ti
20	SOD	6	Mg, Co, Fe, Mn, Zn, Be, Ge, Ga, Li, Ti

Table 1: Summary of framework types and dopants found by Flanigen et al.[15]

Several points of interest surround these substitutions. First of all, the substituted ions can be incorporated into the crystal lattice of the material itself, becoming an inherent part of the structure.[23] This is in contrast with methods commonly employed for functionalising (alumino-)silicates such as grafting, tethering/anchoring and (in the case of aluminosilicates) ion-exchange where the ions end up outside the framework. Substitutions of the kind described here allow one to retain the precisely defined structure of the framework without irregularities as observed with grafting and anchoring of moieties.

Second, the substitutions can be performed isomorphously, *i.e.* the dopant metal takes on the same coordination geometry as that of the original framework elements.[25] As a result, the incorporation of the new metal causes little or no lattice distortion. This is an important consideration for stability, as disruptions of the crystal lattice can lead to framework collapse during calcination or the leaching of metals out of the catalyst and into solution during reactions, leading to catalyst deactivation or homogenisation.

1. Introduction

As outlined by Martens and Jacobs,[25] there are three types of isomorphous substitution, illustrated in Scheme 5. Type I substitution consists of replacement of an aluminium tetrahedral site ("T site") by a dopant metal M. In type II substitution, a phosphorus T site is replaced instead. Meanwhile, type III substitution has both Al and P T sites replaced, in pairs. Although most metals will preferentially engage in one type of substitution, it is possible for metals to engage in multiple types, even at the same time.[10]

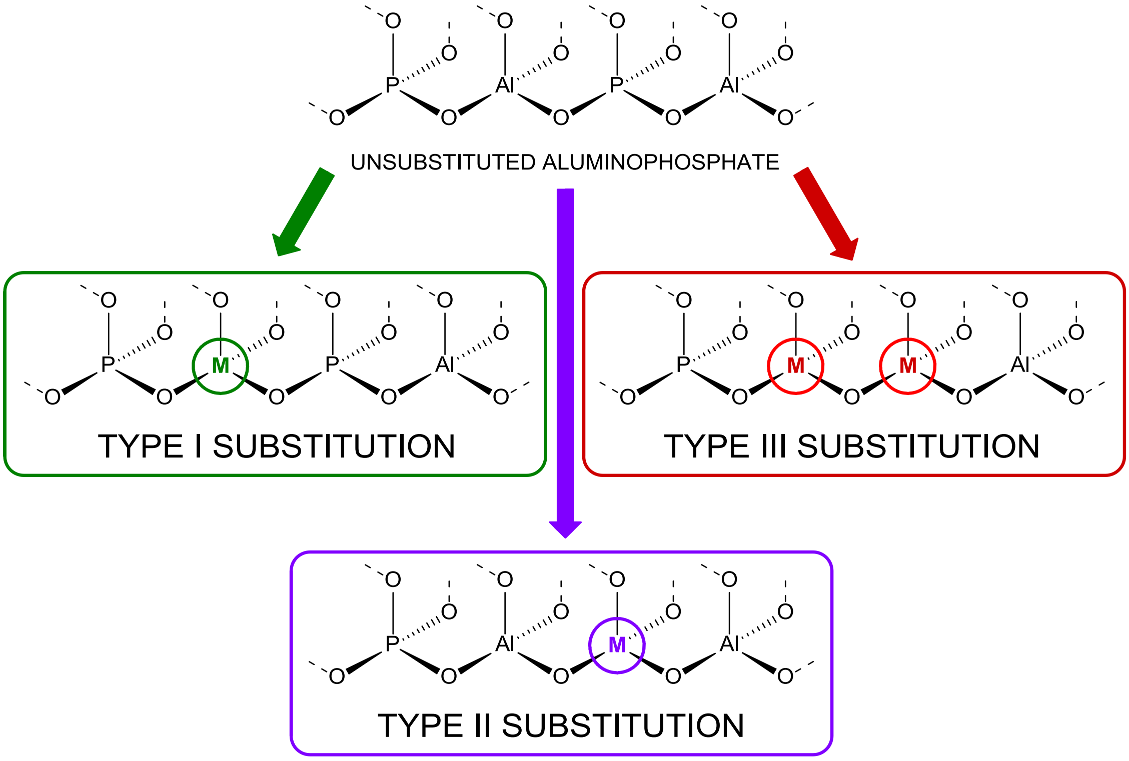

Scheme 5: Outline of types I, II and III isomorphous substitution.

Furthermore, when a metal of a valence different than the parent T site element is introduced, a charge imbalance is created. For example, when an aluminium centre, which in AlPOs has a charge of 3+, is substituted by a divalent metal ion such as Co^{2+}, Mg^{2+}, Zn^{2+} *etc.* a +1 charge deficiency is introduced, which in turn is compensated by a H^+ cation bound to a framework oxygen[29] (Scheme 6). As a result, the framework becomes acidic.[30] Similarly, acidic sites can be generated when an M^{4+} dopant replaces a P^{5+} ion.

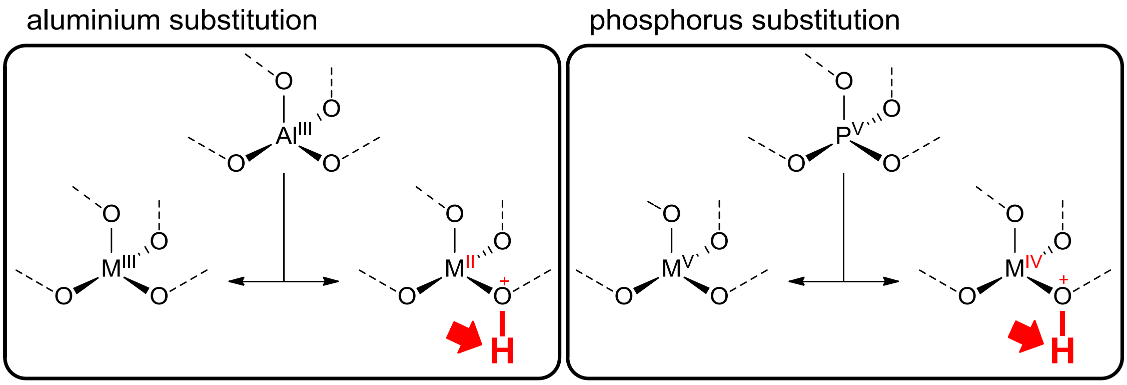

Scheme 6: Demonstration of charge-deficient type I (left) and type II (right) substitution by M^{2+} and M^{4+} metal ions, respectively. A compensatory proton is shown in red, pointed out by the red arrow.

The Brønsted acidity of the resulting sites is dependent on the type of metal dopant employed, their concentration, and the framework type they are substituted into. The variation of Brønsted acidity has been attributed to several factors such as the ionic radius and electronegativity of the heterometal.[30] Several computational studies have concluded that the bond angle between the neighbouring T sites on either side of the oxygen that bears the Brønsted proton is a major factor.[30-32] However, in studies by Elanany[33] and Saadoune[34] it was concluded that this angle-based determination of acidity was not valid for when M^{2+} substitutes for Al^{3+} — only M^{4+} substitution for P^{5+} was found to obey this model.

Moreover, catalytically active transition metal centres can be substituted into the structure, to afford a framework capable of catalytic conversions. This generally concerns redox-active metals such as Co, Ti, V, Cr, or Mn.[29,35] For example, the inclusion of Co^{3+} sites in the framework leads to an AlPO that can catalyse the oxidation of linear alkanes.[36] This concept is explained in more detail in Sections 1.4 and 1.5.

In addition to active metal centres, these aluminophosphates, having zeolite-like networks, can profit from their well-defined pore dimensions. This allows reactions to be conducted under, for instance, shape- and size-selective conditions, limiting the kinds of substrate that can get into the pores, or the kinds of product that can get out of them. As such, these pore environments can be a powerful tool to enhance selectivity during catalysis.[37]

1.4 Single-site catalysis and catalyst design strategies

One of the many modern strategies designers of catalysts try to employ is the use of “single-site” active centres.[37] This means that the catalytically active sites are spatially well-separated from each other, and do not show any inter-site interaction. Because none of the sites “see” each other, they show a high degree of similarity in their properties and reactivity, because the energy with which each reacts with substrates in catalysis is the same.[38] As a result, spatially separated active sites are expected to provide a high selectivity in chemical reactions, and the high dispersion is expected to yield catalysts of superior activity.[37-39]

According to Sir John Meurig Thomas, “It is universally acknowledged that one of the supreme advantages of homogeneous, molecular catalysts — when they operate under ideal conditions — is that their active sites are spatially well separated from one another, just as they are in enzymes.”[37] Conversely, certain heterogeneous catalyst systems, such as those based on metals or alloys, oxides, sulfides and chlorides, contain active sites that are bonded closely to each other, showing considerable inter-site interaction. As a result, these sites show unpredictable behaviour, and even simple catalytic conversions, such as oxidation of CO to CO_2 using O_2 can cause complications.[37]

Furthermore, the strictly defined electronics of single sites carry with them several other advantages. For example, chemical and spectroscopic analysis of active sites of a single nature is considerably more straightforward than those of bulk species. Along similar lines, computational models become more reliable and less complex. Finally, the notion of single sites offers a basis for the design of new solid catalysts.[38]

By designing framework catalysts in which the active sites are incorporated into the structure as single, spatially separated metal ions, for example, one is able to heterogenise and immobilise these sites while still retaining these desirable properties. There are several strategies for functionalising a solid support with metal ions, such as anchoring the sites on the surface of a support (by grafting or tethering), trapping the metal ions or metal ion complexes within pores in the structure (“ship-in-a-bottle”) or including the metal ions within the carrier structure by direct framework substitution (Figure 5).

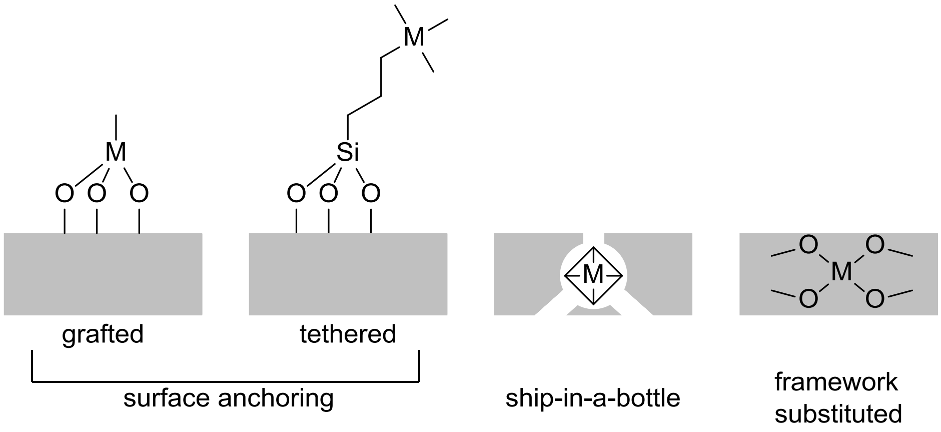

Figure 5: Catalyst functionalisation techniques.

Anchoring a metal site on a solid support can be done directly (by grafting) or by suspending the metal ion or complex from a linker anchored to the surface (tethering). A well-known example of a successful single-site catalyst of this type is the Shell catalyst developed and commercialised during the 1970s for the oxidation of propylene to propylene oxide.[40,41] This catalyst, consisting of titania deposited on silica, was the first "truly heterogeneous epoxidation catalyst for continuous operation in the liquid phase."[8] In this system, the Ti^{4+} centres are anchored to the SiO_2 surface via three SiOH groups[42] which cause an increased Lewis acidity through electron depletion on titanium. As well as this electronic effect, the site-isolation of the titanium ions is believed to be the main reason for the catalyst's superior performance, as well as its excellent stability.[8]

Examples of ship-in-a-bottle catalysts are metal-complexing phthalocyanines (Pc), porphyrins and Schiff-bases immobilised within the pore cavities. These complexes are too large for the pore aperture, and are therefore entrapped in the zeolite cages. The design strategy behind many of these materials is to provide an inorganic mimic to the enzyme cytochrome P450, combining the selectivity of the metal complexes with the molecular sieve properties of the zeolite structure. Moreover, the incarceration stabilises the complexes against dimerisation and clustering.[43] Several reports make mention of selectivity-enhancing or selectivity-changing effects using these materials (summarised in Table 2). For example, Balkus Jr *et al.* noted that in the competitive oxidation of cyclohexane and cyclododecane over perfluorinated Ru-phthalocyanines, there was a clear preference for the oxidation of the smaller cyclohexane, while the two were oxidized at roughly equal speed by the free complex.[44] A similar observation was made between the oxidation of *n*-hexane and cyclohexane.[45,46]

Catalyst	**Substrate(s)**	**Outcome**	**How achieved?**	**Ref**
Perfluorinated RuPc in NaX	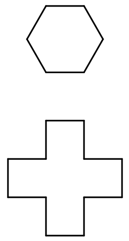	Greater oxidation of the smaller substrate	Steric constraints of the zeolite channels control substrate diffusion	44
FePc in NaX/NaY	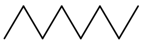	Less C4-oxidation More C2-oxidation	Orienting effect of zeolite facilitates “head-on” approach	49
Fe/Pd-exchanged zeolite 5A	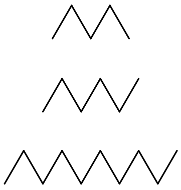	Primary oxidation is enhanced	Control over substrate conformation during oxidation	45,46
	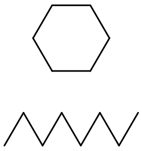	Preference for linear substrate	Molecular sieving action of the framework	*ibid.*
FePcY suspended in PDMS membrane	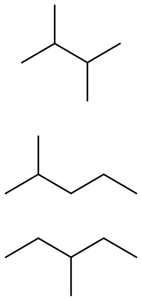	Higher conversion of mono-branched substrates	Steric constraints on the active site	47
FePcY	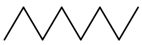	Greater ketone product selectivity	Enhanced constraints by deformation of the active site	48

Table 2: Catalytic results of alkane oxidation.

The shape and size of the zeolitic framework on the active site itself has also been reported to influence selectivity. Jacobs *et al.* reported that in the oxidation of branched C6 hydrocarbons using Fe-phthalocyanines suspended in a polydimethylsiloxane (PDMS) membrane, there was a greater preference for the oxidation of mono-branched substrates due to steric constraints on the active site.[47] They also found that in the oxidation of *n*-octane, there was a greater product selectivity for ketones due to the deformation of the otherwise square-planar phthalocyanine complex into a saddle shape within the pore structure.[48]

Moreover, these materials have been used to affect regioselectivity by controlling in what manner the substrate approaches. Herron *et al.* reported that in the oxidation of *n*-octane, the preference for C2-oxidation increased over that of C4-oxidation.[49] The reason behind this is that the linear alkane, as it “pokes” through the pore window, meets the active site head-on, enhancing the reactivity at the ends. A similar “head-on” strategy was used to increase the preference toward various linear alkanes using Fe/Pd-exchanged zeolites, where the substrate conformation during the oxidation was said to be greater in the zeolitic environment.[45]

The synthetic challenge of trapping the metal complexes inside such materials has been addressed in three different ways (Scheme 7). The first employs a flexible ligand which can deform in such a way that it can diffuse slowly through the pores. Inside the pore cages it encounters the metal ion (included through ion-exchange) which it coordinates. The subsequent complex becomes rigid and can no longer exit the cage. The template synthesis method involves ion-exchange of the metal ion into the cages and subsequently building the coordinating ligand around it by diffusing in building blocks. The zeolite synthesis starts off with the synthesis of the entire metal complex and subsequently builds the framework around it.

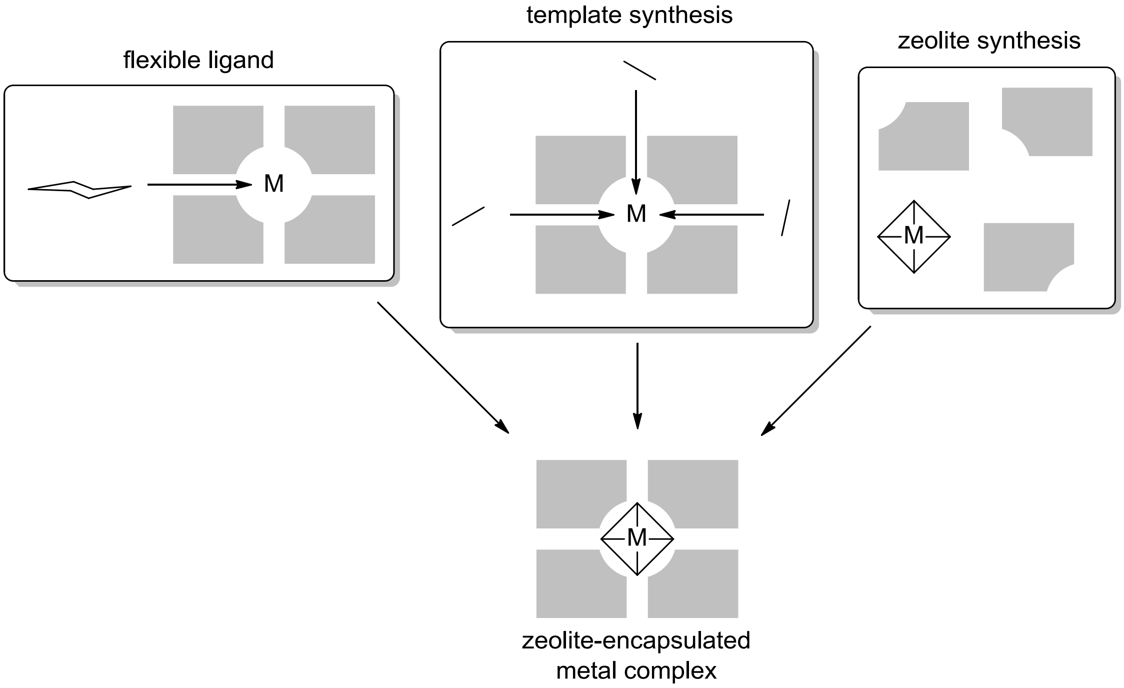

Scheme 7: Synthetic methods for introducing porphyrin/phthalocyanine metal complexes within a zeolitic superstructure.

In framework-substituted catalysts, metal ions are directly incorporated into the carrier material by replacing one of the framework ions (as with isomorphous substitution described in Section 1.3). One advantage of this design is that it can be applied to a wide variety of materials that can be carefully chosen to effect shape- or size-selectivity. Because the structure and dimensions of the pores and cages within the materials is affected less than with grafting, tethering or ship-in-a-bottle catalysts, this allows the full use of the zeolitic framework for shape-selectivity.

Three types of shape-selectivity exist in zeolites (Scheme 8). The first is reactant selectivity. In this process, molecules that cannot diffuse through the pores due to their size and shape cannot gain access to the inner structure, thereby limiting catalysis to substrates of a certain shape and size. Additionally, this can allow one to limit in what orientation certain substrates approach the active site. The second is transition state selectivity, in which transition states of a certain shape or geometry cannot be formed in such pores. This limits the type of product that can be generated in these reactions. Finally, product shape selectivity controls selectivity by limiting the type of product that can exit the pores. Results based on shape-selectivity are given in Section 1.6.

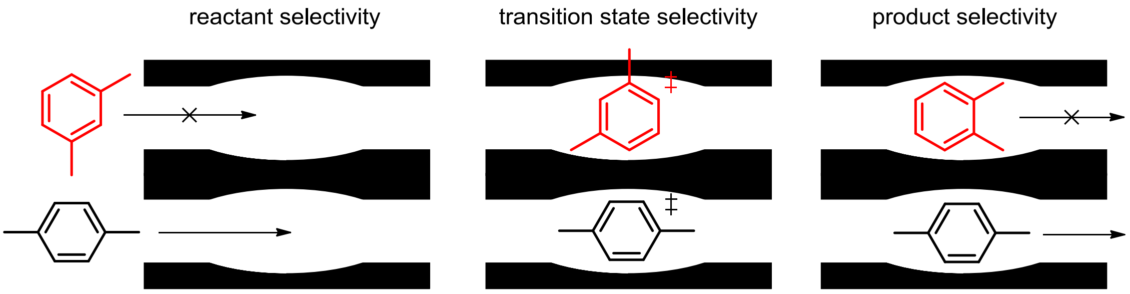

Scheme 8: Schematic representation of different types of shape selectivity. Left: red molecule is the wrong shape and cannot enter the catalyst. Middle: red transition state does not fit inside the catalyst cage and cannot form. Right: red molecule is too bulky and cannot exit the pore.

1.5 C-H oxyfunctionalisation

C-H bond activation, such as some of the results discussed in Section 1.4, has always been one of the “Holy Grails” of organic chemistry. C-H bonds are ubiquitous in nature, and because of this, materials containing them are abundant. In industry, particularly the petrochemical industry, products and by-products consisting of hydrocarbons are legion. As such, being able to activate these materials towards oxyfunctionalisation into more valuable products, such as alcohols, ketones, acids and peroxides carries with it great potential value.[50] Furthermore, because the starting materials tend to be cheap and abundant, economically viable protocols that make their functionalisation possible are highly sought after, especially by the pharmaceutical industry. During the last century, an enormous amount of research effort has been devoted to C-H activation.[51]

The reason that these Holy Grails are so highly prized also constitutes their biggest problem — specific and predictable C–H bond activation is far from trivial. Carbon-hydrogen bonds are generally strong and unpolarised, making them hard to functionalise without resorting to powerful reagents.[52] Despite over 100 years of research into the topic, C-H activation remains one of the hardest transformations in chemistry.[50,53] Indeed, this inertness has long been recognised as evidenced by paraffin, which takes its name from this property (in Latin, *parum affinum* means “slight affinity”).[52] Hexane for example is not attacked by boiling nitric acid, concentrated sulfuric acid, potassium permanganate or by chromic acid.[52,54]

Naturally, these hydrocarbons are not absolutely inert. Indeed, their complete oxidation to CO_2 is readily achieved simply by lighting them in a fire, forming CO_2. Small hydrocarbons are extremely flammable, so this process is not difficult to achieve. Importantly, such exhaustive oxidation adds no value as industrial-scale production of CO_2 from hydrocarbons is wasteful. The real potential lies in selective oxidation but not the *overoxidation* of C–H bonds.[52] Therefore, henceforth, when discussing C–H oxidation, it will refer to oxidation of C–H bonds to a lesser degree than to CO_2.

Although a wide variety of reagents *are* capable of oxidising C–H bonds, many of these have serious shortcomings or disadvantages. Traditionally, many C–H oxidation reactions are performed using oxides or salts of heavy metals such as cobalt, manganese or chromium, generally stoichiometrically or in excess. These expensive reagents are typically very powerful oxidants that are unselective and incompatible with other functional groups.[53] Moreover, their use, especially on a large scale, is concomitant with the production of great amounts of heavy metal waste which is contrary to the increasingly stringent environmental demands set by governments and institutions in today's society.[52,55]

Traditional oxidants in organic chemistry include a wide variety of materials that tend to be extremely toxic, hazardous to handle or store, expensive, polluting, unselective or a combination of the above. Many are still in use today. The "textbook" methodology is by using potassium permanganate or potassium dichromate[55-57] — however, other Cr and Mn salts, a variety of cobalt salts, peroxyacids, oxone, SeO_2, BTSP, DDQ and others have also been employed regularly, often in the presence of strong mineral acids such as H_2SO_4. In addition, these reagents are generally used stoichiometrically or in excess,[55-57] generating large amounts of toxic waste.[58-60]

The industrial production of hydroquinone from a variety of starting materials (Scheme 9) provides a good example. According to *Industrial Organic Chemistry* by Weissermel and Arpe, "as in the USA and Europe, in Japan most hydroquinone is still produced by reducing *p*-quinone with iron [in HCl] at 50–80 °C. The *p*-quinone feed is obtained from aniline involving a complex reaction involving oxidation with MnO_2 or CrO_3 in a solution with H_2SO_4:

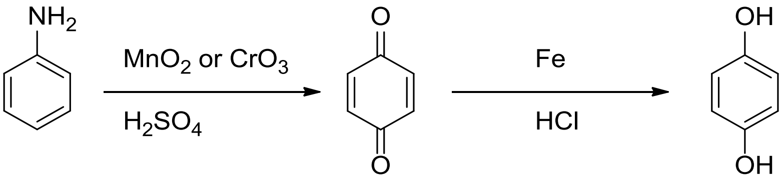

Scheme 9: Industrial production of hydroquinone.

The process is burdened by considerable formation of manganese, chromium and iron salts, and ammonium sulfate. [...] Another process (Rhône-Poulenc) involves the oxidation of phenol with performic acid, or mixtures of H_2O_2 with carboxylic acids or mineral acids such as H_3PO_4 or $HClO_4$, at 90 ˚C and with low phenol conversion (<10%)."[61]

These unacceptable disadvantages have led researchers to develop alternative oxidation catalysts during the last few decades, predominantly based on the use of catalytic transition metals and benign oxidants.[55] Indeed, more and more approaches using less environmentally-demanding protocols are being used today. Among the approaches so far advertised as more environmentally friendly are hypervalent iodine compounds,[56,57] Cp*-Ir complexes with periodate reagents,[62] periodic acid with CrO_3,[63] Cr-ZSM-5,[55] many transition metal complexes and species including ones based on Co,[64] Cr,[65] Mn,[50] Ru,[66,67] Rh[68,69], Zn,[70] Bi,[71] and V,[72] and enzymatic approaches.[53,73] Nonetheless, some problems still persist, as many of these catalysts are based on toxic metals or their applicability is limited due to low turnover numbers and rapid deactivation of the catalyst.[56,57,72] The environmental desirability of some of these solutions, such as the hypervalent iodine and CrO_3 approaches, is also debatable due to the nature of the by-products of their use.

As a result, procedures that open up alternative approaches can be a valuable asset. Catalytic oxidation procedures using aluminophosphate materials have been reported using milder, more ecologically friendly oxidants such as alkyl hydroperoxides, acetyl peroxyborate (APB), H_2O_2 or even molecular oxygen.[54,74-79] As such, in the research presented in this thesis, there will be some focus on avoiding aggressive, highly polluting stoichiometric oxidants in favour of aforementioned mild peroxides or molecular oxygen.

C–H oxidation of alkylbenzenes such as those discussed previously is conducted on a huge scale in industry. In particular, one of the most prominent and well-known processes is the industrial C–H oxidation of ethylbenzene (EB) to form styrene. Virtually all EB is used in the manufacture of styrene.[80] This process is based on the aerial oxidation of EB to ethylbenzene hydroperoxide (EBHP) and subsequent reaction with propylene to form propylene oxide (PO) and 1-methylbenzyl alcohol (MBA), which is subsequently dehydrated to styrene monomer (SM) (Scheme 10). As SM and PO are produced concomitantly in this reaction, production of one is inevitably linked with that of the other. The process also constitutes the primary global source of acetophenone (ACP), as it is the main by-product of the reaction (formed by termination of the secondary 1-methylbenzylperoxy radicals during the oxidation of EB as well as the epoxidation of propylene).[81-83]

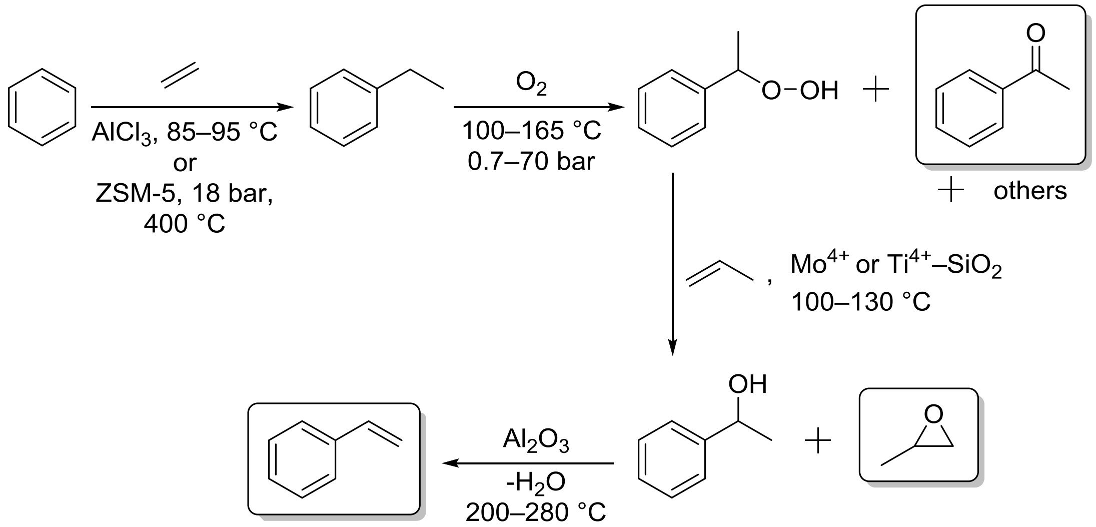

Scheme 10: General outline of the POSM/SMPO process. Products are highlighted in boxes.

The process, known as the POSM (Oxirane/LyondellBasell) or SMPO (Shell) process, is a classic example of a “two-for-one” production process and is responsible for 20% of the world’s SM production and 30% of the world’s PO production.[84] Most of the remaining styrene is made by direct dehydrogenation of ethylbenzene (at 550–600 °C using a metal oxide catalyst composed mainly of iron, cobalt, manganese, chromium, or zirconium, as well as several additives). Because of the demand for both chemicals, EB production is massive, at *ca.* 25 000 ktpa in 1999.[82] Over 90% of ethylbenzene itself is produced in industry using Friedel-Crafts reaction of benzene with ethylene.[80] Originally, $AlCl_3$ or solid H_3PO_4 were used as catalysts, but this posed several problems as they and their by-products are corrosive and hard to get rid of. More recently, acidic zeolites such as ZMS-5 have gained popularity.[84]

The first commercialisation of EB oxidation was by Oxirane (now LyondellBasell), a joint venture between ARCO and Scientific Design, in a plant operated by Repsol under license.[84] In the first step, EB is oxidised (non-catalytically) in air under pressure. The reaction is not selective and many products including aldehydes, ketones, acids and alcohols are formed (Scheme 10).[85] In order to maximise selectivity (to *ca.* 65%), conversions have to be kept low at <12% (usually 10%) — above that, formation of by-products such as ACP and MBA increase significantly.[81,84]

The crucial epoxidation step, which relies on the EBHP reagent thusly prepared, is catalysed by a Lewis-acidic metal in its highest oxidation state, of which Mo is the most reactive (as Mo^{6+}, operated by LyondellBasell), although Shell uses a Ti^{4+} catalyst dispersed on silica. The high selectivity and specificity of the reaction has been ascribed to the tendency of the catalyst to follow a heterolytic, rather than a homolytic, pathway.[81]

Although the exact mechanism remains disputed despite considerable research efforts, it is now generally agreed that the epoxidation step is prefaced by coordination of the peroxo ligand to the (Lewis-acidic) molybdenum centre *via* the distal oxygen, followed by oxygen transfer from the peroxometal complex to the C=C bond on propene. Two slightly different possible mechanisms are shown below (Scheme 11).[81] Finally, the MBA produced during the POSM process is dehydrated over titania/alumina at 200-280 ˚C under vacuum to form styrene.[84,85]

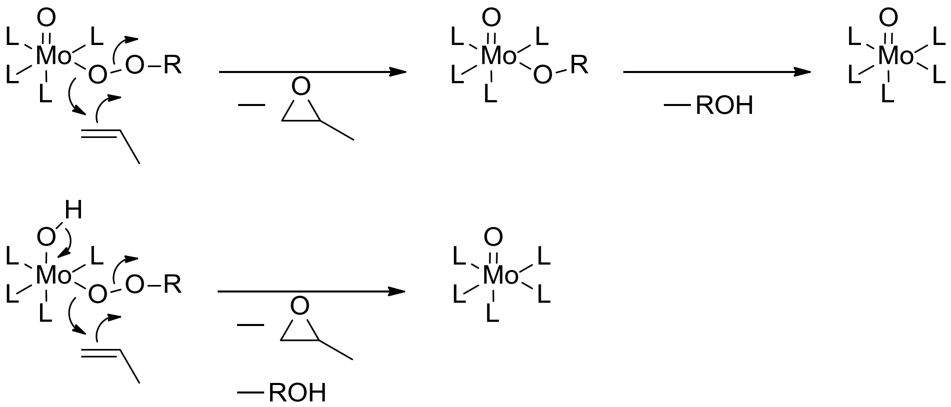

Scheme 11: Possible mechanisms for the epoxidation of propylene in the Mo-catalysed POSM process.

Although the POSM process accounts for a solid 30% of global manufacture of PO producing little waste and operating at a high atom economy, the majority (48%) of PO is produced by the chlorohydrin process (CHPO process).[84-86] This process is non-catalytic in nature and liberates a stoichiometric level of HCl during its formation. The propylene is reacted with chlorine gas and water to form propylene chlorohydrin, which is subsequently dehydrochlorinated, usually in the presence of sodium hydroxide or lime, forming PO as well as brine (see Scheme 12 below). Although this process is complex and costly as well as generative of a large amount of chlorinated waste, it is still used by Dow in the US as well as by several European and Japanese companies, and remains the dominant procedure for PO production.[84]

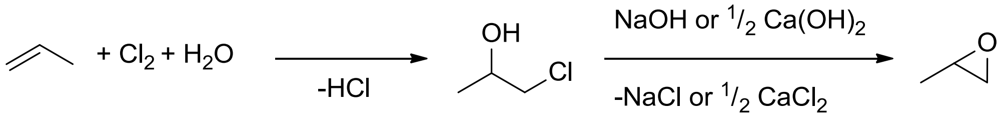

Scheme 12: Outline of the chlorohydrin-propylene oxide (CHPO) process.

A comparable reaction involves the aerial oxidation of isobutane to *tert*-butyl hydroperoxide (TBHP) and *tert*-butyl alcohol (TBA) and subsequent reaction with propylene over a molybdenum naphthenate catalyst to form PO and more TBA (Scheme 13).[84] This process works in a manner analogous to EB oxidation and was again first commercialised by ARCO. It is responsible for another 16% of global PO production.[84] Shell does not operate it, instead focusing solely on EB oxidation. The remaining 8% of global PO production stems from newer, co-product free processes.[84]

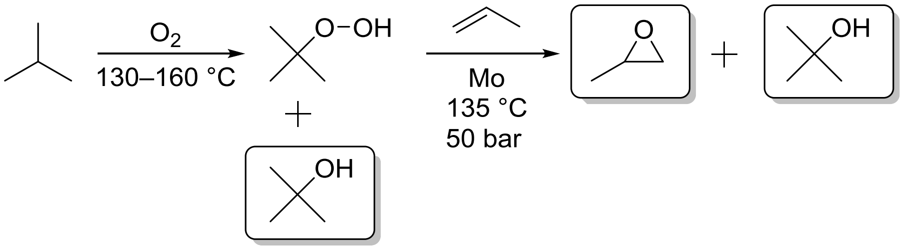

Scheme 13: General outline of the isobutane route to propylene oxide. Products are highlighted in boxes.

Another related process is the oxidation of cumene, also known as the Hock process, after its inventor, Heinrich Hock. Cumene is mainly produced from benzene and propylene using catalytic H_3PO_4, $AlCl_3$ or BF_3. It is then oxidised with air using an emulsifier to form cumene hydroperoxide (CHP) which is first concentrated and subsequently hydrolysed in 10% aqueous H_2SO_4 to form phenol and acetone (Scheme 14).[84] Virtually all cumene is used for this process, and the vast majority of acetone as well as phenol is produced *via* this route at *ca.* 7000 ktpa.[82,84]

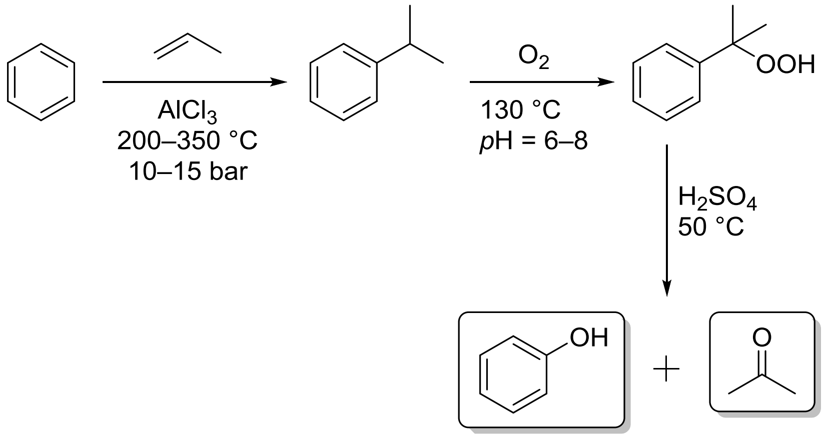

Scheme 14: General outline of the cumene/Hock process. Products are highlighted in boxes.

Another major class of benzylic C–H oxidation is that of toluene, which represents the world's main source of synthetic benzaldehyde, benzyl alcohol, benzoic acid and benzoate salts.[87] Dow performs this process with air as oxidant using aqueous cobalt acetate or cobalt heptanoate as catalyst in a continuous process; average conversion is 35%, and the remaining toluene is distilled off and fed back into the reaction.[87] The reaction is *ca.* 90% selective towards benzoic acid, which among many others is used for the production of phenol (through oxydecarboxylation) alongside the Hock process mentioned above. Other processes use promoters such as AIBN or NaBr to increase the selectivity towards benzaldehyde by preventing over-oxidation at the cost of having to additionally separate the promoters from the product. The promoters also decrease the "lag time" or induction period necessary to form the benzyl radicals that are that are at the heart of this process.[87] At the start of the reaction, these are formed by the Co^{3+} catalyst through hydrogen abstraction. These radicals are vulnerable to attack by O_2, forming the peroxide, which decomposes to form the products through various pathways (Scheme 15).[88]

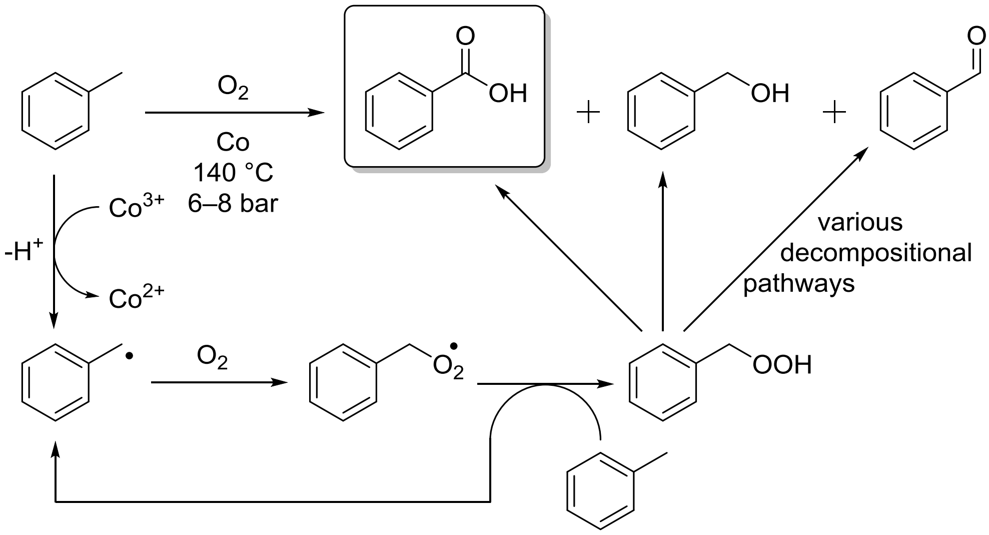

Scheme 15: Toluene autoxidation process.

It should be obvious that although polluting reagents are still being used on large scale in industry, there is a clear trend towards the use of more benign and cheaper oxidants. Apart from the oxidant itself however, a commonly encountered problem with C–H oxidations is regioselectivity — usually of great importance in the fine chemicals industry.

1.6 Catalysis using AlPOs

As mentioned in Section 1.5, two driving forces for the development of new catalysts in C–H oxidation are the search for milder reagents and those processes that are more (regio-)selective. Progress towards this has been achieved using, among others, metal-substituted aluminophosphates. Thomas and Raja *et al.* have used these AlPOs to good effect in a variety of catalytic reactions[89,90] such as the oxidation of alkanes,[36,54,91] lactamisation of ketones,[92] oxidation of cyclohexane and hexane to adipic acid,[52] and the oxidation of toluene to various products[93] (Scheme 16).

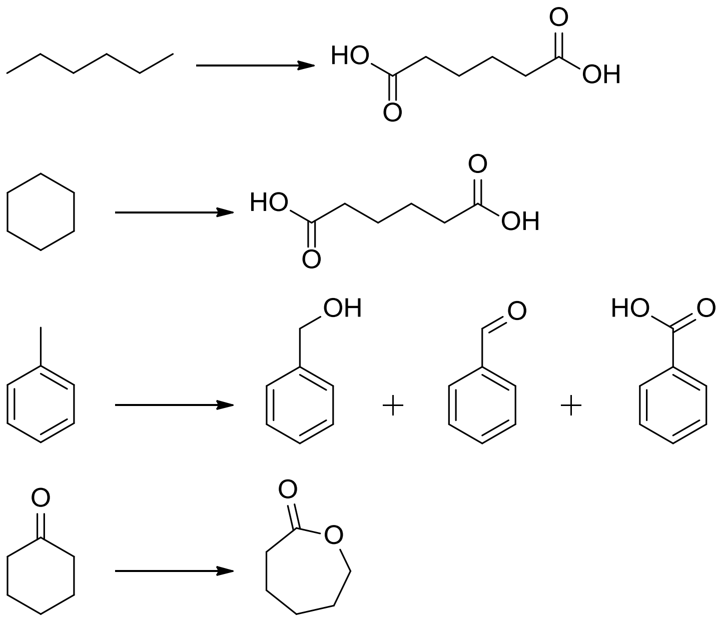

Scheme 16: Examples of the work conducted by Thomas and Raja et al.

Among their findings was the realisation that these materials can provide products in a regioselective manner. For example, the iron-catalysed oxidation of cyclohexane gave different products depending on what framework the iron was substituted in. Thus, FeAlPO-5 yielded primarily cyclohexanol and cyclohexanone, while FeAlPO-31 yielded mostly adipic acid.[94] This difference in reactivity was attributed to the smaller pore size of AlPO-31 (5.5 Å for AlPO-31 compared to 7.4 Å for AlPO-5), through which the cyclohexanol/cyclohexanone product has trouble diffusing, facilitating further oxidation to adipic acid.

A possible break-through was reported in 2006 with the oxidation of hexane to adipic acid using CoAlPO-34 and CoAlPO-18, both of which have narrow pore "cages" (3.7 and 3.6 Å, respectively). The design choices behind the catalyst employed in this reaction are as follows: the catalyst employs two metal ions in its structure to affect catalysis. One metal is used to guide the oxidant toward the redox site in the catalyst structure; another metal is used to perform the oxidation, while pore shape and metal particle distribution in the catalyst itself provides the selectivity the reaction needs.[54,76] Specifically, metal particles at opposite ends of a cage structure encourage oxidation to occur at the termini of the molecule, preferentially forming products such as adipic acid (Figure 6). In a similar procedure, regioselective oxidation of dodecane was performed by forcing an "end-on" approach of the substrate to the catalytic sites. As in order to diffuse through the pore channels, the molecule had to orient itself in such a way that it would go head-first into the pore cavities, oxidation occurred solely at the "head" of the facilitating regioselective oxidation at the terminal carbon.[37]

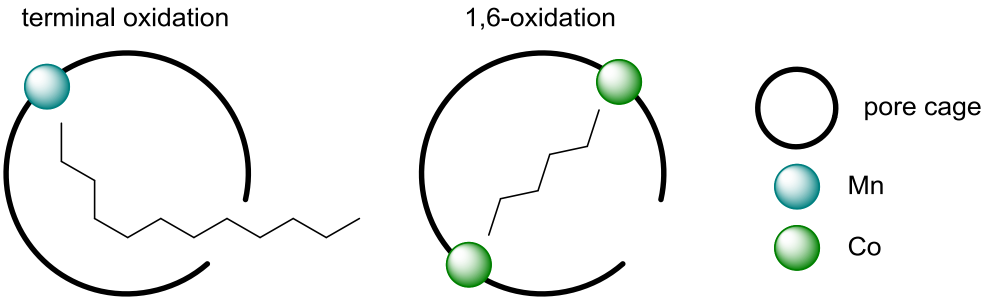

Figure 6: Left; dodecane molecule being only partially inserted into the pore structure of a catalyst due to the limited pore size. Right; a molecule of n-*hexane inserted into a pore structure, facing two redox sites at opposite ends of a catalyst cage unit, promoting terminal oxidation at both ends.*

This oxidation of hexane to adipic acid is quite fascinating if one considers the struggles this reaction should theoretically pose. The oxidant used in the reaction — just air — is very mild, yet it is able to oxidise the compound all the way to the di-acid. Moreover, the attack occurs preferentially at the terminal carbon atoms, which are more stable than secondary C–H bonds by almost 10 kcal/mol (104 v. 94.6 kcal/mol).[36] Though not fully selective (other C1- and C2- and trace C3-oxidised products are also formed), generally selectivity for terminal oxidation is around 65%.[36,54,75] The reaction also gives limited yields,[94] but this can be seen as an advantage, as the production of high amounts of polar compounds can lead to the leaching of transition metals.[8,36,52] Despite this, the immense potential of this reaction should speak for itself. See Scheme 17 for an outline of the results found by Raja *et al.*

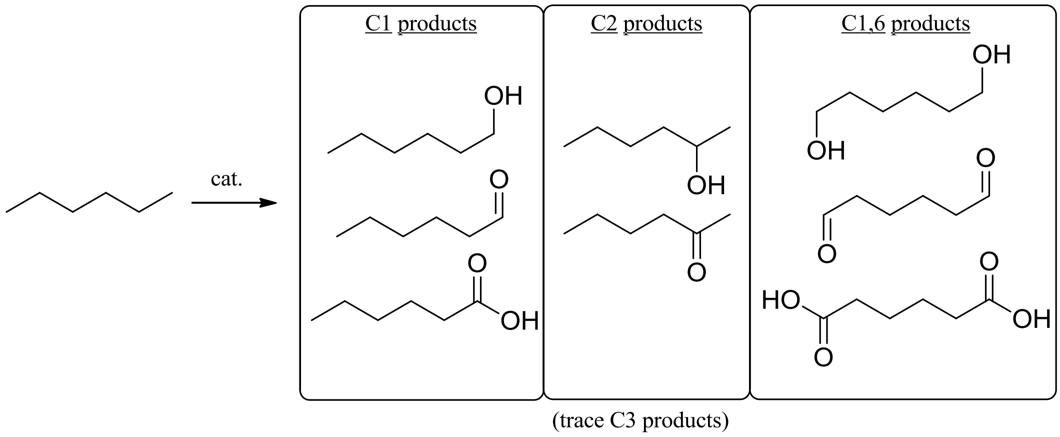

Scheme 17: Oxidation of hexane to adipic acid.[54]

As mentioned before, the main product of this reaction is adipic acid. The primary use of adipic acid is as a precursor to, among others, Nylon 6,6, which in turn is a component of clothing, adhesives, tire reinforcements and upholstery.[77] While this means adipic acid is in constant demand, it is a huge bulk chemical, with over 2 mtpa produced cheaply in industry.[61] While this transformation is unquestionably useful, it would be interesting to see how far this kind of chemistry can be taken, and especially, if it can be applied for the synthesis of higher-value compounds.

Another example of the potential of AlPO chemistry is the (again industrially relevant) conversion of methanol to a variety of hydrocarbons. This process, known as the methanol-to-gasoline (MTG) process, was first put forward by Mobil in 1977 by Chang and Silvestri.[95] The procedure, at first carried out using acidic ZSM-5, ultimately yields mostly C_4–C_{10} products which make up the light petroleum ether/”gasoline” boiling range. This development has piqued considerable interest mainly due to its potential to use non-oil resources such as coal and natural gas to produce basic petrochemicals, thereby providing a link between the coal/gas and petrochemical industries.[96-100] Since then however, it has been found that the use of small-pore zeolites and zeotypes can strongly shift the selectivity to C_2–C_4 olefins, of which ethylene and propylene are particularly attractive. This process, named methanol-to-light-olefins (MTO), was industrialised by UOP and Norsk Hydro using the proprietary silicon-doped small-pore SAPO-34 sieve. The high selectivity towards ethylene and propene during this transformation has been attributed to the small pore cages of the SAPO-34 framework (ø 3.7 Å) from which molecules bigger than propene have difficulty escaping. [98-100] A similar reactivity was observed with a variety of metal-doped AlPO-18 structures (Scheme 18).[37] MTO is most notably practiced in several large plants in North-Western China on a multi-mtpa scale.

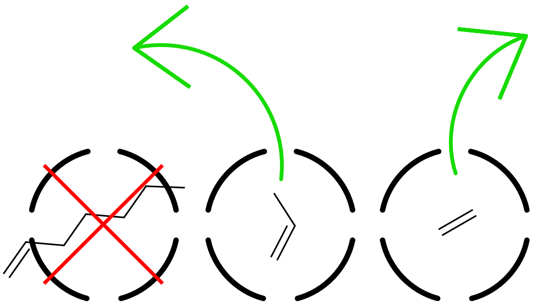

Scheme 18: Illustration of the origin of C_2/C_3-selectivity of MAlPO-18 (M = Zn^{2+}, Mg^{2+}, Mn^{2+} or Co^{2+}). Smaller molecules may exit the pore structure freely (right, middle), but larger molecules are too big for the pore cage (left).

1.6.1 **Vanadium AlPOs**

From an early point on, there has been great interest in the introduction of vanadium into aluminophosphates ("VAPOs") because of their promising catalytic properties.[28,101] Although vanadium was not one of the original thirteen transition metals incorporated by Flanigen in her aforementioned 1986 paper, her group at Union Carbide were the first to patent it.[102] The problem she originally encountered, as did Miyamoto after her,[103] was that the materials synthesised were evidently not pure, based on adsorption data shown, and contained, most likely, V_2O_5 or a similar species. It was not until 1990 that these issues were resolved and pure VAPO-5 was synthesised for the first time, by Montes *et al.* at Virginia State in cooperation with Shell.[104]

As a very large number of V-based catalysts are employed in industry for a variety of transformations, particularly redox transformations (either catalytically or stoichiometrically),[105,106] attempts at extending this technology to capitalise on the attractive qualities of AlPOs discussed previously seems only natural. Vanadium complexes in general are known for their high activity and regioselectivity in the epoxidation of allylic alcohols. They have also been shown to catalyse the epoxidation of unactivated alkenes as well as a variety of other reactions (Scheme 19).[107,108]

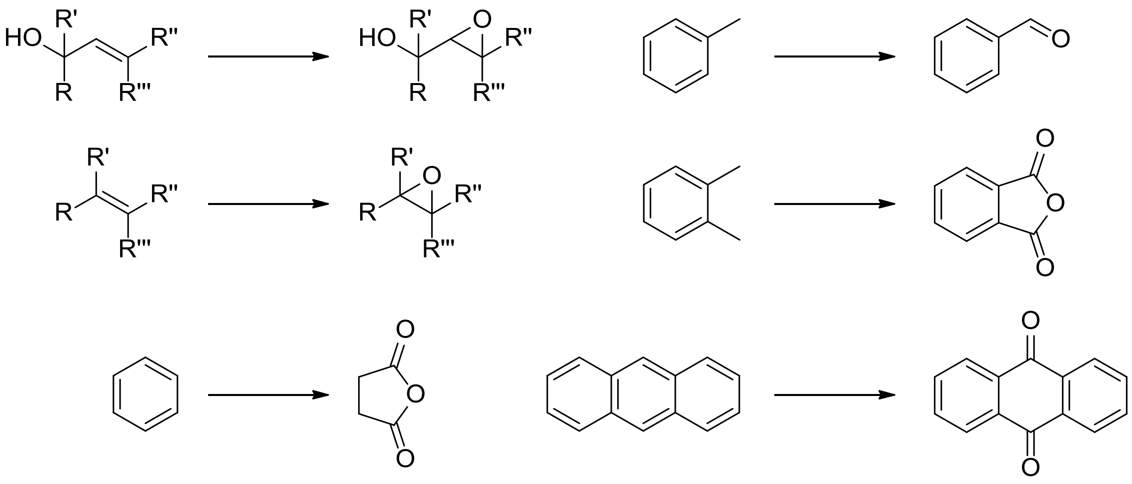

Scheme 19: Outline of several reaction types catalysed by vanadium complexes.

A widely applied class of vanadium catalysts is based on vanadium oxides, particularly V_2O_5, over which a great variety of reactions is conducted, including alkene epoxidation, allylic oxidation, oxidation of alcohols, aromatic oxidation, oxygenation of alkanes, oxidative dehydrogenation (ODH) of small (C_2–C_5, particularly propane) alkanes, benzylic oxidation, sulfoxidation and oxidation of SO_2 to SO_3.[72,107,109-112] Industrially, most of these catalysts are vanadium oxides based on oxidic solid supports, such as MoO_3, P_2O_5, TiO_2, SiO_2, Al_2O_3, MgO, and it has been found that these supported V-oxides have better activity and selectivity than their unsupported cousins.[107,109-112] It has been suggested that the higher activity of these complexes, particularly at low levels of vanadium, is due to the dispersed, isolated nature of the V sites over the surface of the support (Figure 7).[110,112,113]

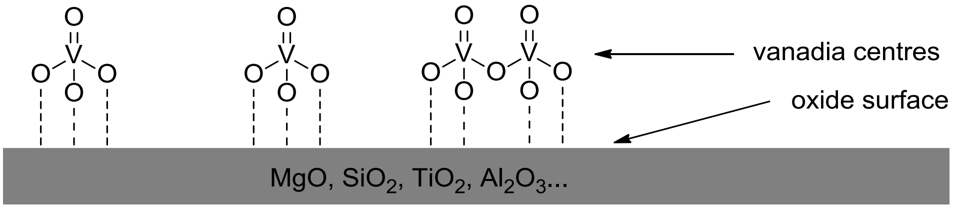

Figure 7: Representation of supported vanadia catalysts.

Another class of vanadium catalysts that have seen much use, particularly in oxidation of alkanes, alkenes and ammoximation reactions as well as alkane ODH, is vanadium phosphorus oxides (VPOs, Scheme 20), a mixture of vanadyl phosphate ($VOPO_4$) and vanadyl pyrophosphate (VPP) phases that readily interconvert during catalysis.[105,110,114] A notable reaction is the so-called “Butox” process for the production of maleic acid anhydride from *n*-butane, which is carried out on a multi-ktpa scale mainly for coating and polymer production.

This process — 14-electron oxidation, 8-hydrogen abstraction and 3-oxygen insertion — is recognised as one of the most complex reactions carried out in industry, and is performed industrially solely through the use of VPOs.[105,115-118]

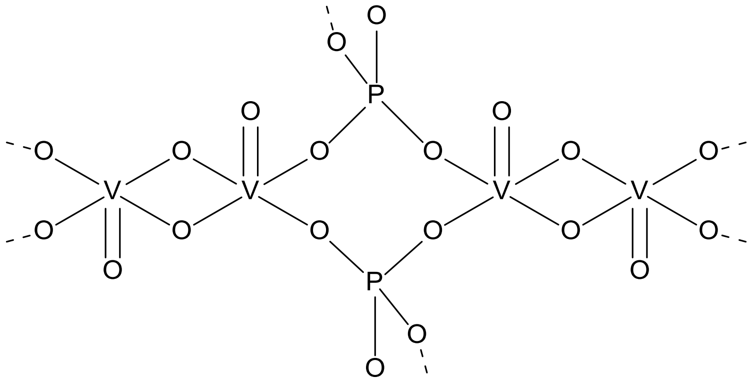

Scheme 20: Schematic representation of VPO catalyst structure as proposed by Centi et al.[114]

The rate-determining step in this process is the initial dehydrogenation of *n*-butane to butene. This process has been theorised to occur through a concerted 2H-abstraction process catalysed by the vanadium centres (Scheme 21). The vanadium cycles through a 3+ state upon loss of water and is regenerated to the starting 4+ state upon oxidation by O_2.[115,119]

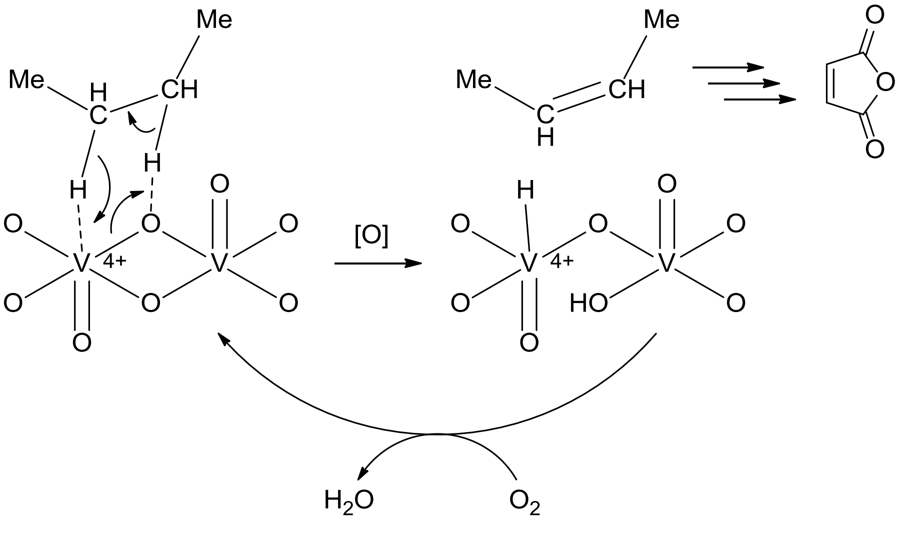

Scheme 21: Mechanism proposed for the Butox process.[115]

The first material to be synthesised that incorporated vanadium into a heterogeneous framework was VAPO-5,[104] but AlPO-11,[120], -21,[120] -31,[121] -17,[107] -41,[122] and -18[123] analogues followed soon (Figure 8), as did non-AlPO frameworks like vanadium silicalite-1 (VS-1, based on the ZSM-5 structure).[124]

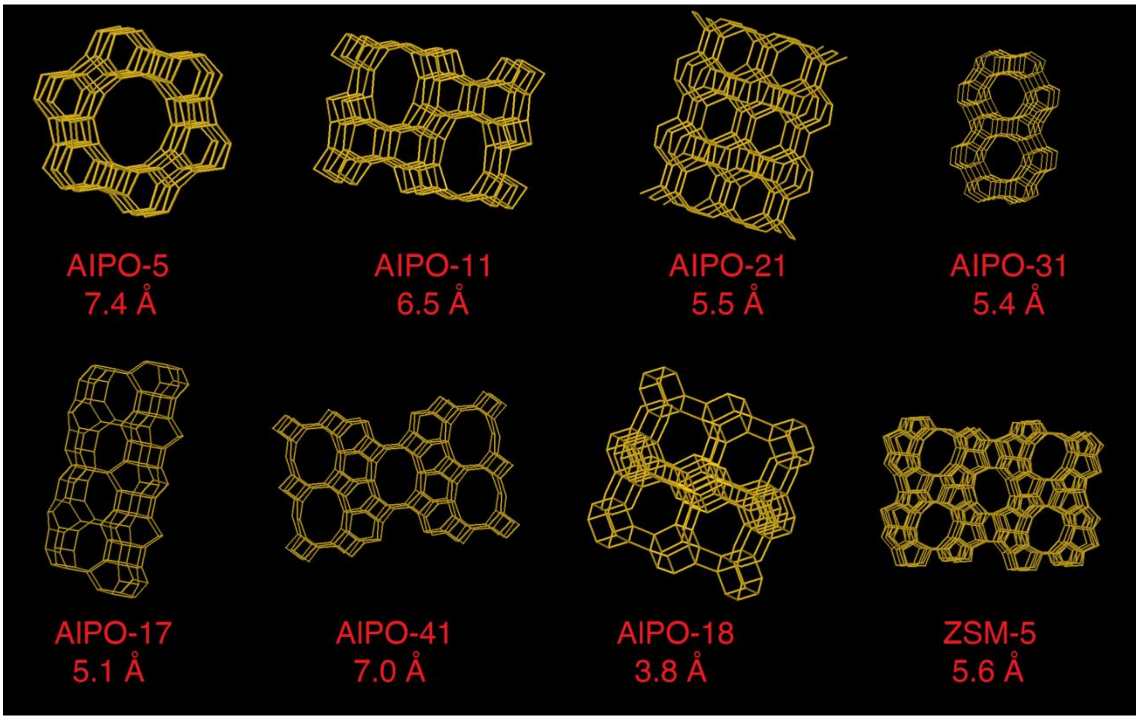

Figure 8: Structures and pore apertures (in Å) of several frameworks that have had seen vanadium-incorporated versions.

Applications of VAPOs include ODH of propane to propene at 550 °C, where they were found to be superior to supported vanadium oxides and V-impregnated AlPO-5 due to the isolated sites VAPO presented,[35,106,123,125] and alkene epoxidation and aromatic oxidation where VAPO-5 was found to be more selective than homogeneous systems and supported V species while retaining similar conversions.[106,108] Needless to say, VAPOs have proven to be powerful catalytic systems whose potential for active, selective redox transformations makes them an attractive system to investigate.

A weakness of VAPOs is touched upon in several studies, particularly earlier ones, which have reported the leaching of small amounts of vanadium from the framework during reactions in the liquid phase.[107] This well-known limitation has prompted several authors to include lixiviation studies in their reports, to ascertain the heterogeneous nature of the catalyst. Reactions in the gas phase do not suffer from vanadium leaching from the framework during catalysis.[107]

1.6.2 **Titanium AlPOs**

Titanium was one of the first elements incorporated into AlPOs by Flanigen in the 80s.[15] The interest in titanium AlPOs (TAPOs), as well as that towards other titanium-containing molecular sieves, originates mostly from two materials, both of which were of monumental importance to the chemical industry: titanium silicalite-1 (TS-1), and titanium-MCM-41 (Ti-MCM-41) (Figure 9).

TS-1 is a titanium-substituted version of silicalite (Figure 9), a siliceous version of zeolite ZSM-5, and is known for its catalytic oxidation potential using H_2O_2.[10,11,76,108,126-129] Patented in 1983 by Taramasso and co-workers at Snamprogetti S.p.A.,[130] it was commercialised by EniChem (both now part of Eni) as part of an optimisation of the Raschig process for the production of ε-caprolactam where it was found to be superior to a range of catalysts including silica-supported titania. Performed in conjunction with Sumitomo in Japan, the project went live in 2006 at a scale of 60 ktpa. The process is selective, simple, high-yielding, does not need hydroxylamine and is not burdened with the emission of NO_x and SO_2 gases, nor the formation of ammonium sulfate as a by-product, all of which are limitations of the Raschig process. Similar major improvements were made by EniChem (and later operated also by BASF/Dow and Degussa) in the hydrogen peroxide propene oxide (HPPO) process for the epoxidation of propene and, on a smaller scale, the oxidation of phenol to catechol and hydroquinone.[131,132] However, due to the small pore aperture of the framework (MFI: ø = 4.5–5.6 Å), TS-1 suffers from diffusion limitations and bulky substrates or oxidations cannot gain access to the active sites within the material, leading to very low activity.[132-134]

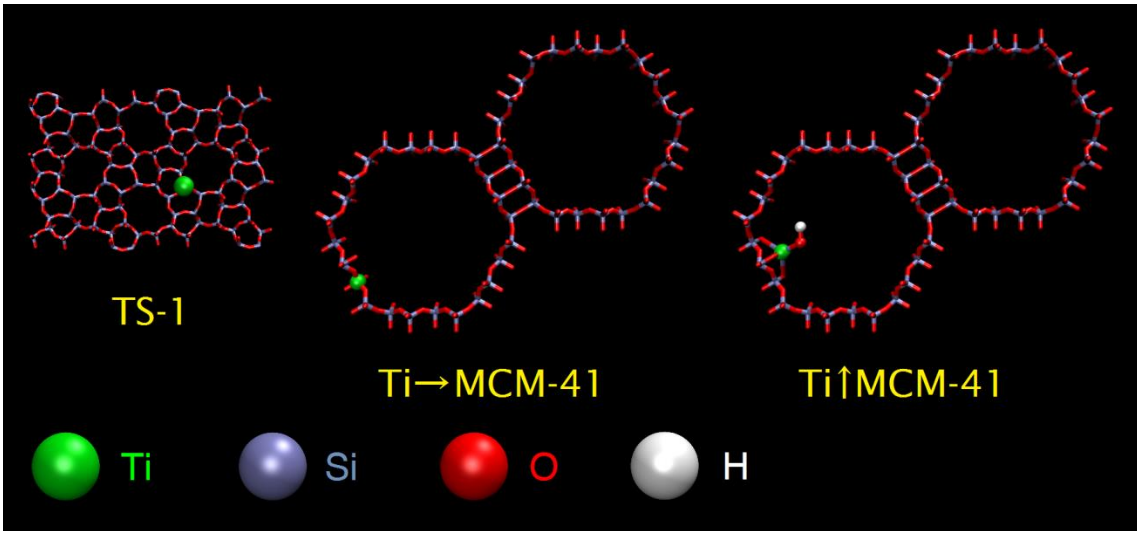

Figure 9: Framework models of TS-1 (left) and MCM-41 (right). Images are not to scale.

MCM-41 ("Mobil Composition of Matter number 41") is a mesoporous material developed by Mobil Oil Company with hexagonal-shaped, uni-directional pores that are much larger than those in TS-1 (ø = 35 Å). A titanium-containing version ("Ti-MCM-41") was developed by Corma *et al.* in 1994 to overcome the small-diameter limitations of the TS-1 MFI framework (among other factors such as hydrophobicity/hydrophilicity).[135,136] Tests have shown it to be much more effective towards the oxidation of large molecules than TS-1 (although these reactions used alkyl hydroperoxides as oxidant, as H_2O_2 was found to be less effective when using Ti-MCM-41).[134,137] Examples of reactions performed are oxidation of benzene, alkane oxidation, epoxidation of cyclohexene and other olefins, and the oxidation of bulky sulfides to sulfones and sulfoxides.[134,136,138]

The reactivity of both catalysts has been ascribed to the tetrahedrally-coordinated, isolated Ti^{4+} sites in these materials.[37,139,140] A notable distinction between the two is the method of incorporation, however. In TS-1, the titanium centres are part of the framework, while in Ti-MCM-41, they are generally grafted onto the pore walls (Figure 9) (for information on these techniques, refer to Section 1.4). Although a framework-embedded version (generally referred to as Ti→MCM-41) does exist, the surface-grafted ("Ti↑MCM-41") variant has been shown to be catalytically superior due to the more exposed nature of the Ti sites.[141,142]

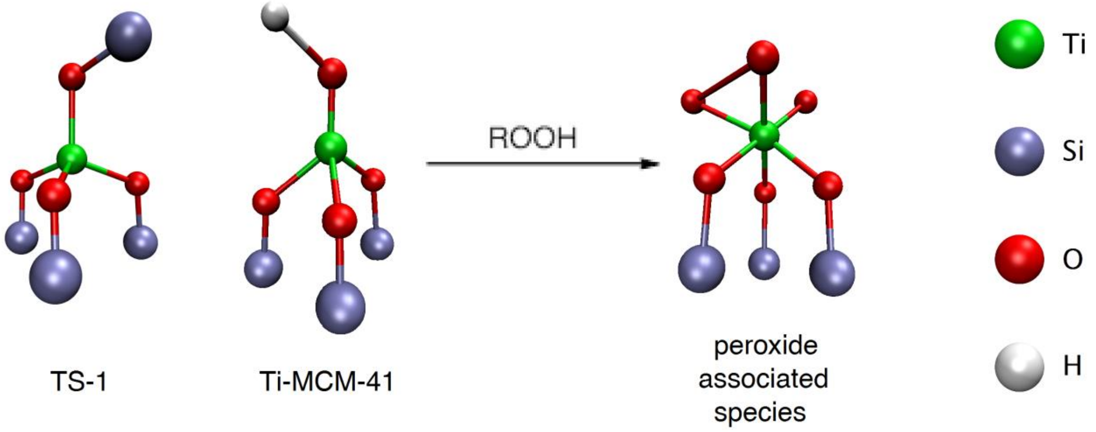

Scheme 22: Illustration of the active titanium sites in TS-1 and Ti-MCM-41.

Although the sites in TS-1 and Ti-MCM-41 take on a slightly different guise (Scheme 22), their coordination geometry is tetrahedral in both cases, and they engage in reactivity in a similar manner. The tetrahedral geometry is coordinatively unsaturated in these materials, and X-ray absorption studies by

Thomas *et al.*[143] show that the coordination increases to octahedral during catalysis (Scheme 22). This happens when the centre coordinates the oxidant, activating it towards reaction.[127,139] The willingness of the titanium centre to engage in this type of reactivity is parallel to its strong tendency to adopt octahedral geometries — to the point where tetrahedral Ti^{4+} compounds were considered rare before the advent of TS-1.[127,144] Various possible mechanisms for the epoxidation of alkenes and oxidation of alkanes with Ti acting as an oxophilic/redox-active species have been suggested; several examples are displayed in Scheme 23 and Scheme 24.

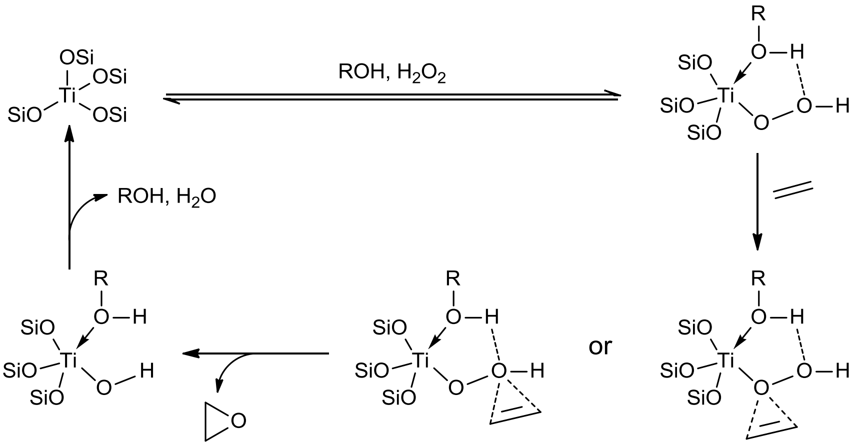

Scheme 23: Possible mechanism for the epoxidation of ethylene as proposed by Jones.[131]

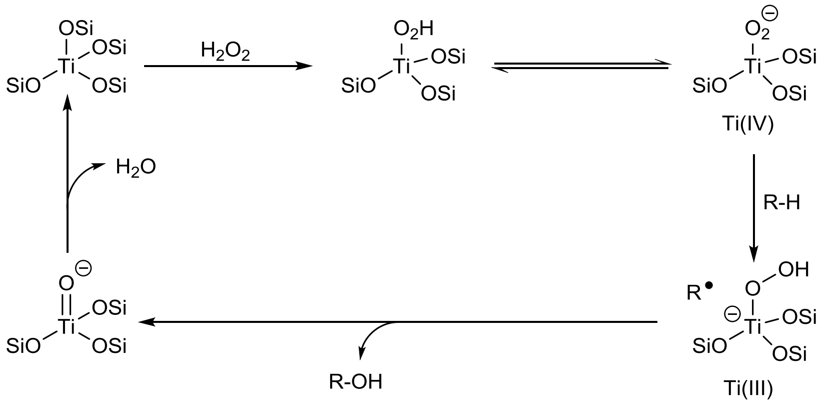

Scheme 24: Possible mechanism for the oxidation of alkanes as proposed by Jones.[131]

Like the reactivity of TS-1 and Ti-MCM-41, the potential of TAPOs for catalysing certain oxyfunctionalisations has been studied, again mostly for their ability to provide isolated, tetrahedral Ti^{4+} sites.[127,129,139,145,146] Materials like TAPO-5 present an intermediate-size pore aperture compared to TS-1 and MCM-41. Consequently, it could potentially allow for such reactions to be conducted on bigger molecules than those that interact with TS-1, while still retaining a more size- and shape-restrictive environment than the very large pores in MCM-41. Being based on aluminophosphates rather than silicates, TAPO-5 also offers a higher hydrophilicity, so different reactivity can be expected.[10,129]

A much less-well studied, yet well-known aspect of TAPOs is the Brønsted acidity caused by titanium incorporation.[145,147] This is derived from charge-balancing proton counterions arising from the net negative charge caused when Ti^{4+} substitutes for P^{5+} (see also Section 1.3). A study of these acid sites has concluded that they are weaker than those in Si AlPO-5, but stronger than those in Zr AlPO-5.[31,147] Experiments exploiting the acidity inherent to TAPO-5 have been performed such as isomerisation of xylenes[120] as well as methanol conversion to olefins.[148]

1.6.3 **Multimetallic AlPOs**

Some experiments have been performed using two different dopants within the framework. Generally speaking, the idea behind these designs is that when adroitly engineered, the two metals can interact in a synergistic manner to achieve a higher reactivity than either metal can on their own.

An example is cobalt-titanium AlPO-5 (CoTi AlPO-5) which was used by Paterson *et al.* for the epoxidation of cyclohexene.[76] According to the author, the rationale behind the design was that the oxophilic Ti^{4+} centres, known to be active in epoxidation reactions, could work together favourably with a redox-active metal like Co^{3+}. The latter's purpose is to liberate the active oxygen species *in situ* from the added acetylperoxyborate (APB) reagent — a stable, convenient source of peroxyacetic acid during oxidation reactions patented by Peroxid-Chemie in Germany (now part of Solvay).[149] The oxophilic nature of the titanium centres, meanwhile, coordinates the peroxo species and activates it towards reaction with the substrate via the Eley-Rideal mechanism (Scheme 25).[76,150]

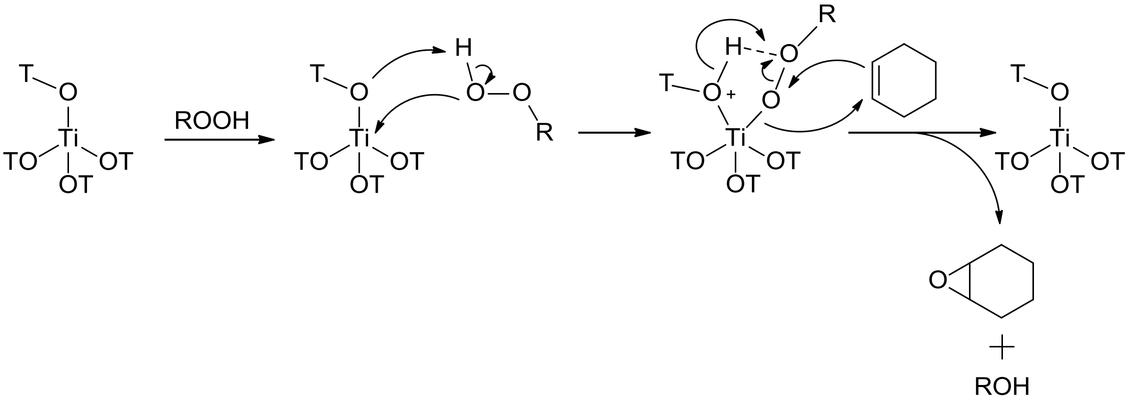

Scheme 25: Oxophilic titanium coordination of the oxidant leads to its activation and subsequent scavenging by the substrate, facilitating epoxidation.

During this study it was found that CoTi AlPO-5 showed higher activity than either its Co- or Ti-based monometallic analogue and, crucially, a physical mixture of the two, suggesting true synergistic interactions were taking place.[76] Computer modelling studies indicate that the two species, Co and Ti, are located in close vicinity to each other within the framework, and this may explain their ability to interact in such an intimate fashion. It should be noted however, that the report mentions that a higher fraction of the titanium introduced was incorporated as tetrahedral species when cobalt was present in the synthesis mixture, which could also explain the higher activity observed.

A similar example was reported by Leithall *et al.*, again in the epoxidation of cyclohexene, using VTi AlPO-5, in which redox-active vanadium is used, and where titanium is again employed as an accompanying oxophile.[139] Presumably because of the lower redox barrier of vanadium compared to titanium, VTi AlPO-5 was found to be even more active than CoTi AlPO-5 and a physical mixture of its monometallic analogues. Furthermore, in this study, no difference was reported in the nature of titanium incorporation as a result of the added vanadium during catalyst synthesis.

A particularly exotic example of multimetallic AlPOs is the synthesis of FeCoMn AlPO-5 by Zhou and co-workers.[151,152] This material was tested against its three monometallic analogues, as well as all three bimetallic combinations (CoMn, FeCo, FeMn) and was found to be superior to all of them in the oxidation of cyclohexane. Although a wide variety of products was observed (cyclohexanol, cyclohexanone, acids including adipic acid, various esters like dicyclohexyl adipate and hexanolactone, and cyclohexyl hydroperoxide (CHHP)), the highest selectivities towards cyclohexanol and cyclohexanone (the constituents of K-A oil) at 31.1% and 34.0% respectively, was observed with the trimetallic system.[151]

Based on the activity profile and product distributions over the systems evaluated, a reaction mechanism was suggested. Among their findings were that the cobalt AlPOs achieved the highest conversion, the manganese ones showed the greatest affinity for decomposing CHHP, and the K/A ratio was highest with iron AlPOs. As a result, they suggested that the mechanism was based on initiation by the Co sites, decomposition of the peroxo intermediate by the Mn centres, and oxidation of the alcohols to ketones over the Fe ions (see Scheme 26). As with Paterson's and Leithall's studies, a physical mixture performed less well, probably because the different sites are not in close proximity unless they are incorporated into the same framework.[151]

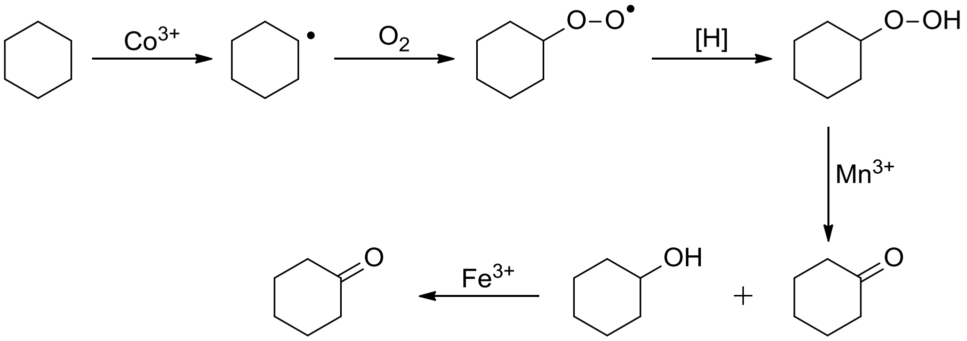

Scheme 26: Mechanism suggested for the oxidation of cyclohexane by Zhou et al.[151]

1.7 Aims and objectives

The aim of this work is to formulate a new procedure for the C–H oxidation of organic substrates, which was hoped to be achieved by employing an appropriate catalyst. The targets are for this procedure to:

- Be applicable to a range of organic substrates;
- Be cheap and facile to perform with a catalyst that is easy to handle and synthesise;
- Be active and selective;
- Make separation from the catalyst material trivial, if possible including catalyst recovery and re-use;
- Offer a greener, more sustainable alternative to existing procedures.

To this end, it was chosen to employ an AlPO molecular sieve catalyst, starting from state-of-the-art materials and procedures and modifying this where necessary to accomplish our goals. The choice of framework started from AlPO-5, which is easy to synthesise, can accommodate a range of active metal ions, and can induce selectivity through favouring end-on approach of the substrate into the structure (Figure 10) without being so narrow as to compromise substrate scope or substantially limit diffusion or mass transfer.

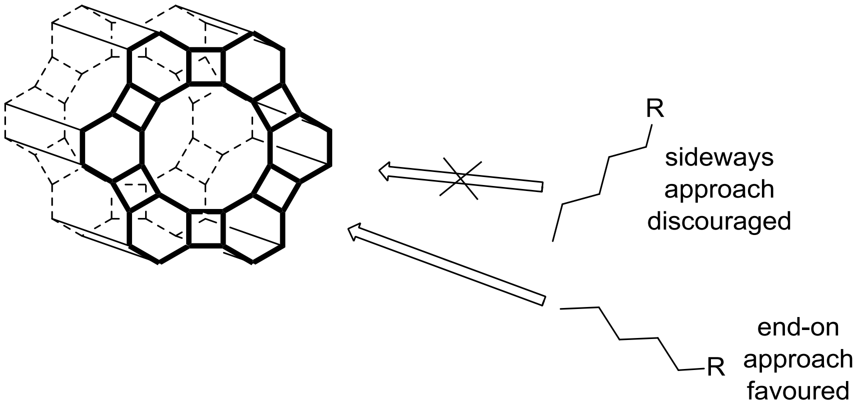

Figure 10: Schematic illustration of framework-induced end-on approach of the substrate being favoured.

It was intended to functionalise this with a redox-active metal and an oxophilic metal in order to affect high activity. Varying the type of catalyst should give trends with regards to reactivity, and in-depth analysis of the catalyst gives us insight into the nature of the catalyst and its active sites, allowing us to establish structure-property relationships. Ideally, this would provide a versatile catalytic system and procedure that can hopefully be adopted in a variety of synthetic strategies. Summarising, the objectives are as follows:

1. Synthesise a variety of AlPO catalysts with varying amounts and types of metal ions to afford a system capable of C–H oxidation;
2. Perform a screening of oxidation conditions on one or more model compounds to discover optimal catalytic conditions and catalytic trends using the synthesised molecular sieve catalysts;
3. Deduce information about the workings of the catalytic system under optimal conditions using the information and trends observed during the screening;
4. Evaluate the substrate scope with which the catalytic conditions work well, moving up to more complex substrates to see how far the system can be taken and to what success;
5. Characterise the selected catalytic materials as well as their active sites to gain insight into the nature and workings of the catalytic entities.

All in all, this project, which is being undertaken in conjunction with organic (Harrowven) and inorganic (Raja) groups at the University of Southampton, is an exciting collaboration project that will hopefully combine the best of both worlds.

2. Experimental methods

2.1 Catalysis

As relatively little literature is available on the use of AlPOs for the types of reaction under investigation, proof of concept must first be established. To that end, the first target is to screen for conditions that will allow one to achieve some degree of regioselectivity in the oxidation of saturated C–H bonds. This boils down to screening for ideal temperatures, concentrations, solvents, oxidants, catalysts and other reaction parameters using a model substrate on which several types of oxidation are possible.

To provide proof of concept that this type of chemistry is possible, propylbenzene was chosen as a model substrate. This choice was due to propylbenzene being a hydrocarbon with several alkyl positions of different reactivities that could be oxidised to varying degrees, and an aromatic ring at its core. The choice of an aromatic core was important as it was intended to exploit the shape of the substrate to guide the substrate into the pores in a preferential orientation (see Section 1.7), and future research into the topic could diverge into size-exclusion catalysis that might disable more reactive C–H bond oxidations by preventing their entry to the pore channels. Similarly, using an arene as a size-excluding functionality would prevent aromatic C–H oxidation which has been reported for substrates on which benzylic oxidation is possible.[72] Furthermore, propylbenzene has a chain length roughly comparable to hexane, the oxidation of which formed the basis of this research.[54]

The screening conditions attempted are started from ones reported previously in the group for olefin epoxidation.[76] Though most previous oxidation reactions have been performed in pressurised reactors, this project started off using an oxidant at atmospheric pressure in a simple round bottom flask. This was done to rule out the necessity of high pressure to perform the oxidations, and in order to keep the reaction as facile as possible.

Reaction conditions for heterogeneously catalysed reactions can be influenced strongly by a wide variety of factors, including variations such as framework type, catalytic metal, metal loading, catalyst loading, type and stoichiometry of oxidant, solvent, concentration, temperature and duration.

However, several less obvious factors can also influence the reaction including reactor size and shape, stirring speed, inclusion or exclusion of air, mode of oxidant addition and whether the reaction is being sampled or not. Finding semi-optimum conditions by varying some or all of these factors is a crucial first step to getting useable results as well as getting a clearer understanding of how the reaction works.

Once a working protocol has been found and optimised and a clearer picture of catalytic trends has been deduced, more time can be spent examining substrates to determine the effectiveness of the catalytic system at oxidising related materials. Depending on the efficiency and type of oxidation observed with the model system, the results can then be extended towards more complex oxidation sequences.

2.2 Catalyst design and synthesis

2.2.1 Nature of the catalyst

To start off, as mentioned in Section 2.1, it must be proven that C–H oxidation of hydrocarbons is achievable using metal-substituted aluminophosphates using simple laboratory conditions, and if so, to find out what selectivity is observed. Therefore, a highly strict shape-selective system is not to be used initially, as it is possible that diffusion of the starting material (or products) is thusly hard that kinetically the catalysis becomes impossible. Alternatively, overly small pores could cause clogging of the catalyst pores and entrapment of products and reactants. As such, it was decided to go with an aluminophosphate with a reasonably large (but not excessively large) pore size compared to the substrate, to impose a degree of selectivity by a guided approach of the substrate without compromising too much on mass transfer. To this end, the AFI network was chosen. This network has a maximum pore size of 7.4 Å (Figure 11) which is a perfect starting size to test the catalytic activity of AlPOs with.

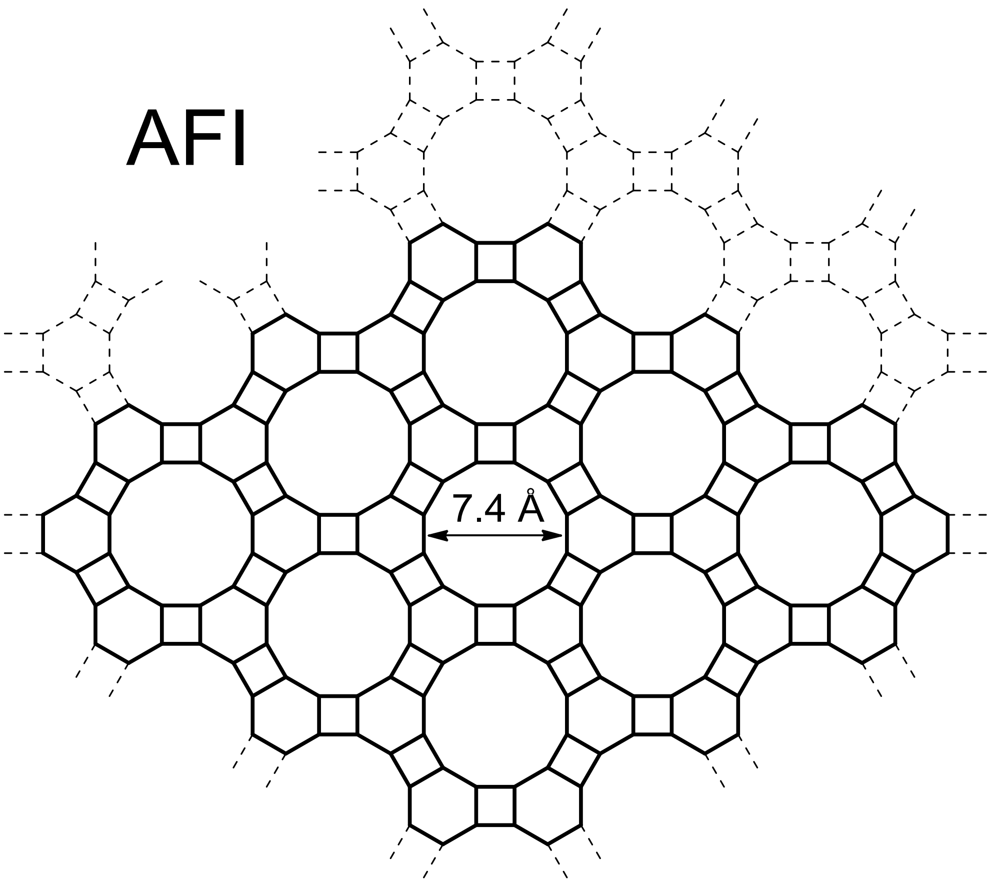

Figure 11: Schematic representation of one of the faces of the AFI framework. The pores are 1-dimensional channels perpendicular to the plane of the page.

The reason for choosing an aluminophosphate to work with rather than a siliceous zeolite material lies in the difference of their binding modes. Corà *et al.* have shown, using electron density mapping, that the former are more molecular-ionic in nature, whereas the latter are described as continuously semicovalent across the network.[153-155] In other words, the bonding mode of AlPOs approaches that of alternating Al^{3+} and PO^{3-} units, with the majority of the electron density being centred on phosphorus, whereas the unpolarised Si–O–Si bonds are closer to being covalent.

This difference in bonding is of central importance in how metal ions are introduced to the catalyst. Whereas siliceous networks are generally modified post-synthesis using cationic exchange, the neutrality of the AlPO network makes this impossible to do, as no cationic counterions are present. Instead, AlPOs are modified by using isomorphous substitution of metals in the framework for other metal ions during synthesis. In other words, whereas siliceous networks are generally modified using metal ions that cling on to the network (but do *not* become an integral part of it) after synthesis, AlPOs are modified to incorporate the metals into their very structure, during synthesis. This particular type of modification is considerably easier for AlPOs than it is for silicates as the ionic bonding mode allows easier substitution of the framework atoms. Furthermore, Corà *et al.* found that AlPOs can fairly readily accommodate substituting metal ions and that the effect of the dopant on the total framework is minimal.[155]

The AlPO equivalent of the aforementioned AFI network is AlPO-5. This material is well-known and characterised, and several reviews on aluminophosphates include information about it.[26,101,156] AlPO-5 is said to be flexible towards substitution, retaining good isomorphicity, is fairly easy to synthesise using many different templates, and at low metal loadings, it is reasonably thermally stable. An NMR study by Meinhold showed that AlPO-5 has a large capacity for adsorbing water — as much as 40% of the framework Al could be made octahedral by coordinating water ligands (28% by dry weight).[157] This is an excellent example of the remarkably flexible framework of AlPO-5. As framework substitution of one ion with that of a different ionic radius is expected to result in a framework distortion, this flexibility is desirable, and AlPO-5 presents a good starting point for our investigations.

2.2.2 Synthesis of the catalysts

The synthesis of these catalysts is performed hydrothermally. Hydrothermal synthesis is a method that relies on elevated temperatures and pressures to dissolve the "building blocks" of the framework and subsequent supersaturation and crystallisation of the material. To achieve crystallisation of the specific framework type desired, an organic "template" or "structure-directing agent" (SDA) is added, which associates with the building blocks in solution and around which the pores and channels are formed during crystallisation. The type of template used then determines the type of framework obtained. The specificity of an SDA towards different structures varies, as does the specificity of structures towards different SDAs.

The general procedure for the synthesis of AlPO-5 used in this work is adapted from PhD theses by Paterson[158] and Leithall.[159] This procedure involves combining the aluminium and phosphate sources with dopant metal salts along with an appropriate SDA, subsequent heating in an autoclave fitted with a Teflon liner under autogeneous pressure, cooling of the vessel, workup of the material and subsequent calcination in air. The material is characterised by powder X-ray diffraction before and after calcination (see Section 2.3.2.1) and to selected catalyst batches, several other analyses were applied.

Hydrothermal synthesis of these materials is a well-known procedure, yet is considered to be highly complicated as a great number of factors are believed to affect it. These include, but are not limited to, temperature, rate of heating and cooling, duration, pressure, ageing, order of reagent addition, gel composition, pH, concentration, purity of reagents, type of SDA, presence of additives and other ill-defined factors.[160,161] To further complicate this, most of these factors are not independent of each other which leads to difficulties studying the influence of each separate factor. Because of this, reproducibility of reported hydrothermal processes is known to be troublesome, and hydrothermal synthesis of heterogeneous catalysts has accordingly been referred to as a “black art”.[160-162]

Because of the reliance on autoclaves to effect crystal growth, *in situ* observation of the growth process is complicated. Nonetheless, a few *in situ* studies using tomographic energy dispersive diffraction imaging (TEDDI)[163], UV Raman spectroscopy[164], small-angle X-ray scattering and wide-angle X-ray scattering (SAXS/WAXS)[165] and synchrotron X-ray diffraction[166] have been reported. From their conclusions as well as earlier work in this field by Oliver *et al.*[167] a reasonably full picture can be painted regarding the actual mechanism of AlPO-5 formation *in situ.* The following is an account of their combined findings.

When the aluminium source is added to water, the aluminium is present as octahedral AlO_6 species. However, upon the addition of phosphoric acid, these immediately react to form nuclei of AlO_4 species with strictly alternating Al–O–P units present as either alternating Al–O–P–O–Al chains[165] or alternating four-membered rings.[164] Both of these types of nuclei are a 1D structure and only grow in one dimension (Scheme 27) and are referred to as a “primary amorphous phase”.[165]

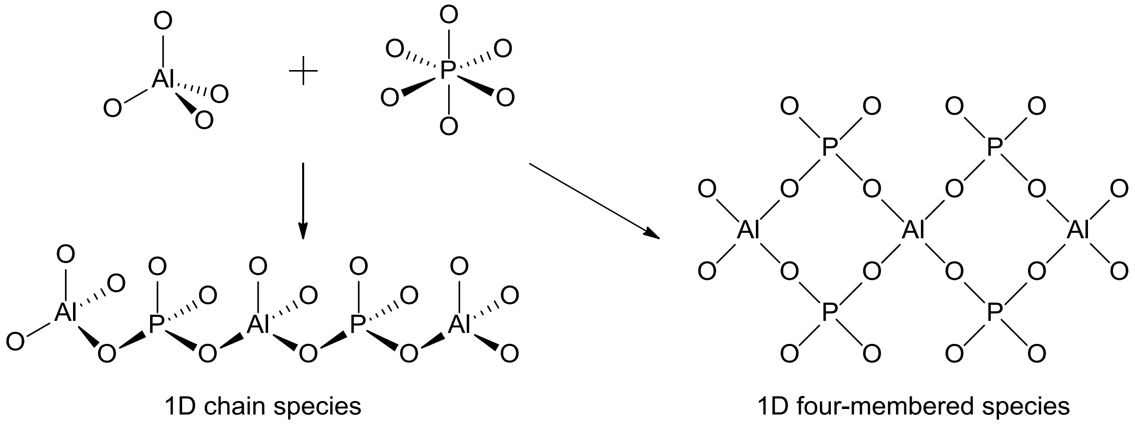

Scheme 27: Illustration of the formation of the two possible suspected species that form upon the gel mixing of the aluminium and phosphorus sources.

Subsequently, the SDA or "template" comes into play, as it is necessary to destabilise denser phases of aluminium phosphate in favour of the desired, more open, microporous structure. The mechanism of the template for structure direction is not yet fully understood and has been attributed to various factors like hydrogen bonding, the Van der Waals shape of the template, steric support and the favoured formation of specific structures. However, there is strong evidence to support that the template associates (mainly through the Al–O–P bridging oxygen atom) with the previously mentioned 1D phases to form a gel of aggregates of a wide size distribution. Between 30 and 150 °C, these aggregates slowly grow in size to form poorly, but partially ordered channel-like structures that eventually trap the template molecules. These structures already possess some microporous characteristics with a micropore volume of 7% and a maximum pore size of 8.9 Å, but no Bragg peaks are observed at this time yet.[164,165] Though the AlPO is formed under acidic pH conditions, these conditions shift to more alkaline as the reaction progresses.[167]

When the temperature reaches 155 °C, crystallisation rapidly (in <15 min) occurs, and the amorphous channels, through reconstruction by hydrolysis of Al–O and P–O bonds and subsequent reconnection with loss of water, form crystalline channels with a maximum pore size of 7.4 Å. As this step noticeably decreases the pore size, a concomitant decrease of the molecular diameter of the template of 4–10% is observed; the template is "squeezed" in between the pores. This forms the final crystalline phase.[164,165,167] The material is then calcined to burn off the template and free up the pores of the material (Scheme 28).

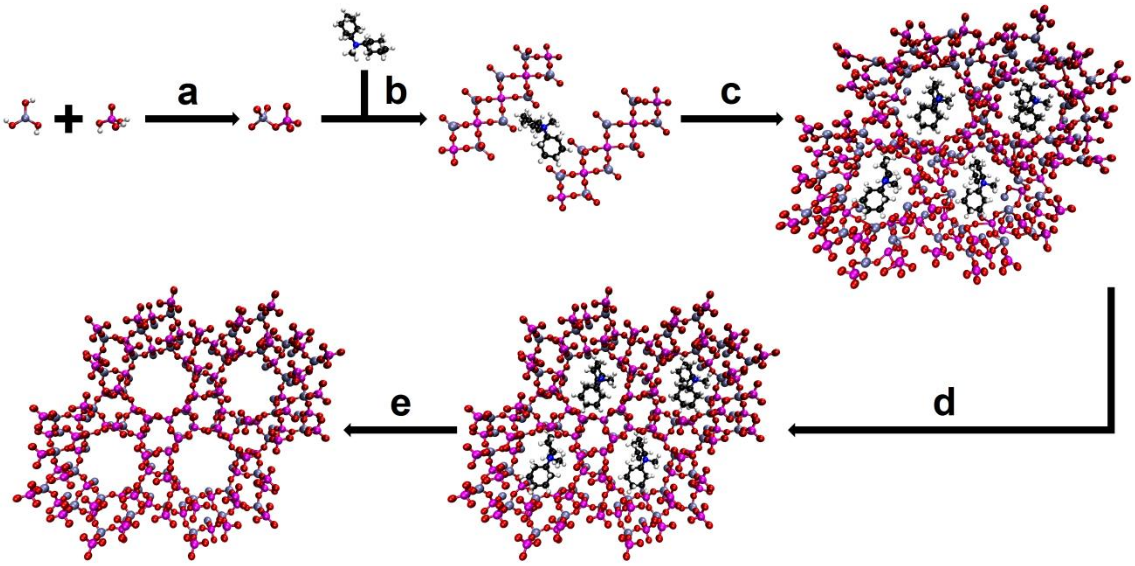

Scheme 28: Outline of the synthesis of AlPO-5. Aluminium is portrayed as grey-blue, phosphorus is depicted in pink. The organic molecule is the SDA, Cy$_2$MeN. a: gel mixing of aluminium hydroxide and phosphoric acid, b: aggregation into 1D phases by association with the SDA, c: bomb assembly, forming rough 3D framework, d: completion of AFI phase, e: calcination to burn off the template, freeing up the pore cavities.

Note that the reaction kinetics of crystal growth have been suggested to vary significantly within the confines of the autoclave.[168] Specifically, at the top of the reaction medium, *i.e.* at the interface of gas and liquid, induction times before crystallisation and the rate of crystallisation itself are significantly shorter and faster, respectively.[163] The formation of other structures and species also occurs faster at the top, though AlPO-5 (AFI) is the first phase formed. Although AlPO-5 itself is formed without an intermediate,[165] it itself is an intermediate for the formation of other framework species.[163] The reason for this locus-dependant rate of crystallisation and length of induction period is attributed to a variety of possible causes including convection and settling of solid particulates among others.[163]

The effect of addition of Co^{2+}, a common dopant for the incorporation of catalytically active metal in AlPO-5, has also been investigated by Weckhuysen *et al.*[165] It was found that the Co^{2+} precursor starts off as an octahedral hexaaqua complex until the temperature hits 75 ˚C, at which point it overcomes an energy barrier and slowly converts to tetrahedral Co^{2+}. Fifteen minutes before the crystallisation temperature, only up to roughly half of the

Co^{2+} is converted to tetrahedral, however as the temperature hits 155 °C the remaining octahedral Co^{2+} is rapidly converted to tetrahedral Co^{2+}. It is observed that at as low as 2.5 wt% cobalt loading, the rate of crystallisation is lowered by a factor of 3, and it is assumed that crystallisation cannot occur without all the Co^{2+} having converted to tetrahedral geometry.[165] The conversion of octahedral Co^{2+} to tetrahedral Co^{2+} was measured using UV-Vis spectroscopy, observing two peaks at 470 and 525 nm corresponding to octahedral Co^{2+} transitions at the start of the heating and the sudden appearance of a prominent triplet (542, 584, and 625 nm) corresponding to pseudo-tetrahedral Co^{2+} at 152 °C. In addition, a shortening of the Co–O bond (from 2.08 to 1.09 Å) and decrease of coordination number was noted, from (roughly) six-coordinate to four-coordinate (Figure 12).[165]

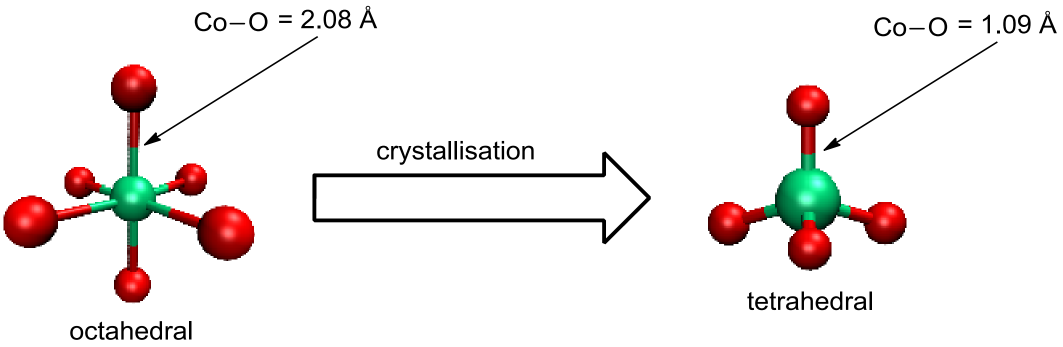

Figure 12: Illustration of coordination geometry of Co^{2+} changing from octahedral (left) to tetrahedral (right) under hydrothermal conditions. This is accompanied by a Co–O bond shortening.

Following that, an XAS study by Barrett *et al.* was able to draw several conclusions based on bond lengths observed in the material. According to their study, the as-synthesised, uncalcined material contains four-coordinate Co^{2+} centres (substituting for aluminium) with three bonds of comparable length and one longer bond, which holds the charge-compensating proton (Scheme 29). Upon calcination, a shortening of the average bond length was observed, indicative of oxidation to Co^{3+}. Various frameworks yielded differing degrees of shortening, from which the relative degree of oxidation was extrapolated. Moreover, it was found that frameworks in which cobalt was more resistant to oxidation, such as AlPO-5 and AlPO-36, showed the formation of Lewis-acidic sites alongside the Brønsted-acidic ones already present (Scheme 29). These Lewis-acid sites are present as lattice vacancies which stabilise the Co^{2+} species, making them resistant to oxidation to Co^{3+}.

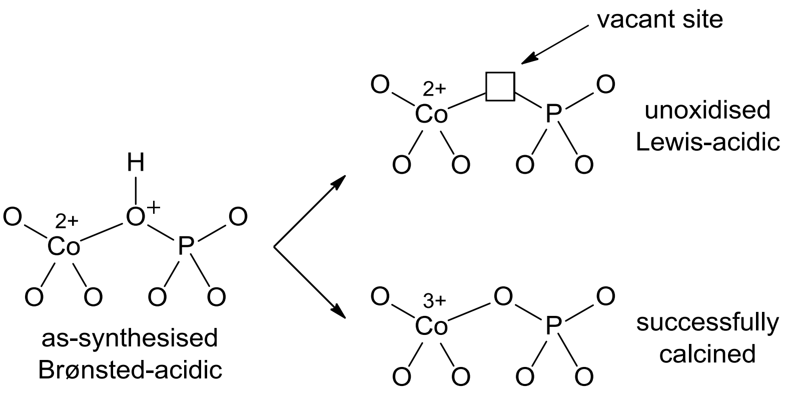

Scheme 29: Cobalt species proposed by Barrett et al.[169]

Alongside Co^{3+}, V^{5+} was chosen for screening as it has proven to be a powerful tool in oxidation catalysis,[108,159,170] is capable of easy redox cycling between several oxidation states[159] as well as for its favourable size, making substitution into phosphorus or aluminium sites possible.[171]

A note on the specific reagents used in the synthesis of AlPO-5; we chose to use aluminium hydroxide hydrate as aluminium source, Cy_2MeN as SDA, Ti(O*i*-Pr)$_4$ as titanium source and $VOSO_4$ as vanadium source. Though several alternatives are available for each of these sources, each with their positives and negatives, the ones used here have been shown in previous work to give superior products. For instance, while Al(O*i*-Pr)$_3$ is known to be a more active source of aluminium with lower amounts of impurities (mostly Na, Fe, Ca and Mg), $Al(OH)_3$-based AlPO-5 was found to be significantly more active in the oxidation of benzyl alcohol.[159] Ti(O*i*-Pr)$_4$ was chosen over $Ti(OBu)_4$, Ti(O*i*-Pr$_2$)acac$_2$ and titanium peroxide precursors for the same reason; higher catalytic activity is observed with the former than with the others.[159] Cy_2MeN was chosen as structure directing agent over about two dozen alternatives as it proved to be more AFI-specific than other templating agents as well as tolerant of a wider range of synthesis conditions.[159] Finally $VOSO_4$ was used over the commonly used V_2O_5 as the latter has been reported by Rigutto *et al.* to produce impurities containing V–O–V chains and $VOPO_4{\cdot}2H_2O$ phases.[108]

Which metal site the dopants occupy is dependent on the type of dopant(s) used and their amounts. While it is generally accepted that cobalt substitutes aluminium as either Co^{2+} or Co^{3+},[159] there is still considerable speculation on the substitution type of titanium, and the substitution of vanadium in particular has caused much controversy.

The confused reports and uncertainties surrounding the substitution type of vanadium can be understood when one considers the various complicating factors at hand. V-incorporation is considered to be more complex than that of Co, partly because of the different gel chemistry and partly because vanadium is liable to condensation reactions leading to V-oxide oligomeric cluster species during synthesis.[28,172,173] Furthermore, vanadium can take on multiple different oxidation states and coordination geometries as well as being able to occupy framework as well as extraframework positions, further complicating vanadium AlPO chemistry.[173]

It is widely accepted vanadium is incorporated as V^{4+} and is oxidised to V^{5+} upon calcination, and originally this led authors such as Montes[104] and Jhung[174] to believe this meant the vanadium would substitute at phosphorus as substitution of Al^{3+} for V^{5+} would lead to too great a charge imbalance for the framework to handle (Scheme 30, path 1).[175,176] The two main arguments for this are as follows:

1. The chemistries of P and V are said to be similar, and the mineral schroderite, in which VO_4^{3-} and PO_4^{3-} are present, suggests exchange of one for the other is possible;[28,104,172]
2. Computational studies have shown substitution of P^{5+} by V^{5+} to be considerably more favourable than substitution of Al^{3+} by V^{3+}, the latter of which would be accompanied by a strong distortion of the framework.[177]

This was contested however by Rigutto and Van Bekkum[108] based on two observations:

1. Incorporation of a certain amount of vanadium led to a concomitant decrease of the fraction of aluminium in the framework, *i.e.* a favourable balance of (Al+V)/P was found;
2. Spectroscopic evidence points out that vanadium is not present as a simple vanadium ion but as vanadyl (V=O) ions which means that the ion would be in $V{=}O^{+2}$ or $V{=}O^{+3}$ state (see Scheme 30, path 2) — V^{4+} conversely was not detected by spectroscopic means.[28,111,178]

This in turn would make substitution at aluminium much more likely. Despite the spectroscopic evidence, some authors[101,106,179] still championed P rather than Al substitution by vanadium.

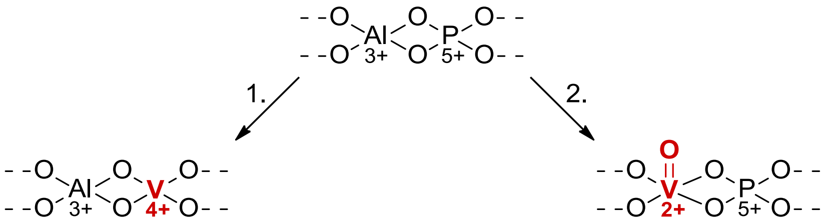

Scheme 30: Outline of suggested substitution of V by 1. Montes and Jhung and 2. Rigutto and Van Bekkum.

More recent spectroscopic evidence by our group[139] in conjunction with groups in Turin and Alessandria using HYSCORE EPR (hyperfine sublevel correlation experiment electron paramagnetic resonance spectroscopy) showed unambiguously that V substituted at aluminium instead of phosphorus. This technique is a pulsed, two-dimensional variation of EPR spectroscopy (see Section 2.3.2.9) that can elucidate the interaction of the spins of unpaired electrons with the nuclear spins of nearby nuclei (known as superhyperfine coupling).

Using this technique it was found that the vanadium sites only show coupling to phosphorus sites, whereas no evidence was found of neighbouring aluminium sites. As AlPOs have a strictly alternating Al–P–Al–P bonding mode, substitution of one type of site is expected to yield coupling only to the sites of the other element (Figure 13). Therefore, coupling of the unpaired V^{4+} electrons to phosphorus sites with no evidence of such coupling to aluminium sites indicates that only Al sites are occupied by the vanadium ions.

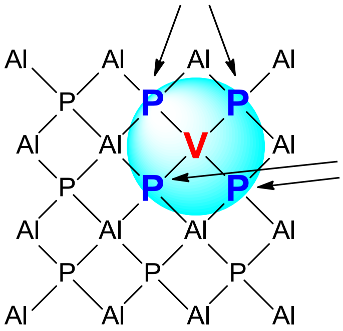

Figure 13: Illustration of superhyperfine coupling in vanadium-AlPOs. The probed vanadium centre (red) can only "see" the phosphorus sites (blue, indicated by arrows) that neighbour it. In the absence of similar couplings to aluminium, vanadium must substitute for aluminium only.

The geometry of vanadium inside the framework is more or less universally believed to be square pyramidal or distorted octahedral.[28,108,111,123,139,172,179-182] Both geometries of vanadium have been reported to be reactive towards *tert*-butyl hydroperoxide (TBHP).[108] However, due to the extreme difficulty of assigning a definitive, exact environment to even compounded spectroscopic evidence, few authors have dared to visually depict a schematic of the exact suspected vanadium environment, and there is substantial disagreement among them. A summary of structures that have been proposed is outlined in Figure 14.

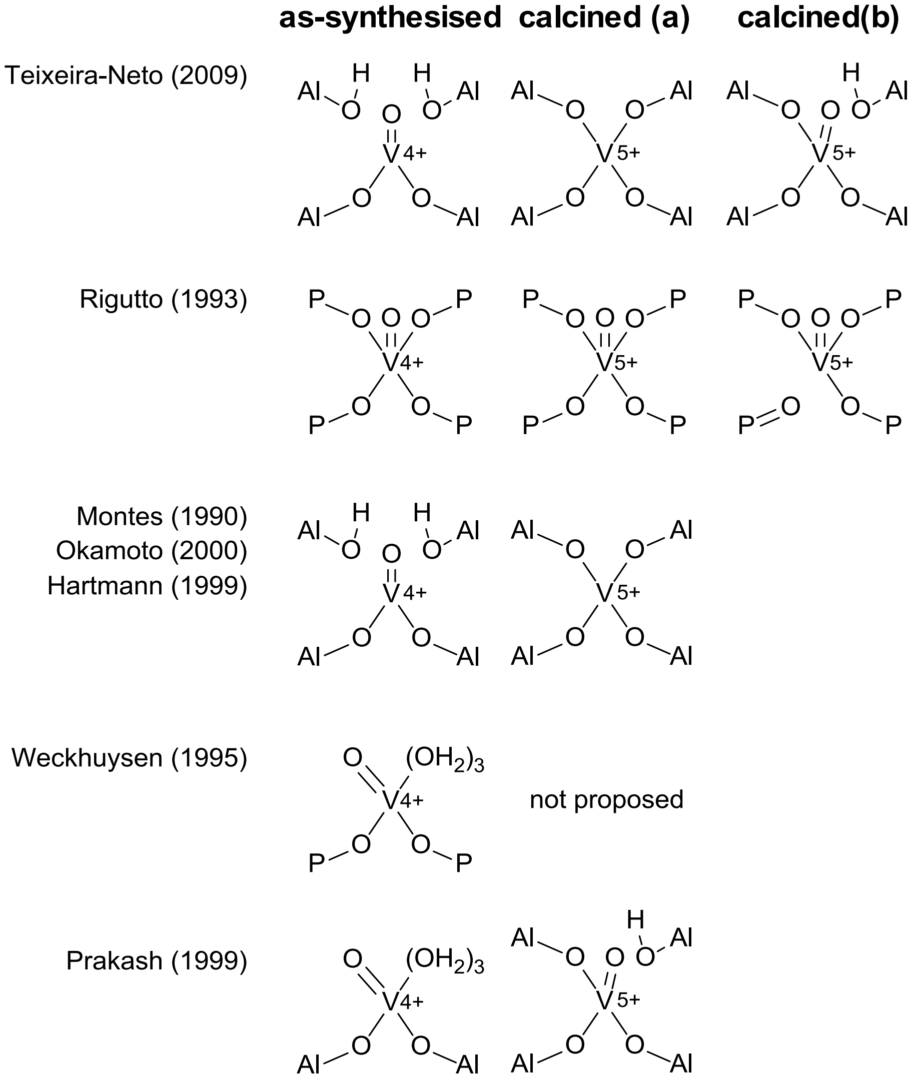
as-synthesised
calcined (a)
calcined(b)
Teixeira-Neto (2009)
Rigutto (1993)
Montes (1990)
Okamoto (2000)
Hartmann (1999)
Weckhuysen (1995)
not proposed
Prakash (1999)

Figure 14: Proposed structures of the in situ vanadium species in VAPO. Shown are as-synthesised and calcined propositions (including alternate possibilities proposed by the authors).[101,104,106,108,172,179,183]

It should be noted that none of the structures of the as-synthesised material proposed by any of the authors depict the coordination geometry of vanadium as tetrahedral. In a 1995 report by Weckhuysen *et al.* it was subsequently pointed out that this disqualifies vanadium for exhibiting true isomorphous substitution, as this would technically entail replacing the (tetrahedral) original framework sites by dopant ions of a similar coordination geometry.[183]

The type of species formed upon calcination shows yet more disagreement, although there is a general agreement that the V^{4+} formed is oxidised to V^{5+}.[101,104,106,108,172,179,183] However, it is not universally agreed whether this substitutes as a vanadium or oxovanadium species and how it is coordinated to the framework. Several authors have proposed a tetrahedral or tetrahedral-like environment on the basis of UV-Vis spectroscopic evidence[101,107,139,174,180,183] but there is considerable disagreement about in what way this manifests itself, and little definitive evidence. The disagreements likely stem from the difficulty associated with the analysis of such species.

Like vanadium, a lively debate has been going on about the substitution mode of titanium, although not quite as much disparity has been shown towards the end results as the only subject of debate is really what ion titanium replaces (Table 3). Titanium was originally believed to substitute phosphorus as Ti^{4+}, requiring the addition of a charge-compensating proton.[23] Indeed, EPR and ESEEM (electron spin echo envelope modulation) experiments by Kevan's group[128,147] strongly suggested that Ti substituted for phosphorus. In this work, gamma rays were used to reduce the Ti^{4+} species to Ti^{3+}, as the former is EPR (and ESEEM) silent (Ti^{4+} is a $3d^0$ ion). According to quantum calculations by Corà *et al.* however, the ionic nature of the AlPO framework bonds would favour substitution of aluminium due to a lower strain on the electronic structure of the carrier material when substituting aluminium.[153]

Subsequent measurements by Maurelli and co-workers at Turin using HYSCORE EPR,[184] in much the same vein as the vanadium experiments described above, show that titanium substitutes for aluminium in TAPO-5, as the titanium sites only show coupling to phosphorus sites. Mention was made that only about 20% (±5%) of the Ti sites were detected in these experiments.[184]

Gallo and co-workers, in conjunction with another group at Turin, more recently published more definitive experiments using combined extended X-ray absorption fine-structure (EXAFS) and valence-to-core X-ray emission spectroscopy (vtc-XES) techniques.[10] In these experiments, it was discovered that the Ti environment was mostly made up of –O–Al ligands, *i.e.* titanium substitutes mostly for phosphorus. Linear quantification of the data showed that 90% (±5%) of the present titanium follows this pattern, with the rest substituting for aluminium. Unlike the experiments conducted by Maurelli *et al.* using EPR, the employed techniques detect all titanium present in the sample, rather than only the fraction that was successfully reduced. As such, it would appear that in the previously mentioned experiments, only the Ti sites substituting for aluminium are actually reduced under the employed conditions.

author	**method**	**findings**	**ref.**
Kevan *et al.*	ESEEM	Ti substitutes P	128,147
Corà *et al.*	DFT	Ti substitutes Al	153
Maurelli *et al.*	HYSCORE	Ti substitutes Al	184
Gallo *et al.*	EXAFS, vtc-XES	Ti substitutes both, mostly P	10

Table 3: Summary of findings by various groups with regards to the substitution mechanism of titanium in TAPOs.

On the coordination geometry of Ti in TAPOs it is generally agreed that the catalytically active species is tetrahedral, which will increase to octahedral upon coordination of (two) water ligands.[10,28,129,139,147,180,184] This possible expansion of the coordination sphere, and by extension its tetrahedral geometry, is said to be essential for its activity as an oxophilic metal ion. A structure proposed in the literature, relatively straightforward compared to that of substituted vanadium, is shown in Figure 15.

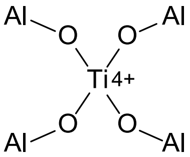

Figure 15: Schematic representation of titanium substituting (for P) in an AlPO lattice.[128,184]

2.3 Analytical methods

2.3.1 Analysis of catalysis products

To establish entities such as conversion, selectivity *etc.* during the screening, analyses were run on the crude mixtures of reaction products rather than separating the products of every reaction individually before analysis. This has the principal advantages of being considerably more faithful to the true results of the reaction, as well as being substantially less time-consuming. Therefore, quantification was done using only analytical techniques, not by obtaining a separated yield, except in certain cases where it was found that selective oxidation occurred to products that could be reliably separated without significant losses (although crude analysis was still performed in these cases to ensure no product was lost during purification). To increase the degree of accuracy, quantification was done by two orthogonal analytical methods (GC and NMR), with characterisation of the products backed up by additional IR and (GC)MS evidence.

2.3.1.1 Nuclear magnetic resonance (NMR) spectroscopy

Nuclear magnetic resonance is a phenomenon in which nuclei respond to an external magnetic field. When this happens, the nuclei are able to absorb and re-emit electromagnetic radiation, which occurs at a specific resonance frequency. This technique allows one to elucidate information about quantum mechanical magnetic properties of a nucleus, which in turn provides information about the electronic structure of a molecule.

Nuclei behave as if they have their own magnetic moments, originating from the spin magnetic moments of the particles they are composed of. When no external magnetic field is present, all orientations of the nucleus and thus of its magnetic field are essentially equally favourable and therefore their energy levels are degenerate. However, when an external magnetic field is applied, some orientations become more favourable and other become less favourable, which is observed as a splitting of energy levels. Two extreme orientations, one where the nuclear moment aligns with the external magnetic moment, and one where it opposes it, are shown in Figure 16.

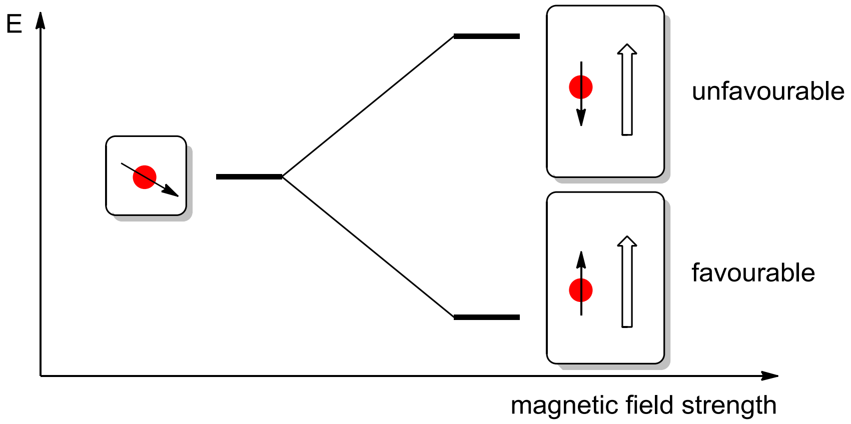

Figure 16: Simplified diagram of a magnetic dipole's energy levels, degenerated in the absence of a magnetic field, and in the presence of a magnetic field which causes a splitting of the energy levels of different orientations.

The workings of the technique are as follows. First, a sample (usually in solution) is subjected to a constant, uniform magnetic field in which the nuclear spins align. Then, this alignment is perturbed using a powerful electromagnetic pulse, preferably orthogonal to the original field. When the nucleus absorbs energy from this pulse, it is said to be in resonance, and the frequency at which this occurs is highly specific for its magnetic (and therefore electronic) makeup.

The electronic, local environment of a nucleus influences the frequency at which resonance occurs. In a molecule, neighbouring atoms and functional groups will have electrons of their own, which respond to the external magnetic field, creating their own magnetic field, which opposes the applied magnetic field. This process is known as shielding and causes the required magnetic strength of the applied field to be higher before resonance occurs, a difference known as shift. Because the molecular magnetic field is generally only a fraction of the (usually very strong) applied magnetic field, the difference between the unshielded and shielded magnetic field required is very small, and is usually expressed in parts per million (ppm) of the applied field.

A key advantage of NMR is that the resonance frequency of a nucleus is directly proportional to the strength of the applied magnetic field. This means that exceptionally strong magnets, built from superconductors, are often used, as the stronger the magnetic field, the higher the resolution of the obtained data. However, as magnetic field strength is a function of distance, field inhomogeneities will be present, unless efforts are made to compensate for this (a process known as shimming). If the field used is not homogeneous, the chemical shifts of the nuclei will be affected by the relative position of the sample, leading to noise and bad signals.

It should be noted that this entire process hinges on the nucleus having a total net magnetic moment, for if this is not the case, they will not respond to any external magnetic fields. This is the case if either the amount of protons or neutrons in a nucleus is uneven. In the case that both are even, the total magnetic moment is zero, and as such the nucleus is undetectable by NMR. For this reason, NMR studies involving carbon scan for the relatively rare ^{13}C isotope (relative abundance 1.1%), as the most abundant isotope of carbon, ^{12}C (relative abundance 98.9%) is NMR silent. Similarly, for ^{1}H NMR experiments, deuterated solvents are used, as ^{2}H has a total spin moment of 1 rather than $^{1}/_{2}$ for ^{1}H making ^{2}H magnetically quadrupolar rather than bipolar and therefore invisible on ^{1}H NMR. If the solvent used is not deuterated, the entire signal would be saturated with those of the solvent as it is present in much higher concentration than the sample to be measured.

A very important feature of NMR is that though protons may have different chemical shifts and peak shapes, their signal strength is theoretically always identical. As such, NMR provides a means of quantification using ^{1}H

NMR. This mode is sufficiently sensitive that compounds can be quantified with an acceptable margin of error. For instance, if a signal peak that is known to originate from a known amount of protons has a total area twice as big as a signal peak of a different compound of the same amount of protons, it can be assumed with reasonable accuracy that the former compound is present in twice as great a concentration as the latter. Generally speaking, NMR spectroscopy is not sensitive enough to perform such quantitative analyses on nuclei other than hydrogen. Due to the presence of a margin of error, these results will be checked against a different, orthogonal quantification method (gas chromatography).

2.3.1.2 Gas chromatography (GC)

As with all modes of chromatography, gas chromatography is a procedure for separating compounds based on one or more of their properties. In the case of gas chromatography, this property is their boiling point (and to some degree, their polarity). It achieves this separation by pushing the sample in a mobile phase (the carrier gas; usually helium or nitrogen) through a long, thin, hollow column lined with a stationary phase (a liquid or polymer). The column is located in a thermostated oven which goes through an appropriate temperature ramp. As the molecules have varying interaction with the stationary phase and varying volatilities and boiling points, some compounds will be retained more than others by this setup and thus separation is achieved. The different compounds then elute at a speed characteristic for the material. In this case, the type of column used was an Elite-5; a polymer column that separates compounds mainly, but not exclusively, by boiling point.

The setup of a gas chromatograph is quite simple. It features a sample injection port which is connected to a carrier gas reservoir and the column, which is located in a thermostated oven. After the sample is blown through the column, it encounters a detector, which gives off a signal, which is interpreted and fed to the user as a chromatogram (Scheme 31). There are many types of detector available; however, for the purpose of this research, it was chosen to employ a flame ionisation detector (FID) which is very sensitive to a large range of organic compounds across a large response range and has intrinsically low noise. Furthermore, FIDs are mass sensitive rather than concentration sensitive which means slight fluctuations in the flow do not affect the response output.

A FID works by using a hydrogen flame to combust the materials presented to it and measuring the resulting ions as a current using a very sensitive ammeter. The magnitude of this signal is a function of the amount of ions generated, which is dependent on the amount and type of material combusted. Although some materials will inherently produce stronger signals per mole than others (a property known as the “response factor” or RF), these factors tend to range from 0.5 to 2, which is a rather small range compared to for instance UV detectors where the UV response for two compounds can be many orders of magnitude apart.

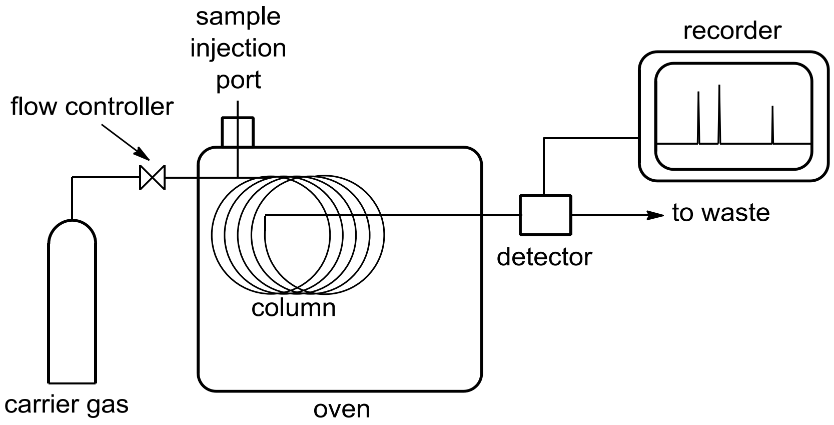

Scheme 31: Schematic representation of a basic GC setup.

RFs are obtained using calibrations of the target compound versus an internal standard. Samples consisting of variable amounts of the compound to be measured and a fixed amount of the internal standard are injected into the GC and the responses are noted. For greater accuracy, the samples should be run multiple times, and in random order. The observed peak areas are correlated with the actual amount of both compounds in the sample, and the relative response factor of the target compound to the internal standard is deduced from this. By plotting the points on a graph and subsequent linearisation, a mole-per-area ratio relative to that of the internal standard can be obtained; this is the response factor. Using the RF, any point on the line in the measured range of relative concentrations can be quantified using GC.

By adding a known amount of the internal standard to a reaction mixture after the reaction and measuring a sample of this mixture, the area ratio of each compound relative to that of the internal standard can, with knowledge of the RF, be used to calculate the amount of each compound in the mixture. This data can then be used to calculate conversion, yield, mass balance *etc.* This is described in more detail in Section 9.2.3.

Note that although the retention times of the different compounds are characteristic for every molecule, to check the identity of the compounds the GC peaks belonged to, mass spectrometry (GCMS) was used to verify the accuracy of the results.

2.3.1.3 Mass spectrometry (MS)

Unlike most methods described here, MS is not a spectroscopic technique, as the output is a measurement rather than an observation. In mass spectrometry, the mass of charged particles is measured and expressed as a mass-per-charge (m/z) ratio. Mass spectrometry is based on four stages: ionisation, acceleration, deflection and detection.

The first stage of mass spectrometry is ionisation of the sample so that charged molecules are obtained — this is imperative as uncharged species cannot be detected by the spectrometer. A wide variety of techniques is available to achieve ionisation, and species may be either positively or negatively charged (although they use different techniques to do so). Examples of different methods include electron ionisation (EI — bombardment of the sample by high-energy electrons), chemical ionisation (CI — reaction of the analyte with a pre-ionised reagent gas), electrospray ionisation (ESI — electrical aerosolisation of the analyte using a high voltage), matrix-assisted laser desorption/ionisation (MALDI — matrix immobilisation followed by laser ablation and gaseous proto-/deprotonation), *etc.* The method of ionisation used is picked depending on several factors including molecular size and weight, chemical nature, form (gas, solid, liquid) and others.

Additionally, both “soft” and “hard” techniques are available. “Hard” techniques such as EI impart so much energy into the analyte that it generally fragments into small parts, which are also detectable. The obtained fragmentation pattern can yield information about the type of functional groups present, as well as serve as a secondary “fingerprint” of the molecule. A disadvantage of hard ionisation techniques is that some molecules, particularly relatively sensitive ones, are so unstable towards the ionisation that they fragment before a noticeable amount of molecules can make it to the detector without having decomposed. This means no full, molecular ion is observed with some molecules. “Soft” techniques such as ESI and MALDI use comparatively mild techniques to ionise the analyte, making it much less likely that this issue occurs, however no additional fragmentation information becomes available, and sometimes the molecule has difficulty ionising at all.

Once ionised, the analyte is accelerated so that all particles move at the same speed, using an electrical or magnetic field. The “beam” of particles is focused to be as thin as possible (Scheme 32). After acceleration, an electromagnet applies a field orthogonal or angled compared to the flight path of the charged analytes. As lighter particles are easier to deflect off a set path using a fixed force than heavier particles would be, the amount of deflection is directly dependent on the mass of the particle.

The deflected particles then hit a metal plate, which neutralises the applied charge by a reshuffling of electrons from the metal matrix. This causes a current in the system, which the machine outputs as a signal. By varying the magnetic field strength, the ion mass that is deflected onto the detector plate can be changed. Ions that are too heavy, or which are too light, will bend off too little, or too much, and will not reach the detector (Scheme 32).

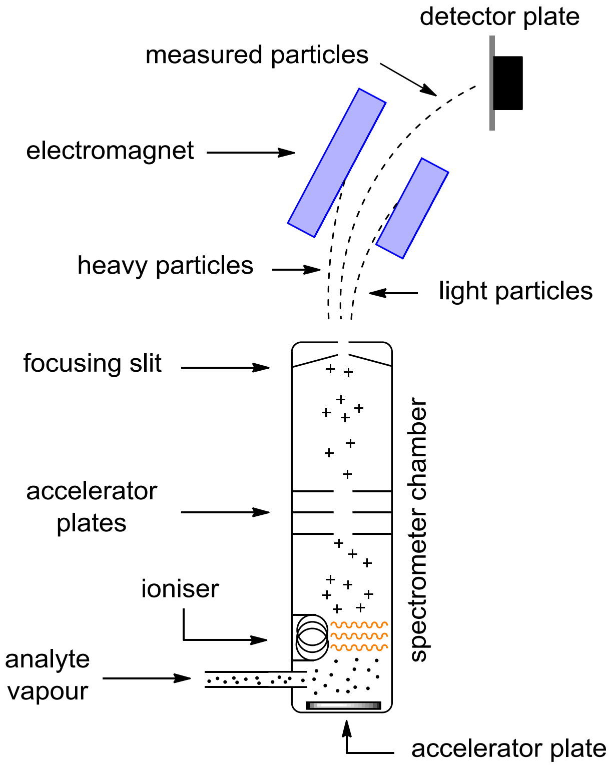
detector plate
measured particles
electromagnet
heavy particles
light particles
focusing slit
accelerator plates
ioniser
analyte vapour
spectrometer chamber
accelerator plate

Scheme 32: Schematic representation of a mass spectrometer.

2.3.1.4 Infrared (IR) spectroscopy

IR spectroscopy is a technique for probing the types of bonds present in a sample. In it, infrared light is used to scan molecules for vibrational modes. At certain frequencies, which correspond to the transitional energies for these vibrational modes, the molecules will absorb the light shone on it. The difference between the light shone through the sample and a reference is calculated and fed back to the user as a spectrum showing absorbance versus wavelength.

The traditional way of using infrared spectroscopy is using a monochromatic beam of light, the wavelength of which is varied, and the absolute difference between the intensity of the reference beam and the beam through the sample is fed back on the spectrum. A more modern way of doing this is using Fourier-transform infrared spectroscopy (FTIR), in which the light beam is not monochromatic but rather made up of many different wavelengths at once. The makeup of the beam is then varied using a Michelson interferometer, which uses a system of moving mirrors to vary the phase of the reflected light beam. With this, each wavelength experiences periodic blocking and transmission due to wave interference resulting from phase differences in the reflected waves. The absorbance of the sample relative to the reference over time is then fed to a computer, which determines which wavelengths were active at the time, and the absorbance of each wavelength is calculated accordingly.

The wavelengths absorbed as well as the strength with which they are absorbed are characteristic of certain types of bonds and vibrational modes. The six main types of vibration are; stretching (symmetrically and asymmetrically), scissoring, rocking, wagging and twisting. Not all types of bonds have all these types of vibration. Thus, using IR spectroscopy, determinations can be made about what kinds of bonds are present in the reaction mixture, providing more information about the nature of the products obtained.

2.3.2 Analysis of catalyst batches

2.3.2.1 Powder X-ray diffraction (PXRD)

Powder X-ray diffraction was used as the main technique for the analysis of catalyst batches, to determine the phase purity of the synthesised material. As each framework has its own characteristic diffraction pattern, PXRD can be used to easily determine whether the synthesised material is actually of the desired framework type. Furthermore, it allows one to determine some measure of the crystallinity of the sample, as well as the presence of other crystalline phases, which are considered to be impurities.

The PXRD machine works using an X-ray laser which is aimed at the sample and swept through a span of two predetermined angles. A detector measures the intensity of the X-rays scattered off the sample. Because of the random alignment of the powdered crystals, these are diffracted in a circle pattern, which is then integrated in one dimension and fed back to the user as a plot of the measured intensity (recorded as counts) of the diffracted X-rays versus the angle (2θ) between the X-ray source and detector (Figure 17).

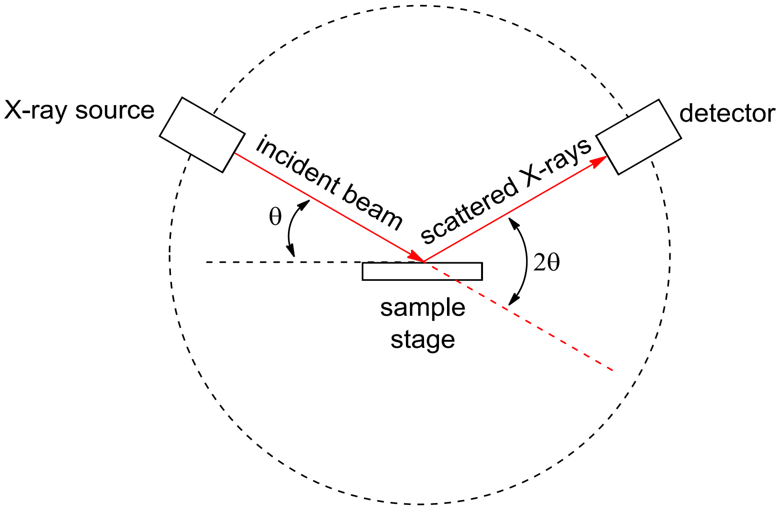

Figure 17: Schematic representation of the setup of a PXRD machine.

The spectrum produced will show peaks only when the sample interacts with the incident (monochromatic) X-rays in such a way that constructive interference takes place; *i.e.* that the diffracted X-ray beams are in phase. When this happens, the intensity of the diffracted beam is at its highest. When the diffracted X-rays are out of phase, destructive interference takes place instead and no visible pattern is produced. When no crystalline phase is present, only (pink) noise is observed.

In order for all the diffracted X-ray beams to be in phase, the interaction of the X-rays with the sample must obey Bragg's law (Figure 18). For this to occur, the difference in length of the diffracted X-ray beams must be an integer amount times the wavelength, *i.e.* $n \cdot \lambda$. This extra distance is related to the lattice spacing *d* by Bragg's law:

$$n\lambda = 2d\sin\theta$$

For each angle that satisfies Bragg's law, full constructive interference is then observed, which leads to a high-intensity peak in the XRD spectrum (Figure 19).

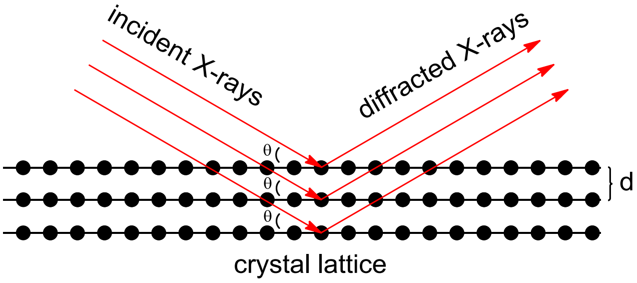

Figure 18: Schematic representation of the underlying principles of Bragg's law. As different X-rays travel to atomic points deeper in the crystal structure, the beam length differs, leading only to constructive interference if Bragg's law is satisfied.

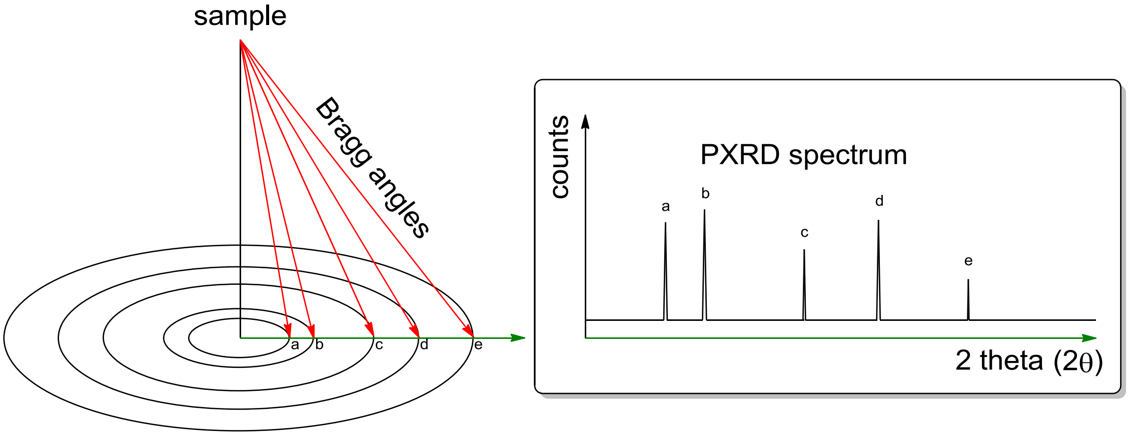

Figure 19: Illustration of the result of a PXRD scan. The reflections that produce visible peaks (i.e. *those at whose angles Bragg's law is satisfied) show as circles around the sample. These circles are integrated from mid-point to the end of the scan which produces a spectrum.*

As the diffraction is dependent on lattice spacing, each peak can be associated with its own set of Miller indices; a nomenclature used to identify lattice planes in a crystal unit cell. Furthermore, as every framework has its own unique morphology and therefore unique lattice spacing constants, every framework will produce its own unique PXRD spectrum. Other than checking whether the desired type of framework is present, this also allows us to check for crystalline impurities, which will show up as peaks that do not belong to the desired framework type. Finally, PXRD gives a measure of the crystallinity of the sample; the higher the amount of amorphous material present, the less defined the produced pattern will be, and the more background signal can be observed.

PXRD also allows us to gather information about the size of crystalline domains, *i.e.* the size of the crystallites in powders, using the Scherrer equation. This equation relates peak widening to crystallite size. To calculate it, the position and width of a peak (generally the largest peak in the spectrum is used) at half its maximum (full width at half maximum or FWHM) is used according to the following formula:

$$\tau = \frac{K \cdot \lambda}{FWHM \cdot \cos \theta}$$

With τ the crystallite size, K the “shape factor” of the material (a dimensionless constant generally set to 0.9), λ the wavelength of the X-rays used, *FWHM* the full width of the peak at half maximum, and θ the Bragg angle of the peak.

Note that because several other factors and imperfections can also contribute to peak broadening, the Scherrer equation represents a minimum.

2.3.2.2 Inductively coupled plasma optical emission spectroscopy (ICP-OES)

ICP-OES is an analytical method that provides bulk elemental analysis, *i.e.* the relative amounts of certain specified elements in the whole of the sample. This technique allows one to make comparisons of catalyst batches of different metal loadings, giving an indication of how much metal was or may have been incorporated, and sometimes, by deduction, if impurities are present. This method is an important part of calculating the turnover number (TON) and turnover frequency (TOF) of a catalyst batch.

ICP-OES is a two-stage technique (first ICP, then OES). During the ICP stage, the sample is first digested in an appropriate reagent (generally concentrated acids like HNO_3 or HCl or borates like $LiBO_2$ or $Li_2B_4O_7$). This mixture is then nebulised and injected into a flow of hot argon plasma at *ca.* 6000–10 000 K which is created by passing argon though a quartz torch and ionising it in a strong electromagnetic field generated by an RF coil (Scheme 33). The ionisation is initiated using a tesla coil. As soon as the sample comes into contact with this plasma, it undergoes complete dissociation into its parent atoms which undergo excitation and ionisation transitions. These transitions are unique to each element.

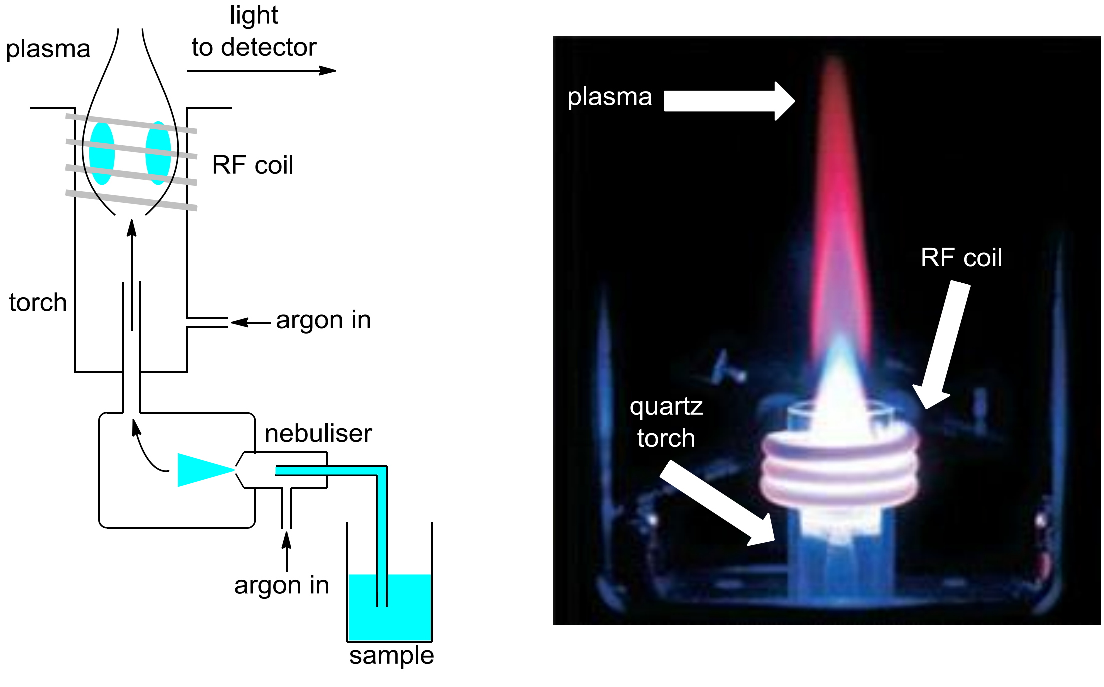

Scheme 33: Left: diagrammatic representation of an ICP unit. Right: image of an ICP unit in operation (image adapted from source[185]).

These transitions can be detected using optical emission spectroscopy (OES). The intensity of the emitted light is measured and related to the element of interest in order to obtain a quantitative value. Note that although giving valuable information, due to the high cost of running every analysis, only a select few batches were analysed using this technique.

For our samples, the samples were digested in a combination of H_2SO_4 and $HClO_4$. Calibrations using standard solutions of the elements under investigation can then be used to quantify the amount of metal present in the sample. This information is used in this project to elucidate trends on metal retention during synthesis and to establish turnover numbers with.

2.3.2.3 Brunauer-Emmett-Teller (BET) surface area techniques

To measure the surface area and pore size diameter of the synthesised catalysts, adsorption studies were conducted. Adsorption occurs due to physical or chemical interactions of molecules with a surface. Though the amount of material adsorbed onto a surface is related to the surface's total area, there are several models to correlate the two. Two models are explained below (Scheme 34).

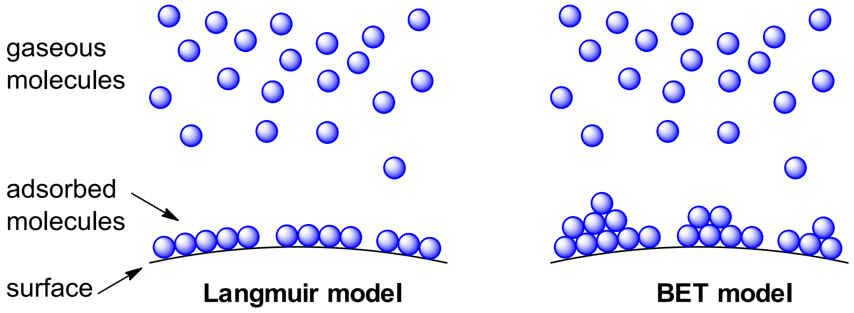

Scheme 34: Schematic representation of the Langmuir (left) and Brunauer-Emmett-Teller (BET, right) models of surface adsorption.

In the Langmuir adsorption model, three fundamental assumptions are postulated:

1. The molecules adsorb as a monolayer;
2. The surface is uniform and all adsorption sites are equivalent;
3. The adsorption of one molecule does not influence the adsorption of any other molecules.

This rather basic model is a fairly stark approximation when one considers many systems do in fact allow adsorption of multilayers however, and this led to the development of the Brunauer-Emmett-Teller (BET) model. In this model, multilayer coverage is considered to be possible, making it more accurate than the earlier Langmuir model and giving rise to substantially different results in certain cases.

From the results obtained, one can elucidate information about the surface area of the material are well as the pore sizes and pore size distribution of the material. The IUPAC classifies six different types of isotherm (Figure 20):

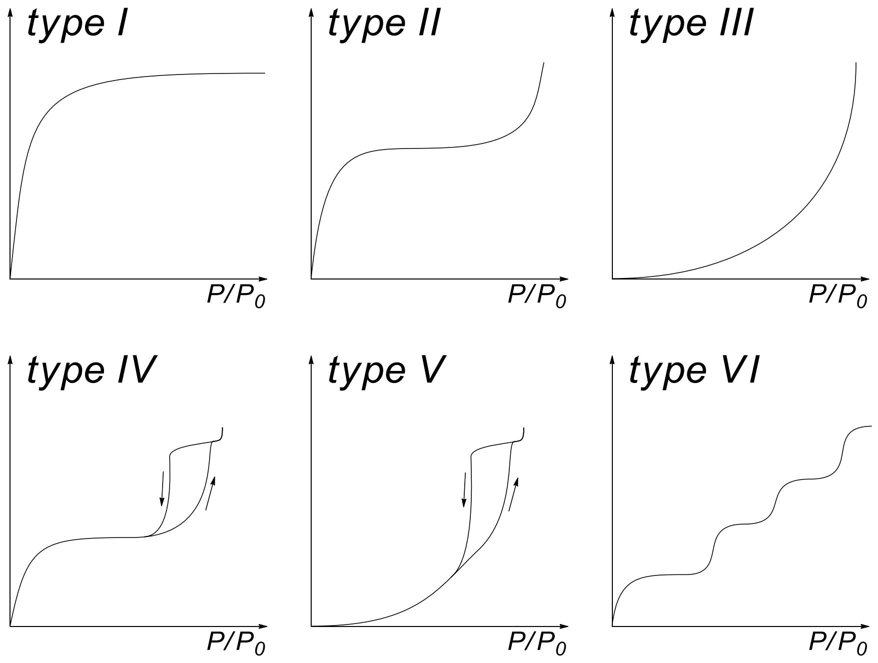

Figure 20: Six general types of BET isotherm.

The different isotherm shapes derive from varying adsorption and desorption trends within materials, and give information about the type of material and surfaces under investigation:

- Type I materials exhibit Langmuir behaviour and therefore the adsorption occurs as a monolayer. This is observed for microporous solids.
- Type II isotherms are observed for materials in which multilayer adsorption does occur, such as macroporous or non-porous materials.
- Type III materials show multilayer adsorption, but have very low interaction with the adsorbate.
- Type IV isotherms show a hysteresis loop (indicated by arrows) which indicate mesopores. These pores cause capillary condensation and desorb in a different way than they adsorb, causing the adsorption-desorption mismatch observed in the isotherm.
- Type V materials show similar behaviour to type IV materials, including the hysteresis loop indicative of mesoporosity, but they show low interaction with the adsorbate.
- Type VI isotherms show discrete steps corresponding to the completion of different layers on a surface, generally a uniform one.

The hysteresis loop in types IV and V isotherm are caused by two different mechanisms for adsorption and desorption in the same material (Scheme 35).

Initially the gas particles adsorb as layers until they get close to each other, at which point they quickly collapse together due to capillary condensation. Subsequent reduction of the pressure leads to an emptying of the pores in a different way, which initially resists desorption, leading to a difference in shape between the adsorption isotherm and the desorption isotherm.

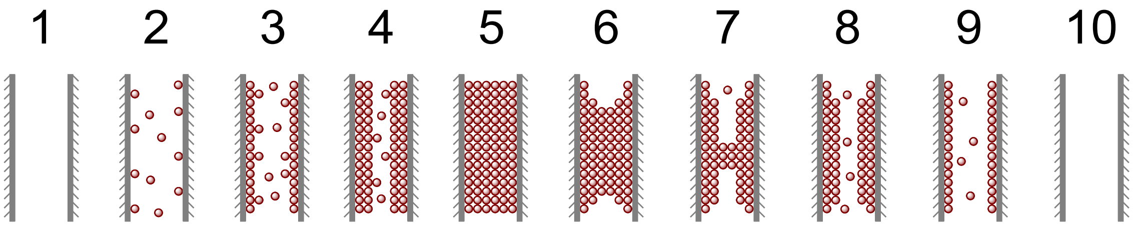

Scheme 35: Illustration of adsorption/desorption in mesoporous materials, leading to type IV/V isotherms with hysteresis loops.

Furthermore, the shape of the hysteresis loop itself can provide information about the type and shape of mesoporosity observed. Four (extreme) examples of different hysteresis loops are shown below (Scheme 36):

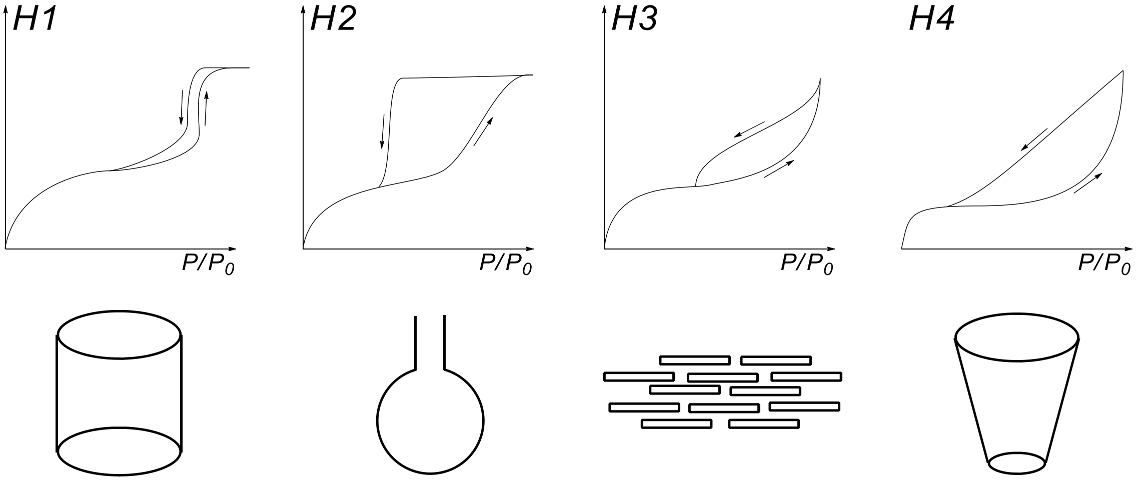

Scheme 36: Four types of hysteresis loop.

- Type H1 loops are often observed for well-aligned materials with conical pores.
- Type H2 loops show a more precipitous desorption curve and are usually indicative of bottleneck-type pores.
- Type H3 loops are often found for materials with slit- or panel-shaped pores.
- Type H4 loops generally indicate materials with conical pores.

Indirectly, surface area measurements can be used to deduce information about impurities and is sensitive to the formation of extraframework species in the sample. If a metal-doped sample shows a comparable surface area and micropore volume compared to an undoped sample, the substitution is concomitant with little or no disruption of the material. However, if a noticeable decrease of surface area occurs, it is likely that dense extraframework species are created as such species have very low surface areas compared to those of porous materials.

2.3.2.4 Scanning electron microscopy (SEM)

Scanning electron microscopy (SEM) is a technique for visually imaging a sample, and was used to determine the morphology and particle size of the synthesised catalysts. The instrument uses a high-energy electron beam (1–30 keV) to scan the sample in a grid-like movement, providing a visual representation of the sample (Scheme 37). As the wavelength of electrons is very short compared to that of visible light, the samples can theoretically be rendered at extremely high resolution, providing enormous magnification. In practice, depending on conditions, magnifications ranging from 10 000 to *ca.* 500 000 times can be reached, though microscopes capable of magnifications up to 10 000 000 times or more exist. Compared to light microscopes, the most powerful of which are limited to magnifications of *ca.* 5000 times, this is a remarkable improvement.

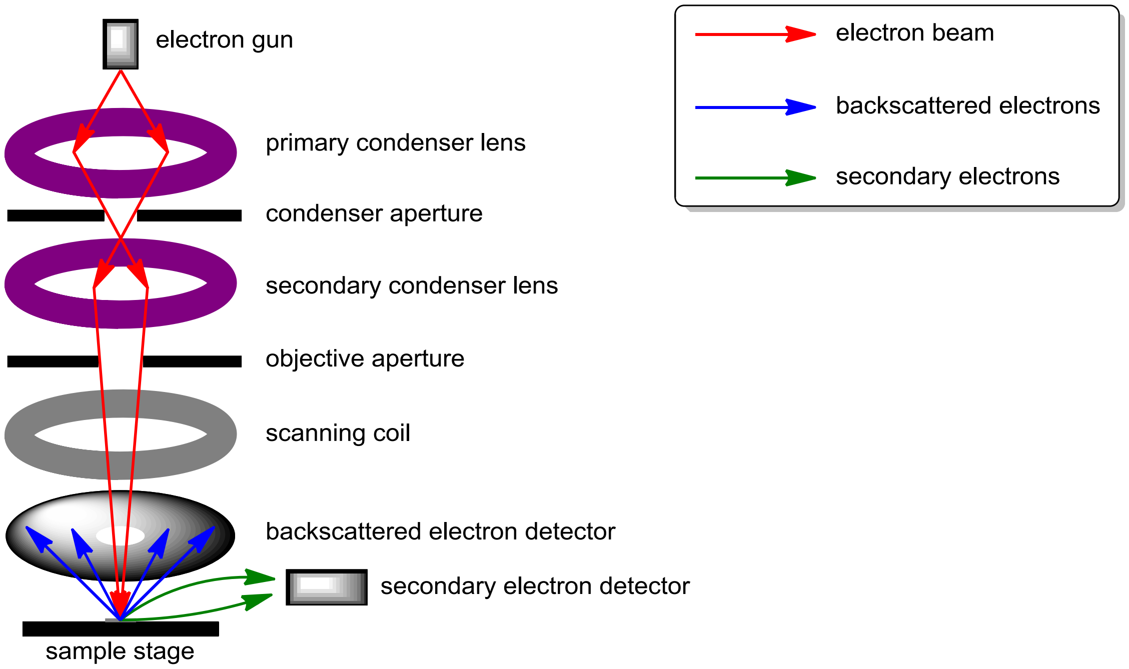
electron gun
primary condenser lens
condenser aperture
secondary condenser lens
objective aperture
scanning coil
backscattered electron detector
secondary electron detector
sample stage
electron beam
backscattered electrons
secondary electrons

Scheme 37: Schematic representation of an SEM imaging unit.

The machine works using an electron beam which is focussed by one or more condenser lenses and passed through an objective before hitting the sample. An orthogonal electromagnetic coil then changes the orientation of the beam accordingly to obtain a scanning motion so that the sample can be imaged over an area. As the electrons from the beam hit the sample, they (inelastically) collide with electrons on the surface of the material, causing them to be ejected from their electron shell. These so-called secondary electrons are then attracted to the (positively charged) secondary electron detector, while the collided primary electrons (originated from the electron beam) are scattered back onto a doughnut-shaped backscattered electron detector.

The two types of electron (backscattered and secondary) provide different information about the sample. As heavy atom types scatter electrons back more strongly than lighter atom types, backscattered electrons provide more information about the composition of the sample, while the more uniformly scattered secondary electrons provide more information about the topology of the sample.

2.3.2.5 Energy dispersive X-ray (EDX) spectroscopy

EDX (or EDS) is an analytical method used to perform (quantitative) elemental analysis on a sample. High-energy particles such as protons, electrons or X-rays are shot at the sample, inciting the excitation and subsequent ejection of an electron out of one of the atoms in the sample. This electron vacancy is then filled up by an electron from a higher-energy shell from the same atom, and the difference in energy may be released in the form of an X-ray, which is then picked up by the machine.

As the difference in energy between the two levels is characteristic for each element, EDX results in a spectrum with peaks showing the amount of each element in a sample. Moreover, unlike ICP-OES (see 2.3.1.2), which conducts bulk analysis of a sample exclusively, EDX can be focused on a small part of a sample, which gives it considerable synergy with electron microscopy (EM) techniques, to which it is usually coupled; EM allows the user to view their sample at a very high magnification, and EDX allows the elemental analysis of a part of it, such as a single particle or cluster within the sample. An example of an SEM image of a five pence coin with measurement target windows 1 and 2 and the resulting EDX spectrum of these parts of the coin is shown in Figure 21.

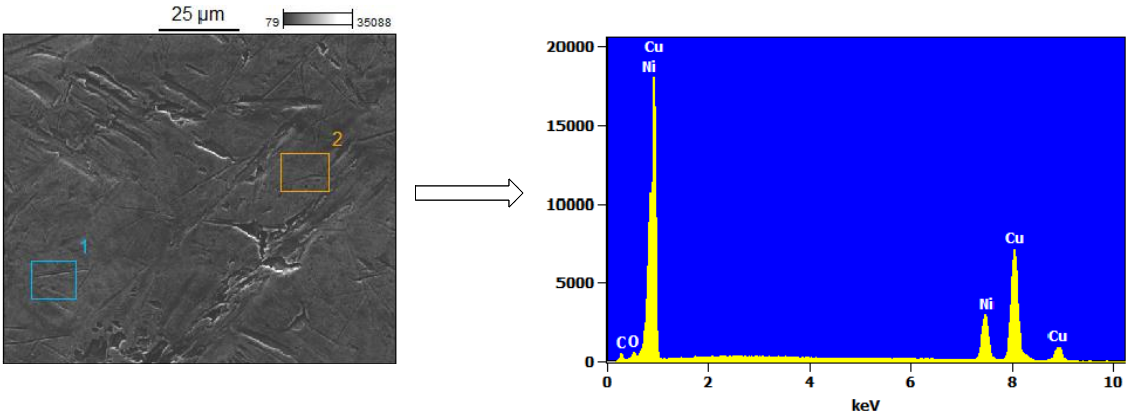

Figure 21: Left: SEM image of a five-pence cupronickel coin with EDX measurement target windows 1 and 2. Right: EDX spectrum of one of these target windows. Resulting quantification showed a 24.3% Ni and 75.4% Cu make-up (by weight): a good match-up with its intended 1:3 minting specification.

2.3.2.6 Ultraviolet-visible (UV-Vis) spectroscopy

UV-Vis spectroscopy was used to probe the oxidation state and coordination geometry of the substituted transition metal centres in the catalysts. Changes in the coordination or oxidation state of these metal centres can be readily detected by the appearance or disappearance of certain peaks or shoulders in the spectrum.

In the case when no ligands are present around the metal centre, the energy levels in all the d-orbitals are degenerate. When ligands do coordinate to the metal centre, the distribution of electron density is non-uniformly disturbed, and the energy levels are no longer equal. This loss of degeneracy in the d (or f) orbitals of a sample is referred to as crystal field splitting and its magnitude is dependent on many factors including size and type of metal ion and ligands. The splitting pattern meanwhile depends on the coordination geometry of the ligands; examples of this are shown in Scheme 38.

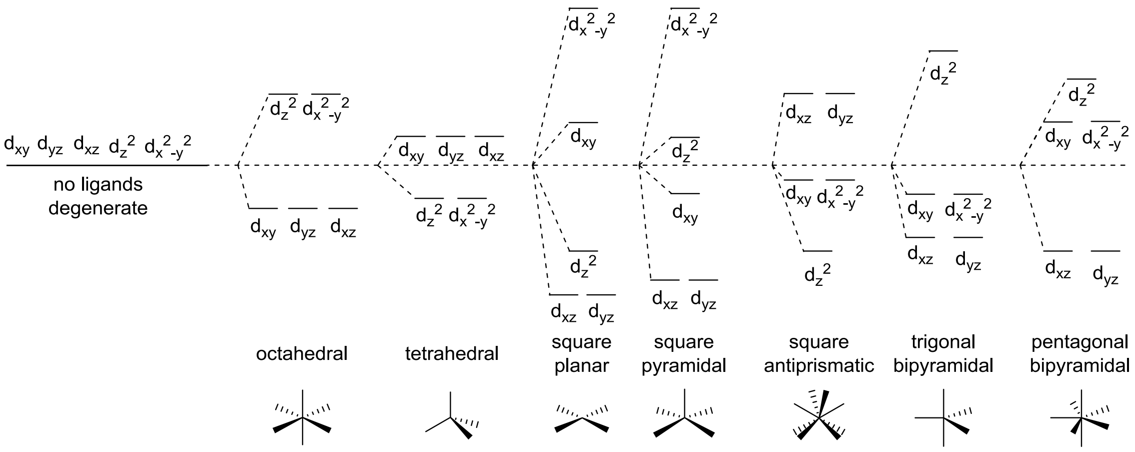
d_{xy} d_{yz} d_{xz} d_{z^2} $d_{x^2-y^2}$
no ligands
degenerate
d_{z^2} $d_{x^2-y^2}$
d_{xy} d_{yz} d_{xz}
octahedral
d_{xy} d_{yz} d_{xz}
d_{z^2} $d_{x^2-y^2}$
tetrahedral
$d_{x^2-y^2}$
d_{xy}
d_{z^2}
d_{xz} d_{yz}
square planar
$d_{x^2-y^2}$
d_{z^2}
d_{xy}
d_{xz} d_{yz}
square pyramidal
d_{xz} d_{yz}
d_{xy} $d_{x^2-y^2}$
d_{z^2}
square antiprismatic
d_{z^2}
d_{xy} $d_{x^2-y^2}$
d_{xz} d_{yz}
trigonal bipyramidal
d_{z^2}
d_{xy} $d_{x^2-y^2}$
d_{xz} d_{yz}
pentagonal bipyramidal

Scheme 38: Energy level diagrams showing different crystal field splitting types for several ligand coordination geometries.

The transitions between these states have different energies and are characteristic for the species involved. Excitation by absorption of energy of a certain wavelength then becomes possible — however, certain transitions are more "allowed" than others and thus will occur more pronouncedly. Transitions are subject to the following rules:

1. Transitions must involve an absolute change of 1 in the azimuthal quantum number ($\Delta \ell = \pm 1$);

2. Transitions must proceed with conservation of spin quantum number ($\Delta S = 0$).

The more these rules are obeyed, the more likely a transition is to occur. Therefore, in an absorption spectrum, the more intense the peak corresponding to this transition will be. Moreover, ligand-to-metal transitions are strongly influenced by the coordination and oxidation state of the ions. As such, this method can be used to elucidate information about the coordination mode of a transition metal. For example, several authors used UV-Vis spectroscopy to illustrate the presence of isolated, tetrahedral Ti^{4+} sites in titanium AlPOs that were deemed crucial for catalytic activity (as is the case with titanium sites in TS-1 and Ti-MCM-41, Section 1.6.2 and Table 4). This result provided direct evidence for the successful incorporation of titanium into the AlPO framework, as well as them possessing the desired coordination geometry. Isolated Ti^{4+} in a tetrahedral coordination shows a signal at *ca.* 215–230 nm, while this value shifts to 240–245 nm for octahedral Ti^{4+}. Extraframework titanium species like anatase (TiO_2) can also be probed for, and shows signals at 300–330 nm. A collection of literature examples and signals is shown below in Table 4.

When using liquids or solutions of a compound, a cuvette is generally employed that holds the sample, and light is shone through — the amount transmitted is then determined by a detector on the other side of the sample.

For (opaque) solids, this is a problem, as the sample will not allow the beam to travel through to the other sides. In these cases, the sample is analysed in terms of reflectance rather than transmittance. Two main types of reflectance can be measured, depending on the nature of the analyte.

When the surface of a solid is smooth, it is expected that incident light rays are all reflected in the same direction (see Scheme 39). This is called specular reflection, and in such a system collecting reflected light rays is theoretically relatively straightforward. When a material possesses a surface that is not smooth, such as a compressed powder, reflection is much more chaotic; although every individual beam will still show specular reflection, obeying the law of reflection, the overall reflected pattern will appear disorganised and highly dispersed. This is known as diffuse reflection, and its study is known as diffuse reflectance spectroscopy (DRS).

material	wavelength (nm)	inference	ref.
TAPO-*n*	215–230	isolated tetrahedral Ti^{4+}	101,129,139
TS-1	215	isolated tetrahedral Ti^{4+}	186
	240	isolated octahedral Ti^{4+}	187
anatase	300–330	polymeric octahedral Ti^{4+}	101
Ti-MCM-41	213	isolated tetrahedral Ti^{4+}	76
VAPO-5	250 (v. broad)	isolated tetrahedral V^{5+}=O	174,180,183
	500–333	isolated octahedral V^{5+}=O	180
	300–340	oligomeric VO_4 tetrahedra	111
	550–800	sq. pyr./dist. oct. V^{4+}=O	107,111,174
V_2O_5	350–450	polymeric V^{5+}	101,111
V_2O_5/SiO_2	250 (v. broad)	isolated tetrahedral V^{5+}=O	188
NH_4VO_3	239, 360	polymeric tetrahedral V^{5+}=O	111

Table 4: UV-Vis signals reported for various titanium and vanadium materials.

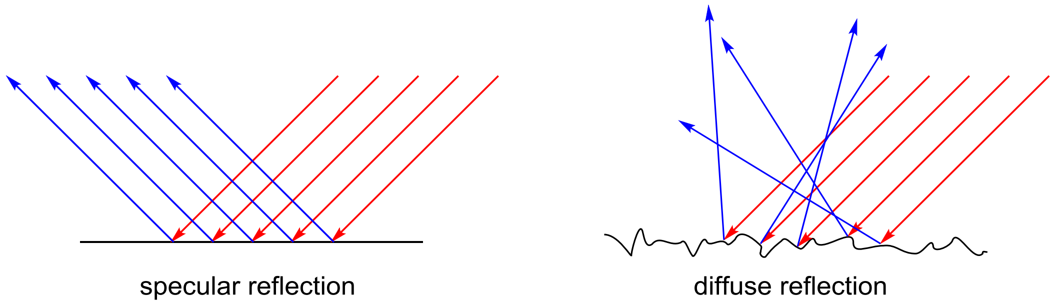

Scheme 39: Specular (left) versus diffuse (right) reflection. Incident rays are shown in red, reflected rays in blue.

Due to the highly scattered nature of diffuse reflection, experiments on powders or solids with rough surfaces have to employ a device that gathers the reflections into a single place. An integrating sphere is used to this end, which is coated with a highly reflective material with no absorption in any of the wavelengths measured; a commonly employed material is $BaSO_4$, which is also used to dilute some concentrated solid samples. The integrating sphere collects reflected rays, using one or more baffles to prevent light from directly reaching the detector. A schematic representation of a UV-Vis diffuse reflectance setup employing an integrating sphere is shown in Scheme 40.

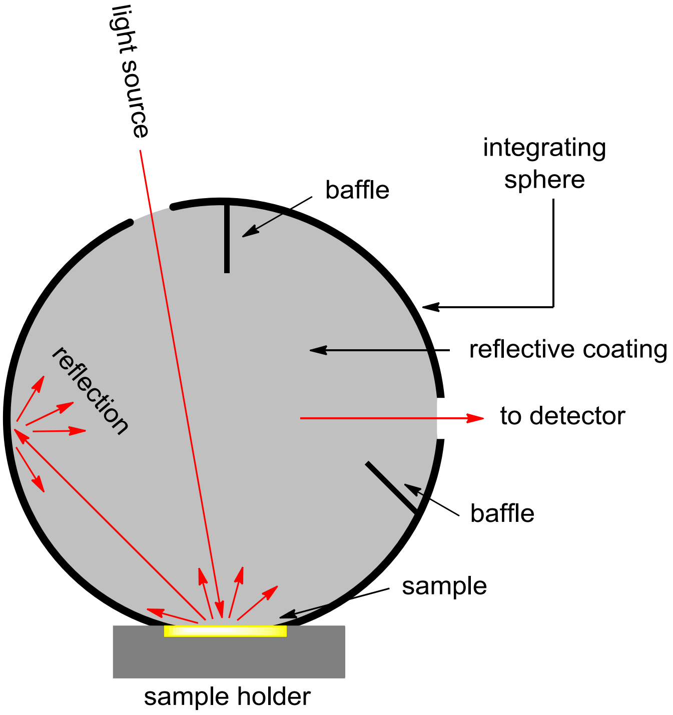
light source
integrating sphere
baffle
reflective coating
reflection
to detector
baffle
sample
sample holder

Scheme 40: Schematic representation of a DRS UV-Vis spectrometer employing an integrating sphere. Light rays are shown in red.

2.3.2.7 Solid-state nuclear magnetic resonance (SSNMR) spectroscopy

Solid-state NMR is an extension of liquid NMR as discussed in section 2.3.1.1. While liquid NMR is often used to analyse reaction products, solid (insoluble) catalysts require several major adjustments to analyse using NMR spectroscopy, although the fundamental principles behind them are the same. Below is a discussion of the complications that arise from performing NMR in the solid state, and the things that can be done to resolve them.

As discussed before, at the start of an NMR experiment, an external magnetic field is applied, and the nuclei will try to re-orient themselves in such a way as to align their magnetic polarisation along this field in order to minimise the energy in the system. In solution, this is quite facile, as the molecules have relatively high freedom of movement and are able to simply "tumble" around, often faster than the instrument can perform the measurement. As such, only a single orientation is observed in practice, resulting in sharp, defined peaks.

In solids, this tumbling is not possible, and anisotropy occurs — that is to say, due to the fixed orientation of the species in all directions, the effect does not occur within a single orientation, but in all orientations at once. As a result, instead of sharp peaks, the spectrum will consist of peaks resulting from all orientations, superimposed, which will appear extremely broad and undefined. To compensate for this, experiments can be performed by spinning the sample at the "magic angle" (θ_m = arctan(√2), *ca.* 54.7°, defined as the angle that divides a cube diagonally across all axes, Figure 22). This technique is referred to as magic angle spinning (MAS). By doing this, any vectors aligned along the z axis (the axis along the direction of the magnetic field, B_0) are also spun through the x and y axes, essentially making them equivalent. As a result, the anisotropy is averaged, and sharper peaks are obtained.

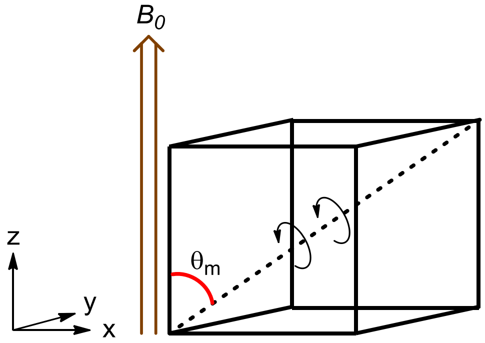

Figure 22: Illustration of the magic angle θ_m and MAS along it. The direction of the magnetic field, B_0 is along the z axis (portrayed in brown).

For nuclei with a spin greater than $I = {}^1/_2$, there is an additional complicating factor in the form of quadrupolar interaction. Unlike nuclei with spin $I = {}^1/_2$, which have a bipolar magnetic moment with spherical charge distribution, quadrupolar nuclei have a non-spherical charge distribution in the nucleus, causing second-order effects and additional asymmetry. This nuclear electric quadrupole moment, under the influence of an electric field gradient (such as within a molecule), then causes additional interactions that are large enough to be visible among Zeeman interactions.

Quadrupolar interactions cannot be averaged out by spinning it at the magic angle alone; in order to compensate for the quadrupolar effects the sample would need to be spun at two angles (30.55° and 70.12°) at the same time. Certain highly specialised probes and techniques are available to do this. However, compounded quadrupolar effects originating from multiple different sites can be very hard to disentangle.

An example of this is in ^{51}V solid-state NMR, which can meet with several complicating factors such as the relatively high nuclear electric quadrupole moment of the ^{51}V nucleus, high chemical shift anisotropy and second-order quadrupolar effects, which can seriously interfere with characterisation efforts.[111,189,190] In some materials such as VAPO-5, such problems resulted in rather low-resolution spectra, which have limited authors to characterisation by, chiefly, chemical shift. However, more recent studies have shown that chemical shielding anisotropy, quadrupolar and asymmetry parameters provide a better insight into vanadium materials.[190,191] For example, in a large work by Lapina *et al.*,[191] a wide range of vanadium oxide materials was characterised and divided into classes:

- Tetrahedral "Q^0" sites such as in orthovanadates (VO_4^{3-});

- Tetrahedral "Q^1" sites such as in pyrovanadates ($V_2O_7^{4-}$);
- Tetrahedral "Q^2" sites such as in monovalent-cation metavanadates (*e.g.* $NaVO_3$);
- Associated non-axial VO_5 and VO_6 sites such in divalent-cation metavanadates (*e.g.* $Mg(VO_3)_2$);
- Isolated and associated trigonal four-coordinate VO_4 pyramids of which one is a short V=O bond;
- Isolated octahedral VO_6 and tetragonal VO_5 pyramids such as in $VOPO_4$;
- Associated tetragonal pyramids, for example in $(NH)_4V_6O_{16}$;
- Strongly associated octahedral sites in decavanadates such as in $V_{10}O_{28}^{4-}$ polyanions (a decamer of VO_6).

As such, asymmetry parameters can elucidate information about the type of coordination present in the materials, leading to distinctions such as those enumerated above, solid-state NMR can potentially provide a wealth of information.

2.3.2.8 X-ray photoelectron spectroscopy (XPS)

XPS, archaically known as electron spectroscopy for chemical analysis (ESCA), is a surface-sensitive technique used for obtaining a variety of chemical information, most notably elemental composition, but also insight into the material's chemical and electronic properties. It is based on the photoelectric effect.

During XPS, the sample is bombarded with X-rays, generally Al K_α or Mg K_α X-rays. Incident X-rays absorbed by the material can induce the ejection of core-level electrons from the material, called photoelectrons (Scheme 41). An electron from a higher energy state then drops down to fill the hole left by the ejected electron. The additional energy derived from this transition results in the ejection of an electron from a higher-energy state, called an Auger electron. The kinetic energy (KE) of the ejected photoelectrons is dependent on several factors: the energy of the X-ray photon that hit it *($E = h\nu$)*, the binding energy (BE) of the electron, and the element and orbital the electron was ejected from. The oxidation state can cause differences in energy as well.

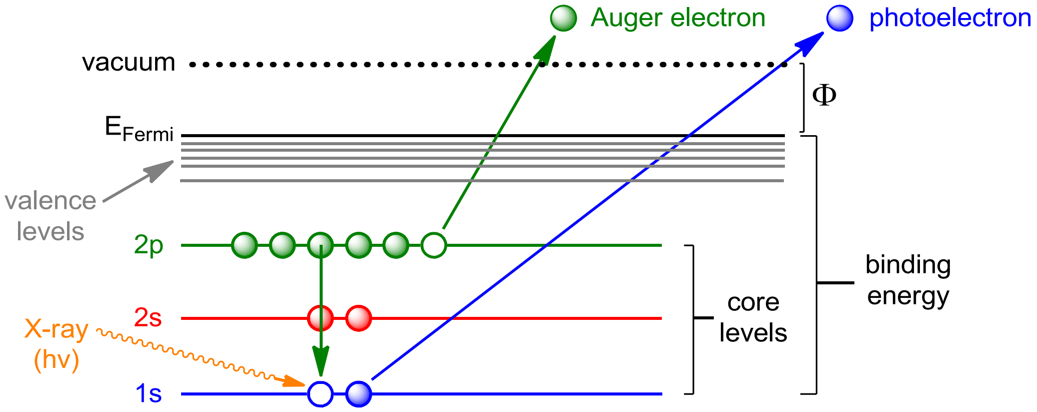

Scheme 41: Energy level diagram showing core and valence levels, photoelectrons and Auger electrons. The Fermi level is indicated as E_{Fermi}.

The BE is the energy needed to remove the electron from its own level to the Fermi level, a precisely defined entity that has an exact 50% probability of being occupied in thermal equilibrium. The Fermi level does not necessarily correspond to a discrete, existing energy level. The additional work required to remove the electron from the surface and into vacuum (denoted Φ) then determines the BE according to the following function:

$$BE = h\nu - KE - \Phi$$

This defines the kinetic energy of the photoelectron as follows:

$$KE = h\nu - BE - \Phi$$

The spectrum is fed back to the user as a plot showing electron count versus binding energy.

The binding energy of the electron is characteristic of a given element and as such every transition can be directly identified. Moreover, as the amount of electrons detected is proportional to the relative amount of atoms of that element within the sample, XPS can be used quantitatively — provided the elements are distributed homogeneously throughout the sample, XPS can give fairly high accuracy. XPS is a non-destructive analytical method.

When some orbitals are non-degenerate, the different energy levels are denoted by fractions in subscript, for example $2p_{3/2}$ and $2p_{1/2}$ (Scheme 42). The ratio of electrons ejected from these orbitals is documented and can be used as a reference check for peak intensities.

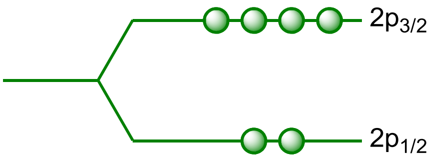

Scheme 42: Example of non-degenerate 2p orbitals split into $2p_{3/2}$ and $2p_{1/2}$ levels.

In theory, XPS detects all elements, although in practice hydrogen cannot be analysed properly. The reason for this is that unlike other elements, hydrogen has no core electrons; only valence electrons (which are engaged in chemical bonds). As such, ejected valance electrons from hydrogen overlap with valence electron excitations from other elements, making it hard to distinguish between the different signals. Moreover, the photoionisation cross-section of hydrogen is extremely small, several orders of magnitude smaller than that of other elements.

XPS spectra are inherently noisy and precise peak areas and locations are hard to determine by hand; however, several computer models exist to provide peak approximations (see Figure 23 for an example). Peak positions are referenced to positions of known peaks, often C1s.

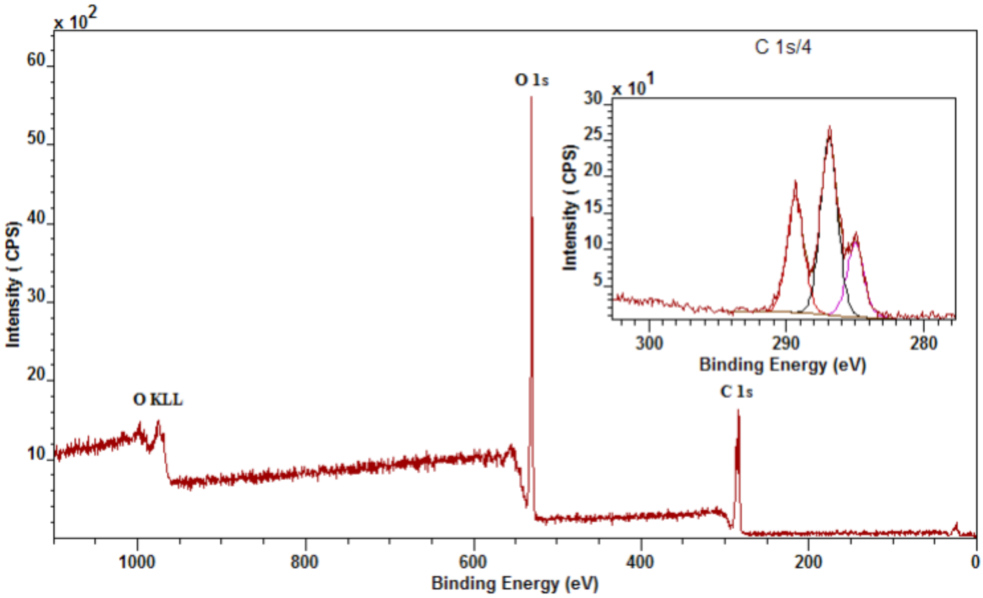

Figure 23: Example XPS spectrum of tartaric acid. Shown are the O and C peaks present in the molecule. H peaks cannot be identified. A magnification of the C1s region is shown in the insert, along with computer-assisted integration of the three peaks (a fourth region is not resolved enough to be visible) that make up this region. Image copied with permission from author.[192]

As only the top 1-10 nm (depending on the type of sample examined) of a sample are analysed, XPS is surface-sensitive. This property is used to selectively analyse surfaces (as compared to bulk techniques) in a wide variety of applications. One of the uses of XPS is in determining the oxidation state of a given element, about which it can give detailed information. For example, in a study by Mendialdua *et al.*[109] a series of vanadium oxide materials was prepared and a wide range of vanadium oxidation states was noted. As the oxidation state increases to higher numbers, the V2p$_{3/2}$ signal blue-shifts to higher values. A summary of their findings is shown in Table 5.

surface phase	BE V2p$_{3/2}$ (eV)
V_2O_5	517
V_4O_9	516.75
V_4O_9-V_3O_7	516.9
V_3O_7?	516.9
V_6O_{13}	516.2
VO_2	515.65
V_2O_3	515.15

Table 5: Summary of vanadium surface species and their binding energies observed by Mendialdua et al.[109]

2.3.2.9 Electron paramagnetic resonance (EPR) spectroscopy

EPR, also known as ESR (electron spin resonance) spectroscopy is a method that studies the interaction of unpaired electrons with external magnetic fields. The governing principles are roughly analogous to those of NMR spectroscopy (see section 2.3.1.1); however, instead of nuclear spins, it is electron spins that are examined. EPR is a powerful technique regularly used to study organic radicals; however, certain metal complexes can also be studied using this method, yielding valuable information about the nature of the species, as well as its environment.

As electrons have a spin quantum number $s = {}^{1}/_{2}$, an applied external magnetic field will lead to degenerate energy levels being split into two extremes ($m_s = +{}^{1}/_{2}$ and $-{}^{1}/_{2}$); parallel to the magnetic field, and antiparallel (Figure 24). This is called the Zeeman effect. The difference between the two energy levels, ΔE, can be traversed by an electron when it absorbs energy, such as from a photon. In EPR spectroscopy, microwaves are used as an energy source, and the absorption is monitored; however, unlike many techniques including NMR spectroscopy, the frequency is kept fixed and it is the magnetic field strength that is varied. Absorption is measured and fed back to the user, generally in the first derivative.

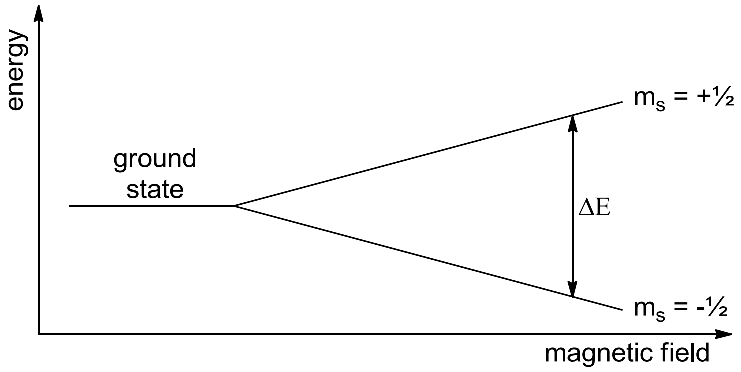

Figure 24: Illustration of the Zeeman effect imposed on an electron in an external magnetic field. The energy difference between parallel and antiparallel states is shown in the figure as ΔE.

One of the principal values measured is *g*, a dimensionless magnetic moment factor. For a free electron, this value is fixed (g_e), but in a molecular environment this value is different. The difference in *g* is derived from spin-orbit coupling of the electron with the molecule. As the orbital on the molecule also possesses an inherent spin, a second angular momentum is observed in addition to the aforementioned *g*. The magnitude of this factor depends on the size of the nucleus of the electron whose orbital it regards, so small molecules such as most organic radicals only have a minor spin-orbit coupling contribution and g will be nearly the same as g_e. In large atoms such as metals, the difference in g is much more pronounced. The value of g can be considered to be more or less a fingerprint for the molecule or chemical environment.

When the orbital orientation in the molecule is not symmetrical and the structure of the material does not average all these orientations out, the interaction is said to be anisotropic. This means that a different g value will be measured depending on along which axis the measurement would be taken. As such, the g-factors of the x, y and z axes are all measured and analysed. When two axes display the same g value, the spectrum is said to show axial symmetry, and g is displayed as $g_\perp$ and $g_\parallel$. When none of the axes display the same value, the spectrum is said to show rhombic symmetry, and the g factors are denoted g_x, g_y, and g_z. When all g-factors are the same, there is no anisotropy, and the spectrum is said to be isotropic. A scheme showing basic absorption patterns and their derivative for isotropic, axial, and rhombic symmetries is shown below (Figure 25).

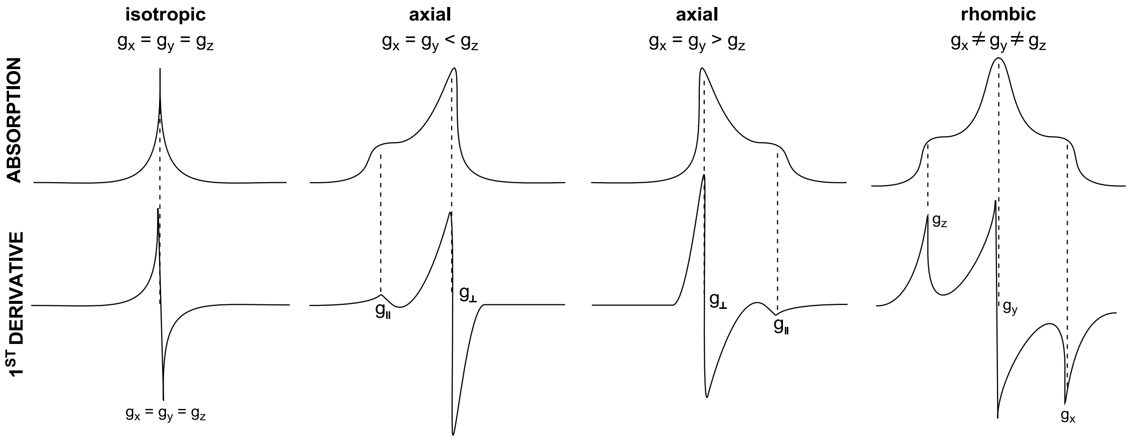

Figure 25: Basic isotropic, axial and rhombic XPS peak patterns. Shown are the raw absorption patterns as well as their first derivative.

Anisotropy within a species can be an indication of the symmetry of the chemical environment. For example, a highly symmetrical species would be expected to show a much smaller degree of anisotropy than an asymmetric one. As such, the measured anisotropy within a sample can be used to provide insights into possible species and environments within it.

Further splitting can occur when the unpaired electron can “see” a nearby nucleus with a non-zero magnetic moment of its own. This phenomenon, called hyperfine coupling, causes further splitting of states, giving rise to additional peaks in the spectrum. Coupling to a nucleus with spin $I = {}^{n}/_{2}$ gives rise to an $(2n + 1)$-fold splitting. Often, this splitting is not detectable as it is hidden in the peaks. However, if the signal arises from a single, well-defined species, the hyperfine splitting becomes apparent. This allows one to elucidate information about the nature of active sites in a material, as a well-resolved hyperfine signal indicates isolated, single sites, whereas clustered species will give broad signals.

When the hyperfine coupling originates from a nucleus that is not the electron's own, it is referred to as superhyperfine coupling. This can provide information about the chemical/electronic environment around the electron, and thus provide insights into the molecular structure. 2-dimensional experiments such as HYSCORE (hyperfine sublevel correlation experiment) can be used to examine superhyperfine coupling.

3. Oxidation of propylbenzene

3.1 Aims and objectives

The objective of this project is to perform a targeted C–H oxidation of molecules in such a way that it would be of value as a synthetic tool for organic chemists. To effect this kind of transformation, it was chosen to use bimetallic isomorphously substituted aluminophosphates as catalysts, as some have shown promise in previous work from the group with regards to synergistic enhancement of oxidative potential (Chapter 1).[76,139] The oxidation of propylbenzene was chosen as a way to gauge the type of reactivity that can be expected using these bimetallic systems.

In addition, it served as a platform to determine a set of workable conditions under which catalysis could take place. Rough optimisation could also be performed, allowing the gathering of information on trends of reactivity for each reaction parameter, as well as for modifications to the catalyst. In this way it was hoped to gain insight into what the optimal catalyst might be for a given reaction and the reactivity that could be expected with other compounds when exploiting the catalyst system under investigation.

3.2 Background

The oxidation of propylbenzene is not practiced on a meaningful scale. A few scattered reports on exotic transformations of propylbenzene have been reported involving the functionalisation of the aromatic unit or at the benzylic position with a group intended to produce a precursor for a multi-step synthesis. As a consequence, relatively very little information is available on propylbenzene functionalisation. A few examples are shown in Scheme 43. An interesting patented modification of propylbenzene is its high-temperature “cracking” over a H-mordenite zeolite catalyst mixed with alumina to produce a mixture of xylenes, toluene and benzene.[193]

3. Oxidation of propylbenzene

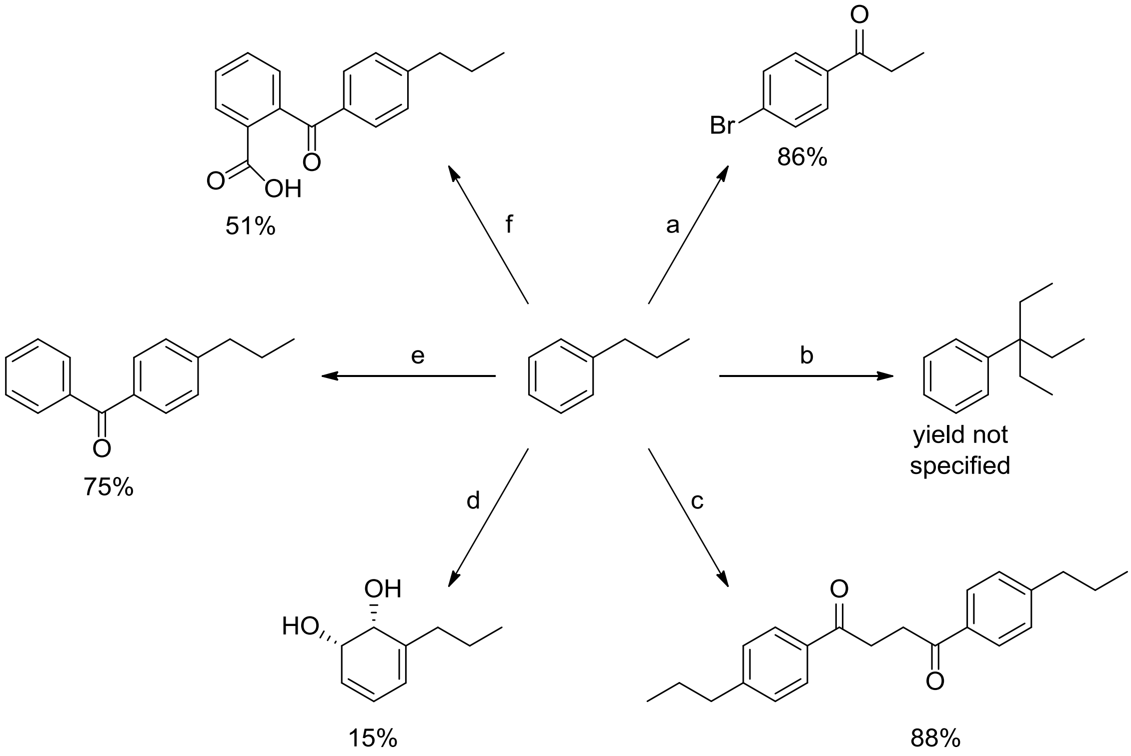

Scheme 43: Overview of a selection of propylbenzene modifications. Reported yields are shown next to the target molecule. Sources: a[194] b[195] c[196] d[197] e[198] f[199].

A few publications exist on the oxyfunctionalisation of propylbenzene, using a wide variety of conditions and oxidants, from deposited permanganates to oxygen to enzymatic approaches. These are summarised in Table 6.

product(s)	**reagents and conditions**	**yield or conversion**	**ref.**
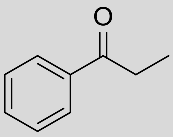	$KMnO_4$, Rexyn 101 H ion exchange resin, DCM, 5.45 h, reflux	93%	200
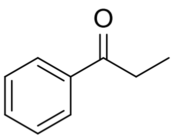	$KMnO_4$ on zeolite Beta, DCE, 96 h, RT	92%	201
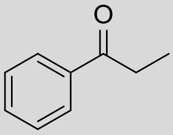	$NaBrO_3$, “silica sulfuric acid”, 3 h, RT	92%	202

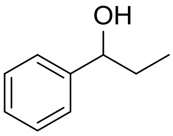	$LiAlH_4$, AIBN, O_2	—	203
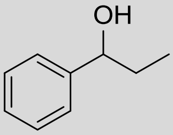	cytochrome P450$_{BM3}$ CYP102A1, NADPH, bovine liver catalase, DMSO, 30 ˚C, *p*H = 7.4	99%	204
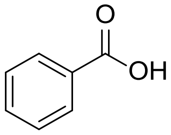	O_2, $CHCl_3$, irradiation	80%	205
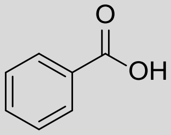	O_2, allyl bromide, EtOAc, 10 h, RT, irradiation	51%	206
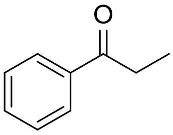 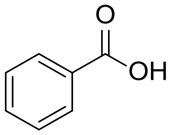	TBHP, $[(\text{pymox-Me}_2)_2\text{RuCl}_2]^+\text{BF}_4^-$, RT	—	207
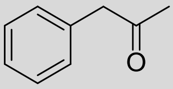 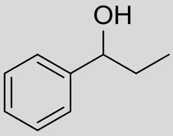	*i*-PrOOH, MeCN, Au nanoparticles on SBA-15, 70 ˚C, 36 h	68–89%	208
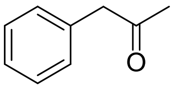	$IrCl_3$, $CeSO_4$, AcOH, 3 h, 100 ˚C	71%	209
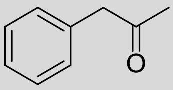	CrO_2Cl_2	—	210

3. Oxidation of propylbenzene

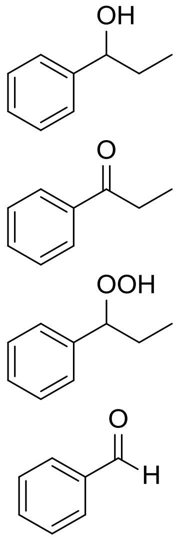	CHP, 40-80 ˚C, AUROlite gold nanoparticles on TiO_2	—	211
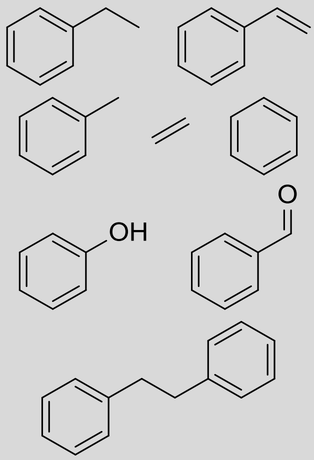	O_2, 25–50 atm, 838–1669 K	—	212
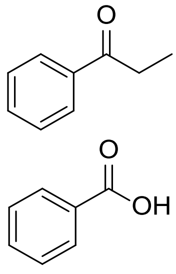	$MnBr_2(py)_2$, dibromobis(pyridine)cobalt(II), AcOH, 140 ˚C, 10 bar, 0.83 h	97%	213
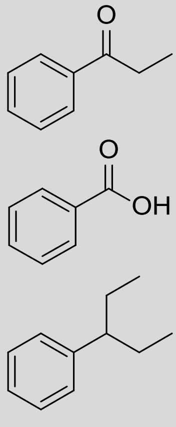	HNO_3, [bmim][methanesulfonate], H_2O, 80 h, reflux	15%	214

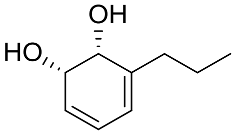	O_2, *Pseudomonas putida* UV_4	15%	197
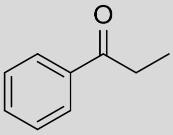	Au nanoparticles on TiO_2, O_2, 1 atm, 24 h, 90 °C	16%	215

Table 6: Overview of literature reports on the oxyfunctionalisation of propylbenzene.

3.3 Results & Discussion

3.3.1 Screening tests

To begin with, a procedure had to be established to oxidise the model substrate. Starting from conditions based on those previously employed within the group for the epoxidation of cyclohexene,[76,139] catalysis was at first attempted with a cobalt-titanium (CoTi) AlPO-5 catalyst (3 atom% Co, 3 atom% Ti — refer to Section 8.13 for synthetic details) using H_2O_2 as oxidant, in H_2O, at 60 °C, for 68 h, at ambient temperature, in a round bottom flask.

When this was found to be completely ineffective, different combinations of temperature (65 °C, 80 °C, 100 °C, 130 °C), solvent (H_2O, MeCN, DCM, PhCN, DCM/H_2O and neat), reaction time (8–68 h) and oxidant (H_2O_2, APB, TBHP) were screened (Table 7). Although some runs using TBHP showed traces of products being formed, all others showed no signs at all of product formation, and it was decided that CoTi AlPO-5 was in all probability not a good catalyst to effect oxidation of the substrate even after subsequent optimisation.

3. Oxidation of propylbenzene

oxidant	temp. (˚C)	time (h)	solvent	conversion
H_2O_2	60	68	H_2O	none
H_2O_2	60	16	MeCN	none
H_2O_2	60	18	neat	none
H_2O_2	65	22	neat	none
H_2O_2	80	23	neat	none
H_2O_2	100	23	neat	none
H_2O_2	130	8	neat	none
APB	65	8	DCM/H_2O	none
APB	80	23	DCM/H_2O	none
TBHP	65	8	PhCN	trace
TBHP	65	8	DCM	trace
TBHP	65	8	DCM/H_2O	none
TBHP	65	8	neat	none
TBHP	80	23	neat	trace

Table 7: Outline of the catalytic results of PhPr oxidation using CoTi AlPO-5 (3 atom% Co, 3 atom% Ti). Reactions all carried out under ambient pressure in a roundbottom flask. Conditions: 1 g (8.32 mmol) substrate, 100 mg catalyst, 1.1 equiv. oxidant, 20 mL solvent (if applicable). Conversion by GC and NMR, averaged.

As such, it was elected to employ vanadium instead of cobalt, as the former has a lower redox barrier and has shown greater activity than cobalt-based materials .[159] Therefore, a vanadium-titanium (VTi) AlPO-5 analogue was tried out instead, using the various temperatures above, and using H_2O_2 as well as TBHP, which had previously shown some promise with the CoTi catalyst. The results of these runs are shown in Table 8. It was found that using 10 mass% of this catalyst, at 100 ˚C, for 23 h, without a solvent, and using TBHP as oxidant, a good conversion of starting material into three main products was observed. The main product was propiophenone, with smaller amounts of benzoic acid and 1-phenyl-1-propanol (Scheme 44). This result became the basis of further screening and experiments.

catalyst	oxidant	temp. (°C)	time (h)	solvent	conversion
VTi AlPO-5	H_2O_2	65	23	neat	none
VTi AlPO-5	H_2O_2	80	23	neat	none
VTi AlPO-5	H_2O_2	100	27	neat	none
VTi AlPO-5	H_2O_2	130	8	neat	none
VTi AlPO-5	APB	100	23	DCM/H_2O	none
VTi AlPO-5	TBHP	100	23	neat	82%

Table 8: Outline of the catalytic results of PhPr oxidation using VTi AlPO-5 (6 atom% V, 1 atom% Ti). Reactions all carried out under ambient pressure in a roundbottom flask. Conditions: 1 g (8.32 mmol) substrate, 1.1 equiv. oxidant, 100 mg catalyst. Conversion by GC and NMR, averaged.

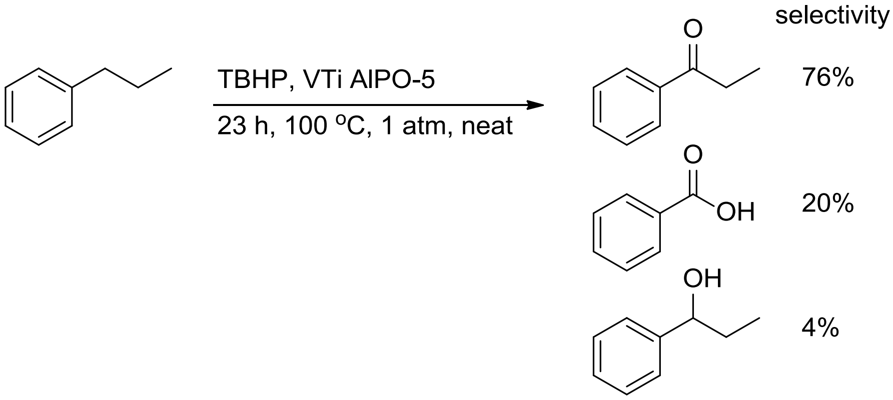

Scheme 44: Delineation of the basic propylbenzene oxidation reaction.

Using ^{1}H-NMR as well as GC employing a calibrated internal standard (see Sections 2.3.1.2. and 9.1), it was found that this experiment returned a *ca.* 80% conversion of the starting material with a selectivity of about 75% towards propiophenone, 20% towards benzoic acid, and 5% 1-phenyl-1-propanol. In other words, the reaction showed high selectivity towards benzylic oxidation.

It is interesting to note that TBHP worked effectively in this reaction, while H_2O_2 showed no conversion under identical reaction conditions. As the oxidative power of peroxides is inversely dependent on the electron density on the O–O bond, H_2O_2 is a stronger oxidant than TBHP.[216,217] However, the homolytic bond dissociation enthalpy of TBHP is lower than that of H_2O_2,[218] which could explain why no reactivity was observed at all for H_2O_2 under the conditions employed.

Having established a working procedure, the objective changed to trying to optimise this procedure, as well as trying to establish how strict tolerances for a successful oxidation were. In addition, it was hoped to possibly gain insight into the mechanism, to determine the active site or species, and to establish some trends surrounding the reaction.

In an effort to optimise the reaction, screening was performed with other oxidants than TBHP, which is fairly mild as an oxidant. As such, H_2O_2, APB, peroxyacetic acid (PAA) and cumene hydroperoxide (CHP) were also tested in catalysis under otherwise identical conditions. It was found that, surprisingly, all of these oxidants returned no observable conversion to any products. Interestingly, a similar trend was observed by Xia *et al.* in catalytic benzylic oxidation using Cp_2VCl_2.[72] It is suspected that these oxidants, due to their limited lifetime compared to TBHP, do not survive long enough at the reaction temperature to affect oxidation of the substrate. Indeed, TBHP has been documented to decompose in 24 h (to *t*-butanol and O_2, Scheme 45) at an *in-situ* temperature of 100 °C.[219] This indicates that degradation of TBHP at the reaction temperature is not rapid, and that the oxidant has a sufficient lifetime to effectively oxidise the substrate. To confirm the stability of TBHP to the employed conditions, iodometric titrations of the reaction mixture after 23 h and 50 h were performed, revealing a TBHP (or radical) concentration of 7.40% and 0.81%, respectively. Furthermore, this conclusion is corroborated by experiments using a syringe pump to feed the oxidant into the reaction gradually over the entire course of the reaction which returned *lower* conversion rates (49%), suggesting that the reaction is starved of oxidant during the reaction.

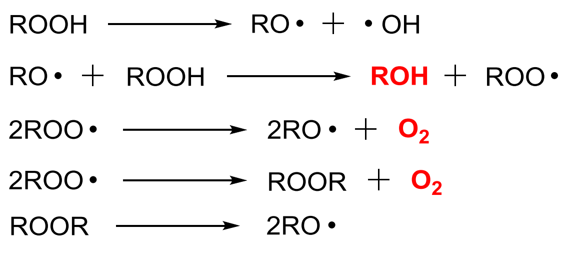

Scheme 45: Decompositional pathways and radical products of TBHP. Final products t-*butanol and molecular oxygen are highlighted in red. R ≡* t-*Bu.*

Turning next to the best solvent for TBHP — water or decane — it was found that there was little difference in outcome. However, as the catalyst coagulates in the water layer, yet flows freely through the reaction mixture when using TBHP in decane, the reaction proved more manageable and was deemed more likely to give consistent results than TBHP in water. Interestingly, it was found that using TBHP in decane produced a small amount of unidentified oxidation products. This result was verified by using decane itself as substrate (rather than propylbenzene) and running a typical reaction. These products do not appear to hinder the main reaction (of propylbenzene) however. Nonetheless, in order to prevent this oxidation from interfering with the stoichiometry of the reaction, the amount of TBHP was increased from 1.1 equivalents to 1.35 when using TBHP in decane instead of TBHP in water.

In addition, a series of higher temperatures (120–150 °C) were examined, as well as running the reaction for two days instead of one (50 h). It was shown that at 120 °C the reaction was akin to those run at 100 °C, but that at 150 °C conversions dropped sharply to only 12%. A possible explanation for this behaviour is (partial) solvolysis of the active vanadium species from the framework. This would concur with the findings of Rigutto *et al.* who found that vanadium AlPO-5 was prone to hydrolysis and solvolysis at metal loadings above 1.3% (the loadings employed for these experiment were 9% V, 1% Ti).[108] Alternatively, it is possible that at this temperature, the oxidant breaks down too fast to oxidise the substrate (see Scheme 45). Iodometric titration of a reaction after 23 h at 120 °C revealed that only traces of TBHP were left (<0.183%, below measurement threshold) which corroborates this conclusion. At a reaction time of 50 h, the conversion increased slightly to 90%, but this increase was not deemed worthy of a doubling of the reaction time to two full days which would have severely limited screening productivity.

To establish the uniqueness of the procedure and the importance of vanadium and titanium, as well as to partially exclude the possibility of extra-framework metals effecting catalysis, a test was carried out using commercially available titanium silicalite-1 (TS-1), a well-studied titanium-based industrially-applied catalyst. To check against extra-framework vanadium salts performing catalysis, $VOSO_4$, the vanadium salt used in making VTi AlPO-5, as well as V_2O_5, a V^{5+} salt that has been shown to be capable of benzylic oxidation of alkylbenzenes using TBHP, were tried out.[72] It was found however, that V_2O_5

underperformed compared to our catalytic system at a conversion of only 41%. We attribute the superior results of our catalyst to the dispersed, single-site nature of the vanadium ions in the material compared to the oligo-/polymeric V centres in V_2O_5 (see Section 1.4). Meanwhile, TS-1 and $VOSO_4$ both returned conversions no higher than a blank reaction. This shows that any leftover $VOSO_4$ present in the catalyst after thorough washing was unlikely to be affecting catalysis. Similarly, it is unlikely that V_2O_5 clusters formed during synthesis, calcination or leaching could be the sole catalytic species.

Having established what works and what does not work, a more rigorous quantification scheme was developed for the establishment of a general mass balance of reactions, as hitherto, products that were not propiophenone, 1-phenyl-1-propanol or benzoic acid were ignored, as was loss of starting material due to evaporation. Alarmingly, it was found that the mass balance for this experiment was as low as 64%. In an attempt to minimise loss of materials by evaporation along the joints of the glassware, Teflon tape was used as a makeshift seal, which increased the mass balance to a more satisfactory 90%. Reduction from a two-necked flask to a one-necked flask and using high-vacuum grease pushed the mass balance to 95%. As it appeared that the loss of mass balance was overwhelmingly due to evaporation of starting material rather than chemical transformation, it was decided that the conversion figures should be normalised with the loss of mass balance subtracted from conversion figures:

$$normalised\ conversion = conversion - (100\% - mass\ balance)$$

The mass balance itself consists of the total measured amount of moles of starting material and products added together, divided by the amount of moles of starting product:

$$Mass\ balance = \frac{n_{SM,t} + n_{x,t} + n_{y,t} + n_{z,t}}{n_{SM,0}}$$

This means that the mass balance in this context is based on moles, rather than mass, as it is classically taken to mean. For more information refer to Section 9.2.

It was found that the original figures obtained had been skewed by the loss of mass balance, as a typical experiment now returned *ca.* 60–65% conversion instead of 80–85% (Table 9). Although analysis of the crude reaction mixture by GC, NMR and TLC confirmed the presence of traces of other oxidation products than propiophenone, benzoic acid and 1-phenyl-1-propanol, the total amount was not sufficient for these minor oxidation products to be characterised or quantified — especially as they may have resulted from impurities in the starting material (propylbenzene was used as commercially received; 98% pure). To verify the accuracy of our procedure for determining the mass balance of the reaction, the mass balance of a reaction was determined before it had been run, with and without catalyst, returning excellent matches (99.6–100.4% mass balance respectively).

sealing method	catalyst	temp. (°C)	time (h)	conversion	mass balance	normalised conversion
none	VTi AlPO-5	100	23	87.7%	63.9%	51.6%
PTFE tape	VTi AlPO-5	100	23	74.7%	89.5%	64.1%
silicone grease	VTi AlPO-5	100	23	70.0%	94.9%	64.8%
n/a	VTi AlPO-5	RT	0	0.4%	99.6%	0.0%
n/a	none	RT	0	-0.4%	100.4%	0.0%

Table 9: Outline of mass balance experiment results. Non-listed conditions: 1 g (8.32 mmol) substrate, 100 mg catalyst, 1.1 equiv. TBHP in H_2O, no solvent. Analysis conducted by GC only. The bottom two entries represent reaction mixtures that were not run at all, only put together and analysed, to verify the accuracy of the mass balance tests.

3.3.2 **Reaction trends**

So far, the catalysts used in the key experiment were all batches of AlPO-5 with 6% vanadium and 1% titanium isomorphously substituted in (from now on; “6/1 VTi AlPO-5”). As comparatively little information is available in the literature on the effect of differing amounts of dopant metal on catalysis, two series of VTi catalysts were prepared; one with 1% Ti and a variable amount of vanadium (“X/1 VTi AlPO-5”) and the other with 6% V and a variable amount of titanium (“6/X VTi AlPO-5”). These series included monometallic batches (*i.e.* X = 0) and where the metal was present at 1%, 3%, 6%, and 9%. Synthesis parameters for these series are shown in Table 10. Each was examined at catalysis to compare their effectiveness and the results are summarised in Figure 26:

Index	gel composition	cooling	T (˚C)	t (h)	colour (as synth)	colour (calcined)
1% Ti	1.00:1.49:0:0.01:0.8:55	in ice	180	2	white	white
1/1 VTi	0.99:1.49:0.01:0.01:0.8:55	in ice	180	2	off-white	light yellow
3/1 VTi	0.97:1.49:0.03:0.01:0.8:57	in ice	180	2	light cyan	yellow
6/1 VTi	0.94:1.49:0.06:0.01:0.8:63	in ice	180	2	grey-blue	gold
7.5/1 VTi	0.925:1.49:0.075:0.01:0.8:66	in ice	180	2	grey-blue	gold
9/1 VTi	0.91:1.49:0.09:0.01:0.8:68	in ice	180	2	grey-blue	gold
12/1 VTi	0.88:1.49:0.12:0.01:0.8:74	in ice	180	2	grey-blue	orange
6% V	0.94:1.50:0.06:0:0.8:63	in ice	180	2	grey-blue	gold
6/3 VTi	0.94:1.47:0.06:0.03:0.8:63	in ice	180	2	grey-blue	amber
6/6 VTi	0.94:1.44:0.06:0.06:0.8:63	in ice	180	2	grey-green	amber
6/9 VTi	0.94:1.41:0.06:0.09:0.8:63	in ice	180	2	light yellow	yellow
6/12 VTi	0.94:1.38:0.06:0.12:0.8:63	in ice	180	2	yellow	yellow

Table 10: Synthesis parameters for X/1 VTi and 6/X VTi series of catalysts. Gel composition is listed as follows: Al:P:V:Ti:SDA:H_2O.

The catalysts thus synthesised showed differing structural, textural and spectroscopic properties. These results are shown in detail in Chapter 5.

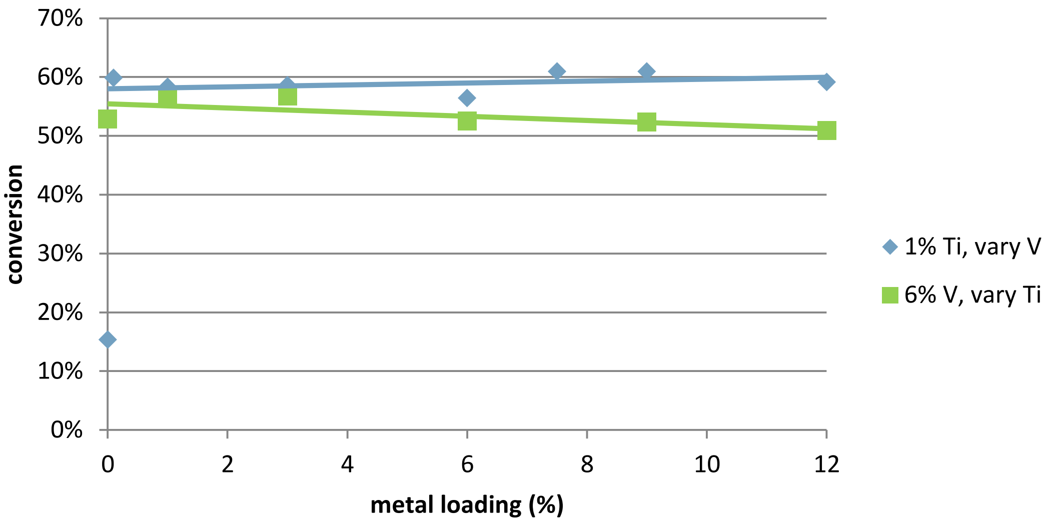

Figure 26: Conversion versus % metal loading of two series of VTi AlPO-5 catalysts; with fixed 6% V and variable Ti loading (green squares) and with fixed 1% Ti and variable V loading (blue diamonds). Conditions: 1 g (8.32 mmol) substrate, 100 mg catalyst, 1.1 equiv. oxidant, 23 h at 100 °C.

This series of experiments exposed some interesting trends. Looking at the series with a variable degree of vanadium (X/1 VTi, blue) we see that even a small amount of vanadium (0.1%) makes the framework catalytically active towards the reaction, but without it (*i.e.* 1% Ti only), very little activity is observed. Curiously, varying the amounts of vanadium or titanium in the framework appeared to have little or no effect on performance.

The remarkable and surprising similarity of the results suggested a plateauing of some sort under the conditions applied. Therefore, the conversion of propylbenzene was measured over time to see if this was the case. A reaction profile for the oxidation of propylbenzene over three days (72 h) is shown in Figure 27 (dark blue diamonds) where each data point represents a separate reaction that was run until the indicated point, rather than a single reaction that was monitored in time. This was found necessary as continuous monitoring required the repeated dismantling and reassembly of the reaction apparatus and sampling of such small reaction volumes resulted in a considerable loss of material, especially for the higher-time data points. Therefore, to avoid these difficulties, each reaction was carried out separately.

3. Oxidation of propylbenzene

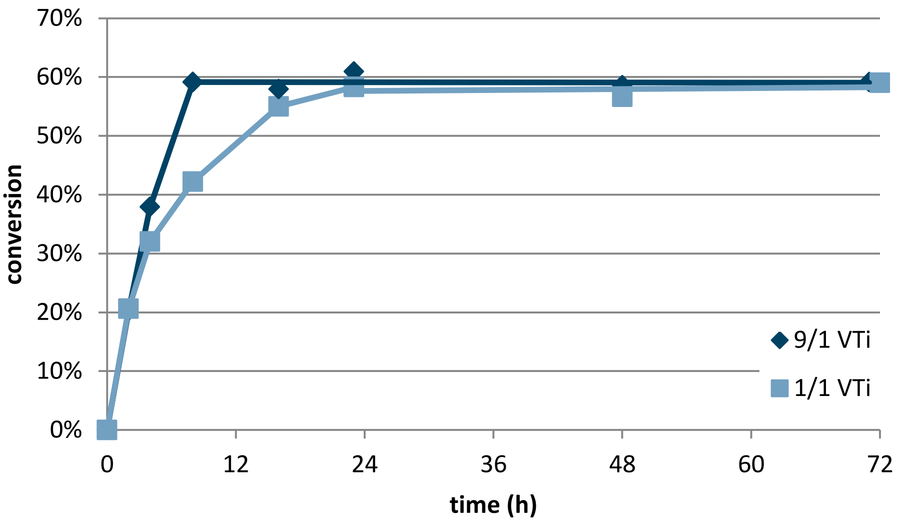

Figure 27: Propylbenzene conversion, normalised, versus time. Dark blue diamonds: 9/1 VTi AlPO-5. Light blue squares: 1/1 VTi. Conditions: 1 g (8.32 mmol) substrate, 100 mg catalyst (9/1 VTi AlPO-5), 1.1 equiv. oxidant, 100 °C.

As can be clearly seen from Figure 27, the reaction shows a strong drop-off after 8 hours, with a plateauing of the reaction afterwards where only evaporation of the starting material was noted as the process advanced. It was now suspected that the overly long reaction time had resulted in the different samples achieving the same plateau. To ascertain if this were true, several further reactions were performed. Firstly, the above reactions were repeated using a low-vanadium (1/1 VTi) catalyst sample, where one might expect the reaction to plateau at a later time than the 9/1 VTi sample (Figure 27, light blue squares). Indeed, using 1/1 VTi AlPO-5 and running the oxidation of propylbenzene for different times revealed that, as expected, the reaction plateaus to the same level, but reaches this state after a longer time period, roughly 23 h as opposed to 8 h for 9/1 VTi AlPO-5.

Second, the reaction was run at different loadings of vanadium and titanium for a period of 4 h (in other words, halfway what had been determined to be the "optimal" time index) and the results are summarised in Figure 28. Under these conditions it was clear that the amount of vanadium in the catalyst was of critical importance, while the amount of titanium had little influence. It is notable that although the conversion increases as the amount of vanadium was increased, the relationship is not linear and drops off completely after 9% V.

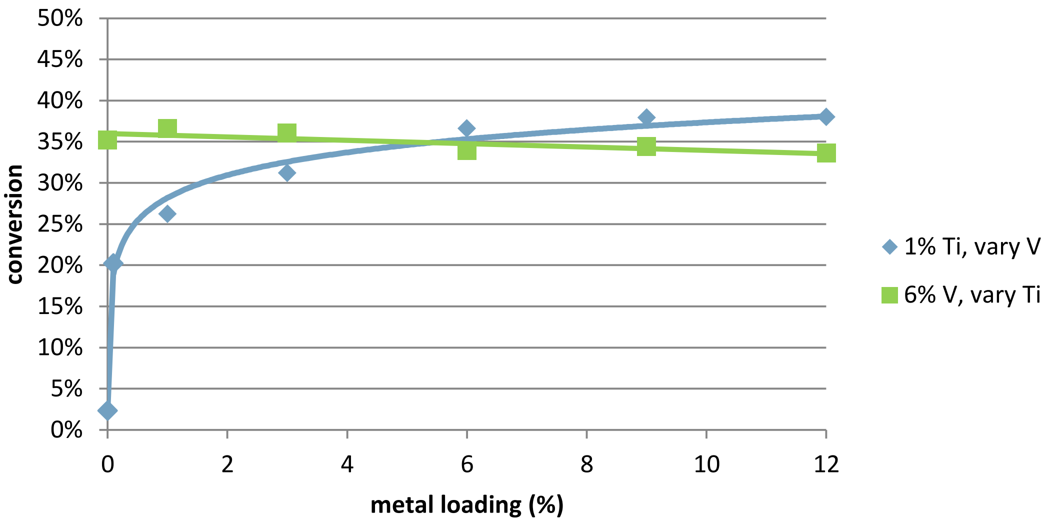

Figure 28: Conversion versus % metal loading of two series of VTi AlPO-5 catalysts; with fixed 6% V and variable Ti loading (green squares) and with fixed 1% Ti and variable V loading (blue diamonds). Conditions: 1 g (8.32 mmol) substrate, 100 mg catalyst, 1.1 equiv. oxidant, 4 h at 100 °C.

This result strongly suggests that a counter-productive process occurs at such high levels. There are several possible explanations for this result:

1. Not all the vanadium is incorporated into the sample at higher amounts of metal;
2. At higher levels of vanadium, catalytically less active or inactive species start to form;
3. Compounds are formed which result in pore blocking and/or occlusion of active vanadium sites.

It has been reported by several authors that inclusion of vanadium into the framework of vanadium-containing aluminophosphates is not quantitative.[35,108,174] These reports indicate varying degrees of incorporation, ranging from 30–60%, which has been reported to vary based on synthesis parameters and especially the type of SDA employed, rather than the amount of vanadium precursor. This dependency has been attributed to the variable generation of lattice vacancies which could bind vanadyl ions.[108]

Analysis of the samples by ICP-OES (see Section 5.1 for details) shows that a much higher, nearly quantitative degree of vanadium is incorporated when using Cy_2MeN as SDA, with amounts dropping off to *ca.* 80% at high metal loadings, suggesting that metal loading is in fact an important factor when using Cy_2MeN in the synthetic procedure. Incomplete vanadium uptake by the sample is visually identifiable as a pronounced blue colour of the washing filtrate of the as-synthesised material was observed (Scheme 46, pathway I.). Furthermore, the gel chemistry of vanadium has been reported to be more complex than that of other metals such as Co and Mn as vanadium is liable to condensation reactions forming a variety of oligomeric species.[28,106,172,173]

Second, spectroscopic and physicochemical analysis of the catalysts (Chapter 5) strongly suggests the formation of extraframework vanadium oxide species as well as the formation of dense $AlPO_4$ phases at high levels of vanadium (Scheme 46, pathway II).[107,111,179,220] Being clustered/bulk species, these vanadium oxides do not show the higher activity and selectivity that isolated, single-site catalysts can offer. Therefore, the generation of such species is expected to be detrimental to catalytic activity.

Third, the generation of extraframework species can result in pore blocking, which limits diffusion of the substrate and/or oxidant into the framework, and occlusion of active species located within the pore structure. Again, this is expected to result in decreased catalytic activity (Scheme 46, pathway III.).

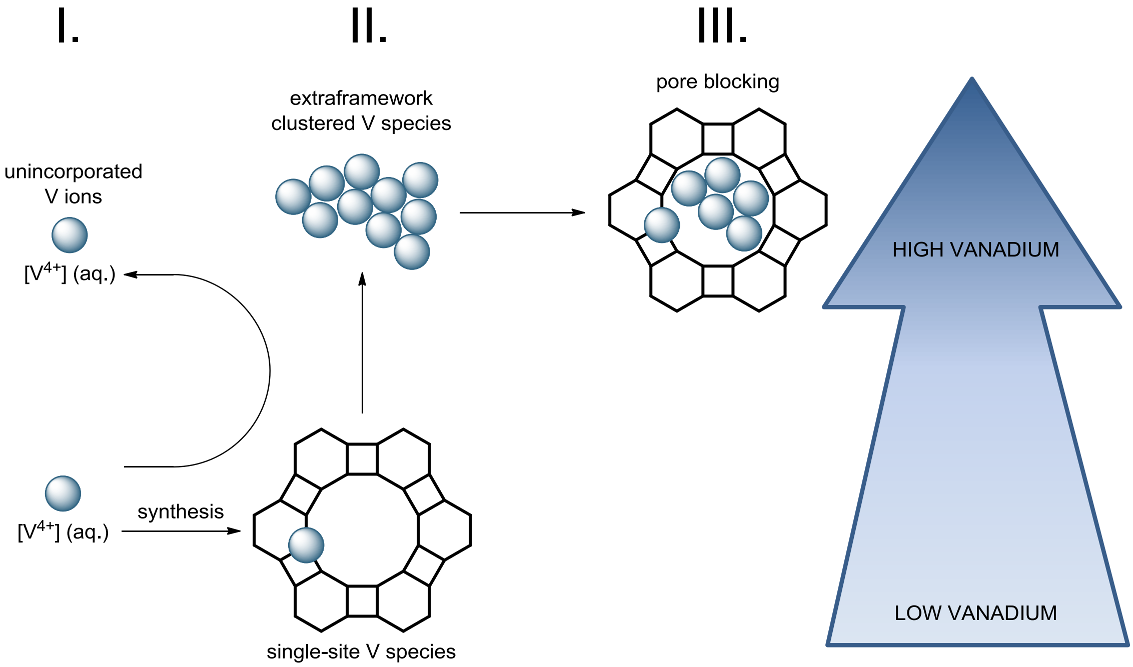

Scheme 46: Illustration of various processes occurring at low and high vanadium loading in VTi AlPO-5. I. Non-incorporation of vanadium ions; II. formation of extraframework vanadium oxide clusters; III. pore blocking and metal site occlusion resulting from cluster formation.

Conversely, the amount of titanium employed appears to have very little impact on the catalytic activity, with a slight downward trend observed at higher loadings (presumably due to formation of extraframework titanium clusters analogous to the vanadium clusters described above). It appears that the optimal amount of titanium to employ is 1%, so this was used as the basis for most catalytic studies thenceforth. Further in-depth studies as to the effect of varying amounts of titanium in the samples with respect to for example the active sites or material properties were deemed unnecessary.

Using ICP-OES analysis briefly mentioned above (see Section 5.1), turnover numbers (TONs) for these reactions were determined (based on the actual vanadium content of the samples). It was found that the standard 10 mass% loading of 9/1 VTi AlPO-5 had a TON of 91 after 23 h. Close examination of data by Rigutto *et al.* who performed oxidation of alkylbenzenes using VAPO-5 in the oxidation of alkylbenzenes[108] showed TONs between 87 and 223. On the basis of the results shown above, it was expected that considerably higher turnover numbers could be achieved by decreasing the amount of vanadium in the framework and/or the amount of catalyst employed, as our standard conditions appeared to employ a vast excess of both. Therefore, to see whether the moderate TON was due to low activity of the catalyst or its use in excess, three series of reactions were performed: in the first, the amount of catalyst used in each run was decreased. In the second, the same amount of catalyst was used in each run, but with a decreasing vanadium loading per sample. Finally, these two factors were simultaneously varied, *i.e.* using a low amount of a catalyst with a low vanadium loading. The results are detailed in Table 11, Table 12 and Table 13.

3. Oxidation of propylbenzene

catalyst	loading	conversion	selectivity	TON
9/1 VTi	10 mass%	64%	78%	91
7.5/1 VTi	10 mass%	64%	79%	105
6/1 VTi	10 mass%	61%	75%	109
3/1 VTi	10 mass%	61%	77%	186
1/1 VTi	10 mass%	61%	78%	640
0.1/1 VTi	10 mass%	60%	73%	6352

Table 11: Oxidation of propylbenzene using a decreasing vanadium loading per sample. Conditions: 23 h at 100 ˚C, no solvent, 1 g (8.32 mmol) substrate, 100 mg catalyst, 1.35 equiv. TBHP in decane. Selectivity listed is towards propiophenone. TONs are based on vanadium levels.

catalyst	loading	conversion	selectivity	TON
9/1 VTi	10 mass%	64%	78%	91
9/1 VTi	5 mass%	63%	77%	186
9/1 VTi	2.5 mass%	70%	70%	404
9/1 VTi	1 mass%	61%	74%	832
9/1 VTi	0.3 mass%	57%	79%	2177

Table 12: Oxidation of propylbenzene using a decreasing catalyst loading per run. Conditions: 23 h at 100 ˚C, no solvent, 1 g (8.32 mmol) substrate, 1.35 equiv. TBHP in decane. Selectivity listed is towards propiophenone. TONs are based on vanadium levels.

catalyst	loading	conversion	selectivity	TON
9/1 VTi	0.3 mass%	57%	79%	2177
7.5/1 VTi	0.3 mass%	56%	79%	2259
6/1 VTi	0.3 mass%	56%	78%	2813
3/1 VTi	0.3 mass%	57%	77%	5146
1/1 VTi	0.3 mass%	46%	74%	12347
0.1/1 VTi	0.3 mass%	30%	30%	80540

Table 13: Oxidation of propylbenzene using a decreasing vanadium loading per sample at low catalyst loadings per run. Conditions: 23 h at 100 ˚C, no solvent, 1 g (8.32 mmol) substrate, 3 mg catalyst, 1.35 equiv. TBHP in decane. Selectivity listed is towards propiophenone. TONs are based on vanadium levels.

These results clearly show that high vanadium loadings and catalyst amounts were unnecessary and responsible for the moderate TONs obtained in earlier experiments. As can be seen from the tables above, and expected from the previous results, 9/1 VTi gives the best results, but conversion drops only slightly when going from 9% V to as little as 0.1%. Decreasing the catalyst amount leads to a gradual, but small decrease in conversion. The exception is when 0.1% vanadium is employed at 0.3 mass% of catalyst where the conversion and selectivity drop off significantly, with a shift toward benzoic acid as by-product. It is presumed this is due to the comparatively high amount of titanium (*versus* vanadium) in the framework of this sample.

Nonetheless, even at these low levels of active metal in the sample, a 30% normalised conversion is maintained which is a considerable improvement over a blank reaction (14% conversion) in which 1-phenyl-1-propanol is the main product (22% selectivity to propiophenone). This indicates that the catalytic system is extremely active, as TONs of over 80 000 are obtained at these levels. A visual summarisation of TON results is presented in Figure 29. The high activity of these materials was attributed to the well-defined, isolated, single-site vanadium centres that were deemed crucial to achieve these goals (as outlined in Chapters 1 and 2). The strong drop-off in TONs observed when using high vanadium loadings, caused by the formation of inefficient clustered species (Scheme 46) corroborates this, suggesting that these single sites are formed predominantly at low levels of vanadium.

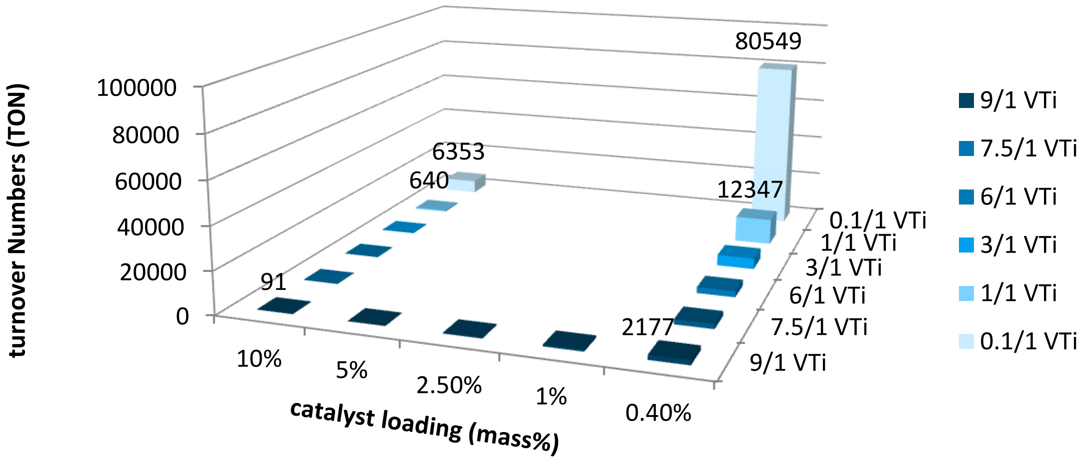

Figure 29: Visual summary of propylbenzene TON experiments are varying levels of catalyst and vanadium loading.

3. Oxidation of propylbenzene

As one of the design strategies was the inclusion of both vanadium and titanium in the framework in order to benefit from a synergistic relationship between the redox-active vanadium and oxophilic titanium, as had been observed before in the group in the oxidation of benzyl alcohol,[139] we were keen to see if there was any influence of titanium on the catalytic turnover of propylbenzene. The above figures suggested this was not the case, possibly due to the use of alkyl hydroperoxides rather than pressurised air as oxidant. Therefore, in order to screen for a more effective secondary metal than titanium, a series of vanadium AlPO-5 catalysts were synthesised with cobalt, chromium, manganese or nickel substituting for titanium. These metals were introduced at a high loading (9%) in order to get a feel for the influence of each metal, whether positive or negative. Moreover, runs with vanadium-only AlPO-5 (VAPO-5) and a physical mixture of VAPO-5 and TAPO-5 were also conducted to further substantiate whether synergistic effects were actually present. The results are summarised in Figure 30.

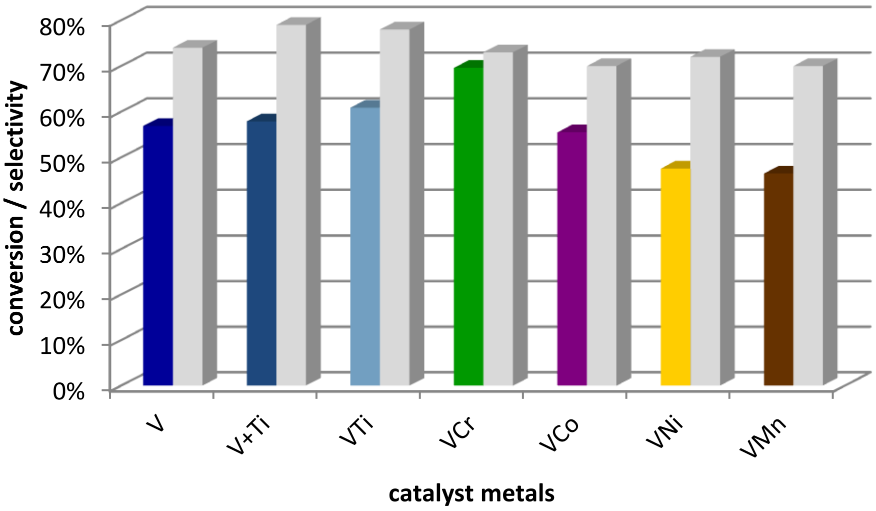

Figure 30: Catalytic results of "secondary metal" tests of VTi AlPO-5. Conversions are shown in colour, selectivities in grey. Entry "V+Ti" denotes a physical 50:50 mixture of VAPO-5 and TAPO-5. Conditions: 23 h at 100 °C, no solvent, 1 g (8.32 mmol) substrate, 100 mg catalyst, 1.35 equiv. TBHP in decane. Selectivity listed is towards propiophenone. Powder diffractograms of catalysts are listed in the Appendix (Figure 93).

The results show that 9/1 VTi AlPO-5 yields slightly better results than 9% VAPO-5 as well as a physical mixture of 9% VAPO-5 and 1% TAPO-5, but if catalytic oxidative synergy is present, its influence is very small. VCr AlPO-5 returned marginally higher conversions, but slightly lower selectivity, and was found to be unstable towards the reaction conditions. Furthermore, the sample showed dubious particle morphology (see Section 5.1) and as it contains a high amount of the toxic metal chromium, was deemed unsuitable to pursue further. VCo, VNi, and VMn AlPO-5 all showed lower conversions than VTi AlPO-5 and V-only AlPO-5, suggesting that the inclusion of high amounts of cobalt, nickel and manganese affected catalysis negatively. It was presumed that these materials caused competitive framework inclusion with vanadium and/or caused the formation of extraframework species, blocking pore channels and restricting access to active vanadium sites *(v.s.)*. Overall, it was judged that titanium was the best secondary metal of the options we examined.

Relatively little data is available on the reaction mechanism, kinetics and types of interactivity of vanadium AlPO-5 and related materials with alkyl arenes. Consequently, some experiments were performed to gain an insight into the action of these VTi AlPO-5 catalysts.

During catalyst synthesis, reaction vessels were generally quenched in ice after hydrothermal synthesis, and this affords very small catalyst particles (based on analysis by electron microscopy *ca.* 10–30 µm, see Section 5.1). However, to examine diffusion effects that could result by employing different particle sizes, the synthesis vessels were allowed to cool to room temperature overnight, thereby producing much larger particles (30–100 µm by SEM, see Section 5.1). These particles were then used for the oxidation of propylbenzene, with reactions monitored over time, to see whether particle size had any effect on catalysis or turnover frequency. Surprisingly, the results were similar to those attained with the smaller particles (Figure 27). Subsequent XRD analysis suggested (see Section 5.1) that the larger particles are not larger crystals but larger aggregates with interparticular cavities between the tiny crystals. This would explain why diffusion is not an issue through these larger particles, and why similar results are obtained across different particles sizes.

To establish whether the reaction involved radical intermediates, two experiments were performed using butylated hydroxytoluene as a radical scavenger (BHT, Scheme 47). In one experiment, 0.1 equivalents of BHT were added to the reaction mixture before starting, while in another, a full equivalent was used. It was found that both showed a considerable lowering of activity, returning a 39% conversion when using 0.1 equivalents of BHT and halting the reaction when a full equivalent was used. As BHT consumes two radical intermediates per molecule (Scheme 47), addition of 0.1 equivalents would be expected to result in a loss of 0.2 equivalents of oxidant. Indeed, in the corresponding experiment conversion drops by roughly 20%. The result provides strong evidence for a radical-based mechanism.

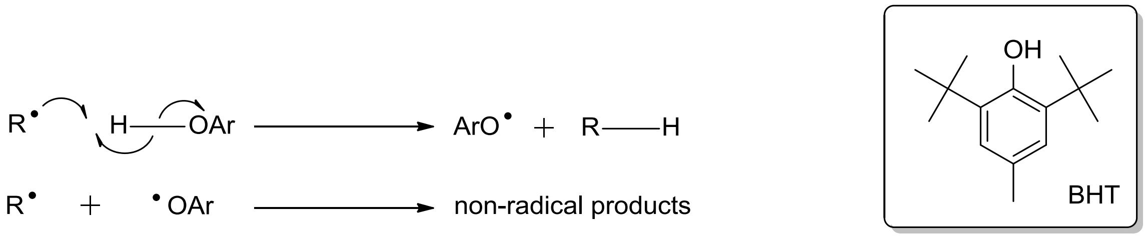

Scheme 47: BHT and an outline of its mechanism of radical scavenging. The radical species is denoted by R·; BHT is abbreviated as HOAr.

Furthermore, in order to establish rough ideas about the reaction mechanism, the reaction was performed using 1-phenyl-1-propanol and propiophenone as substrates instead of propylbenzene. This was done as it was suspected that the products were derived from a linear series of oxidations, first forming 1-phenyl-1-propanol, then propiophenone, then benzoic acid (Scheme 48).

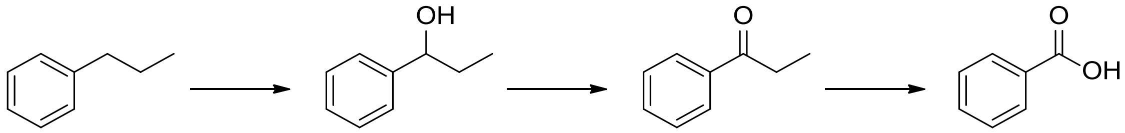

Scheme 48: Theorised sequence of propylbenzene oxidation product formation.

During these experiments, it was found that the conversion of 1-phenyl-1-propanol (1P1P) proceeds with high conversion (*ca.* 90%), while the oxidation of propiophenone to benzoic acid occurs at a much lower conversion (*ca.* 17%). This result suggests that the oxidation does proceed *via* a linear pathway, and that oxidation of the alcohol to the ketone happens much faster than oxidation of the ketone to benzoic acid. This in turn would explain why 1P1P is observed only as a minor product, and why propiophenone is the major product.

The effect of using different amounts of oxidant was also investigated. The results are outlined in Figure 31. As the amount of oxidant was increased, the conversion increased, with a remarkably uniform selectivity. It should be noted however, that the increase in conversion is not linear, but decreases over the amount of TBHP. This suggests that a secondary oxidant, such as air or lattice oxygen (see *Mars-Van Krevelen mechanism,* Section 1.1) is involved, and possibly that the role of TBHP is that of an initiator rather than a simple oxidant.

To try and exploit this, tests were undertaken using a sealed high-pressure reactor, with pressurised air as oxidant rather than TBHP. Tests were also performed using a small amount of TBHP as an initiator (5%) in the presence of pressurised air. Disappointingly, these tests met with very little success, showing only minor conversions. This suggests that the catalyst is able to activate TBHP, but not molecular oxygen. If O_2 plays a role as a co-oxidant in the reaction, it might be restricted to reaction with radical intermediates only, rather than the substrate. In that case, O_2 would not be able to affect oxidation to a meaningful degree in the presence of only small amounts of TBHP. Therefore, it appears that TBHP is not an initiator in this reaction.

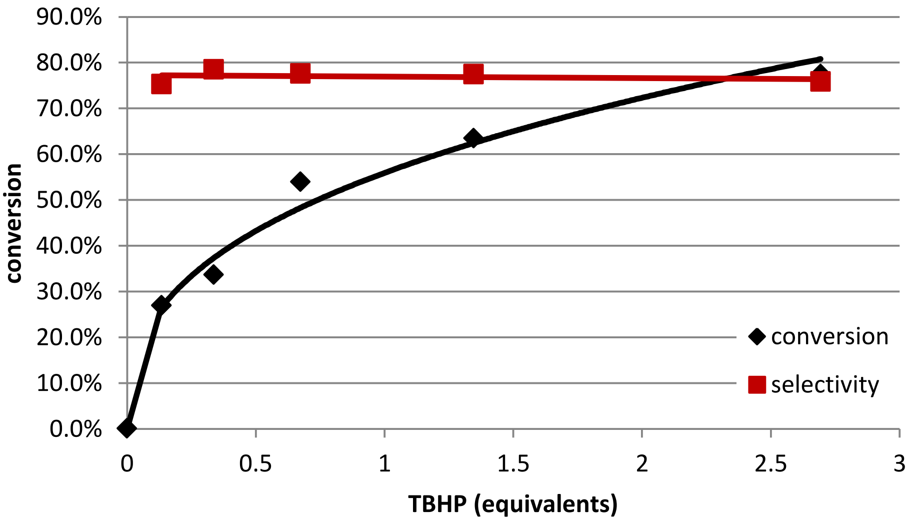

Figure 31: Conversion v. amounts of oxidant in equivalents of TBHP. Black; conversion. Red; selectivity towards propiophenone. Conditions: 23 h at 100 °C, no solvent, 1 g (8.32 mmol) substrate, 100 mg catalyst, varying amounts of TBHP in decane.

3.3.3 **Catalyst recyclability**

Finally, several series of recycling tests were performed to determine the recyclability of the catalyst. As mentioned in the introduction, several previous studies have reported the collapse of the framework after calcination at higher metal loadings and/or the leaching of vanadium. Therefore, it was prudent to study the stability of the system towards the catalytic conditions and calcination temperatures. Furthermore, leaching of V^{5+} species such as V_2O_5

may result in catalytic activity. As vanadium in V_2O_5 is not coordinatively saturated, it may be that this species is catalytically active. Because of this, tests were undertaken to ascertain the nature and heterogeneity of the system — a critical observation in determining the active species of the catalyst.

Several series of recycling studies were performed. The first series of recycling tests used a simple recycling protocol in which the standard reaction (1 g substrate, 0.1 g 9/1 VTi AlPO-5, 1.35 equiv. TBHP in decane, 23 h, 100 °C) was run once, then the liquids were removed by syringe. After this, the reactants and reagents were replenished, and the reaction was run again. This process was done three times, for a total of four runs. The results are shown in Table 14.

run	conversion	selectivity
run 1	63%	72%
run 2	62%	64%
run 3	43%	42%
run 4	36%	58%

Table 14: Summary of the catalytic results of recycling study 1. Conditions: 1 g (8.32 mmol) substrate, 0.1 g 9/1 VTi AlPO-5, 1.35 equiv. TBHP in decane, 23 h, 100 °C. Conversion by GC and NMR, averaged.

The results show that the conversion for the first two runs remains fairly constant. However, after the third run a notable decrease in effectiveness had taken place. At the same time, the catalyst that remained was found to have undergone a colour change from yellow to off-white, possibly suggesting a framework collapse or some other form of structural change. An XRD diffractogram was recorded of the catalyst after it had been used for the fourth time and subsequently washed with acetone. Analysis indicated that no traces of the AFI framework remained, instead showing that the sample had completely degraded to aluminium phosphates (Figure 32), of which the spectrum presents an excellent match:

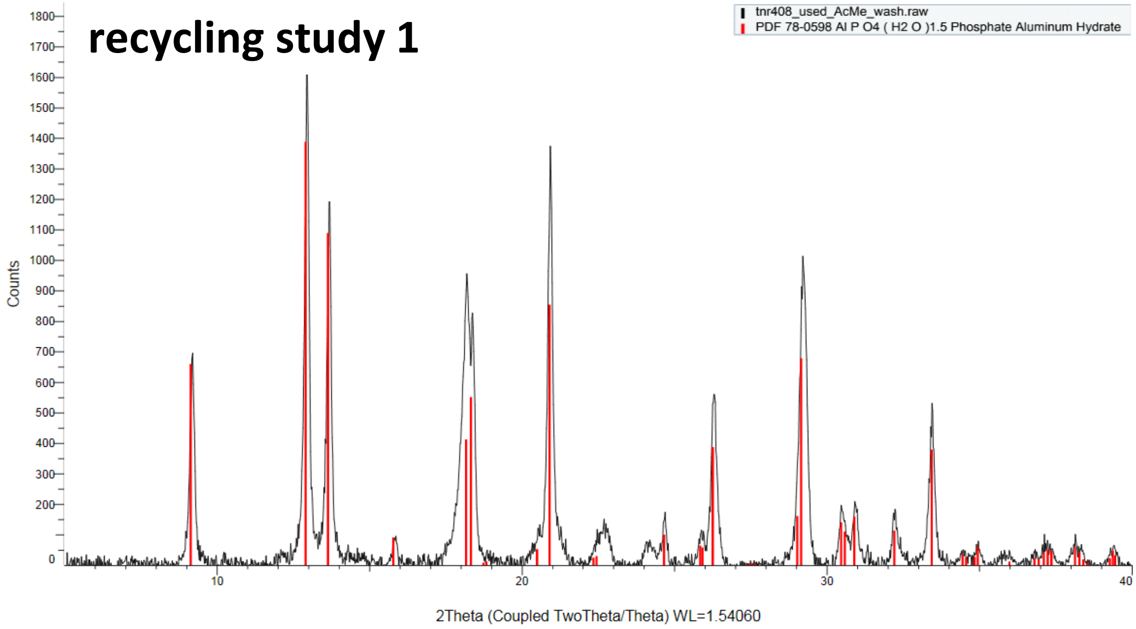

Figure 32: Powder XRD spectrum of 9/1 VTi AlPO-5 after four runs (three reruns). Lines in red represent literature references for aluminium phosphate hydrate.

The results clearly indicated that the framework was, disappointingly, unstable towards the reaction conditions. In addition, the destruction of the framework would be expected to result in the concomitant formation of a polymeric vanadium species like V_2O_5. Indeed, the results obtained for the last run are quite similar to the experiment using V_2O_5 as the catalyst, mentioned earlier.

Although it was obvious that framework destruction had occurred, it was unclear as to when that had occurred. To gain more insight into what was happening at various stages, the reaction was performed as before and the solids were collected by filtration, washed with acetone, recalcined, examined by XRD, and then reused.

These tests showed that the material degraded sequentially with each step, and that after two reactions and two calcinations the material had decomposed completely (Figure 33 and Figure 34). Furthermore, as was observed before, conversion dropped off at the third reaction (Table 15). Again, analysis showed that the material had decomposed completely to aluminium phosphates at this stage, although of a different species than the one seen before.

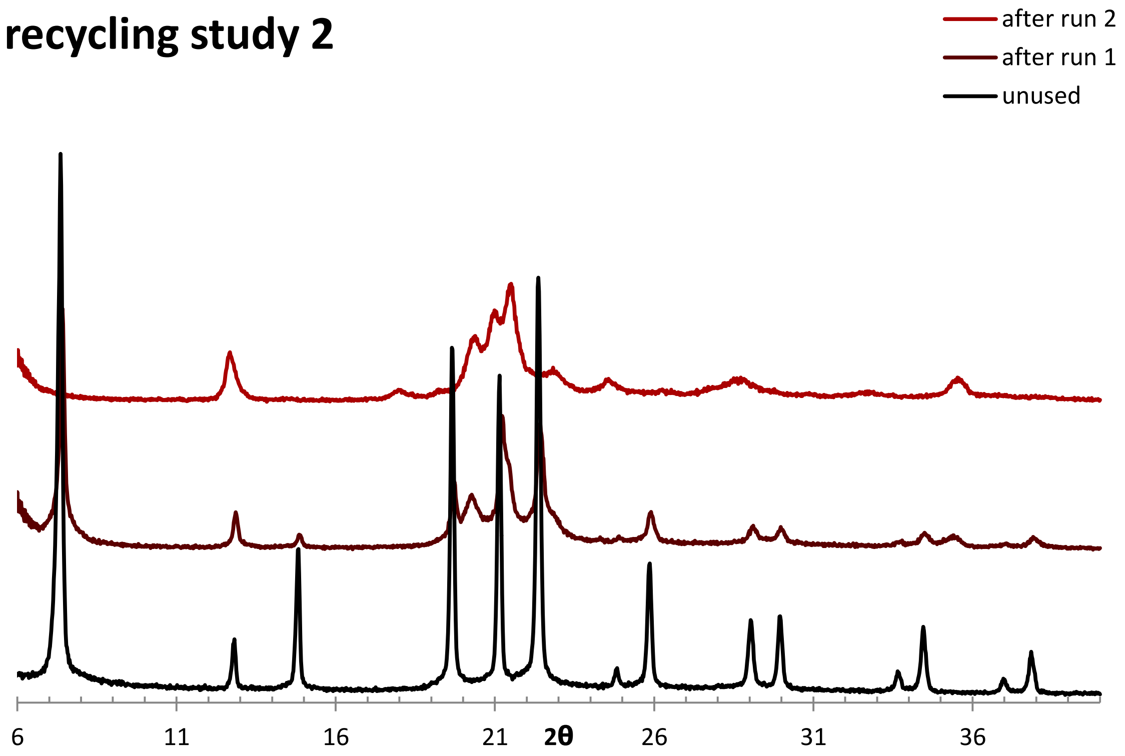

Figure 33: Stacked PXRD plots of the catalyst in recycling study 2. Note that the series "after run 1" and "after run 2" depict the spectrum of the catalyst after that particular run and *subsequent calcination.*

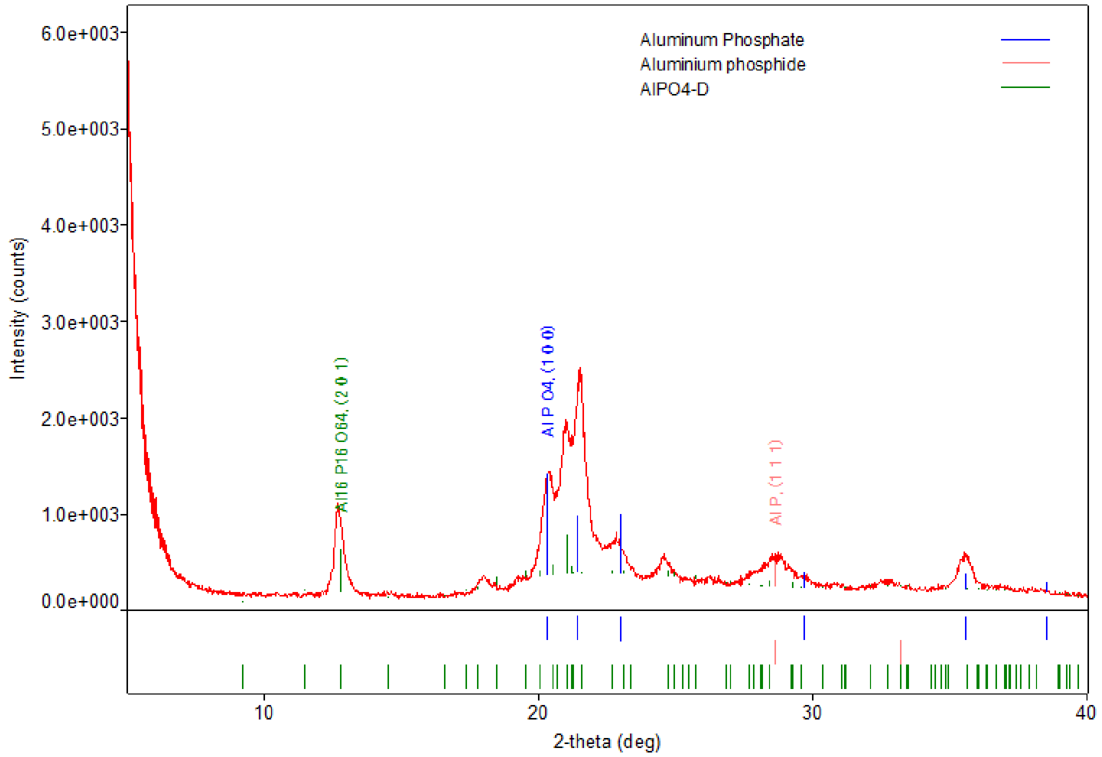

Figure 34: PXRD plot of the catalyst in recycle study 2 after the last run (in red) with spectral lines of $AlPO_4$ highlighted in blue.

run	conversion	selectivity
run 1	63%	67%
run 2	64%	75%
run 3	41%	70%

Table 15: Summary of the catalytic results of recycling study 2. Conditions: 1 g (8.32 mmol) substrate, 0.1 g 9/1 VTi AlPO-5, 1.35 equiv. TBHP in decane, 23 h, 100 °C. Conversion by GC and NMR, averaged.

There were several possible causes and explanations for the behaviour that was witnessed. In an effort to determine whether the fast degradation of the catalyst was due to the high metal loading of the sample, and to determine whether it was the reaction or the calcination step that was causing the most damage to the catalyst, the series was run yet again. This time, a much lower loading of vanadium was used in the form of a 1/1 VTi catalyst which was examined by XRD before recalcination as well as after it (recycling study 3). The resulting PXRD plots (and cell parameters) are shown in Figure 35:

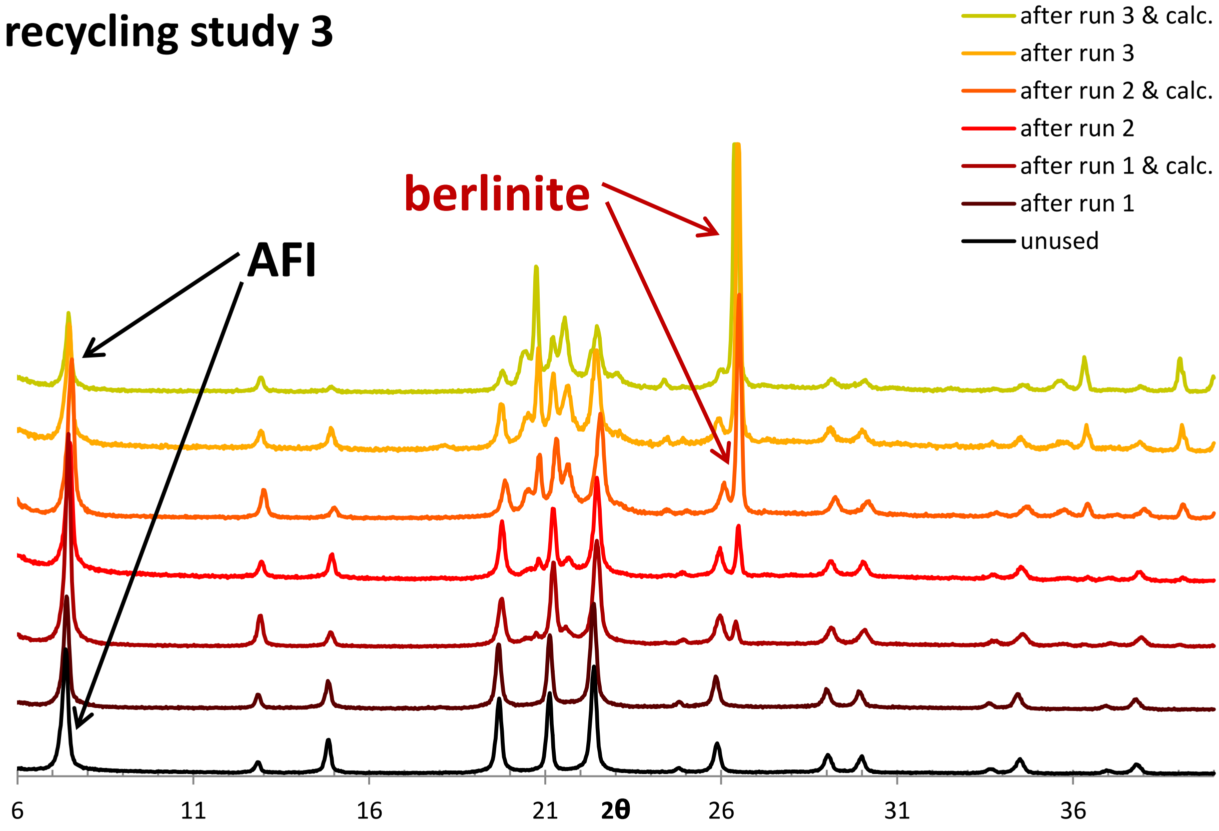

Figure 35: Stacked PXRD plots of the catalyst in recycling study 3. Note that the series "after run" depicts spectra recorded after *that run, but* before *recalcination, whereas series "after run*

& calc." depicts spectra recorded after that run and *after subsequent recalcination. Cell parameters are shown in Table 16.*

run	a (=b) (Å)	c (Å)	V (Å^3)
unused	13.7076 (0.0202)	8.3571 (0.0018)	1359.9
run 1	13.7781 (0.0111)	8.4003 (0.0011)	1381
run 1 calc.	13.7227 (0.0188)	8.3686 (0.0018)	1364.8
run 2	13.7227 (0.0279)	8.3821 (0.0019)	1367
run 2 calc.	13.6332 (0.0594)	8.5070 (0.0109)	1369.3
run 3	13.6981 (0.0641)	8.4519 (0.0091)	1373.4
run 3 calc.	13.7120 (0.0157)	8.3776 (0.0013)	1364.1

Table 16: Cell parameters for recycled VTi AlPO-5 at various stages. Errors are noted in parentheses.

The patterns recorded during this study show that the catalyst degrades more slowly when a low vanadium loading is employed, as after all three runs *and* recalcinations the AFI phase is still readily detectable, albeit in the presence of increasing amounts of dense aluminium phosphate phases and berlinite (Figure 36), a quartzomorphic $AlPO_4$ mineral found in high-temperature hydrothermal deposits in nature. In other words, a dense phase had again formed, at the expense of the AFI framework, but at a much slower rate than was previously observed. It also suggested that the calcination step is destructive, as after run 1 (but before recalcination), the catalyst appears untouched, while after subsequent recalcination, traces of berlinite start to appear. Similarly, roughly the same degree of impurity appears to be present after the second run (but before calcination), while after recalcination, the most intense AFI peak (Miller index (100), $2\theta = 7.4^\circ$, indicated by the black arrow in the spectrum) is lower than the major berlinite peak ($2\theta = 26.5^\circ$, indicated by the red arrow in the spectrum).

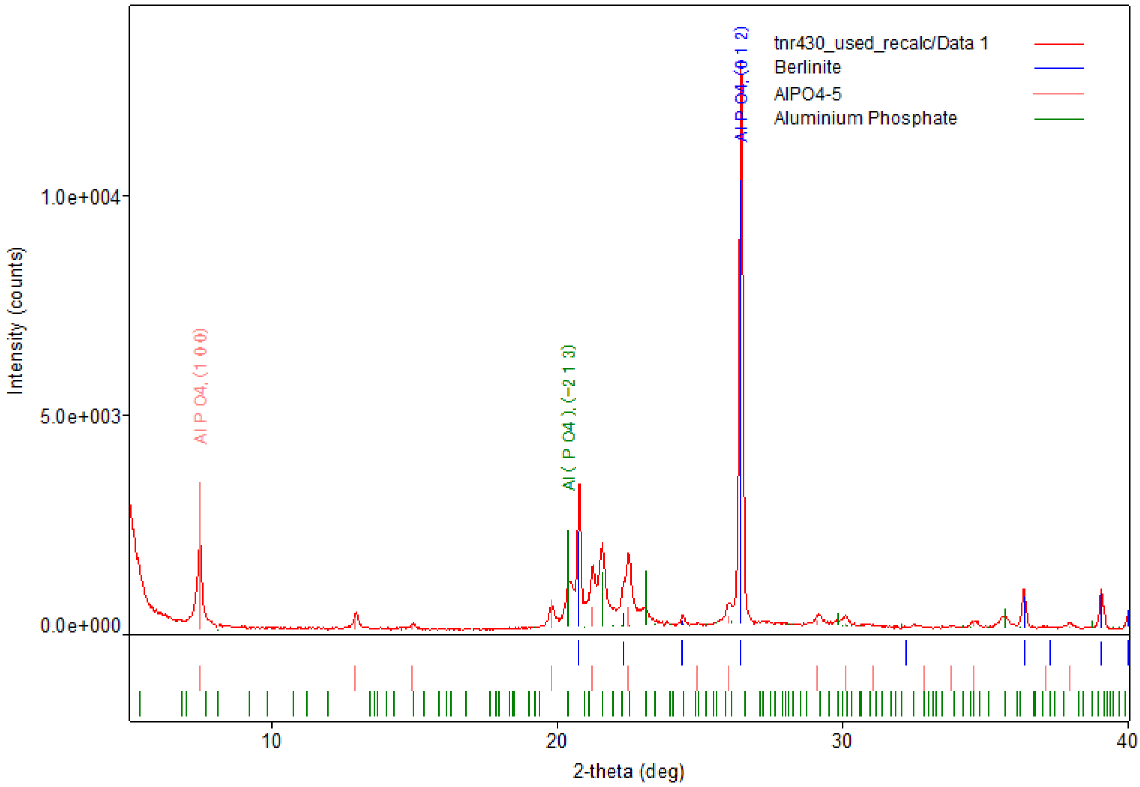

Figure 36: PXRD plot of the catalyst in recycle study 3 after the last run (in red) with spectral lines of berlinite (blue), AlPO-5 (pink) and $AlPO_4$ (green).

Given the destructive nature of alternating successive reaction steps with calcinations, a procedure was then set up in which the catalyst was interfered with as little as possible, only siphoning off the liquids after each reaction. High (9/1 VTi), low (1/1 VTi) and very low (0.1/1 VTi) loadings of vanadium were compared over successive runs ("recycling study 4"). This would also allow insight into the need for calcinations after use, *i.e.* whether the catalyst required reactivation after the oxidation reactions. The catalytic results of each run, compared between 9%, 1% and 0.1% V, are shown in Figure 37.

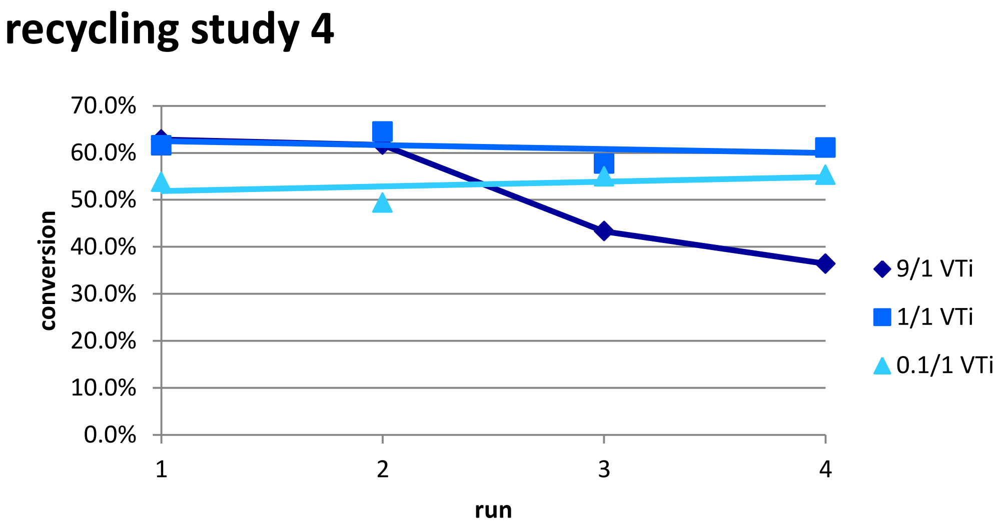

Figure 37: Catalytic results of recycling study 4, showing conversion during each run, using varying amounts of vanadium. Dark blue diamonds; 9% V. Blue squares: 1% V. Light blue triangles: 0.1% V. Conditions: 23 h at 100 °C, no solvent, 1 g (8.32 mmol) substrate, 100 mg catalyst, 1.35 equiv. TBHP in decane. After the reaction, liquids were siphoned off and replenished for a new run.

As mentioned previously, it is possible that leaching of vanadium occurs, and that the leached species are responsible for catalysis. As framework breakdown occurred over time, it was essential to monitor the reaction for leaching of vanadium to establish whether or not VTi AlPO-5 is the catalytic material or a pre-catalyst for a solvated vanadium species. Thus, to back up our recycling studies, catalytic runs were conducted after which ICP-OES analysis was performed on each of the reaction mixtures. It was found that the vanadium content of the reaction mixtures (after one run), after separating off the catalyst by centrifugation, is 54.1 ppm in runs using 9/1 VTi AlPO-5 samples, and only 7.6 ppm in runs using 1/1 VTi AlPO-5. The higher amount of vanadium observed in runs with high-vanadium catalyst samples is in line with the results previously presented as far as the higher instability of high-loading vanadium samples is concerned. Alternatively, the higher vanadium count could be simply due to the higher loading of vanadium to begin with.

Regardless, as leached vanadium *was* observed in the reaction mixture, it now had to be established whether or not this was responsible for the catalytic activity observed. To that end, a hot-filtration test was performed. As the reaction was shown to hit a plateau after 8 hours, it was hot-filtered after 4 hours and then run for the full 23 h to determine whether the removal of the (solid) catalyst would halt the oxidation. Analysis of the reaction revealed a conversion of 38%, in accordance with the previously observed conversion of 38% at 4 hours (Figure 38), indicating that no further reaction took place after filtration. This result suggests that that the solvated vanadium species detected by ICP-OES could not have been responsible for the catalytic activity, as if they were, the observed conversion cutoff would not have occurred, and a higher final conversion of *ca.* 60% would have been obtained.

As stipulated by Sheldon *et al.*, there are three scenarios in the context of leaching of metals from a catalyst:[221]

1. The metal leaches but is not homogeneously active;
2. The metal leaches and is homogeneously active;
3. The metal does not leach.

The results suggest that in this case scenario 1 is observed, as leaching occurs, but upon hot-filtration no further reaction occurs, strongly suggesting that the leached species are not active during catalysis. It should be noted however that it cannot be ruled out that catalytic species had formed which were occluded inside the pore structure and therefore were removed upon filtration.

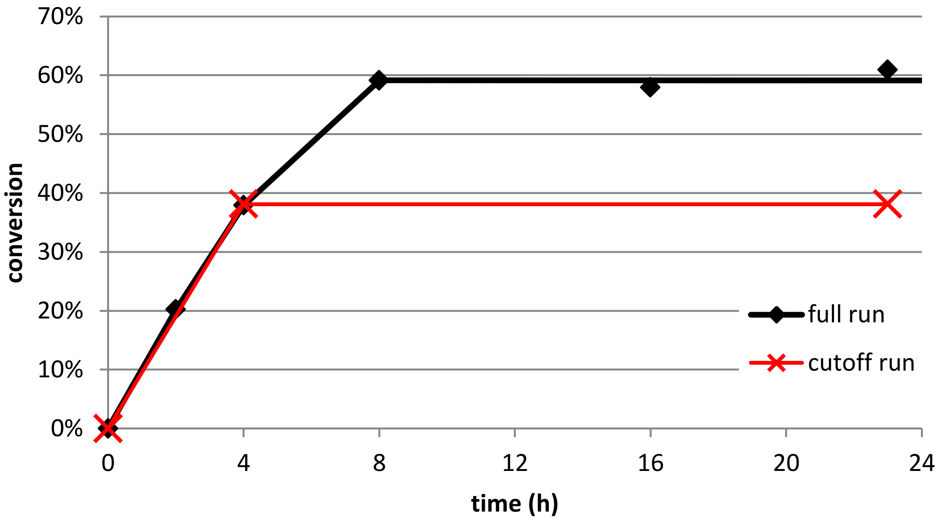

Figure 38: Cutoff run, with filtration at t = 4 h, measured after 23 h (red), compared to conversion measured at various points in time without filtration (black). Conditions: 23 h at 100 ˚C with hot filtration at t = 4 h, no solvent, 1 g (8.32 mmol) substrate, 100 mg catalyst, 1.35 equiv. TBHP in decane.

Based on the available evidence, and on reported literature on vanadium-catalysed oxidations involving TBHP, the following mechanism was tentatively proposed (Scheme 49). Thus, reaction between the oxidant and V^{5+} leads to an oxo-radical on vanadium capable of H-atom abstraction. Single-electron transfer (SET) from the radical intermediate **1** to vanadium next generates a carbocation **2** which reacts with hydroxide from vanadium to regenerate V^{5+}. The alcohol **3** so generated then goes through the same cycle leading to hydrate **4**, which can dehydrate to form the ketone **5** *in situ*, or react further to eliminate R· and form carboxylic acid **6.**

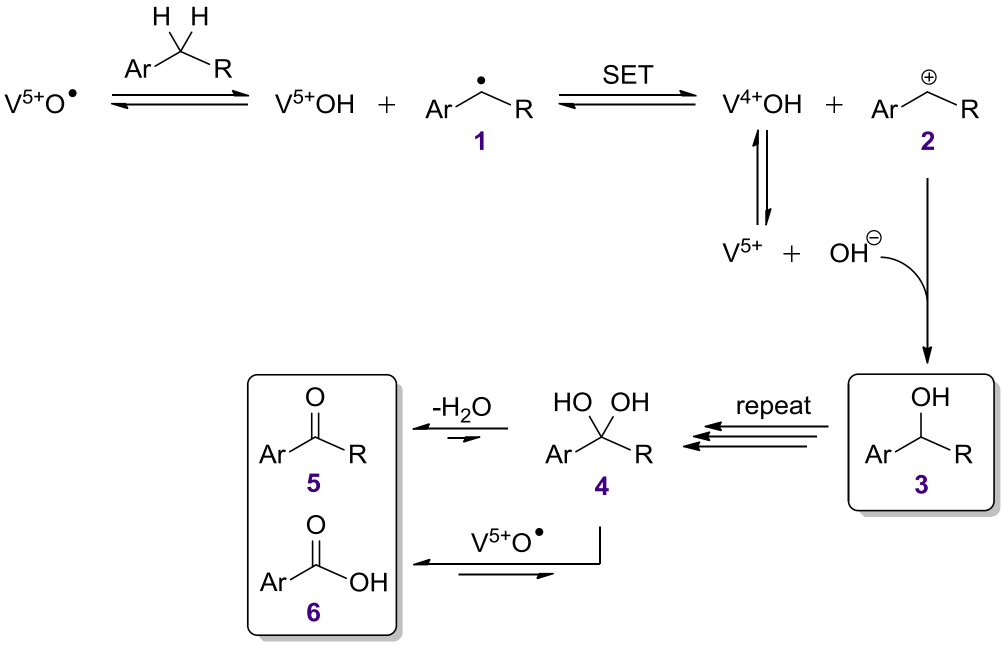

Scheme 49: Preliminary reaction mechanism proposed for the oxidation of propylbenzene. Products are highlighted in boxes.

3.4 Conclusions

A large amount of screening was performed on the oxidative properties of VTi AlPO-5 using propylbenzene and an oxidant. This led to a working procedure being established involving performing the reaction at 100 °C using TBHP as oxidant, for 23 h. Under these conditions with PhPr as substrate, the catalyst displayed excellent selectivity towards benzylic oxidation, yielding mainly propiophenone with the corresponding benzylic alcohol and benzoic acid side-products. Various parameters were altered to gain a basic insight into the influence of oxidants, time, amount and type of metal, *etc.* A brief summary of some of the trends found is presented in Table 17.

Parameter	Outcome	Effect on catalysis
varying vanadium level, reaction time 23 h	all reactions have plateaued at 23 h	similar conversions were noted with all catalysts
varying vanadium level, reaction time 4 h	higher vanadium levels cause conversion at a higher pace	greater vanadium loadings showed better conversions
varying time, low or high vanadium level	higher vanadium levels reached the reaction plateau faster than low-vanadium catalysts	lower vanadium levels necessitated longer reaction times but ultimately reached the same end point
varying titanium level and reaction time	titanium level does not influence conversion	Similar conversions were noted across all titanium levels. Possible slight optimum at 1% Ti
varying catalyst amount	conversion is linearly related up to a point	conversion decreases at low loadings and goes up at higher loadings
lowering vanadium count AND catalyst loading	high activities are still observed at low vanadium loadings and catalyst amounts	turnover numbers soar
varying catalyst particle size by employing slower cooling during synthesis	aggregates increase in size but crystallite size is unchanged	conversions and reaction times are unaffected
employing a radical scavenger	radical count is decreased stoichiometrically	stoichiometric amounts of conversion are lost depending on the amount of scavenger employed
varying oxidant amount	there appears to be a contribution from a secondary oxidant	conversion increases/decreases in a non-linear fashion
varying secondary metal or leaving it (Ti) out	VTi is superior to alternatives. VCr attains higher conversions but has undesirable properties. VTi shows only minor synergistic effects over V + Ti if any.	VTi AlPO-5 attains best overall results of the catalysts examined

3. Oxidation of propylbenzene

stability of catalysts versus metal loading	high-vanadium samples are more unstable towards reaction and calcination, high-vanadium samples leach more than low-vanadium samples	recyclability suffers sooner on high-vanadium samples than low-loading ones, conversions remain stable for fewer runs and greater catalyst decomposition is noted
leaching of metal into reaction solvent	homogeneous leached vanadium species do not affect catalysis	reactions show sharp cutoff when hot-filtered

Table 17: Summary of trends observed with propylbenzene oxidation using VTi AlPO-5 and related materials.

4. Substrate scope and new opportunities

Armed with the experience and knowledge gained from the propylbenzene oxidation tests presented in Chapter 3, it was decided to extend the catalytic system to other substrates. To that end, a series of substrates with benzylic carbon centres with which to perform VTi AlPO-5-catalysed oxidation were chosen. In this way, it was hoped to expand the scope of the methodology and extend the reactivity profile.

4.1 Tetralin oxidation

4.1.1 Introduction

As discussed previously, the system showed a propensity for benzylic oxidation, to which the catalyst appeared to be quite selective. Although a varying degree of oxidation was observed in the product, as expected based on the findings surrounding the model substrate, the system showed excellent regioselectivity. Therefore, in order to achieve a higher-value transformation, the oxidation of tetralin was performed. Considering the propensity for benzylic oxidation and the tendency to form ketones, it was expected for this reaction to yield mainly 1-tetralone with amounts of tetralol and possibly phthalic acid (or similar species) (Scheme 50):

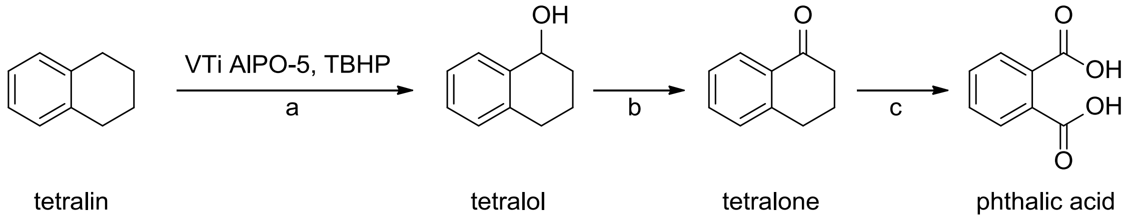

Scheme 50: Oxidation of tetralin.

Tetralin, or 1,2,3,4-tetrahydronaphthalene, is industrially produced in bulk as a by-product of naphthalene purification, and can be produced directly through hydrogenation of naphthalene over a nickel catalyst at 200 °C under 10–15 bar of hydrogen gas pressure.[222] It is produced on an industrial scale at around 25 ktpa. A well-known legacy use of tetralin from World War II is the Pott-Broche process, where it was used at high temperatures and pressures in large scale (30 ktpa) coal extraction as a hydrogen donor to yield low-sulfur fuel. After the war this process fell out of favour, and modern uses are mainly restricted to its employment as a niche solvent and in the production of 1-tetralone, commonly referred to as tetralone.[222]

Tetralone and its derivatives are intermediates and starting materials for a variety of chemicals with a wide field of applications, in some cases *via* 1-naphthol, a compound derived industrially by dehydrogenation of tetralone. Perhaps most famously, tetralone is a starting material for the synthesis of Sertraline (Figure 39),[223,224] a serotonin uptake inhibitor marketed as Zoloft by Pfizer in 1991, and one of the most widely used antidepressants on the market.[225] The tetralone-based process itself is a major improvement over a previous process that employed 1,2-dichlorobenzene and was considerably less cost-effective. Propanolol, a prominent β-blocker developed by ICI used to treat high blood pressure and heart problems (worldwide production 500 tpa) is also dependent on tetralone production.[222] Other pharmaceuticals that use tetralone as a starting material include Hepalande (a choleretic) and Alphol (an antirheumatic) (Figure 39).[222,226] ABT-200, another antidepressant derived from tetralone, shows fewer side effects than have been associated with sertraline.[227] Indazoline tetralone, which is also synthesised directly from tetralone, has been shown to have highly potent antimicrobial activity.[228] Tetrophine derivatives produced from Pfitzinger reaction of 1-tetralone with isatin have been used to treat autoimmune disorders such as donor organ rejection, psoriasis and chronic inflammation.[229]

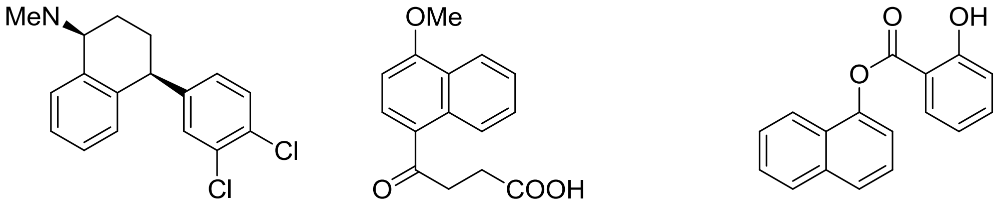

Sertraline Hepalande Alphol

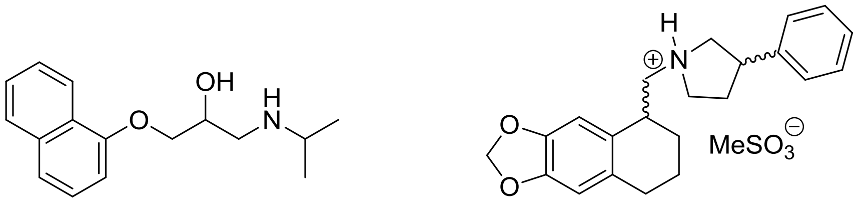

Propanolol ABT-200

Figure 39: Several pharmaceuticals derived from tetralone.

Another major use for tetralone is in agrochemical products, most notably for the production of the insecticide Carbaryl on a 10–20 ktpa scale. This compound also doubles as a veterinary drug (as Carbaril).[222] Initially it was produced by Union Carbide by reacting tetralone with methyl isocyanate in their plant at Bhopal, India, but a massive leak of the isocyanate led to the deaths of over 2000 people. This prompted Israeli company Makhteshim to develop an alternate route in which the same chemicals were used, but in a different order, to bypass the extremely toxic isocyanate intermediate (Scheme 51).[230]

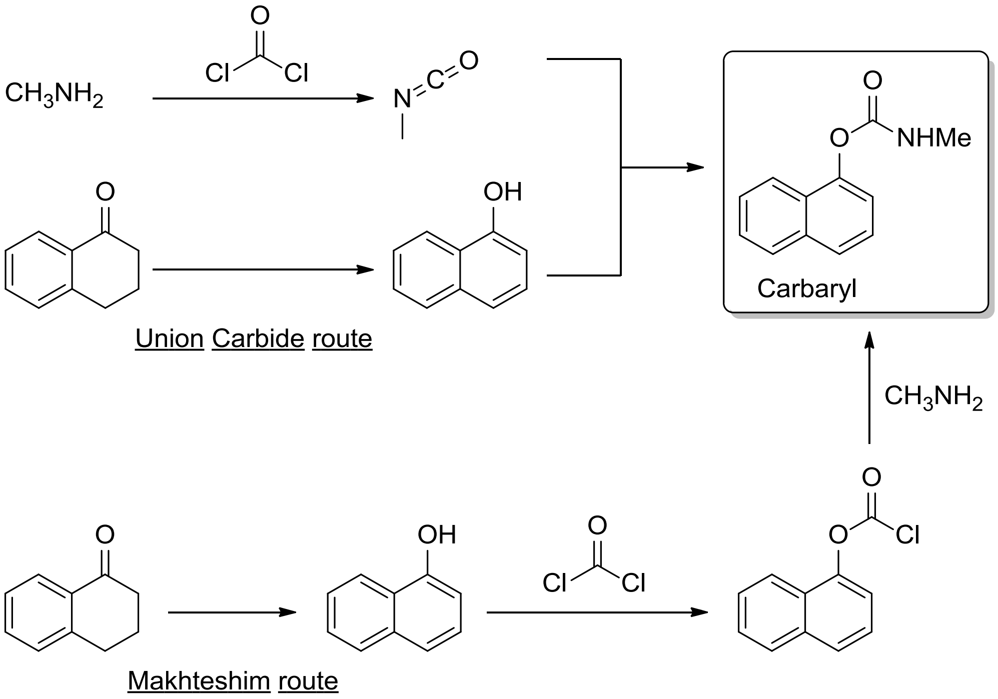

Scheme 51: Union Carbide and Makhteshim routes to carbaryl from tetralone.

Tetralone also fathers a series of compounds that are used as dyes in industry, including Juglone, which is also employed as a herbicide.[82] Tetralone is also one of the starting materials for the production of azo dyes such as Acid Orange 19.[222]

The classical way to produce tetralone is by the Haworth reaction, published in 1932.[231,232] In this reaction, benzene is reacted with succinic anhydride, aluminium trichloride, zinc, hydrochloric acid and sulfuric acid in a multi-step reaction to produce tetralone. The reaction is based on a Friedel-Crafts acylation reaction followed by Zn-mediated reduction, and subsequently a second, intramolecular Friedel-Crafts acylation (Scheme 52).

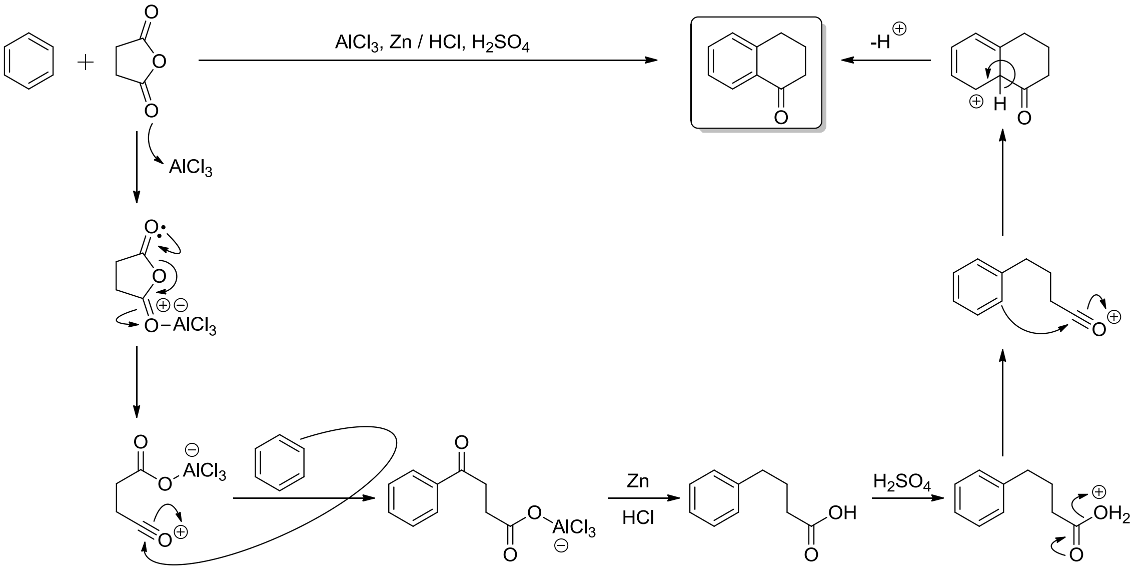

Scheme 52: The Haworth reaction and mechanism.

This process is conducted on a large scale and with enormous amounts of waste, leading to the development of more environmentally friendly protocols. A more modern and much more benign protocol for its synthesis was developed by Union Carbide and involves the aerial oxidation of tetralin at 200 °C at 10–15 bar.[222,230,233] Initially this produces tetralin hydroperoxide (THP), which in turn yields a mixture of tetralone and its alcohol derivative, tetralol (Scheme 53). Although this process yielded tetralol as a side-product, it is a considerable improvement over the previously mentioned procedure. Production of 1-naphthol from tetralone necessitates separation of the two products to avoid dehydration of the tetralol fraction. Dehydrogenation of tetralone makes up the vast majority of 1-naphthol production.

Because of the need to separate these products and the sensitivity of tetralol to dehydration, it is highly desirable to maximise the tetralone/tetralol ratio. The THP produced in industry decomposes to these two products in a ratio dependent on the means of decomposition. Thermal decomposition yields equimolar mixtures of the two. However, UCC developed a series of catalysts to improve upon this and managed to achieve up to 85% selectivity towards the ketone at 22% conversion.[234] An earlier protocol for the production of 1-naphthol that depended on direct nitration of naphthalene was found to liberate toxic by-products and was phased out in favour of the tetralone route.[222,230,233]

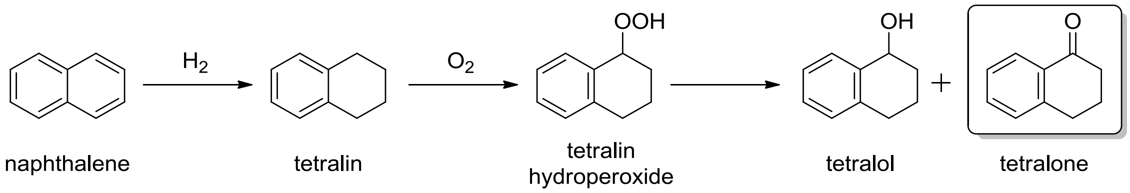

Scheme 53: Schematic representation of modern, industrial production of tetralone from tetralin. The reaction is unselective and produces tetralol as a by-product.

Because of the great potential to improve upon the industrial production of tetralone from tetralin, a great amount of research into superior catalysts and conditions has been conducted over the year. A selection of results from different catalytic systems is presented in Table 18.

conditions	product(s) reported	conversion / yield (%)	ketone selectivity (%)	ref.
O_2, 140 ˚C, MEP, Sn^{2+}-exchanged Dowex CCR-2 resin catalyst (Union Carbide)	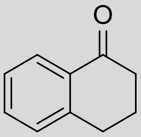 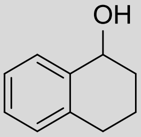	22	85	234
Cp_2VCl_2, TBHP, 5 days, 30 ˚C	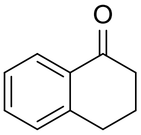	87–90	not specified	235
CrO_3, TBHP, DCM, RT, 6 h, closed flask	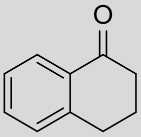 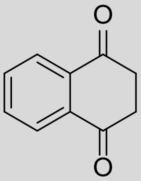	69	93	236
$Mn(OAc)_2{\cdot}4H_2O$, chiral camphor-derived N,N-bidentate ligand, THBP, DCM, 10 min, 0 ˚C	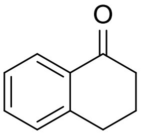	88	not specified	237

Au nanoparticles on TiO_2, O_2, 90 °C, 24 h	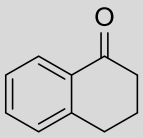	27	85	215
NHTPPI / CuCl, MeCN, O_2, 6 h, 35 °C	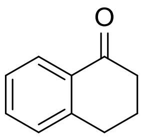	84	not specified	238
NHPI, acridine yellow or analogues, Br_2, MeCN, 0.3 MPa, 50 °C	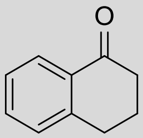 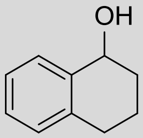	93	95	239
$KMnO_4$ deposited on montmorillonite K10, 20 h, RT, ultrasonic/μv	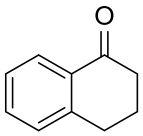	85	not specified	240
$Cu(OH)_2$, O_2, 200 psig, 1 h, 100 °C	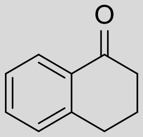 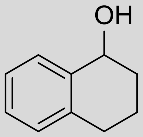	47	73	241

chromium terephthalate MOF MIL-101, chlorobenzene, TBHP, 8 h, 80 ˚C	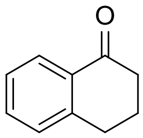 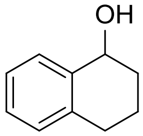 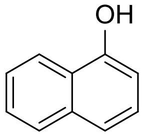 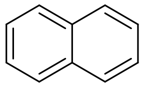	70	85	242
Cr-MCM-41, O_2, 2 MPa, supercritical CO_2, 14 h, 80 ˚C	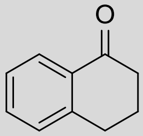 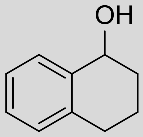	66	96	243
$K_8HP_2V_3W_{15}O_{62}\cdot 9H_2O$, O_2, 8 h, 120 ˚C	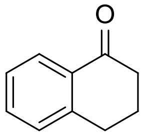 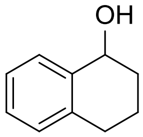 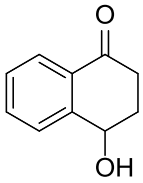 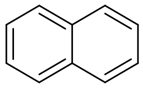	49	56	244

Mn_2O_3, O_2, AcOH, 1 h, 80 °C	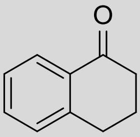 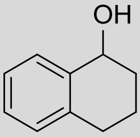 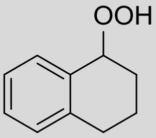	77	45	245

Table 18: Selected literature examples of tetralin oxidation.

4.1.2 Results and discussion

As was hoped, preliminary results showed good conversions in the oxidation of tetralin using our system. However, at the temperatures previously employed to oxidise propylbenzene (100 °C), the mass balance suffered considerably (~67%), and therefore, the validity of this result was questioned. To investigate what was causing this problem, several tests were carried out. The reaction was screened at different temperatures using a high-vanadium (9/1 VTi AlPO-5) and low-vanadium (1/1 VTi AlPO-5) catalyst. The results are shown in Figure 40.

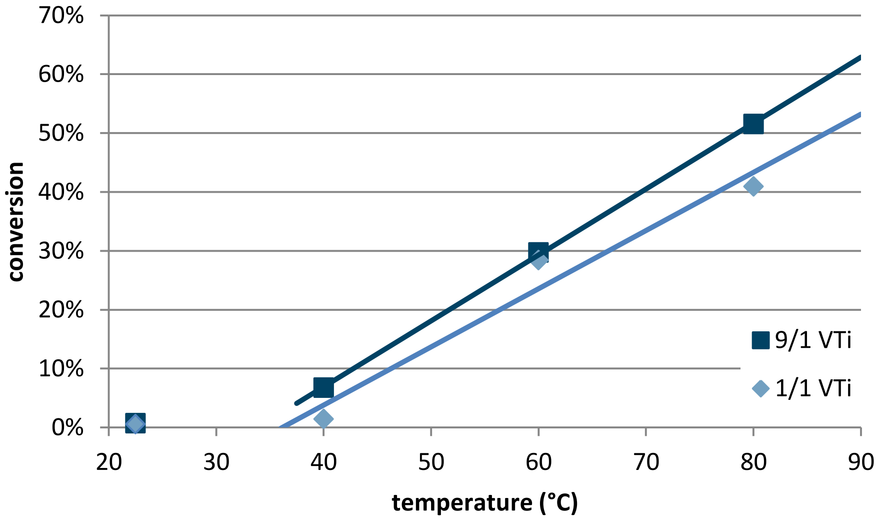

Figure 40: Oxidation of tetralin, conversion versus temperature. Conditions: 23 h at 100 °C, no solvent, 1 g substrate, 100 mg catalyst, 1.35 equiv. TBHP in decane.

The results showed that at room temperature, there is virtually no conversion. At 40 ˚C there is a very small amount of activity, while conversion steadily climbs to 30% at 60 ˚C and 52% at 80 ˚C for 9/1 VTi AlPO-5. Slightly lower conversions were achieved with 1/1 VTi. At 80 ˚C, the mass balance for these experiments had improved (*ca.* 80% at 80˚), but was not ideal. To determine what was causing the loss of mass balance, several tests were conducted. These included re-calibrations of both the GC and NMR internal standards, testing alternative standards, as well as evaporation tests at various temperatures. Using the latter, it was found that tetralin undergoes partial evaporation at 80 ˚C, which explained our lower mass balances. Blank experiments (*i.e.* conducted without a catalyst) returned poor conversions but near identical mass balances. To ascertain if we were combusting the substrate to form CO_2, we conducted an experiment using limewater to test for exhausted CO_2. This was negative. Consequently, the loss of mass balance was presumed to be due to evaporation of the starting material, so, as before, normalised conversions were used.

The results obtained were instructive. Firstly, the reaction was quite selective. Although propylbenzene was fairly (~75–80%) selective towards the ketone, with some amounts of acid and alcohol observed as side-products, there were only very small amounts of alcohol (~5%) present, and no carboxylic acid, indicating very high selectivity. This suggests that the oxidation of the alcohol to tetralone (step **b**, Scheme 50) proceeds very rapidly and that initial oxidation (step **a**) is the rate-limiting step. Indeed, this seems reasonable, as abstraction of the second benzylic hydrogen atom is expected to be more facile than abstraction of the first as the hydroxy group weakens the adjacent C–H bond. Meanwhile, cleavage of the aliphatic ring in tetralin appears to be very unfavourable as no such products were observed in the product mixture.

Second, it was noted that conversions were higher than those of propylbenzene at 80 ˚C. This would suggest that tetralin as a substrate is more easily oxidised than propylbenzene. Indeed, literature references[246,247] quote higher (homolytic) C–H bond dissociation energies (BDEs) for ethylbenzene than for tetralin (see Figure 41). This in turn would indicate that the α-hydrogen atoms of tetralin are more weakly bound than those in propylbenzene, which would explain the activity at lower temperatures. Indeed, a blank reaction (*i.e.* with no catalyst present) conducted at 90 ˚C showed a higher conversion than that of propylbenzene at 100 °C (17% *versus* 13%, respectively).

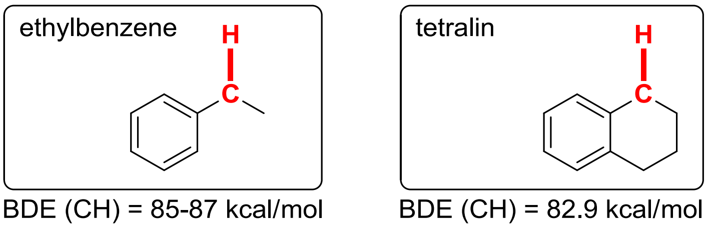

Figure 41: Relative α-C-H bond stabilities of ethylbenzene and tetralin.

To establish a reactivity profile of the oxidation of tetralin using different amounts of metal and catalyst, much like before, a series of tests were executed, though the study was limited to fewer data points. The results are shown in Table 19.

catalyst	V	catalyst amount	conversion	TON
9/1 VTi AlPO-5	9%	10 mass%	55%	72
1/1 VTi AlPO-5	1%	10 mass%	56%	589
0.1/1 VTi AlPO-5	0.1%	10 mass%	27%	4744
1/1 VTi AlPO-5	1%	0.5 mass%	27%	7362
0.1/1 VTi AlPO-5	0.1%	1 mass%	26%	47859
0.1/1 VTi AlPO-5	0.1%	0.1 mass%	16%	n/a

Table 19: Catalytic results of tetralin TON screening. Conditions: 23 h at 90 °C, no solvent, 1 g (7.56 mmol) substrate, 1.35 equiv. TBHP in decane. Conversion by GC and NMR, averaged.

As can be gathered from the results, very high turnover numbers were again obtained at low vanadium loadings and catalyst amounts. A concomitant drop in conversion was again noted in compensation, but the high activity of the catalyst was notable. An ultra-low metal experiment, at 0.1 mass% catalyst and 0.1% V returned conversions virtually identical to a blank, suggesting that at loadings this low the catalyst offers no genuine contribution. Therefore, turnover numbers for this experiment were considered invalid.

All in all, these results compare favourably with those reported in literature, including Union Carbide's patented methodology.[234] Though the conversions obtained are better than some and worse than others, the selectivities obtained were among the highest. It is tentatively proposed that the increased specificity could be due to the porous nature of the system, the high catalytic activity of the dispersed vanadium sites, or a combination of both. The porous nature of the AlPO, and especially the 1-dimensional channels present in the AFI framework, would be expected to prolong exposure of the substrate (and its products) to the catalytic sites. Prolonged exposure would in turn promote oxidation of the alcohol to the ketone, thereby favouring formation of tetralone. Moreover, our system accomplishes this with benign oxidants that are cheap, easily obtained, and employed under relatively mild conditions and atmospheric pressure. In addition, the catalyst is easy to remove or recover and has been shown to be reusable in catalysis.

4.2 Oxidation of indan

4.2.1 **Introduction**

Compared to the oxidation of tetralin, which is of industrial importance, the oxidation of indan is described less well in literature. In instances where it does appear, it is generally employed as a model substrate for benzylic oxidation of alkylbenzenes, and is often used alongside tetralin.[238,239] Benzylic oxidation is of major industrial significance for the production of pharmaceuticals and fine chemicals, and is classically achieved using polluting metal salts (often chromium or manganese), often in environmentally unfriendly or toxic organic solvents. As a consequence there is considerable interest in the discovery of more efficient, safer and greener procedures.[215,239]

Several studies have been published on the benzylic oxidation of indan to its ketone which, unlike tetralone, does not have a major industrial application. Nonetheless, the indan motif appears in several compounds that are of biological significance, and commercial indanone prices are higher than those of tetralone, adding significant value to any effective oxidation process for the oxyfunctionalisation of indan. A variety of methods for indan oxidation have been reported as illustrated by the examples shown in Table 20.

conditions	product(s) reported	conversion / yield (%)	ketone selectivity (%)	ref.
Au nanoparticles on TiO_2, O_2, 90 °C, 24 h	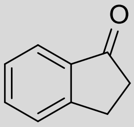	46	90	215
NHTPPI / CuCl, MeCN, O_2, 6 h, 35 °C	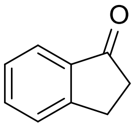	83	not specified	238
NHPI, acridine yellow or analogues, Br_2, MeCN, 0.3 MPa, 50 °C	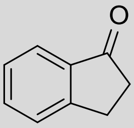 OH 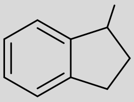 OOH 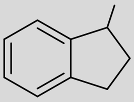	87	54	239
$KMnO_4$ deposited on montmorillonite K10, 20 h, RT, ultrasonic/μv	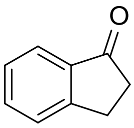	85	not specified	240
$Mn(OAc)_2·4H_2O$, chiral camphor-derived N,N-bidentate ligand, THBP, DCM, 5 min, 0 °C	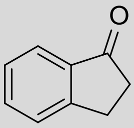	92	not specified	237
CrO_3, TBHP, DCM, RT, 6 h, closed flask	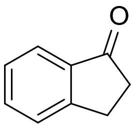	quant.	63%	236

livers from Purdue-Wistar rats sacrificed by decapitation buffered at pH = 7.4, air, RT, 1 h, TPNH	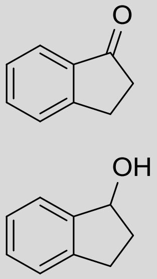	1%	75%	248

Table 20: Literature results for the oxidation of indan. Selectivities reported are towards 1-indanone which is the major product in all instances.

4.2.2 **Results and discussion**

Studies into indan oxidation were complicated by a low mass balance (65–70%). Under these conditions, a 59% conversion was noted after 23 h *(cf.* 55% for tetralin oxidation) (Scheme 54).

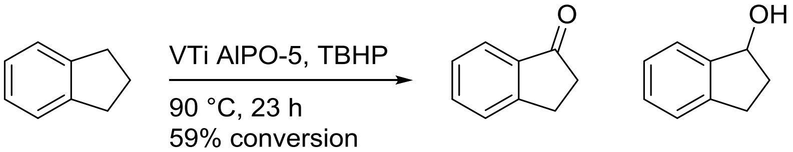

Scheme 54: Results of indan oxidation. Conditions: 23 h at 90 °C, no solvent, 1 g (8.46 mmol) substrate, 1.35 equiv. TBHP in decane. Conversion by GC and NMR, averaged.

The results obtained were better than some literature values in terms of conversion, and lower than others. However, compared to the selectivities reported in the literature, the reaction compared favourably. Analysis and quantification of the reaction mixture revealed that only *ca.* 3% of the alcohol is present, and only traces of other products. As such, the reaction appears to be very selective.

Again, this result is attributed to the porous nature of the catalyst and/or the high activity of the single-site vanadium species. Despite the low mass balance, this encouraging result showed VTi AlPO-5 to be a competitive choice for the oxidation of indan when high product specificity is warranted, such as in industrial applications. It is notable that the system uses benign reagents, produced little waste, and can be recovered very easily, which is of paramount importance in such settings. As trends had already been established using other substrates, no further investigative work was performed on this substrate.

4.3 Oxidation of methylbenzenes

4.3.1 Introduction

The previous results had shown a strong propensity for benzylic oxidation to form ketones, due to the fast reactivity of the catalyst towards benzylic alcohols and slow C–C bond cleavage to form carboxylic acids. However, as the oxidation of methyl groups to primary alcohols, aldehydes and carboxylic acids had not been examined, it was chosen to extend the reaction scope to methylbenzenes.

Such reactions might permit exploiting the titanium sites incorporated into the material. As mentioned before (see Chapter 1), while titanium AlPOs are generally used as an oxophilic or redox-active catalysts, a by-product of titanium incorporation is the generation of Brønsted acid sites in the framework as charge-compensation for the substitution of a P^{5+} site for a Ti^{4+} ion (Scheme 55).

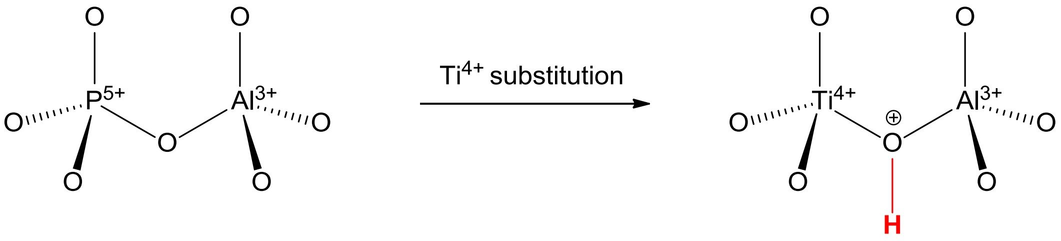

Scheme 55: Incorporation of a hypovalent metal into AlPO frameworks is accompanied by the association of a charge-balancing counterion such as a proton, generating Brønsted acidity.

As an acidic medium would favour hydration of an aldehyde towards the formation of its hydrate, this reaction was expected to display a greater selectivity towards a carboxylic acid product (Scheme 56). In that way the bifunctional character of VTi AlPO-5 would be exploited using the different roles afforded by the active vanadium metal and titanium sites.

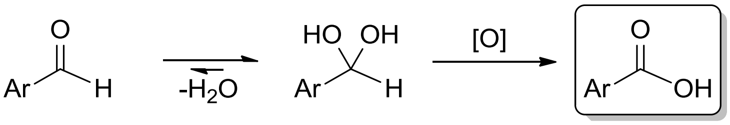

Scheme 56: Equilibrium of hydrate versus aldehyde and its concomitant oxidation to carboxylic acid.

The three most important industrial processes regarding methylbenzenes are the hydrodealkylation of toluene, isomerisation of *m*-xylene, and the disproportionation of toluene (see Scheme 57).[61]

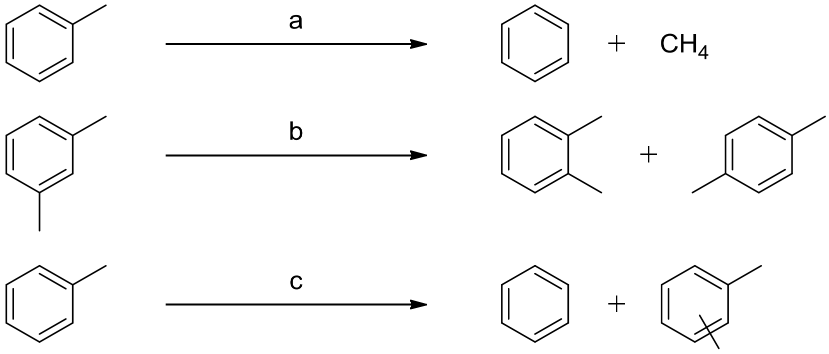

Scheme 57: The three most prominent industrial processes of benzene, toluene and xylenes; a: dehydroalkylation of toluene to benzene and methane; b: isomerisation of m-*xylene to* p- *and* o-*xylene; c: disproportionation of toluene to benzene and xylenes.*

Processes *a* and *c* both yield benzene, which is primarily used for the production of ethylbenzene and cumene (by alkylation with ethylene and propylene, respectively), which are in turn feedstocks for the production of styrene and phenol, respectively (see Chapter 1).

Other uses for toluene include its role as a solvent, and the production of benzaldehyde and benzoic acid, both of which are chemicals of major industrial importance as well, mostly as intermediates to various other compounds. Both compounds are also directly employed in the food industry, as flavouring and preservative, respectively.[61,82]

Xylenes are mostly employed for the production of phthalates and derivatives (known as the Amoco process). Of particular importance is the *para* isomer, which is oxidised almost exclusively to terephthalic acid, the precursor to polyethylene terephthalate (PET), a plastic used on enormous scale for the production of plastic bottles and similar consumer products. The *ortho*-isomer is mostly used for the production of phthalic anhydride, whose esters are employed as plasticisers. The demand for *m*-xylene, which is oxidised to isophthalic acid (a precursor to high-melting plastics), is used on a smaller scale, and therefore not considered as valuable; hence its industrial isomerisation process (over a zeolite catalyst).[61]

Numerous protocols have been developed for toluene and polymethylbenzene oxidations, a selection of which is presented in Table 21.

4. Substrate scope and new opportunities

Selectivities given refer to the first product shown in column 2, where the side-products are listed in order decreasing of magnitude.

conditions	product(s) reported	conversion / yield (%)	main product selectivity (%)	ref.
Co(II)TTP, air, 0.8 MPa, 3.5 h, 160 ˚C 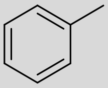	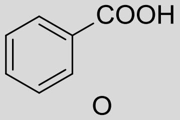 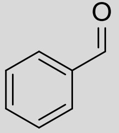 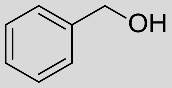	9	39	249
NO_2, dry air, UV-irradiated TiO_2, 10 min 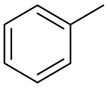	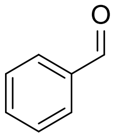 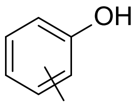 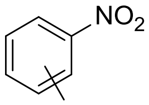 CO_2	0.1	46	250
Au nanoparticles on C, O_2, 10 bar, 7 h, 160 ˚C 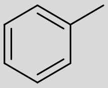	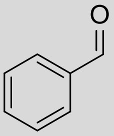 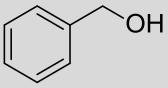 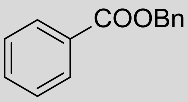	0.2	82	251

Riboflavin tetraacetate, O_2, photocatalytic, $MeCN/H_2O$, 270 min 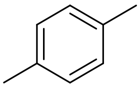	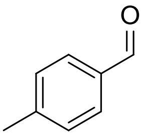	43	not specified	252
$[MoO(O_2)(QO)_2]$, H_2O_2, O_2, MeCN, 1 h, reflux 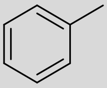	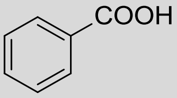	95	not specified	253
id. 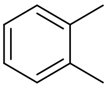	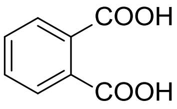	76	not specified	*ibid.*
id. 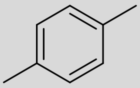	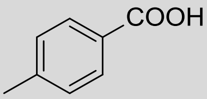	88	not specified	*ibid.*
$Co(OAc)_2$, $Cu(OAc)_2$, NaBr, O_2, 40 $kgcm^{-2}$, 1 h, 150 °C 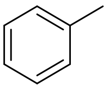	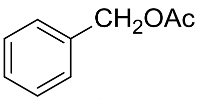 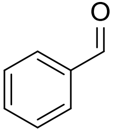	55	73	254

V_2O_5 on Nb_2O_3, 1 monolayer, 370 °C 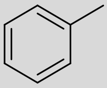	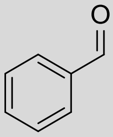 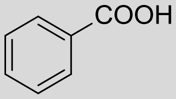 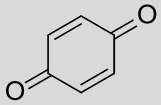 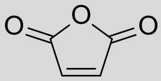 coupling products CO_2	not specified	54	[255]
V_2O_5 on TiO_2, O_2 in Ar, 310 °C 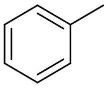	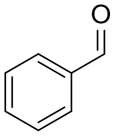 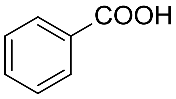 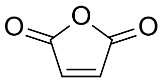 CO_x	<13	not specified	[256]

VAPO-5, O_2, 400 ˚C 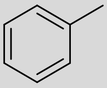	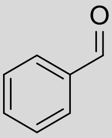 CO_x 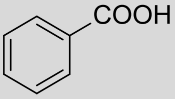 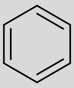 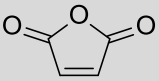 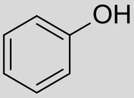 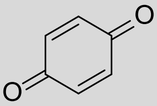	12	not specified	107
VAPO-5, TBHP, AcMe, 6 h, 60 ˚C	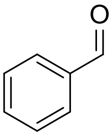 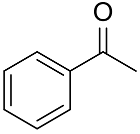 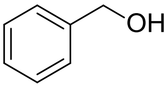	27	77	181

V_2O_5 on TiO_2, O_2, 350 ˚C 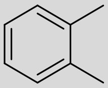	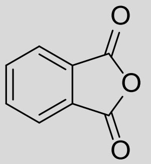 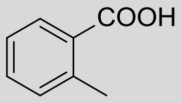 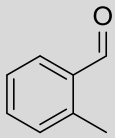 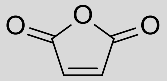	51	41	[257]

Table 21: A selection of results obtained in the oxidation of various methylbenzenes.

4.3.2 **Results & discussion**

First, toluene was oxidised using the standard propylbenzene conditions. Preliminary results showed that these conditions produced benzoic acid with very high selectivity. Indeed, benzyl alcohol and benzaldehyde were virtually absent from the product mixture, and no more than trace amounts of other products were observed (see Section 9.6). Moreover, upon standing, the reaction mixture solidified due to the large amounts of benzoic acid formed during catalysis. As a result, it was decided to separate the product from the reaction mixture by base/acid extraction to confirm quantification by isolation, as it was theorised that this procedure could be performed with minimal loss of product and would therefore not skew figures relating to catalytic results. Moreover, due to the involatile nature of arylcarboxylic acids, GC analysis of large amounts of these compounds was deemed unsuitable. Extraction gave benzoic acid in 38% yield w.r.t. the substrate (see Table 22).

The high selectivity observed is at odds with many previous results in the oxidation of toluene, including ones obtained using VAPO-5 with oxygen and TBHP.[107,181] Although the conditions used for our runs and those seen in the literature differ, the high selectivity for benzoic acid was remarkable. It suggested that the Brønsted acid sites had driven the selectivity by ensuring that the hydrate intermediate was produced rapidly and then oxidised to the acid. In other words, the incorporation of titanium and its concomitant acid sites drives the selectivity towards this product. The previously suggested reaction mechanism can now be augmented for methylbenzene oxidation as shown in Scheme 58, with several different possible pathways to the product:

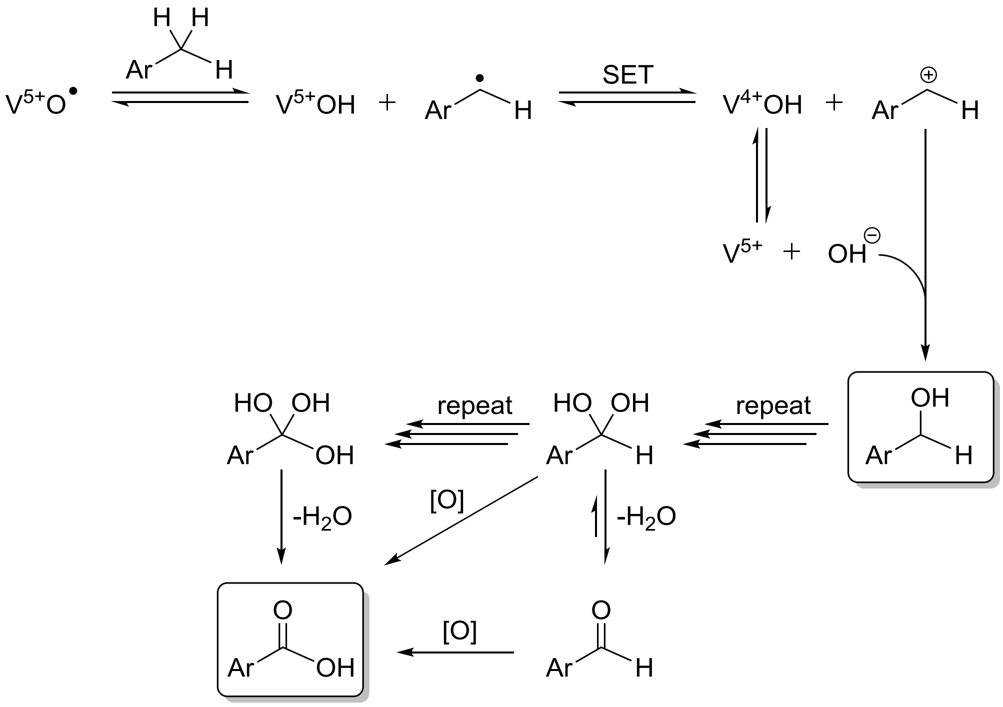

Scheme 58: Proposed reaction mechanism for the benzylic oxidation of methylbenzenes.

The yields were also higher than comparable protocols in the literature.[107,181] Because of this encouraging result the reaction was performed with other methylated arenes including xylenes, mesitylene and durene, using the same procedure. As before, it was noted that the reaction was highly selective towards the acid, but to our surprise, another trend quickly became apparent as all substrates had been oxidised exclusively to a mono-acid. Therefore, as before with toluene, the reactions were extracted by basic workup and an isolated yield was determined. A summary of the results of oxidation of methylbenzenes are given in Table 22.

substrate	product	isolated yield
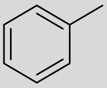	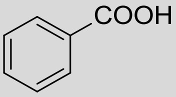	38%
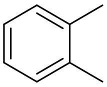	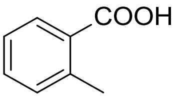	33%
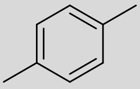	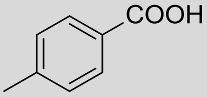	27%
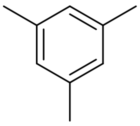	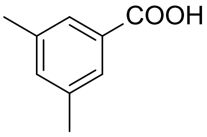	32%
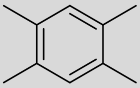	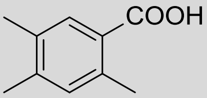	44%
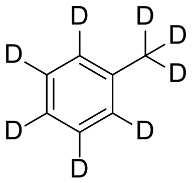	none	0%

Table 22: Summary of the results of catalytic oxidation of methylbenzenes. Conditions: 23 h at 100 °C, no solvent, 1 g substrate, 100 mg of 9/1 VTi AlPO-5, 1.35 equiv. TBHP in decane.

The results were intriguing as they showed remarkable consistency and the selectivity for monomethyl oxidation was neither expected nor precedented. Two reasons are postulated to explain the result observed. First, the sudden shift in polarity in going from an aldehyde to a carboxylic acid might cause the product to be ejected from the pore cavities, as AlPOs are only mildly hydrophilic. Second, as the acid products are all solids they may crash out of solution preventing further reaction. A combination of the above is also plausible. The formation of the solids may also prove to be self-limiting for reactions conducted without solvent as pore blocking would disable further substrate from entering the catalyst cavities, explaining its lack of full conversion.

The relative activities of the substrates towards oxidation varies to some degree, but were not hugely different, in keeping with the fact all substrates are oxidised to the same level. Steric effects appear to be limited, as crowded substrates like durene, mesitylene and *o*-xylene gave comparable conversions to toluene and *p*-xylene.

These results show that the high catalytic activity of VTi AlPO-5, combined with the defined environment brought about by the zeotype framework, make highly selective transformations possible. The isolated, single-site nature of the active vanadium sites causes optimal activity per metal ion as well as a strictly defined energetic interaction with the substrate, resulting in high turnovers at low metal loadings as well as site-selective oxidation. Combined with the product selectivity brought about by the Brønsted acid sites resulting from titanium incorporation, this presents new opportunities for dual catalysis. It should be noted that the reaction was not attempted in the presence of a large excess of oxidant. Therefore, it cannot be excluded that polyacid formation would have been possible due to a greater amount of available oxidant. Moreover, at very high concentrations of TBHP, it is possible that other products such as esters could have formed.

Interestingly, toluene-d^8, which is readily available as an NMR solvent, was also used as a test substrate in this reaction, but no formation of *any* products was observed. Similarly, a 50:50 mixture of toluene and toluene-d^8 yielded only products derived from the non-deuterated starting material. This strongly suggests that the C–D bond strength is too great for this reaction to occur. This result is a striking example of the kinetic isotope effect (KIE) which exploits relative reactivities of different isotopes as a result of their mass. Although the kinetic isotope effect does not affect the reaction, it can strongly influence the rate of a reaction.

The theory behind the kinetic isotope effect is derived from the relative vibrational frequency of bonds to different isotopes. As isotopes are electronically virtually identical, but of a different mass (due to a varying number of neutrons present in the core), a lower vibrational frequency is expected for isotopes with greater mass. This corresponds to a lower zero-point energy, and therefore a greater amount of energy is needed to break the bond. A schematic representation of this is shown in Figure 42.

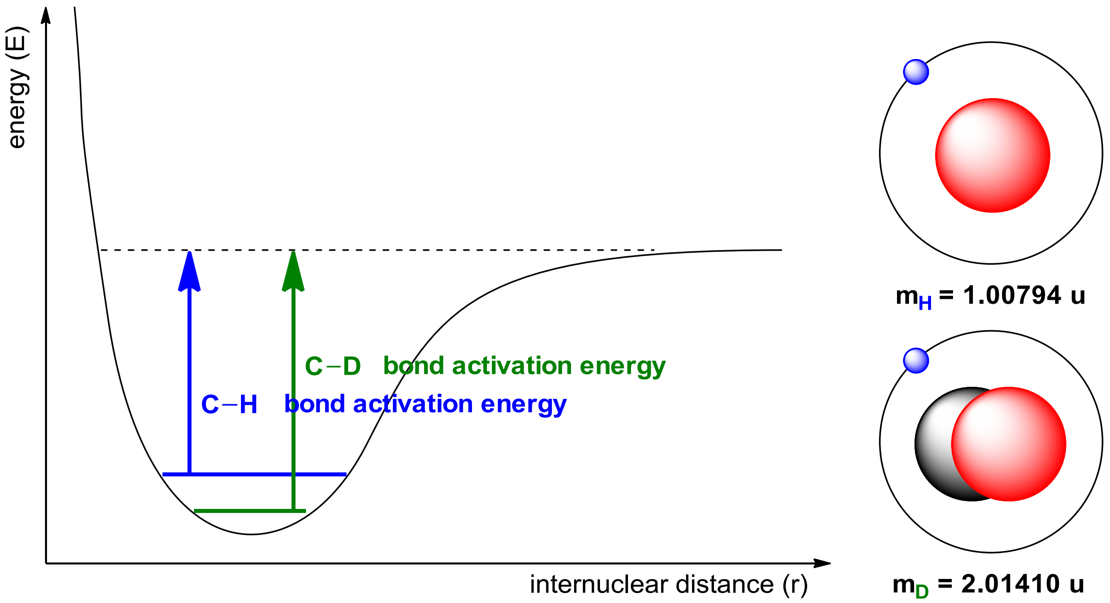
energy (E)
C–D bond activation energy
C–H bond activation energy
internuclear distance (r)
m_H = 1.00794 u
m_D = 2.01410 u

Figure 42: Energy v. distance plot illustrating the kinetic isotope effect. The lower zero-point energy level (shown in blue for the C–H bond, in red for the C–D bond) of a carbon-deuterium bond results in a greater amount of energy required to activate the bond compared to a carbon-hydrogen bond.

As the kinetic isotope effect is based on the relative masses of two isotopes, the greatest kinetic isotope effects are found in hydrogen, where substitution of isotopes can lead to a doubling (^{1}H *vs* ^{2}H) or even tripling (^{1}H *vs* ^{3}H) of the atomic mass. The resulting vibrational frequency of a C–D bond is considerably lower than that of a C–H bond (*ca.* 2100 cm^{-1} *vs* 3000 cm^{-1}), resulting in noticeably greater bond strength. For isotopes with greater mass than hydrogen, the difference between two isotopes is generally sufficiently small that it is not noticeable; therefore, most KIEs are based on isotopes of hydrogen.

The magnitude of the measured KIE can give vital information about the mechanism or kinetics of a reaction. Two types of KIE are distinguished. If the isotopic bond is being broken during the reaction, it is referred to as a primary KIE. If the bond does not break during the reaction, but influences the rate of the reaction indirectly, it is called a secondary KIE. For example, the lower bond strength of a C–H bond compared that of a C–D bond results in a longer bond for C–H than for C–D, and as a result, a hybridisation change from sp^3 to sp^2 is more facile for a C–H bond than for a C–D one. In general, primary KIEs tend to be greater than secondary KIEs.

The result, which shows a complete stop of the reaction, is suggestive of a primary KIE, and would indicate that the C–D bond is too strong to break during the reaction. This in turn suggests that the initial C–H bond cleavage is the rate-limiting step in the reaction. Classically, the rate difference is a factor up to 8 for a C–H/C–D cleavage process. However, for reactions involving H-atom abstraction they can be much greater. A notable example where KIEs up to 13 000 were reported was observed by Ingold *et al.* in 1976 for radical H-abstraction in *t*-butyl aryl systems.[258]

4.4 Heterocycle oxidation

4.4.1 Introduction

Pleased with the success of the cooperative effects between the vanadium redox-active centres and the titanium-derived Brønsted acid sites, the combination was sought to be exploited in another way. Thus, it was aimed to employ the titanium's acid sites directly in a separate reaction, such as dehydration. To make use of this bifunctionality, a heterocyclic substrate was chosen in the form of indoline (**1**, Scheme 59). Assuming the selectivity towards benzylic oxidation as was witnessed before, its oxidation was expected to first yield benzylic alcohol **2**, which could undergo fast acid-catalysed (**3**) dehydration to form indole (**4**).

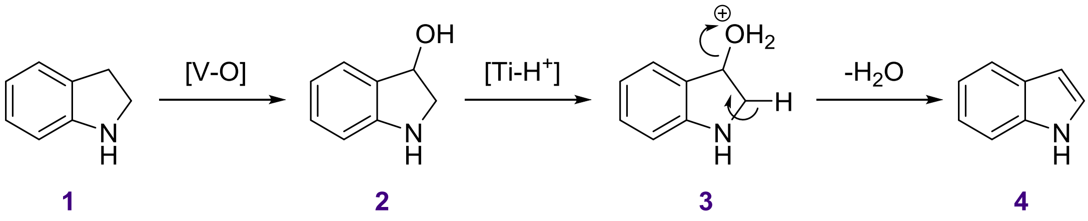

Scheme 59: Expected reactivity of indoline towards VTi AlPO-5. First, vanadium-catalysed benzylic oxidation to the alcohol. Second, acid sites caused by titanium incorporation forming a fraction of aqua groups. Third, fast dehydration of the aqua compound to form indole.

Another possible route to the product involves oxidation of the lone pair on nitrogen rather than the benzylic oxidation observed so far. In this instance, the mechanism proceeds from indoline (**1**, Scheme 60) to radical cation **5** upon oxidation of the nitrogen lone pair. This species can then release a benzylic proton to aromatise, forming indole (**4**). This process does not involve acid-based catalysis, however, it hinges on the highly unfavourable leaving group H·.

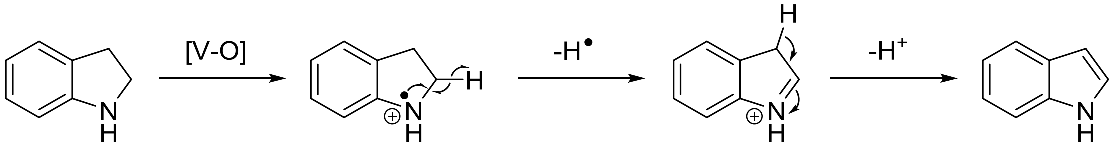

1 **5** **6** **4**

Scheme 60: Alternative pathway for oxidation of indoline.

Industrially, indole is used for the synthesis of tryptophan and indigo. Tryptophan is produced from indole and serine using the enzyme *tryptophan synthase* or a number of bio-organisms including *Escherichia Coli, Bacillus Subtilis, Brevibacterium Flavum,* and *Pseudomonas Aeruginosa.* The reverse process, producing indole from tryptophan, is also possible using *E. Coli*. Indigo is produced from indole by oxidation and subsequent homocoupling (see Scheme 61). Other uses of indole include the production of a wide range of pharmaceuticals (often antidepressants).[259-263]

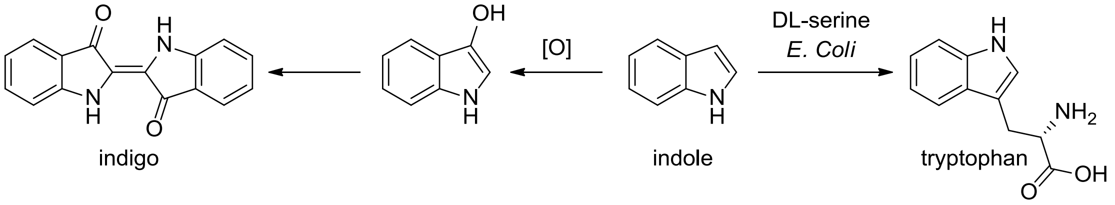

Scheme 61: Industrial conversion of indole to tryptophan (right) and indigo (left).

In the laboratory, the ability to interconvert between an indoline motif and an indole could be quite important as the two display different reactivities, for example, in electrophilic aromatic substitution. In indoles, the C3 position is most activated towards electrophiles, meaning that electrophiles add there preferentially. In indolines, this reactivity is shut down and electrophilic substitution takes place instead at C5 (Scheme 62). This difference allows one to use an indoline to protect against C3-substitution and then convert the substrate back to the indole as desired using our catalyst. Thus, it could prove to be a powerful tool for synthetic chemists in the laboratory.

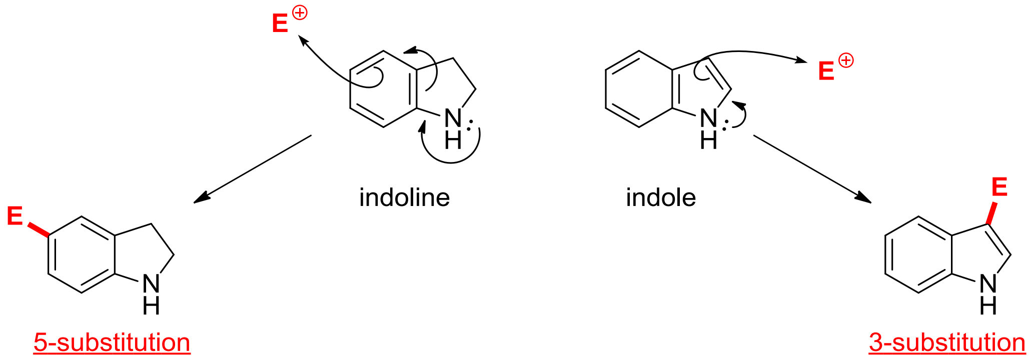

Scheme 62: Expected reactivities of indoline versus indole towards electrophiles. With indole, substitution at the 3-position is expected, while indoline would more likely undergo substitution at the 5-position.

4.4.2 Results & discussion

Results, even from preliminary tests, were highly encouraging. It was found that indoline was converted to indole with high selectivity. Indeed, no trace of the supposed intermediary alcohol product or other oxidation products was observed (see Section 9.6). At 80 °C and 23 h, it was found that a 40% conversion to the product was achieved.

This result was most pleasing, as it demonstrated the bifunctional acid-redox catalysis that was hoped for as a benefit that arises from using a combination of vanadium and titanium which results in high selectivity.

The explanation posed for this was as follows. The first stage of the reaction, C–H oxidation of the benzylic position to the alcohol (exactly as with the oxidation of propylbenzene), appeared to be much slower than the second stage of the reaction; acid-catalysed dehydration to form the indole (Figure 43). As a result, no trace of the alcohol intermediate persists for a very long time as it is immediately dehydrated to form the only product observed. In other words, the bifunctionality of the catalyst not only allows one to perform two reactions with the same catalyst and reagent, within the same pot; it also drives the selectivity of the reaction to a single product.

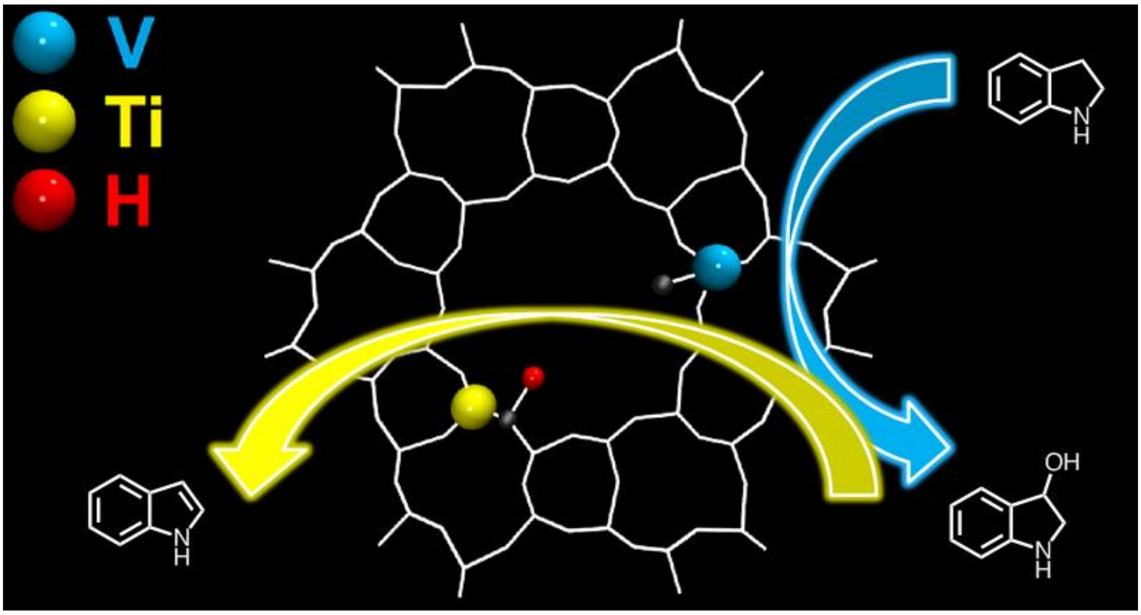

Figure 43: Bifunctional oxidation of indoline to indole.

As before, to see if higher turnover numbers for this reaction could be obtained, less catalyst and metal were used, moving away from the standard 10 mass% of a 9% vanadium VTi AlPO-5. As with the oxidation of tetralin, the study was restricted to fewer data points than in the propylbenzene oxidation study. The results obtained are summarised in Figure 44.

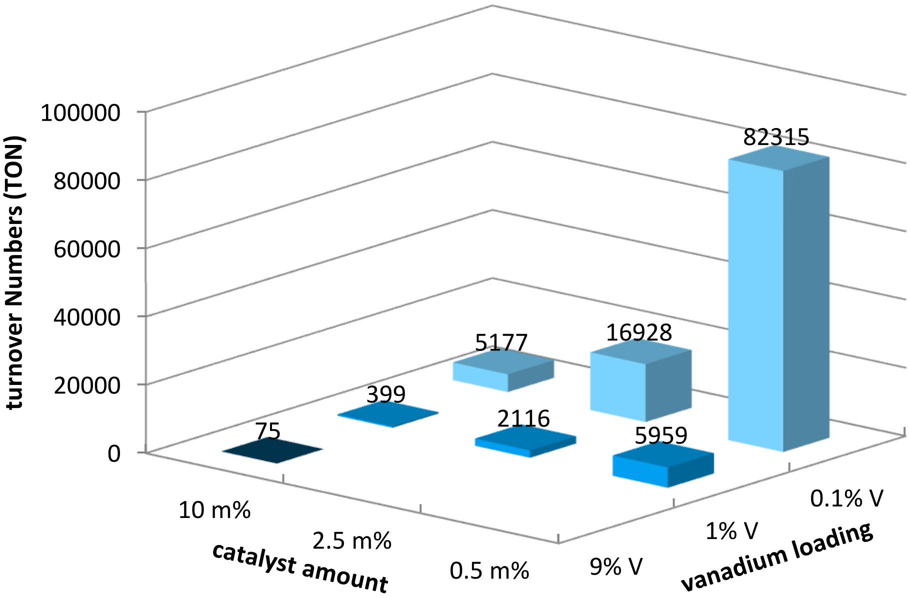

Figure 44: Turnover numbers (TON) for the oxidation of indoline versus the catalyst amount and vanadium loading. TONs are shown above each data bar.

Again, extremely high turnover numbers were obtained at low catalyst levels and vanadium loadings. At the lowest amount of vanadium in the system

— 0.5 mass% of a 0.1 atom% catalyst — conversion dropped to 19%, but was still significantly superior to a blank reaction (9%).

Attempting to see how far reactivity could be taken, the same reaction was also performed on tetrahydroquinoline. To our surprise, quinoline was obtained with high selectivity (100 ˚C, 23 h, 64% conversion). Based on the results obtained from indoline, this could indicate that dehydration had occurred not once but twice to form the aromatic product. Although the aromatisation during the second dehydration is expected to be extremely favourable and fast, no ketone products were observed, suggesting that dehydration after the first oxidation is fast enough to prevent this product from being formed (pathway 1, Scheme 63). However, as the intermediate product could not be observed, and no kinetic studies were undertaken, the possibility of a different reaction pathway cannot be ruled out. Indeed, an alternative pathway involving oxidation of the lone pair on nitrogen akin to the alternative mechanism proposed for the oxidation of indoline (Section 4.4.2) is also possible (pathway 2):

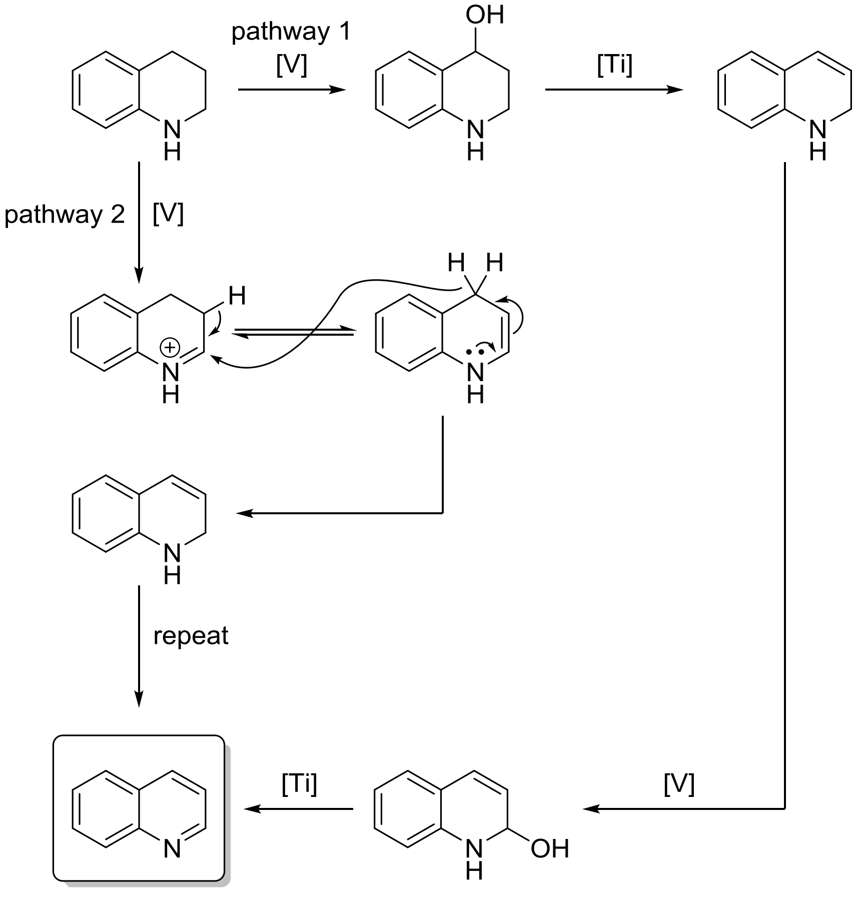

Scheme 63: Proposed reaction process for the oxidative dehydration of tetrahydroquinoline to quinolone.

Use of tetrahydroisoquinoline as a substrate led to a mixture of amide **8** (dihydroisoquinolinone) and the dehydrated isoquinoline **9** with poor selectivity (Scheme 64). Oxidation of dihydrobenzofuran was similar, leading to three distinct products, including benzofuran (**10**) and the benzylic ketone **11.** Due to the disappointing, non-selective nature of these two reactions, no rigorous quantification or further investigation was performed on tetrahydroisoquinoline or dihydrobenzofuran (Scheme 64).

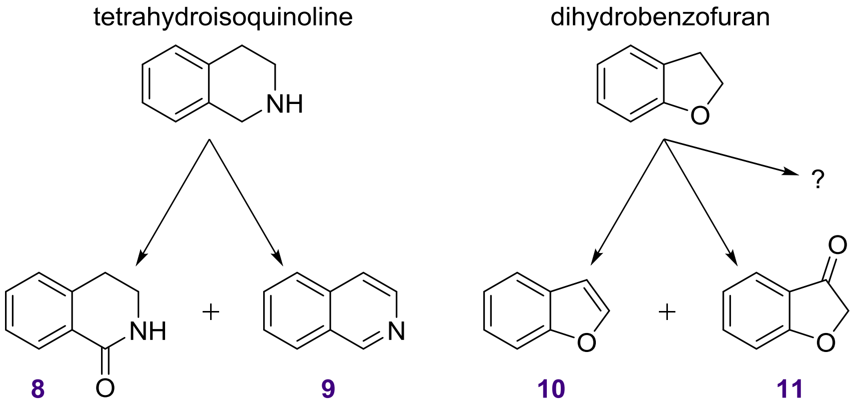

8 **9** **10** **11**

Scheme 64: Catalysis results of the oxidation of tetrahydroisoquinoline and dihydrobenzofuran. A mixture of products was observed in both cases.

In conclusion, the results obtained with heterocyclic substrates are highly encouraging. Although some heterocycles performed poorly, the reaction of indoline and tetrahydroquinoline show how aromatisation can drive reactions with extremely high selectivity — especially when the substrate has a nitrogen atom next to the arene. Oxygen heterocycles appear to respond less predictably, as did tetrahydroisoquinoline. Nonetheless, our catalyst could afford a viable procedure for the “protection” of indoles or quinolines as indolines and hydroquinolines with facile interconversion during synthesis.

5. Analysis of catalysts

Catalyst batches were analysed by a variety of spectroscopic and non-spectroscopic techniques in order to ascertain two matters; first, to determine whether the synthesis of the material was successful; and second, to learn more about the physicochemical properties of the material as well as some information about the nature of the active sites and other species present in the framework.

As during initial screening it was found that vanadium-titanium AlPO-5 proved to be considerably superior to other catalysts (see Chapter 3), this was turned to as the catalyst of choice. Because of this, characterisation efforts were focused mostly on characterising this material.

EPR analysis data simulations and calculations were performed by Stuart Elliott with help from Dr Chris Wedge. Solid-state NMR measurements, simulations and calculations were performed by Prof. Marina Carravetta.

5.1 Physicochemical characteristics

5.1.1 Physical appearance

The first, most elementary observation of the physical properties of VTi AlPO-5 is its colour. In the as-synthesised material, colour contributions from both metals can be found, with vanadium exerting a blue-grey colour, while titanium imparts little colour except when used in high concentrations. This is also apparent from their monometallic analogues: VAPO-5 has a fairly desaturated blue-grey colour, while TAPO-5 is white (at low concentrations of Ti). The typical catalyst used for screening, which uses 9% V and 1% Ti ("9/1 VTi AlPO-5"), has a strongly apparent colour which can be said to be somewhere between Dark Electric Blue and Air Superiority Blue (FindTheData Graphiq colour scale). This is in agreement with the colour described for VAPO-5.[108,183] As more titanium is added, the material turns gradually slightly greenish due to an increasing yellow contribution from the titanium, presumably due to the presence of extraframework titanium species.

When calcined, VTi AlPO-5 turns a very bright yellow colour — for 9/1 VTi AlPO-5, the colour is somewhere between Selective Yellow and USC Gold. At higher concentrations of titanium, the material becomes a paler shade of yellow. The overall difference in colour is not as pronounced, however. Figure 45 below shows as-synthesised and calcined VTi AlPO-5 with increasing amounts of vanadium, and Figure 46 shows as-synthesised VTi AlPO-5 with increasing amounts of titanium.

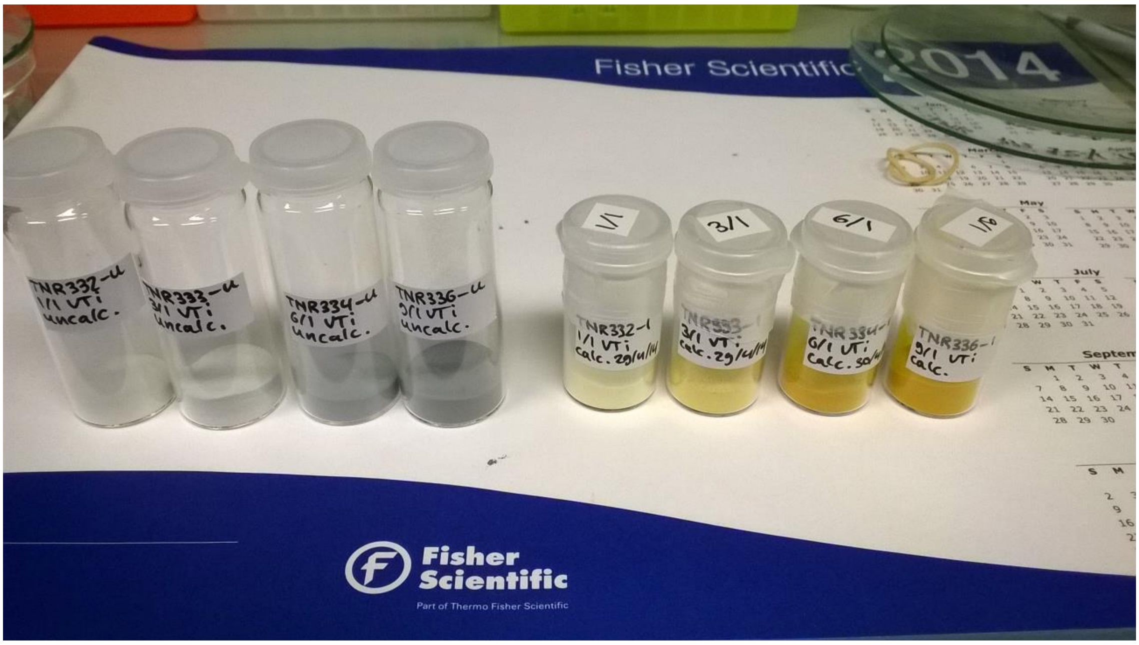
Fisher Scientific
2014
TNR332-u 1/1 VTi uncalc.
TNR333-u 3/1 VTi uncalc.
TNR334-u 6/1 VTi uncalc.
TNR336-u 9/1 VTi uncalc.
1/1
3/1
6/1
9/1
TNR332-1 1/1 VTi Calc. 29/4/14
TNR333-1 3/1 VTi calc. 29/4/14
TNR334-1 6/1 VTi Calc.
TNR336-1 9/1 VTi Calc.
Fisher Scientific
Part of Thermo Fisher Scientific

Figure 45: As-synthesised (left) and calcined (right) VTi AlPO-5 with a fixed 1% Ti and a varying loading of vanadium; from left to right: 1%, 3%, 6%, 7.5%, 9%.

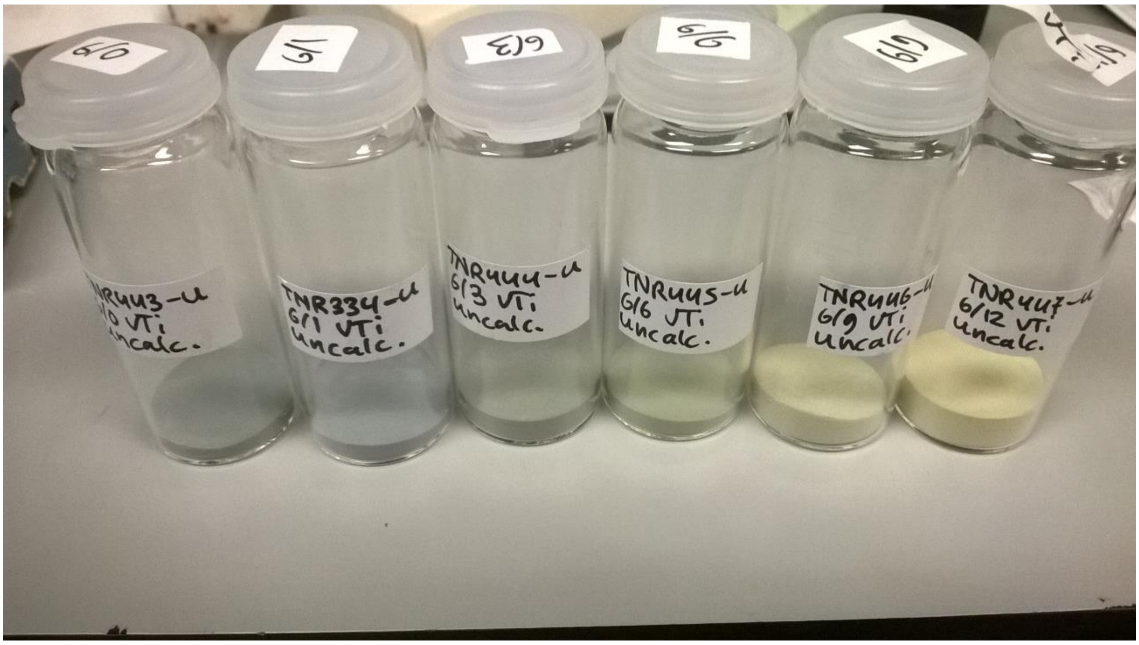
6/0
6/1
6/3
6/6
6/9
NR443-u
/0 VTi
ncalc.
TNR334-u 6/1 VTi uncalc.
TNR444-u 6/3 VTi uncalc.
TNR445-u 6/6 VTi uncalc.
TNR446-u 6/9 VTi uncalc.
TNR447-u 6/12 VTi uncalc.

Figure 46: As-synthesised VTi AlPO-5 with a fixed 6% V and a varying loading of titanium; from left to right: 0%, 1%, 3%, 6%, 9%, 12%.

Bimetallic vanadium catalysts with secondary metals other than titanium show a range of different colours. In these samples, both metals were present in high (9%) loading. VNi AlPO-5 is a greyish green colour in the as-synthesised form, while VMn AlPO-5 is a greenish grey, with the former being a more saturated colour. VCr AlPO-5 is a much deeper, darker shade of green, meanwhile. VCo AlPO-5 is an especially deep saturated, darkish shade of blue. When calcined most materials turn a shade of yellow. VNi is very bright yellow, while VMn has an ochre-like colour. VCo is a yellow/brown shade of green, while VCr has a strong green-brown colour.

The main analytical technique used to characterise samples was PXRD (see Section 2.3.2.1). Unlike most other techniques, this was applied to every catalyst batch synthesised, in order to ascertain the phase purity of the material. Using phase-impure materials carries with it the risk that the catalytic activity is dominated by these phases, so care was taken to avoid the use of phase-impure materials whenever possible. Samples were therefore analysed by PXRD before and after calcination to ascertain their successful synthesis and calcination.

Compared to a calculated X-ray diffractogram of the AFI framework, VTi AlPO-5 shows an essentially unchanged pattern with the exception of some slight peak shifts and changes in relative peak intensity. A comparison between a typical VTi AlPO-5 pattern (9% V, 1% Ti) and a calculated diffractogram of the AFI framework is shown in Figure 47.

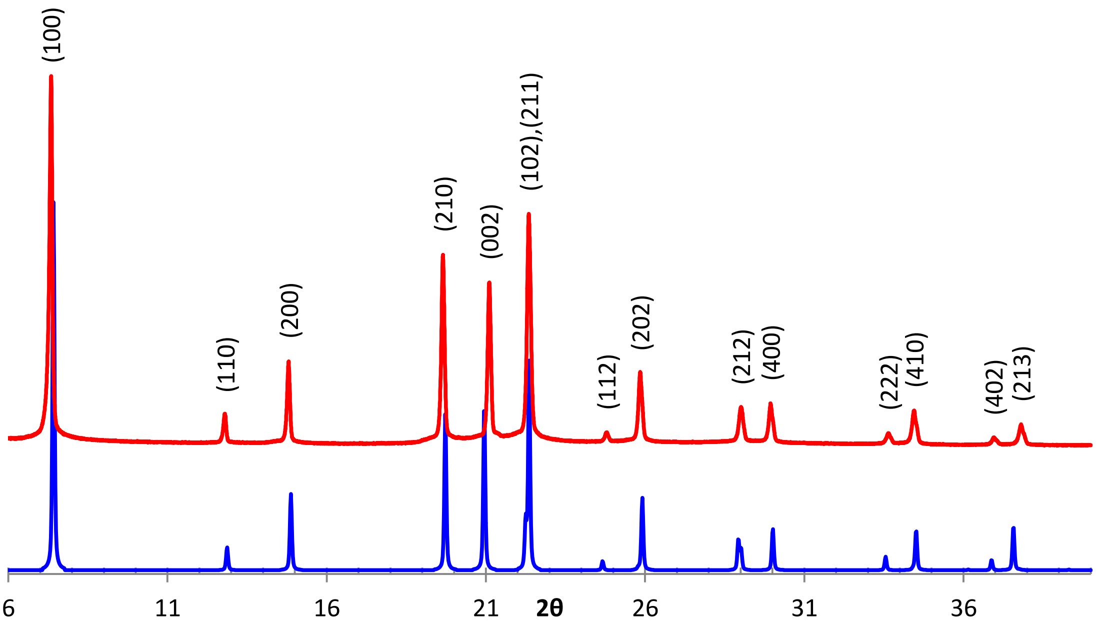

Figure 47: Comparison between 9/1 VTi AlPO-5 (red) and a calculated AFI pattern (blue). AFI pattern data obtained from the IZA structure database.[13] Miller indices are shown above Bragg peaks in parentheses.

Pattern indexing shows that refined patterns have cell parameters with only a small amount of distortion. A table outlining pattern indexing results is shown in Table 23.

H	K	L	2θ	2θ$_{calc.}$	Δ2θ
1	0	0	7.352	7.4064	-0.0544
1	1	0	12.821	12.8462	-0.0252
2	0	0	14.827	14.844	-0.017
2	1	0	19.648	19.6785	-0.0305
0	0	2	21.147	21.1723	-0.0253
2	1	1	22.363	22.3735	-0.0105
1	1	2	24.834	24.8421	-0.0081
2	2	0	25.867	25.8576	0.0094
3	1	1	29.027	28.995	0.032
2	1	2	29.108	29.0619	0.0461
4	0	0	29.959	29.9447	0.0143
2	2	2	33.646	33.6561	-0.0101
3	2	1	34.456	34.4518	0.0042
4	0	2	36.968	36.9647	0.0033
2	1	3	37.839	37.8408	-0.0018

λ (Å)	1.5406
a (Å)	13.771 (0.0165)
b (Å)	13.771 (0.0165)
c (Å)	8.3859 (0.0016)
α (°)	90
β (°)	90
γ (°)	120
Vol. (Å^3)	1377.3

Table 23: Left, Miller indices and 2θ values for 9/1 VTi AlPO-5 (as-synthesised), refined, compared to that of calculated AFI. The difference between 2θ is shown in the rightmost column. Right; final cell parameters for VTi AlPO-5. Errors are shown in parentheses.

A comparison was also made between VTi AlPO-5 at different loadings of metal, as well as before and after calcination. A series of overlaid spectra is shown in Figure 48 and Figure 49.

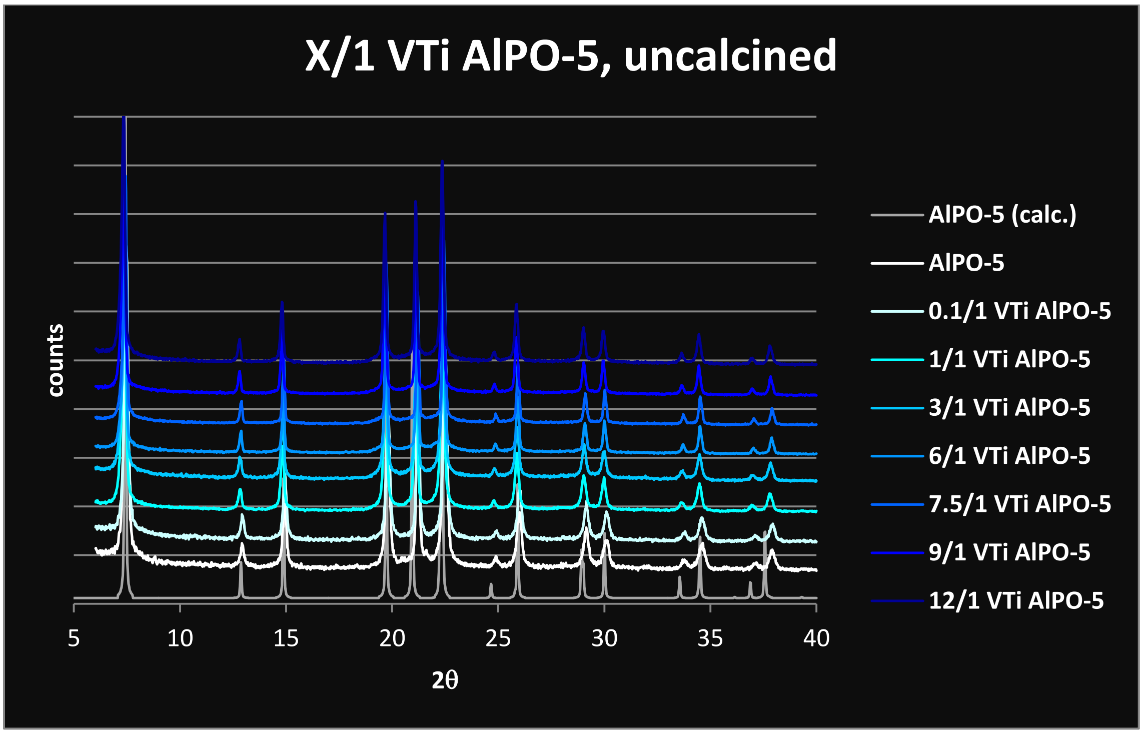

Figure 48: Overlaid powder X-ray diffractograms of VTi AlPO-5 at various loadings of vanadium, as-synthesised. A calculated AFI pattern is shown at the bottom.

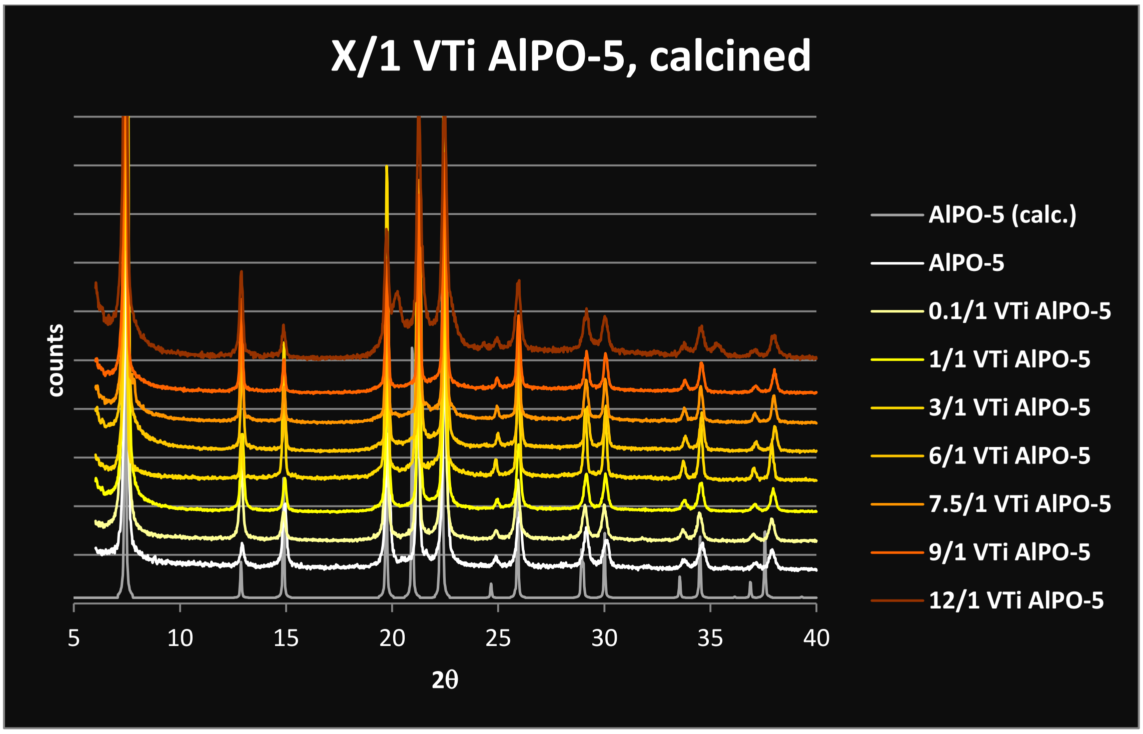

Figure 49: Overlaid powder X-ray diffractograms of VTi AlPO-5 at various loadings of vanadium, as-synthesised. A calculated AFI pattern is shown at the bottom.

VTi AlPO-5 shows nearly identical diffractograms compared to a calculated AFI pattern, with only small peak shifts and changes in relative intensity. A non-substituted, pure AlPO-5 sample was also synthesised for comparison, which shows the same changes in relative peak intensity and slight peak shifts as VTi AlPO-5. Both results strongly suggest no significant distortions occur in the framework upon V and Ti substitution of AlPO-5. The peak shape and intensity shows that the material is highly crystalline.

In the as-synthesised material, the framework remains remarkably phase-pure, even at the very high metal loading of 12% vanadium. This could possibly be attributed to the flexibility of the AlPO-5 framework which has been reported before.[101,157] However, upon calcination, at 12 atom% vanadium, it can be clearly seen that the material partly decomposes — at lower loadings, the material does not suffer from this problem. Presumably, this is due to strain experienced by the framework as the vanadium changes its coordination geometry.

This result is in partial agreement with previous findings for VAPO-5, where a similar instability of the framework towards calcination was reported, resulting in the formation of an extraframework vanadium oxide species as well as framework collapse to form tridymite.[108] However, unlike our results, Rigutto *et al.* found that this instability occurred at as little as 3% V, while our material is stable all the way up to and including 9% V. While it is possible that the incorporation of a slight amount of titanium somehow stabilises the framework against collapse under calcining conditions, it is perhaps more likely that the difference is mainly due to the difference in synthesis protocol used. In their study of VAPO-5, Rigutto *et al.* used different conditions, gel compositions and precursors, including the use of the less structure-specific $NHPr_3$ / NPr_4F. The SDA employed in this work, Cy_2MeN, has been reported (several years after Rigutto's study) to have exceptionally high selectivity towards the AFI structure.[264]

A summary of final, indexed cell parameters for VTi AlPO-5 at different metal loadings is shown in Table 24. All samples show a slight distortion of cell parameters and a slight decrease of cell volume, as expected for a metal-substituted framework.

Index	a (=b) (Å)	c (Å)	V (Å^3)	phase pure?
AlPO-5 (calc.)	13.740	8.747	1420.6	—
1/1 VTi AlPO-5	13.7076 (0.0202)	8.3571 (0.0018)	1359.9	yes
3/1 VTi AlPO-5	13.6488 (0.0235)	8.3209 (0.0031)	1342.4	yes
6/1 VTi AlPO-5	13.7017 (0.0164)	8.3404 (0.0014)	1356.0	yes
7.5/1 VTi AlPO-5	13.7223 (0.0104)	8.3492 (0.0009)	1361.5	yes
9/1 VTi AlPO-5	13.7174 (0.0107)	8.3487 (0.0008)	1360.5	yes
12/1 VTi AlPO-5	13.7182 (0.0185)	8.3549 (0.0027)	1361.7	no

Table 24: Summary of cell refinement parameters of calcined VTi AlPO-5 at different loadings of vanadium, versus calculated parameters (entry 1). Errors are shown in parentheses.

The Scherrer equation can be used to elucidate information about crystallite size in powders (Section 2.3.2.1), relating the size of crystalline domains to peak broadening in the spectrum. Using this formula, it was found that crystallite sizes varied from *ca.* 40–60 nm in the samples.

Note that although the Scherrer equation described above can give information about the size of the crystallites, this does not necessarily correlate with the size of the particles. Indeed, physical inspection suggests that the actual particle size is considerably bigger.

SEM allows us to inspect these particles under high magnification, giving clear information about size and distribution. Indeed, SEM confirmed that the particle size is much bigger than the crystallite size; roughly 10–30 μm. As our XRD data suggested, using the Scherrer equation described above, that crystallite size varied from roughly 40–60 nm, it would seem that the samples consist of polycrystals or aggregates.

Particles of varying metal loading were also examined by SEM (see Section 2.3.2.4); however, no visible change in average size was observed across the range of metal loadings examined (0.1% to 12% V). However, it was found that increasing vanadium loading does affect particle morphology. At low loadings, the particles are clearly spherical in shape, but at higher loadings, the particles become increasingly more barrel-shaped, starting from 6% vanadium onwards. The surface morphology of the VTi catalyst particles showed that the surface is composed of densely staggered plaquettes.

5. Analysis of catalysts

An undoped sample of AlPO-5 and an extremely high-vanadium sample prepared at the theoretical maximum of 50% V were also prepared for comparison. Results are shown in Figure 50, Figure 51 and Figure 52 and the accompanying table (Table 25).

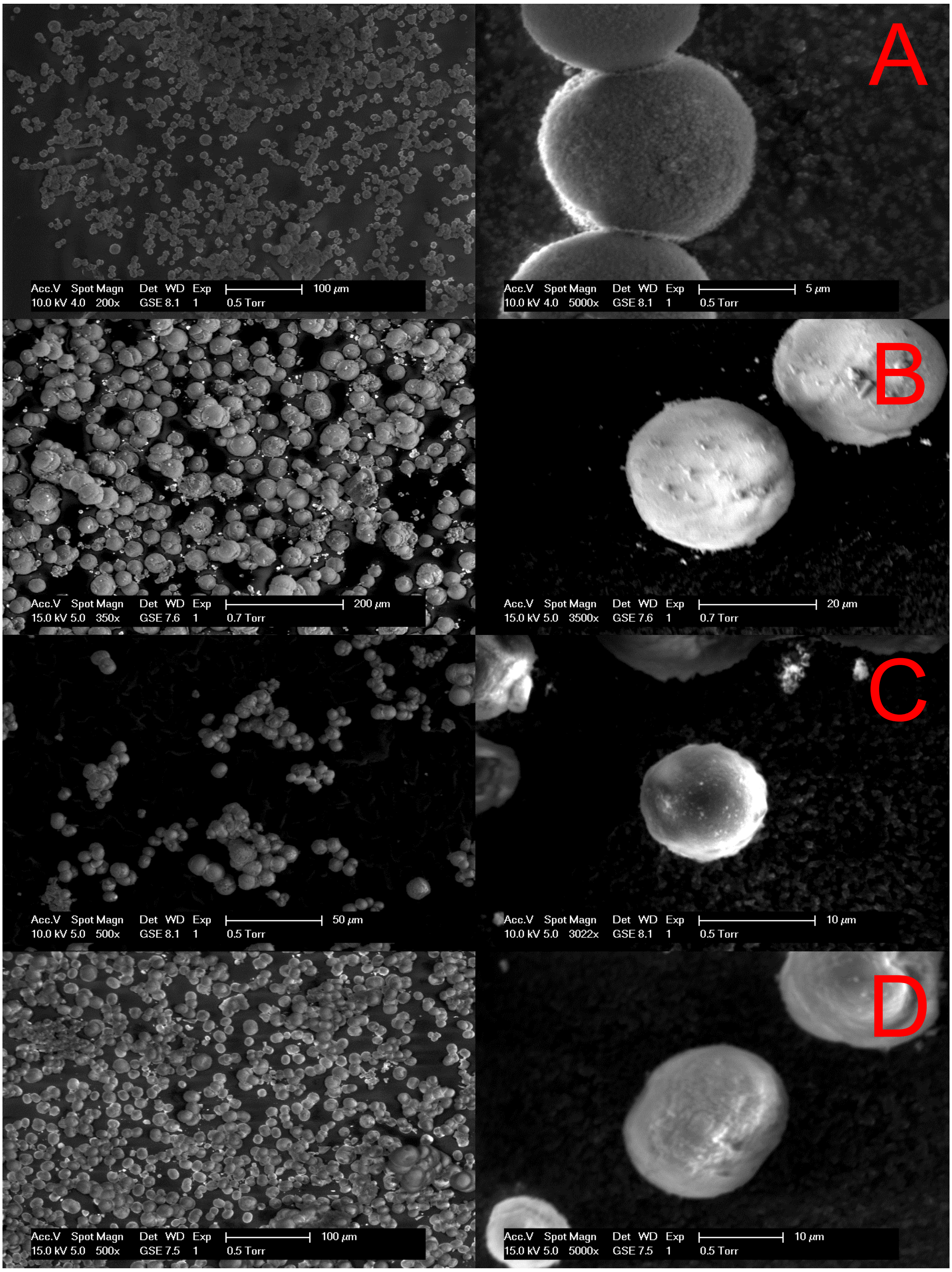
A
B
C
D
Acc.V Spot Magn Det WD Exp 100 µm
10.0 kV 4.0 200x GSE 8.1 1 0.5 Torr
Acc.V Spot Magn Det WD Exp 5 µm
10.0 kV 4.0 5000x GSE 8.1 1 0.5 Torr
Acc.V Spot Magn Det WD Exp 200 µm
15.0 kV 5.0 350x GSE 7.6 1 0.7 Torr
Acc.V Spot Magn Det WD Exp 20 µm
15.0 kV 5.0 3500x GSE 7.6 1 0.7 Torr
Acc.V Spot Magn Det WD Exp 50 µm
10.0 kV 5.0 500x GSE 8.1 1 0.5 Torr
Acc.V Spot Magn Det WD Exp 10 µm
10.0 kV 5.0 3022x GSE 8.1 1 0.5 Torr
Acc.V Spot Magn Det WD Exp 100 µm
15.0 kV 5.0 500x GSE 7.5 1 0.5 Torr
Acc.V Spot Magn Det WD Exp 10 µm
15.0 kV 5.0 5000x GSE 7.5 1 0.5 Torr

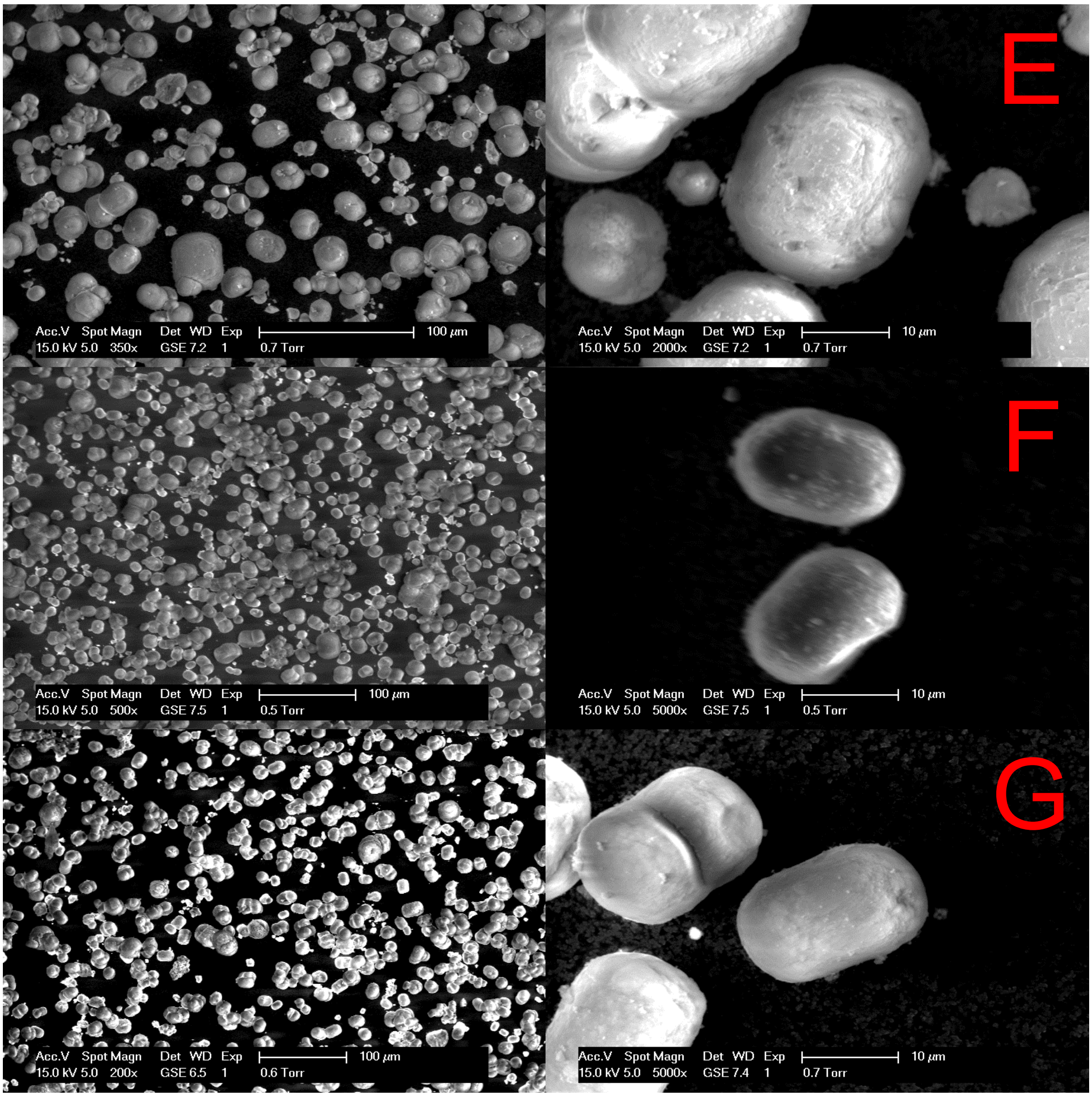
E
Acc.V Spot Magn Det WD Exp 100 µm
15.0 kV 5.0 350x GSE 7.2 1 0.7 Torr
Acc.V Spot Magn Det WD Exp 10 µm
15.0 kV 5.0 2000x GSE 7.2 1 0.7 Torr
F
Acc.V Spot Magn Det WD Exp 100 µm
15.0 kV 5.0 500x GSE 7.5 1 0.5 Torr
Acc.V Spot Magn Det WD Exp 10 µm
15.0 kV 5.0 5000x GSE 7.5 1 0.5 Torr
G
Acc.V Spot Magn Det WD Exp 100 µm
15.0 kV 5.0 200x GSE 6.5 1 0.6 Torr
Acc.V Spot Magn Det WD Exp 10 µm
15.0 kV 5.0 5000x GSE 7.4 1 0.7 Torr

Figure 50: SEM micrographs of A: 0.1/1 VTi, B: 1/1 VTi, C: 3/1 VTi, D: 6/1 VTi, E: 7.5/1 VTi, F: 9/1 VTi, and G: 12/1 VTi AlPO-5. Magnifications and scale bars are provided for each picture. Wide-field pictures are shown on the left, close-up pictures on the right.

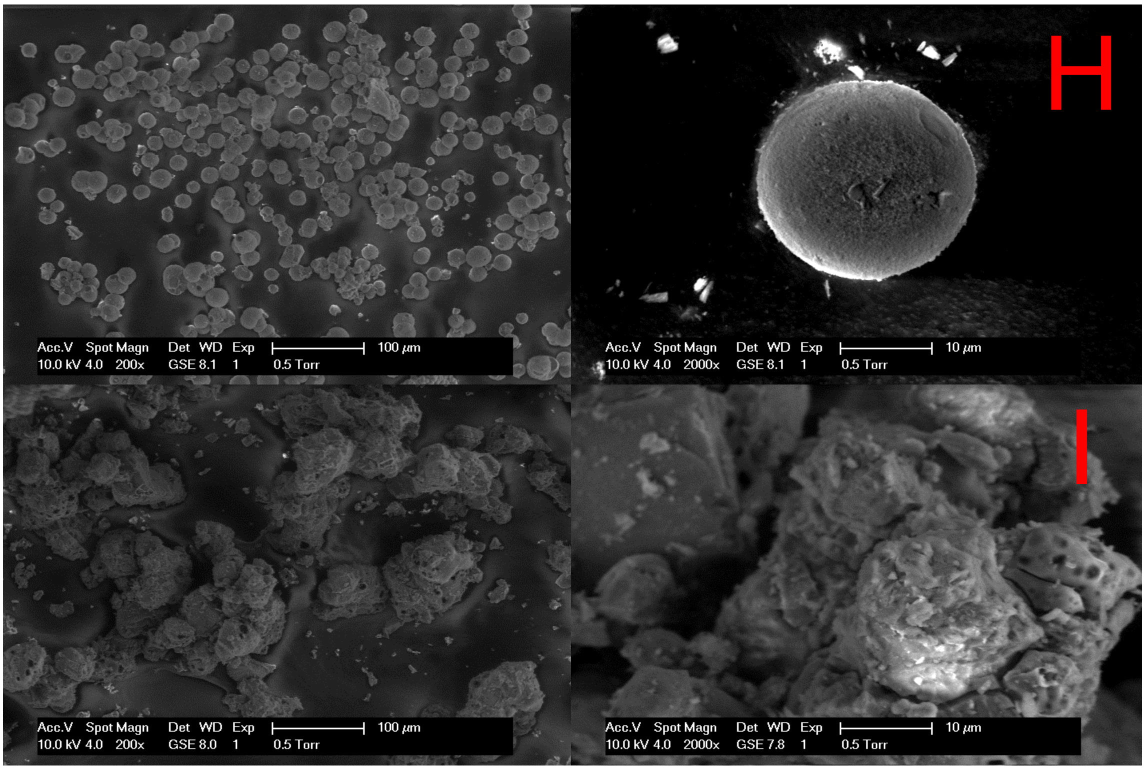
H
I
Acc.V Spot Magn Det WD Exp 100 μm
10.0 kV 4.0 200x GSE 8.1 1 0.5 Torr
Acc.V Spot Magn Det WD Exp 10 μm
10.0 kV 4.0 2000x GSE 8.1 1 0.5 Torr
Acc.V Spot Magn Det WD Exp 100 μm
10.0 kV 4.0 200x GSE 8.0 1 0.5 Torr
Acc.V Spot Magn Det WD Exp 10 μm
10.0 kV 4.0 2000x GSE 7.8 1 0.5 Torr

Figure 51: SEM micrographs of undoped AlPO-5 (H) and 50/1 VTi AlPO-5 (I). Magnifications and scale bars are provided for each picture. Wide-field pictures are shown on the left, close-up pictures on the right.

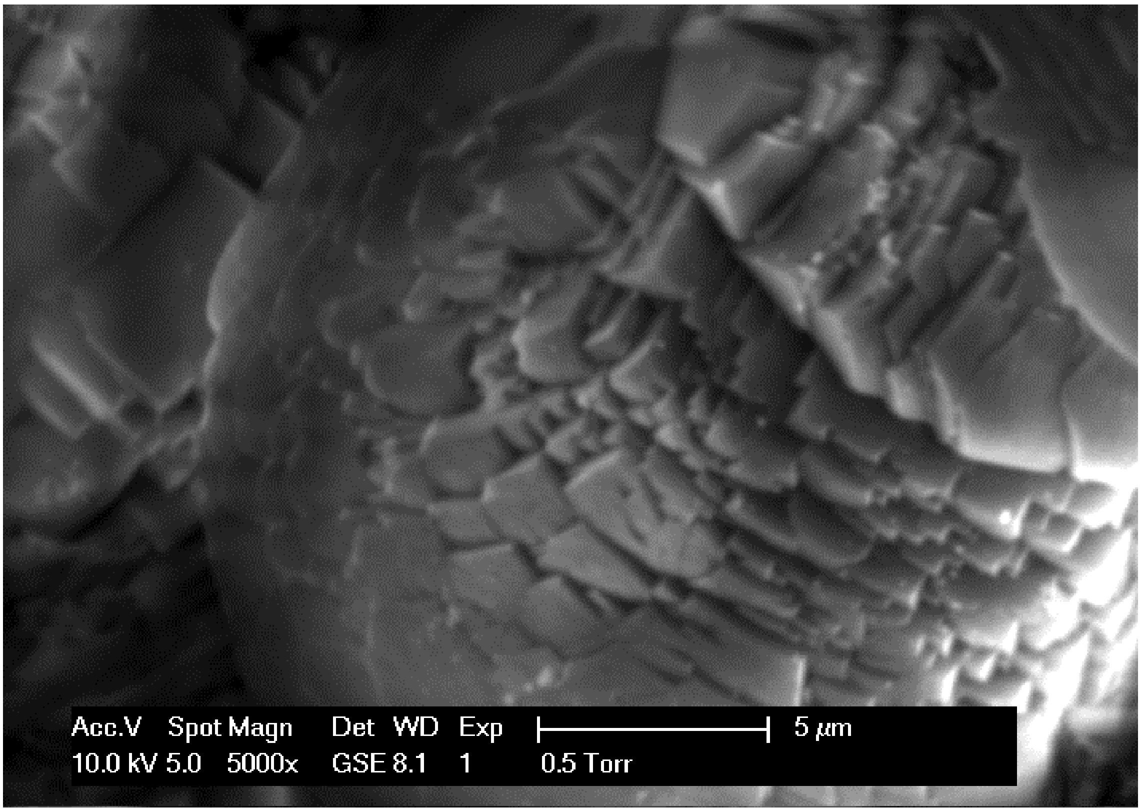
Acc.V Spot Magn Det WD Exp 5 μm
10.0 kV 5.0 5000x GSE 8.1 1 0.5 Torr

Figure 52: SEM close-up micrograph of 3/1 VTi AlPO-5, clearly showing the surface morphology of the sample. Staggered plaquettes of crystallites dot the surface of the catalyst particle.

Index	particle size (μm)	particle shape	crystallite size (nm)
1/1 VTi AlPO-5	10–30	spherical	43
3/1 VTi AlPO-5	10–30	spherical	43
6/1 VTi AlPO-5	10–30	spherical	52
7.5/1 VTi AlPO-5	10–30	slight barrel	60
9/1 VTi AlPO-5	10–30	barrel-shaped	60
12/1 VTi AlPO-5	10–30	barrel-shaped	44

Table 25: Summary of particle size ranges and shapes, determined by SEM, as well as crystallite size (determined by XRD using the Scherrer equation). All samples specified are calcined.

A series of catalysts with a fixed percentage of vanadium (6%) and an increasing amount of titanium was also synthesised and analysed by SEM. The resulting collection of micrographs is shown in Figure 53. As can be seen from these pictures, samples with a low-to-medium (0–6%) vanadium loading show the characteristic barrel-like shape associated with VAPO-5 at medium loadings of vanadium. However, at high loadings (9–12%) of vanadium, the sample morphology quickly degrades, especially at 12% V. These samples show much more irregular shapes of aggregates.

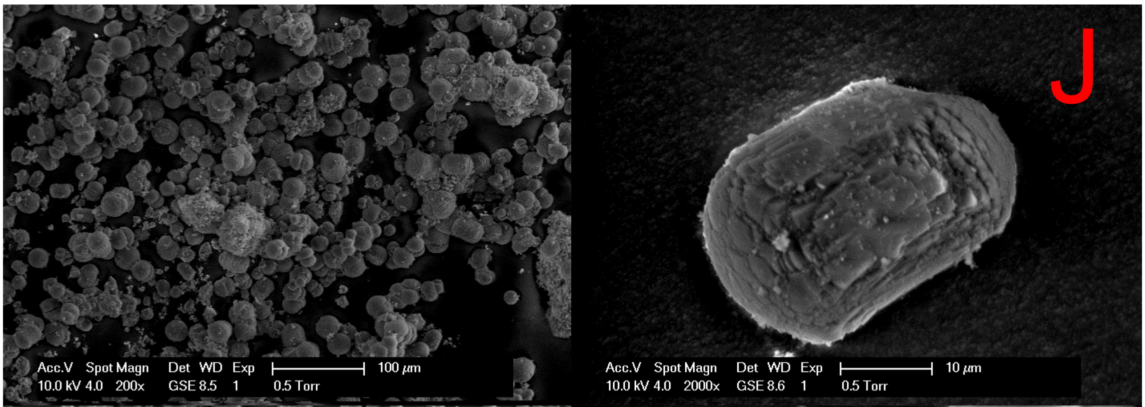
J
Acc.V Spot Magn Det WD Exp 100 µm
10.0 kV 4.0 200x GSE 8.5 1 0.5 Torr
Acc.V Spot Magn Det WD Exp 10 µm
10.0 kV 4.0 2000x GSE 8.6 1 0.5 Torr

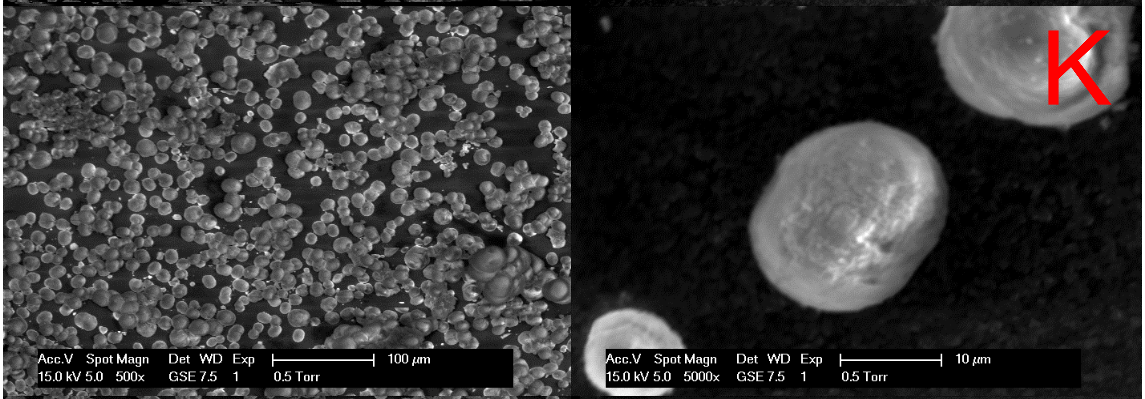
K
Acc.V Spot Magn Det WD Exp 100 µm
15.0 kV 5.0 500x GSE 7.5 1 0.5 Torr
Acc.V Spot Magn Det WD Exp 10 µm
15.0 kV 5.0 5000x GSE 7.5 1 0.5 Torr

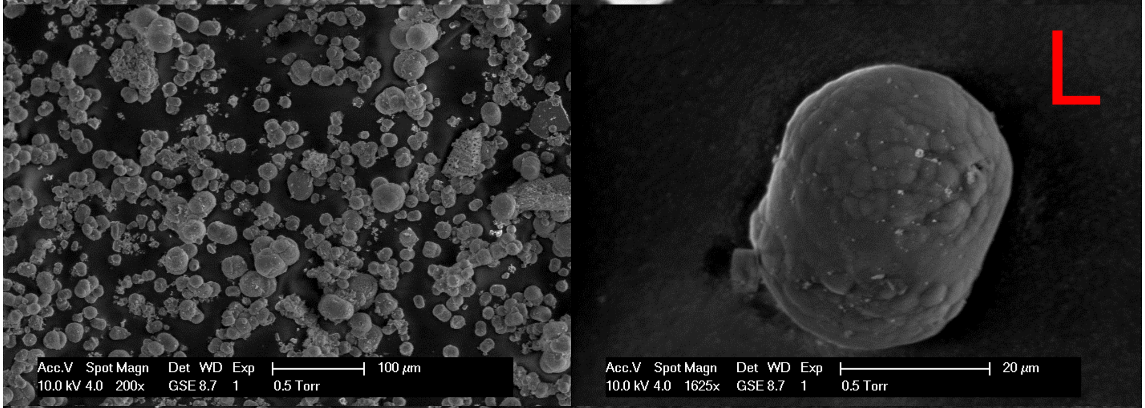
L
Acc.V Spot Magn Det WD Exp 100 µm
10.0 kV 4.0 200x GSE 8.7 1 0.5 Torr
Acc.V Spot Magn Det WD Exp 20 µm
10.0 kV 4.0 1625x GSE 8.7 1 0.5 Torr

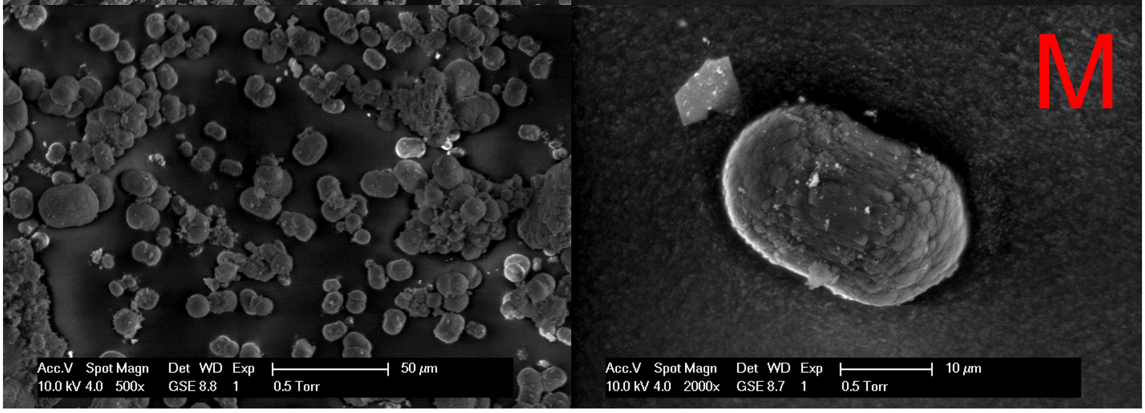
M
Acc.V Spot Magn Det WD Exp 50 µm
10.0 kV 4.0 500x GSE 8.8 1 0.5 Torr
Acc.V Spot Magn Det WD Exp 10 µm
10.0 kV 4.0 2000x GSE 8.7 1 0.5 Torr

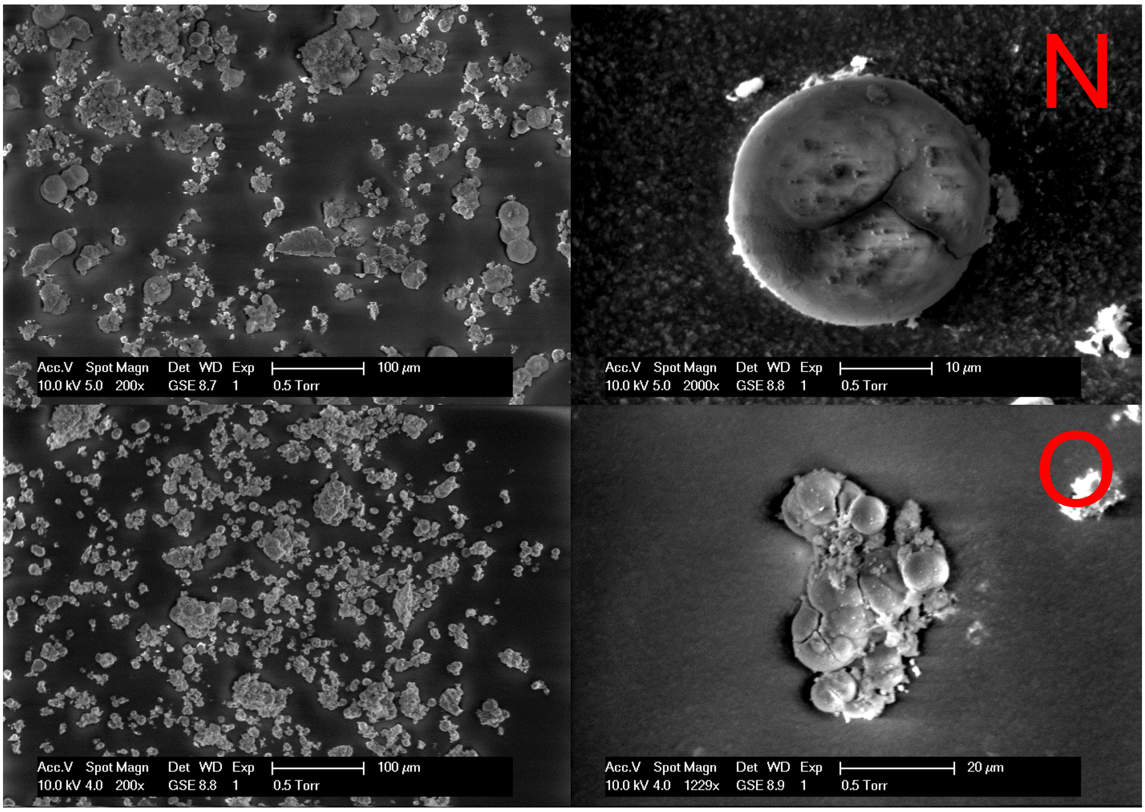
N
O
Acc.V Spot Magn Det WD Exp 100 µm
10.0 kV 5.0 200x GSE 8.7 1 0.5 Torr
Acc.V Spot Magn Det WD Exp 10 µm
10.0 kV 5.0 2000x GSE 8.8 1 0.5 Torr
Acc.V Spot Magn Det WD Exp 100 µm
10.0 kV 4.0 200x GSE 8.8 1 0.5 Torr
Acc.V Spot Magn Det WD Exp 20 µm
10.0 kV 4.0 1229x GSE 8.9 1 0.5 Torr

Figure 53: SEM micrographs of VTi AlPO-5 at different loadings of titanium. J: 6% V AlPO-5, K: 6/1 VTi, L: 6/3 VTi, M: 6/6 VTi, N: 6/9 VTi, O: 6/12 VTi AlPO-5. Magnifications and scale bars are provided for each picture. Wide-field pictures are shown on the left, close-up pictures on the right.

In addition, the series of titanium-replacing heterometal samples (high-metal VCo, VCr, VMn, and VNi AlPO-5) were also analysed. The results are shown in Figure 54. VCo, VMn, and VNi samples show the fairly selective formation of sharply-defined hexagonal rods, while VCr saw only the formation of ill-defined particles and aggregates.

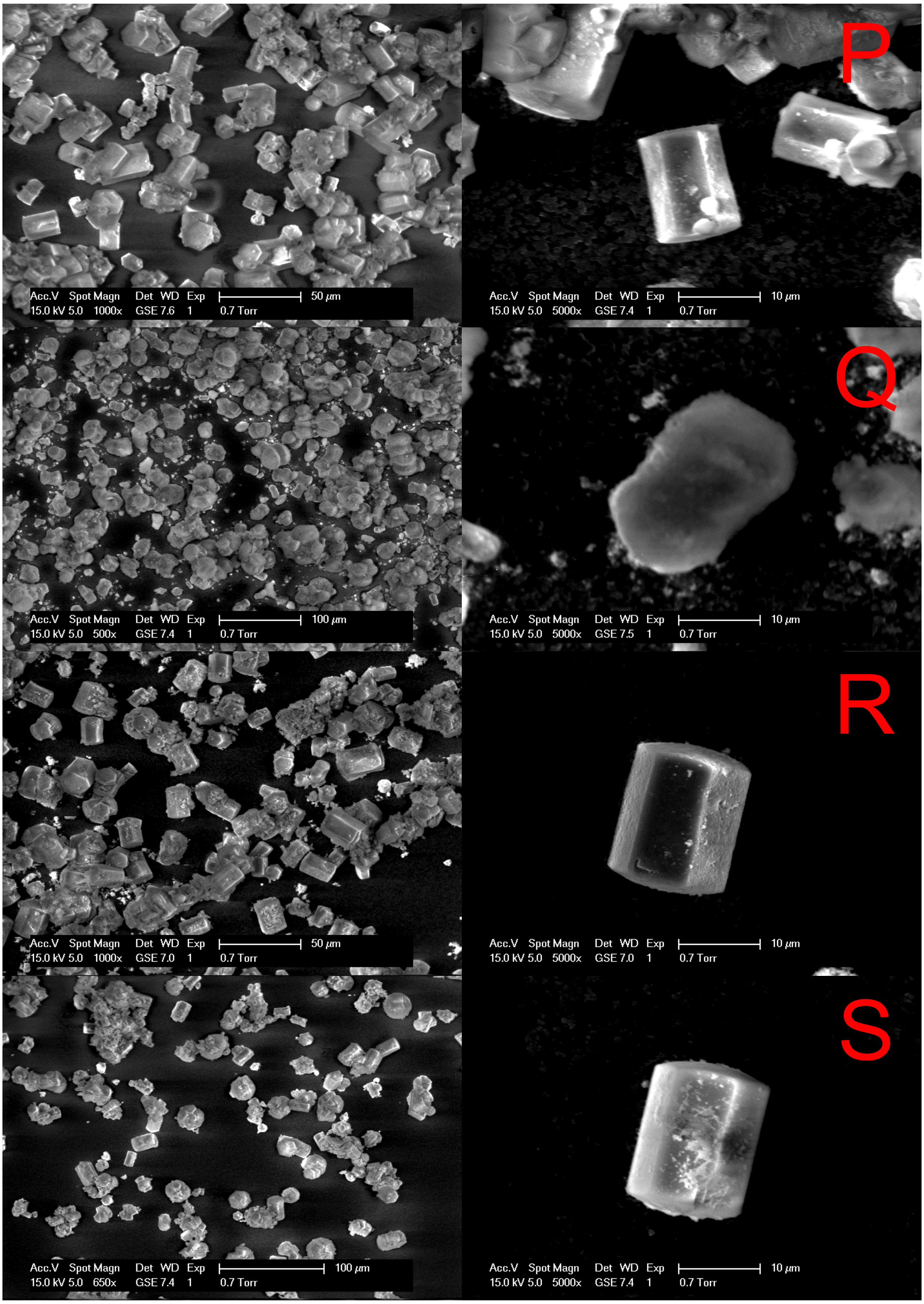
P
Acc.V Spot Magn Det WD Exp 50 µm
15.0 kV 5.0 1000x GSE 7.6 1 0.7 Torr
Acc.V Spot Magn Det WD Exp 10 µm
15.0 kV 5.0 5000x GSE 7.4 1 0.7 Torr
Q
Acc.V Spot Magn Det WD Exp 100 µm
15.0 kV 5.0 500x GSE 7.4 1 0.7 Torr
Acc.V Spot Magn Det WD Exp 10 µm
15.0 kV 5.0 5000x GSE 7.5 1 0.7 Torr
R
Acc.V Spot Magn Det WD Exp 50 µm
15.0 kV 5.0 1000x GSE 7.0 1 0.7 Torr
Acc.V Spot Magn Det WD Exp 10 µm
15.0 kV 5.0 5000x GSE 7.0 1 0.7 Torr
S
Acc.V Spot Magn Det WD Exp 100 µm
15.0 kV 5.0 650x GSE 7.4 1 0.7 Torr
Acc.V Spot Magn Det WD Exp 10 µm
15.0 kV 5.0 5000x GSE 7.4 1 0.7 Torr

Figure 54: SEM micrographs of heterometal AlPO-5 samples. P: VCo, Q: VCr, R: VMn, S: VNi AlPO-5. Both metals were present in 9% concentration in all samples. Magnifications and scale bars are provided for each picture. Wide-field pictures are shown on the left, close-up pictures on the right.

Finally, SEM pictures were taken of samples that were allowed to cool down overnight, instead of being quenched in ice, as was performed on most samples. The particles resulting from this cooling technique were overall much larger (30–100 µm, Figure 55) than the particles obtained by fast cooling; however, as shown by XRD, the actual crystallites are of comparable size to the ones obtained by fast cooling. Therefore, we are left to conclude that it is only the size of the aggregates that grows using this process. This might explain why the results obtained in the catalytic oxidation of propylbenzene are roughly similar between the two (see chapter 3).

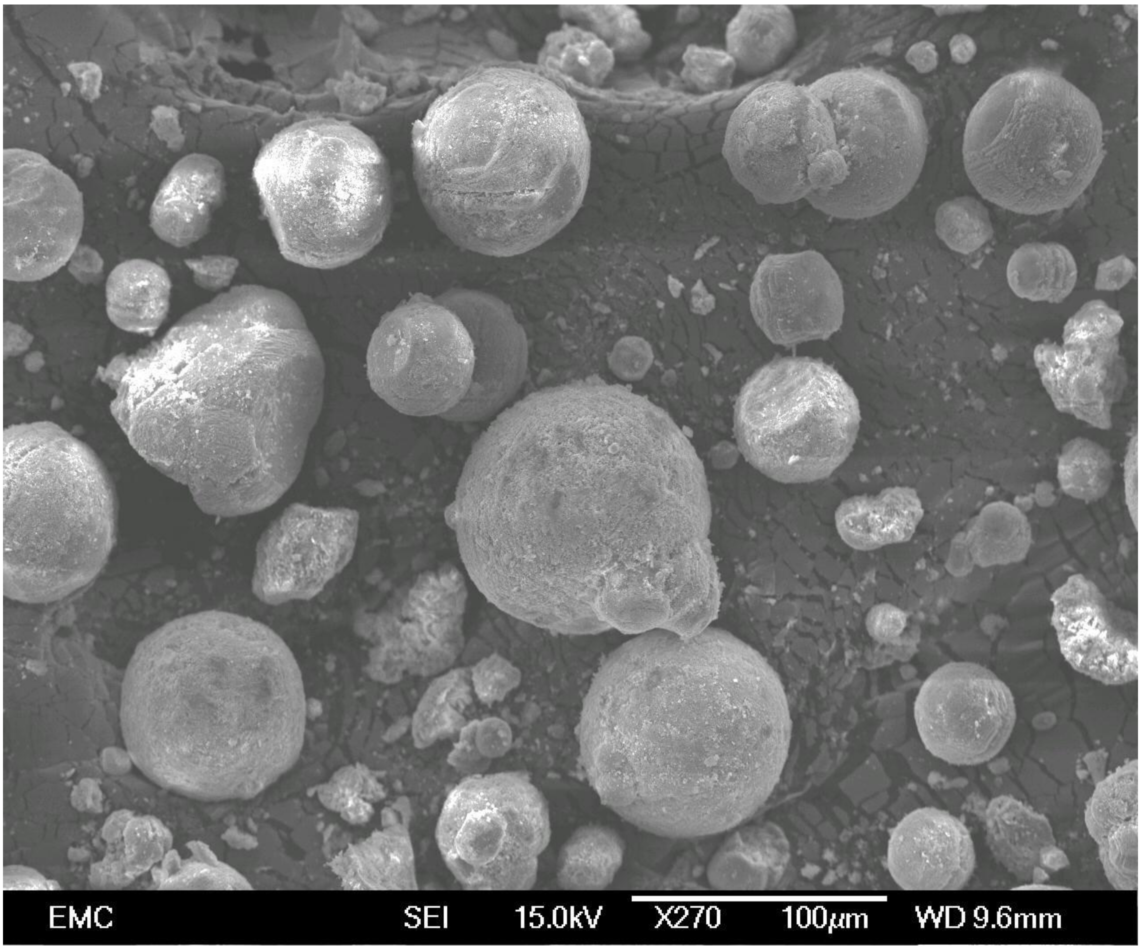

Figure 55: SEM micrograph of slow-cooled VTi AlPO-5. Note the considerably size increase of the particles compared to those obtained by quenching in ice.

Nitrogen adsorption techniques (see Section 2.3.2.3) were used to analyse surface area and pore characteristics of the material. Brunauer-Emmett-Teller (BET) surface analysis of the materials showed good matches with previous findings, showing high surface area (>300 m^2g^{-1}, typical of AlPO-5), a graph shape typical of porous materials, and a hysteresis loop.[159] The overall shape of the graph corresponds to that of a Type IV adsorption isotherm (see Section

2.3.2.3), indicating the presence of mesopores alongside the micropores that are inherent in the AFI framework.

No mesopores are present in the AFI framework. However, the hysteresis we observed may be explained by the combination of XRD and SEM results, which indicate that the material is made up of aggregates of small crystallites. It is possible, then, that the hysteresis is caused by the interparticulate space between the microporous crystallites. If these spaces were of a size on the order of magnitude of mesopores, this would explain the analytical results. A schematic representation of this is shown in Figure 56.

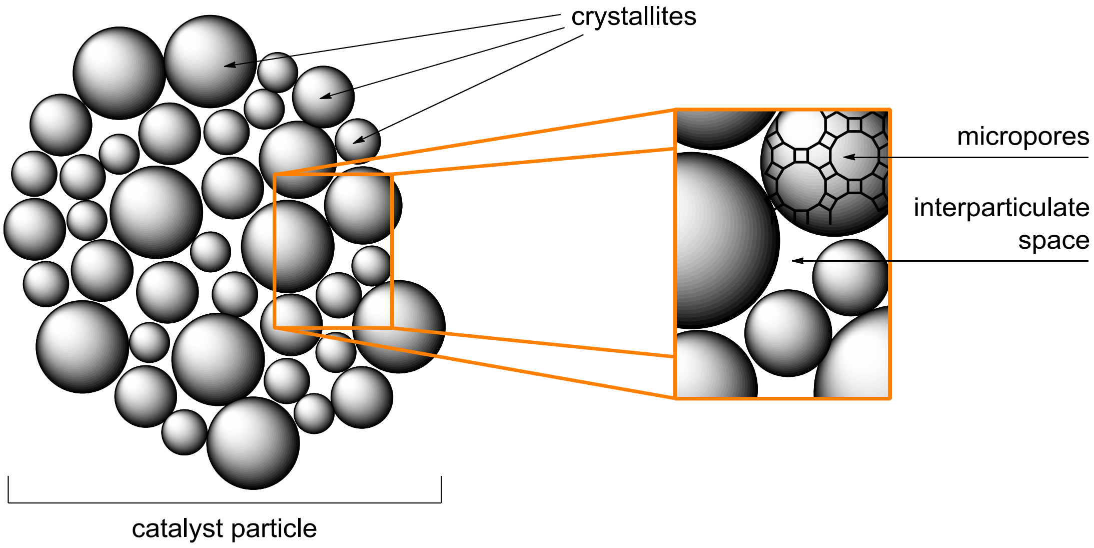

Figure 56: Schematic representation of crystallite aggregates and the origin of inter-crystallite space-derived mesoporosity.

A series of VTi AlPO-5 samples were prepared at varying levels of vanadium to probe the system for changes in surface area and micropore volume, including an undoped sample of AlPO-5 for comparing properties to our VTi AlPO-5 catalyst series. The results are summarised in Figure 57. As can be clearly seen, the surface area and micropore volume are fairly constant at low loadings and comparable to the sample of undoped AlPO-5. However, above 6% V, the sample starts to experience a drop-off of both values, which becomes fairly dramatic at 12%. The experimental 50/1 VTi AlPO-5 sample prepared at the theoretical maximum value of 50% V shows almost no surface area (2.5 m^2g^{-1}) and no micropore volume at all (value not shown in graph below). The decreasing values of both would suggest that at higher metal loadings, impurities and/or extraframework species begin to develop. This would be consistent with previous reports on VAPO-5 that at higher metal loadings, poly- or oligomeric vanadium oxide species such as V_2O_5 and dense aluminium phosphate phases begin to form.[108] As nitrogen adsorption techniques are highly sensitive to the presence of such species, these results are a strong indication that such species might well be present, even if only in small quantities.

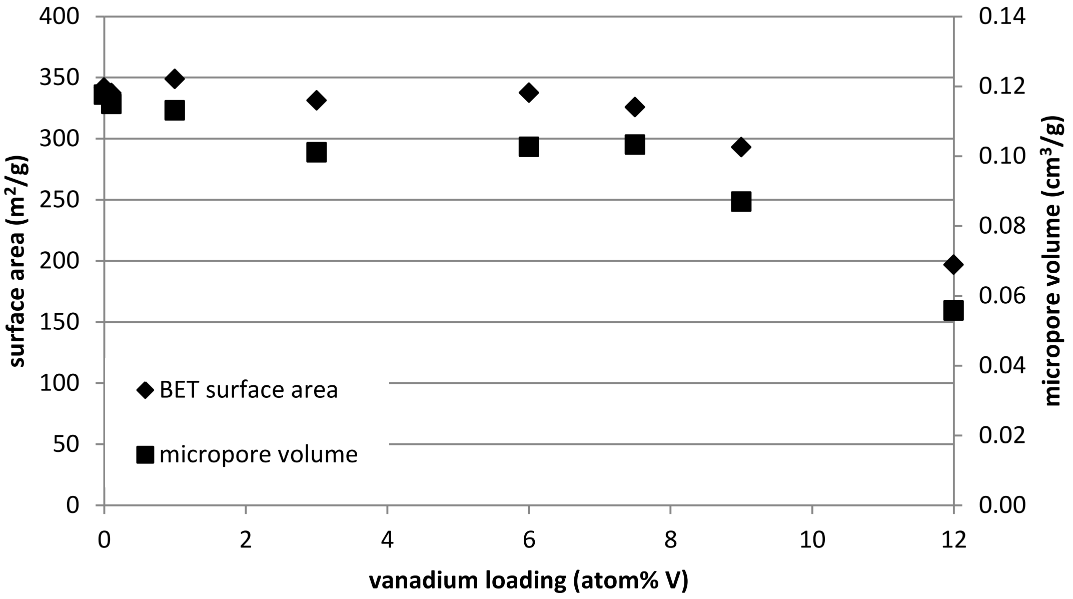

Figure 57: BET analysis results of VTi AlPO-5 at various different levels of V (fixed at 1% Ti), including completely undoped AlPO-5 (shown as 0% V). Diamonds: BET surface area. Squares: micropore volume.

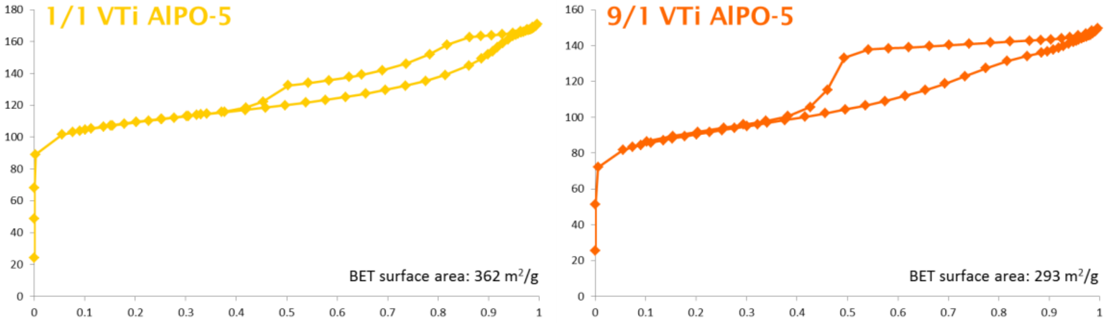

Figure 58: BET isotherms for 1/1 VTi AlPO-5 (left, yellow) and 9/1 VTi AlPO-5 (right, orange). Displayed are volume of N_2 adsorbed (cc/STP, y-axis) versus relative pressure (x-axis).

Another interesting trend is that the shapes of the hysteresis loops present in the samples change depending on the vanadium loading of the sample. At lower loadings, the hysteresis loop is closer and more parallel to the adsorption line, while at high loadings, it moves further away, and becomes more orthogonal (Figure 58). This indicates a change in the type of mesoporosity (in our case; interparticular cavities) of the material.

The graphs at low loading are comparable to a type H1 hysteresis loop as proposed by Wang *et al.,*[265] (see Section 2.3.2.3) while the high-vanadium samples show a type of hysteresis closer to H2 (Figure 59). The first has been reported to be typical of system with relatively well-aligned particles with a small pore size distribution, while the latter has been associated with a wider range of (meso-)pore sizes. This would indicate less efficient alignment or stacking. This could indicate that the crystallites aggregate in a more regular manner in low-loading vanadium samples than in high-loading ones.

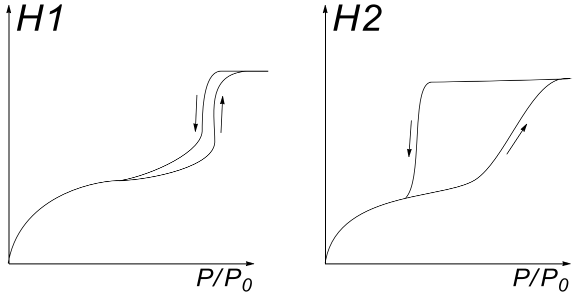

Figure 59: Type H1 and H2 hysteresis loops as proposed by Wang et al.[265] *Both cases are an exaggerated representation for schematic purposes.*

In addition, one of the fundamental properties of these materials is the amount of metal contained in the sample. As the catalysis in this work is based around the inclusion of metal ions, a sample which, after synthesis, turns out to contain no metals, is meaningless. Moreover, several of our studies are based around trends involving the amount of metals present. Therefore, measuring the true metal content of the samples is crucial. Hence, to ascertain our methodology results in the inclusion of metal in the sample, and exactly how much, elemental analyses of the samples were performed.

A prominent technique for identifying and quantifying elements in a sample is ICP-OES (see Section 2.3.2.4). This technique is extremely accurate and sensitive, with a detection limit of 1 ppb, and with effectively no upper detection limit as calibrations can be performed at any concentration necessary. Samples of various vanadium loadings (at a set 1% level of titanium) were analysed using this technique, calibrated, and tabulated; then compared against the expected, theoretical values. The results are shown in Figure 60.

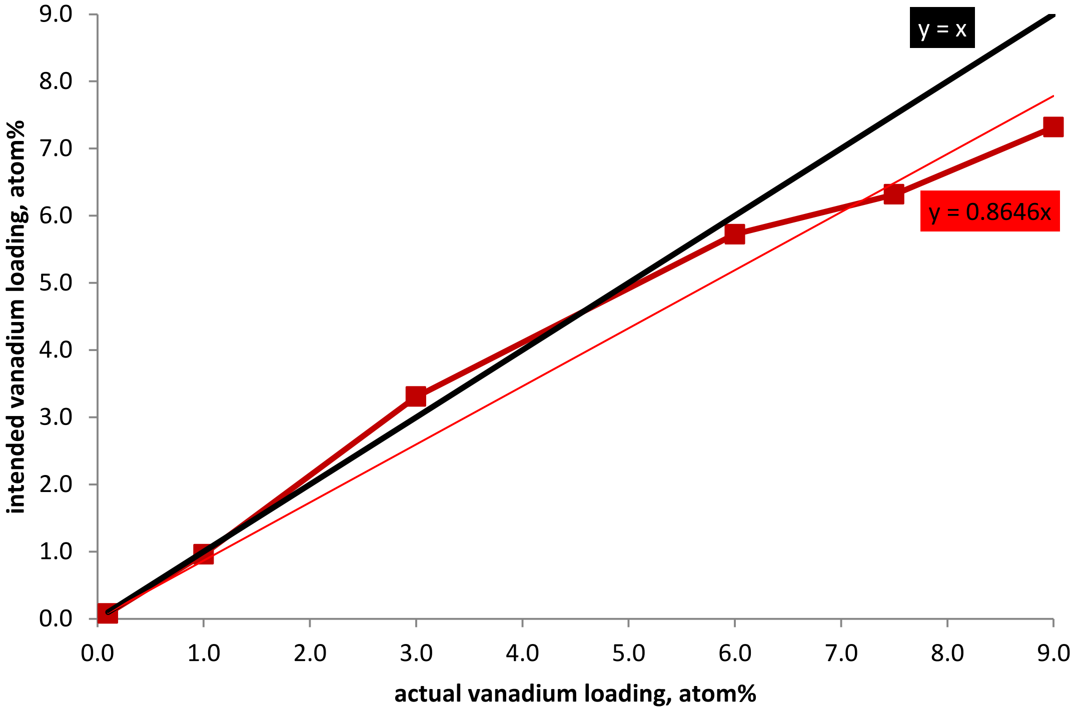

Figure 60: Elemental analysis results as measured by ICP-OES. Dark red; vanadium loadings measured versus expected values. At higher loadings, the incorporated metal drops below the expected amount, indicating incomplete incorporation. In bright red is a trendline between the extreme points showing a ca. *86.5% incorporation trend. The black line is a 100% line.*

As can be clearly seen from the results, at lower loadings, the amount of metal in the samples is fairly consistent with the intended metal counts at low-to-medium values. However, at high metal loadings (7.5% and higher — the last two data points), the incorporation starts to drop significantly below the intended line, showing a gradually decreasing degree of incorporation. A linear trendline, shown in bright red in the graph above, shows an average of 86.5% vanadium incorporated into the sample.

These findings are consistent with trends observed *in situ* after synthesis of the catalysts. The precursor vanadium compound, $VOSO_4$, is a bright blue salt that gives similarly bright blue solutions when dissolved in water. After the hydrothermal synthesis step, gradually more strongly coloured mother liquors were observed during filtration as the amount of metal precursor increased. As this colour is obviously derived from vanadium in solution, and therefore not incorporated into the material, this observation would seem to corroborate these findings.

An alternative method for elemental analysis is EDX (see Section 2.3.2.5), a method often coupled with SEM, as they operate under the same conditions. Unlike ICP-OES, which is a bulk technique in which the average of the entire sample is measured at once, EDX allows one to locally probe the same in a specific area and perform elemental analysis of only that part of the sample. As SEM allows one to examine a sample locally, the partnership with EDX is a natural one. An example of the type of multipoint analysis performed is shown below in Figure 61.

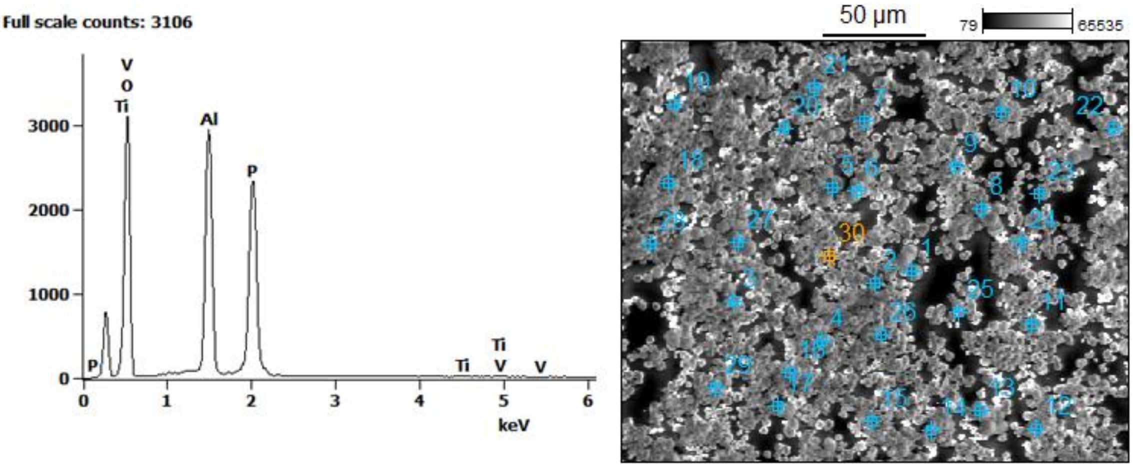

Figure 61: Example EDX spectrum of VTi AlPO-5 (1% V, 1% Ti), showing sample morphology and measurement points (indicated by crosshairs).

During SEM analyses, EDX analysis was performed on 30 points of varying topology within each sample, and subsequently averaged to obtain a single value. Although this analysis allows us to find topological analysis information about the sample, the accuracy of EDX is considerably less than that of ICP-OES. This is particularly true for non-homogeneous samples, powdered samples and oxides (due to the poor spectral resolution of EDX, peak overlap (especially with oxygen), and varying sample thickness and angles). Unfortunately, our samples qualify for all of these factors. The detection limit is also higher at *ca.* 0.1%. Furthermore, the low loading of the metals makes analysis of the metal levels harder. As such, it should be noted that while informative, the accuracy of these measurements cannot approach those of the analyses by ICP-OES.

Regardless, useful data could be obtained from these scans. For low-loading samples like 3/1 VTi AlPO-5, the vanadium count was fairly consistent between particles of various shapes and sizes, with the lowest recorded 1.4% and the highest 3.3%. At high loadings, such as 12% V, the vanadium distribution is much more heterogeneous, ranging from 4.3% to 18.4%. Although no particles were found that appear to consist solely of V_2O_5 or similar dense vanadium oxide species, it is very possible that some particles are more enriched in it than others, or carry deposits of it. In addition, no particles were found that consist solely of aluminium and/or phosphorus at any loading of vanadium, suggesting that no “dead” particles are formed during synthesis and that the vanadium is dispersed throughout the entire sample. The exception is the 0.1% V sample, which is measured at the detection limit of the instrument; as such, in this case, a fairly high amount of data points were found that appeared to contain no vanadium at all.

In all cases, the average vanadium count was considerably lower than that found using ICP-OES analysis, and therefore, a much lower trendline was found (Figure 62). This can be explained by the aforementioned limitations of using EDX, especially for these types of samples. Nonetheless, a similar trend was found; at high metal loadings, the metal count increases at a considerably lower rate, corroborating our ICP-OES data.

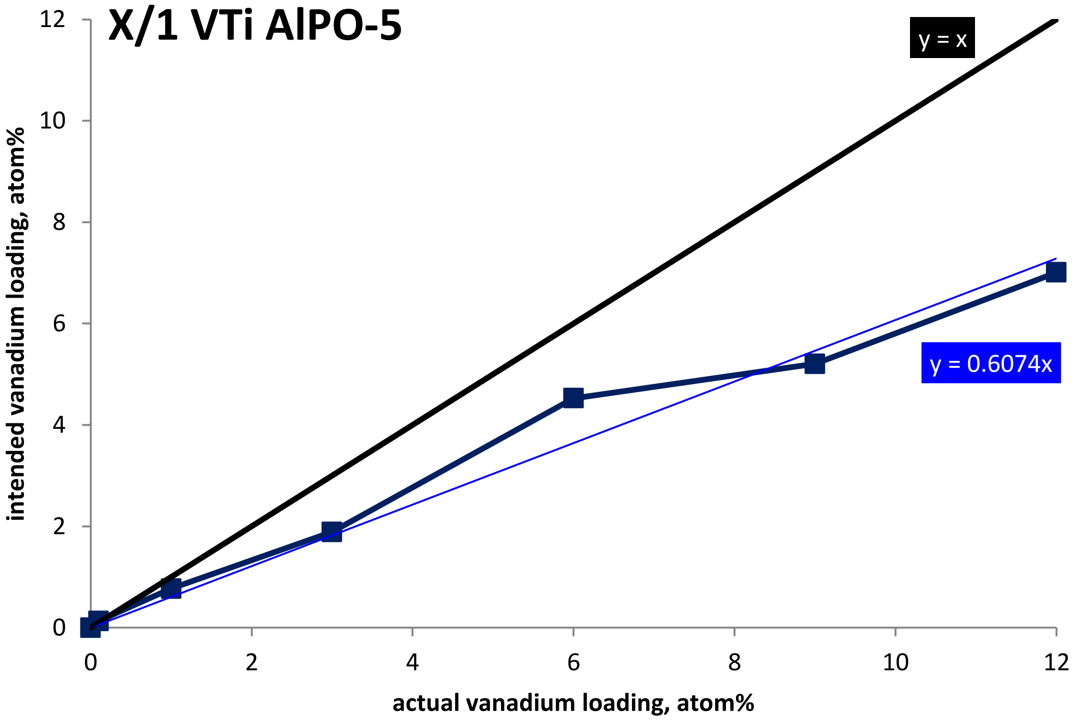

Figure 62: EDX analysis of VTi AlPO-5 at a static 1% of titanium and a varying amount of vanadium (X/1 VTi AlPO-5). Dark blue; vanadium loadings measured versus expected values. At higher loadings, the incorporated metal drops below the expected amount, indicating incomplete incorporation. In bright blue is a trendline between the extreme points showing a ca. 60.7% incorporation trend. The black line is a 100% line.

The incorporation of various amounts of titanium and a static (6%) amount of vanadium was also measured using EDX. Similar to vanadium, these samples showed a drop-off, but in the case of titanium, the drop-off was much more pronounced than that seen with vanadium. Up to 3% titanium, the incorporation is quite consistent with the values intended (Figure 63), but above this, a quite slow titanium count increase is observed. Moreover, at high titanium loadings, particles with very high amounts of titanium (25-30%) are observed, suggesting the presence of particles that consist chiefly or even almost entirely of titania (TiO_2).

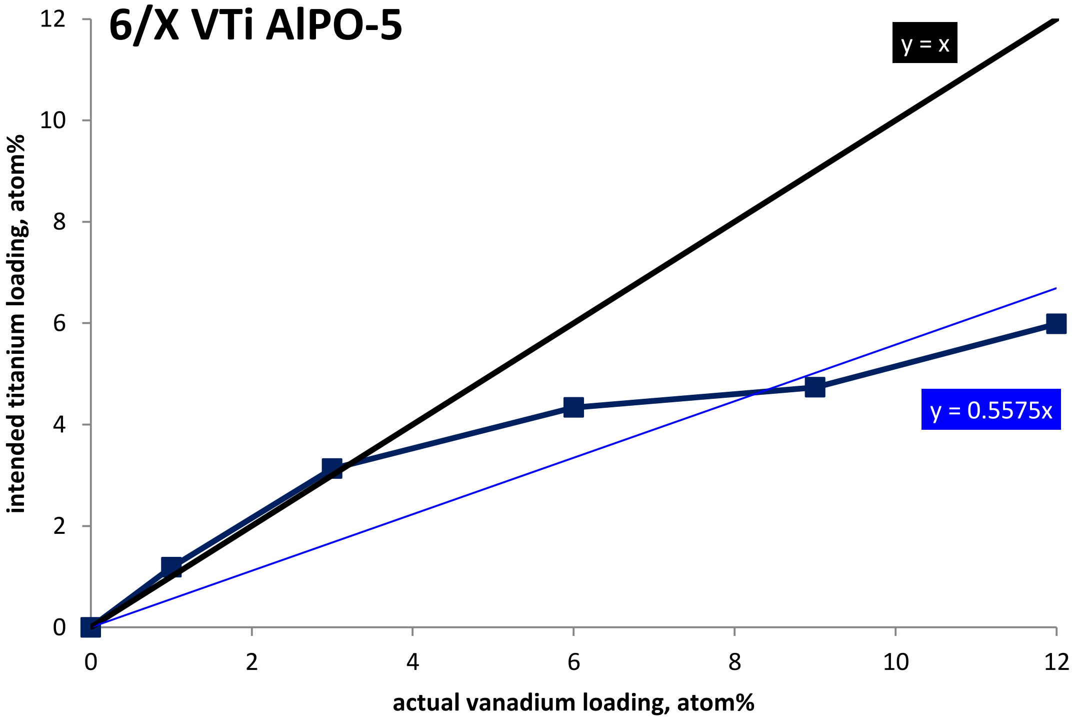

Figure 63: EDX analysis of VTi AlPO-5 at a static 6% of vanadium and a varying amount of titanium (6/1 VTi AlPO-5). Dark blue; titanium loadings measured versus expected values. At higher loadings, the incorporated metal drops below the expected amount, indicating incomplete incorporation. In bright blue is a trendline between the extreme points showing a ca. *55.7% incorporation trend. The black line is a 100% line.*

5.2 Spectroscopic analysis

Apart from establishing information about the physical properties of the materials themselves, a considerable amount of work was put into attempts to elucidate information about the precise nature of the catalytic ions in the framework. Moreover, although ICP-OES and EDX afford information about the metal content in the sample, these methods cannot establish unambiguously whether the metals are genuinely incorporated into the framework. In order to establish both, we employed a variety of spectroscopic techniques which allowed investigation of the chemical and electronic environment of the metal ions, including whether they were successfully incorporated into the AlPO-5 matrix.

Electron paramagnetic resonance (EPR) spectroscopy is a very powerful tool that can afford us valuable information in several ways. Analogous to nuclear magnetic resonance, EPR is essentially the electron-based version of NMR. Through manipulation of the electrons, information about their parent nuclei can be deduced.

All as-synthesised samples show a strong vanadium signal. Simulations using EasySpin (a MatLab-based EPR simulation software package) conform closely to the measured signal (Figure 64) and reveal a species with rhombic symmetry. Effective *g*-factors and hyperfine coupling constants with accompanying margins of error have been determined to be:

$g_1 = 1.978 \pm 0.001$ $g_2 = 1.973 \pm 0.001$ $g_3 = 1.930 \pm 0.001$

$A_1 = 212 \pm 5$ $A_2 = 186 \pm 5$ $A_3 = 540 \pm 1$

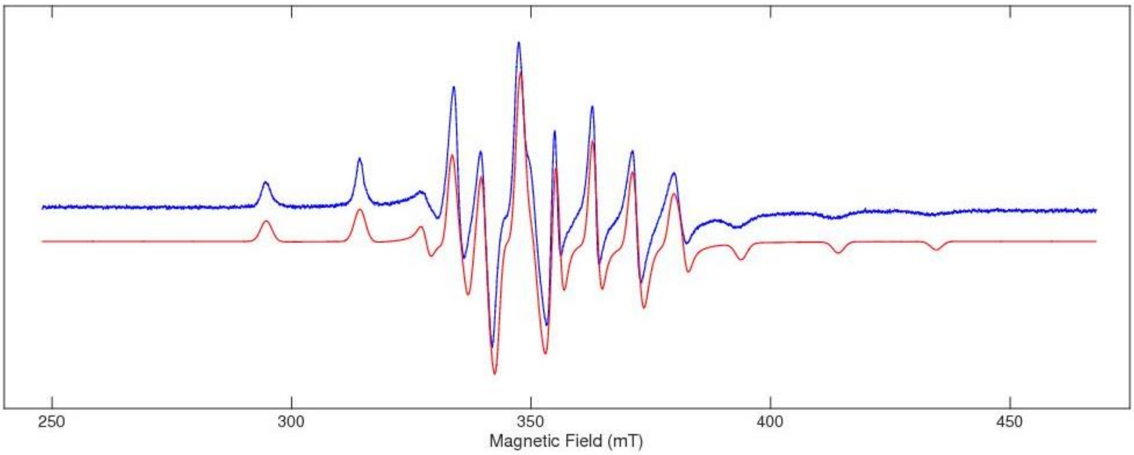

Figure 64: Simulated (red) versus experimental (blue) CW EPR spectrum of 1/1 VTi AlPO-5, as-synthesised.

The obtained values conform closely to those reported in the literature as being characteristic of a vanadyl ($V{=}O^{2+}$) species in a square-pyramidal or tetrahedrally-distorted octahedral coordination geometry.[107,108,111,124,173,183,266] A more detailed description has been proposed as a C_{4v} site symmetry with four V–O bonds in the equatorial plane and one axial V=O bond. A sixth ligand may lie opposite this bond in the –z axis.[111] The parameters obtained are incompatible with simple, non-vanadyl V^{4+} species, as EPR can distinguish between VO^{2+} and V^{4+} sites — this indicates with certainty that the species observed is a genuine vanadyl ion.[173]

The hyperfine signal shows an eight-fold splitting of all anisotropic components, caused by the interaction of the unpaired $3d^1$ electron with the nucleus. The major isotope of vanadium (^{51}V, natural abundance ≈ 99.8%) constitutes the entirety of the signal and its nuclear moment of $I = {}^7/_2$ causes the observed 8-peak ($2n + 1 = 8$) pattern, several of which overlap. The outermost splitting peaks have been assigned to parallel components, with the perpendicular ones being less well-resolved, weaker and located in the centre of the spectrum.[111]

Although some sources report an axial symmetry instead of a rhombic one, it has been reported that in VAPO-5, the parallel components consist of two nearly identical signals that are not sufficiently resolved to determine A and g values, leading authors to formulate only parallel and perpendicular ones. The two species have been attributed to identical vanadyl species as described above, except with and without the coordination of water ligands.[111,172] Another explanation for this phenomenon has been proposed by Montes & David who suggested the two species are derived from the occupation of two different crystallographic sites;[104] however, this seems highly unlikely as all T-sites in AlPO-5 are crystallographically identical, meaning no such distinction could occur.

The hyperfine structure of the separate signals themselves however is highly resolved, even though the spectra were recorded at room temperature instead of -77 or -196 °C. This is indicative of highly dispersed species, meaning that the vanadium is present as isolated, single sites.[107,108,111,124,172,173,183,267] This observation is crucial as it provides direct evidence for the incorporation of vanadium into the framework, as failure to do so would have inevitably led to clustering of the vanadium species and concomitant loss of hyperfine signal structure through line-broadening due to V–V interactions. This proves two things; first, that the synthesis of vanadium-modified AlPO-5 was successful, second; that the site-isolation that was deemed to be of supreme importance to high catalytic activity and selectivity (see chapter 1) had been achieved.

Furthermore, in order to back up the trends we observed during catalysis with spectroscopic evidence on the nature of the vanadium sites when varying amounts of metals are employed, a series of X/1 VTi AlPO-5 samples was subjected to EPR analysis. A collection of overlaid spectra of VTi AlPO-5 at varying loadings of vanadium is shown in Figure 65.

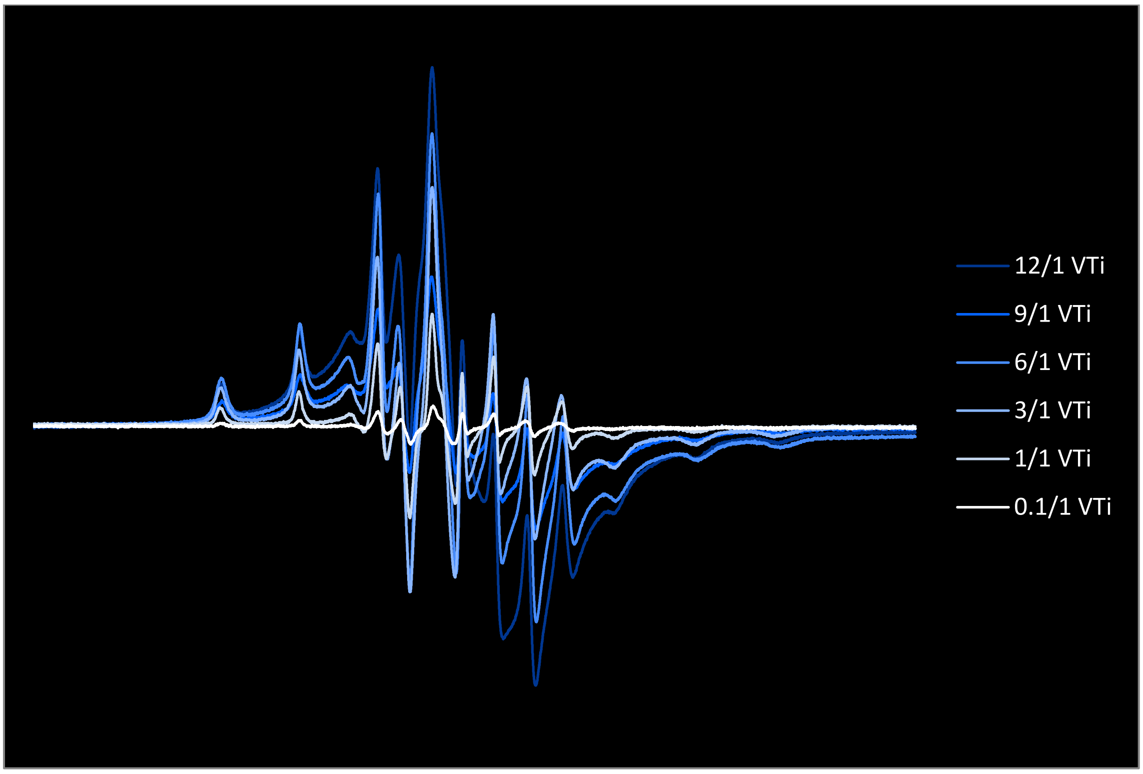

Figure 65: Overlaid spectra of VTi AlPO-5 at varying levels of vanadium. Lighter colours indicate lower loadings of vanadium.

From these spectra, it is apparent that at lower loadings of vanadium, the signal becomes less intense, as one would expect. However, upon closer inspection, it becomes clear that at high loadings of vanadium (≥9% V), the signal is overlaid with a broad singlet. This sort of signal would be expected for vanadium species that show V–V interactions, such as oligo- and polymeric vanadium oxide species; in other words, this trend suggests that the higher the vanadium loading of the synthesis gel, the more extraframework impurities are formed during synthesis. This directly corroborates our BET analysis results which show a drop-off of surface area at these high loadings, as well as our catalytic results, which show diminishing improvements upon the addition of more metal to the sample. Moreover, in conjunction with the ICP/EDX elemental analysis results, the EPR spectra strongly suggest that while able to cope with low-to-medium amounts of metal, the framework struggles to uptake vanadium at high levels. The excess metal is either washed away after synthesis during filtration (resulting in a blue supernatant as described above) or results in extraframework impurities (as described here).

Upon calcination, the signal intensity decreases dramatically (Figure 66). This indicates successful oxidation of the vast majority of the framework V^{4+} ions to the catalytically active V^{5+},[101,104,172,174] which, being a $3d^0$ species, is EPR silent. The V^{4+} that remains is still present as isolated single sites, and shows the same pattern as the uncalcined sample, indicating that the ions are still present in the same oxidation state and coordination geometry.[104,172,174]

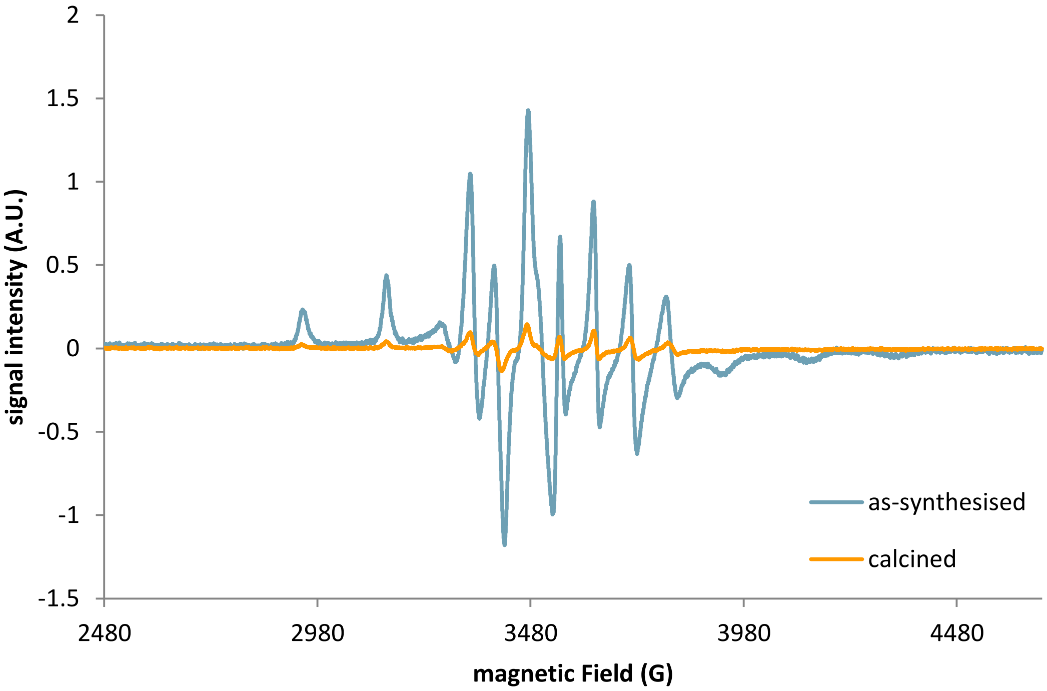

Figure 66: EPR spectra, overlaid, of 1/1 VTi AlPO-5, as-synthesised (blue), and calcined (orange). The two signals are measured to the same scale. Note the dramatic decrease in signal intensity of the calcined sample, indicating oxidation of V^{4+} to V^{5+}.

EPR analysis of the calcined materials was also performed at varying levels of vanadium, to elucidate further trends. The results are shown in Figure 67. Note that the spectra use the same intensity scale as Figure 66 and are therefore directly comparable. When normalised to the same scale, the calcined and uncalcined spectra look virtually indistinguishable, apart from the much noisier baseline.

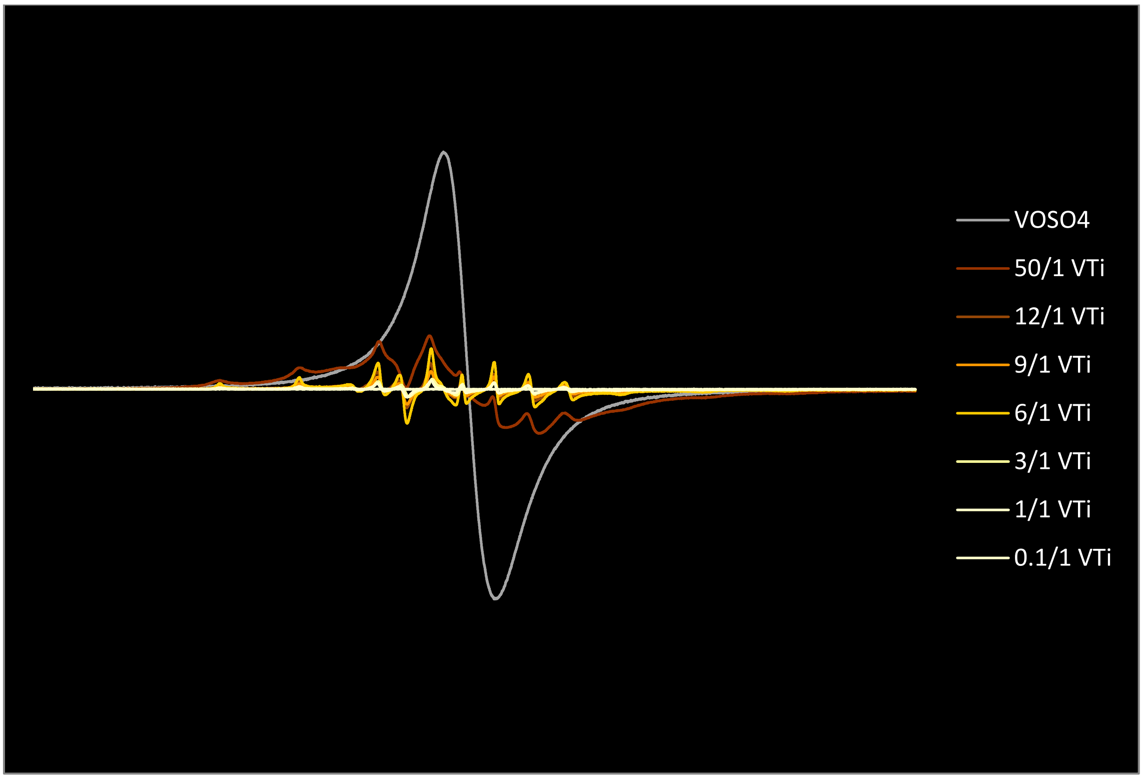

Figure 67: Overlaid spectra of VTi AlPO-5 at varying levels of vanadium. Lighter colours indicate lower loadings of vanadium. In grey: vanadyl sulfate ($VOSO_4$).

Although the intensities of the calcined spectra are vastly lower than those of their as-synthesised counterparts, the same trend is still visible; at higher amounts of vanadium, a stronger signal is present, and a broad singlet overlaps the main signal, although this is only sparingly visible without artificially increasing the spectrum intensity. However, an extreme-vanadium sample (50/1 VTi), which had already been determined to contain no AFI phase, very low surface area and no discernible ordered shape, was also measured, and shows the overlaid singlet to a much stronger degree. To illustrate this concept, a spectrum of vanadyl sulfate ($VOSO_4$) was also measured and included in the spectrum. $VOSO_4$, as a non-dispersed species, exhibits V–V interaction in the sample, and therefore appears as a broad singlet signal with no hyperfine structure.

It should be noted that although the EPR results suggest that impurities are present in the high-V samples, no trace of crystalline V-oxide or similar impurities was found in any of the XRD spectra of the materials. This would suggest that these species are present as very minute particles too small or amorphous to be detected by a long-range sensitive technique such as X-ray diffraction.

Concluding, EPR shows that the vanadium is successfully incorporated into the framework and is present as single, isolated sites. The species present in the as-synthesised material is a $V=O^{2+}$ species with square pyramidal or tetrahedrally distorted octahedral coordination geometry. Two slightly different species, assumed to be identical apart from the coordination of water, are present, both of which are oxidised to V^{5+} upon calcination, with the $V=O^{2+}$ that remains still present as isolated, single sites. At high V loadings, extraframework impurities start to appear.

While extremely valuable in elucidating information about the species of vanadium present in the as-synthesised material, EPR has limitations as well, as it cannot detect the V^{5+} species present after calcination, nor the species of titanium in the material, which was expected to be present as Ti^{4+} ions. Like V^{5+}, Ti^{4+} is a $3d^0$ species, and therefore EPR silent. To bolster the EPR findings, UV-Vis diffuse reflectance spectroscopy (DRS) was explored, as this method is not limited to unpaired-electron entities like EPR. UV-Vis DRS is another very powerful tool as it allows one to elucidate information from a wide variety of species, and is highly sensitive to the ligand environments and coordination numbers of metal centres.[111,174] This allows precise information about the nature of the metal centres under investigation as well as the type of coordination present. A summary of the UV-Vis DRS results is shown in Figure 68.

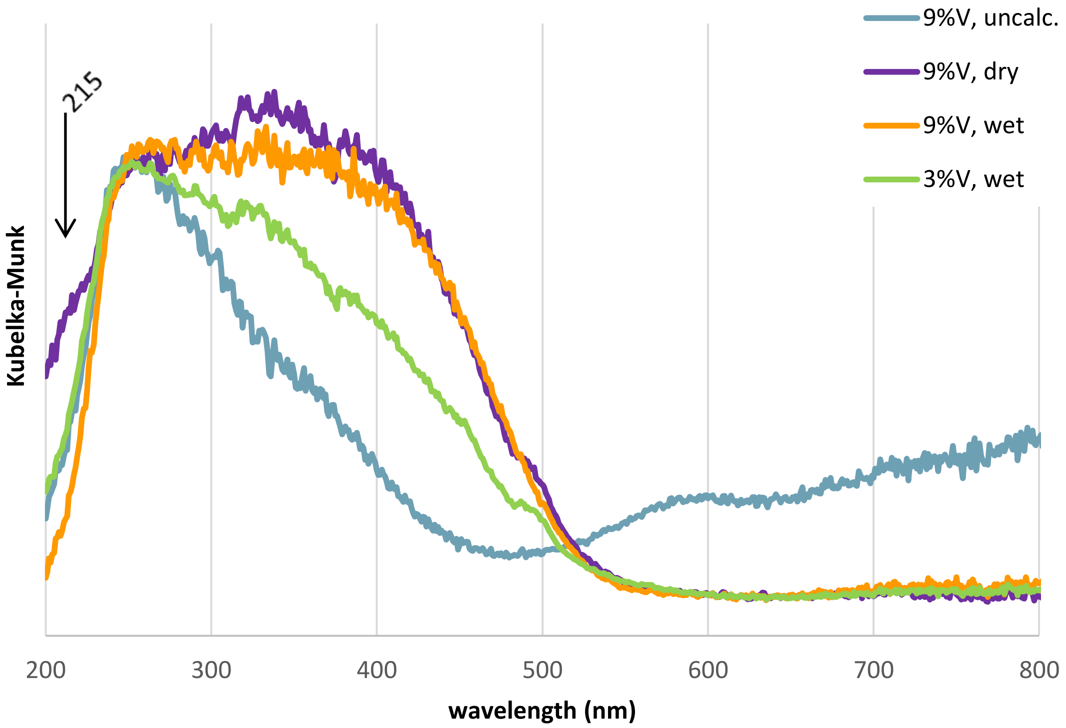

Figure 68: Overlaid UV-Vis DRS spectra of VTi AlPO-5. Blue: 9/1 VTi AlPO-5, as-synthesised. Purple: 9/1 VTi AlPO-5, freshly calcined. Orange: 9/1 VTi AlPO-5, calcined but air-exposed. Green: 3/1 VTi AlPO-5, calcined but air-exposed. For viewing convenience, the spectra are normalised to the same intensity. The arrow indicates position v = 215 nm.

Samples of the calcined material show a very strong, broad band between 500 and 250 nm, corroborating the deep orange-yellow colour of the powders. The signal is strong enough that when undiluted the detector becomes massively over-saturated, so all spectra were recorded as 5% dilutions in $BaSO_4$. The main band is made up of several signals. The maximum, which is centred around *ca.* 250 nm, is characteristic of isolated oxovanadium(5+) sites in a tetrahedral environment caused by $O—V^{5+}$ (d^0) charge-transfer transitions.[101,107,111,123,139,174,180,183] This tells us several things.

First of all, corroborating the EPR findings, the vanadium is highly dispersed throughout the material, meaning that the UV-Vis DRS results too provide direct proof for the successful incorporation of vanadium into the framework. Second, this result suggests that the material undergoes a coordination geometry change (from square-pyramidal or distorted octahedral to tetrahedral), possibly upon reversible release of one of the framework oxygen ligands. The change in coordination could explain the reported instability of VAPO-5 at high loadings of vanadium, as this could be expected to induce extra lattice strain. Third, it confirms the above hypothesis deduced from the obtained EPR data that upon calcination of the materials, the vanadium undergoes a V^{4+}-to-V^{5+} change, explaining the massive signal loss observed in EPR, and indicating successful oxidation of the vanadium.

When an uncalcined, as-synthesised sample is used for analysis, the previously unpopulated 550–800 nm region gains considerable features. The two bands present in this region have been attributed to d—d transitions in $V{=}O^{2+}$ environments with a pseudo-octahedral coordination geometry.[111,174,183] This band also explains the desaturated grey-blue colour of the as-synthesised samples compared to the bright yellow colour of the calcined ones. The fact that this region is completely featureless in all the calcined samples further lends credence to the successful oxidation of V^{4+} to V^{5+} upon calcination as deduced from the EPR findings.

In samples with higher vanadium content, such as 9/1 VTi AlPO-5, the region in 350–450 nm starts to show increased activity suggesting the presence of a polymeric or oligomeric oxide species, presumably V_2O_5, as well as polymeric VO_4 tetrahedra.[101,111] This is in agreement with the conclusions drawn earlier from the EPR results, strengthening the suspicion that at these elevated vanadium levels, oxidic vanadium impurities are present. This band is also present, albeit to a smaller degree, in low-vanadium samples, which can be explained through an overlapping signal derived from isolated $V^{5+}{=}O$ centres in an octahedral coordination geometry.[107,123] Indeed, it has been reported that tetrahedral V=O environments can change their coordination geometry to octahedral in the presence of water molecules (as ligands).[180]

The first measurements of the samples, both calcined and uncalcined, did not, unfortunately, establish the presence of titanium. As titanium was positively detected by EDX and ICP-OES elemental analysis, this suggested that the titanium, while present in the physical sample, was in a state where its signal overlaps with that of another species in the material. Presumably this would be TiO_2 (anatase), which has a fingerprint at 300 nm, or non-anatase oligomeric species at 270 nm, both of which would be obumbrated by the enormous vanadium signal.[101,147]

Another possibility however, was that the species in question was Ti^{4+} that had turned from tetrahedral to octahedral coordination upon the uptake of two water molecules, which causes a red-shift of the signal to 240 nm.[268,269] At this position, it is again masked by the intense vanadium transitions. According to literature reports, these signals could be made to disappear upon dehydration of the sample.[268,269] Indeed, a freshly calcined sample that was measured as quickly as possible after calcination revealed a strong shoulder at 215 nm characteristic of isolated Ti^{4+} sites in a tetrahedral environment, providing direct evidence for the incorporation of titanium into the AlPO-5 framework.[101,129,139]

Concluding, UV-Vis DRS has provided strong and direct proof for the incorporation of both V and Ti as isolated, single-site ions; in the case of vanadium as tetrahedral V^{5+} and for titanium as tetrahedral Ti^{4+}. Both species can uptake water and change their coordination to octahedral. In uncalcined samples, the vanadium is present as isolated, pseudo-octahedral $V{=}O^{2+}$ sites. Inclusion of large amounts of vanadium leads to the formation of extra-lattice V_2O_5-like species.

Another method that can determine oxidation states of a given system is X-ray photoelectron spectroscopy (XPS). For VAPO-5, it has been reported that the binding energy (BE) of the V2p region increases as the oxidation state of vanadium goes up.[112] Therefore, monitoring this value allows one to determine the oxidation state of vanadium in our system.

Although generally XPS signals are calibrated to the C1s signal, a study into a wide variety of vanadium species conducted by Mendialdua *et al.* showed that this is not viable for vanadium. A high degree of inaccuracy and large variability in the results obtained from the analyses occurs when C1s is used as calibration region for vanadium. Instead, they concluded in their report that O1s provides much more accurate, consistent results.[109] A similar conclusion was drawn by Silversmit *et al.*[112] who found that the use of any signal other than O1s, including $Au4f_{7/2}$, C1s and the Fermi level produced inconsistent, inaccurate results. As a result, we followed suit and likewise employed O1s as a calibration signal. As performed by Mendialdua *et al.* the value of the O1s region was set to the reported literature value of 530.0 eV and the BEs were calibrated from there.

The XPS results, after calibration and refinement, show that the binding energy for the $V2p_{3/2}$ region in the samples equates to 517.13 eV (Figure 69). The $V2p_{1/2}$ region is found at 524.35 eV, but this value is typically ignored in the literature, instead focusing on the (inherently) stronger and more well-resolved $V2p_{3/2}$ region (the $V2p_{1/2}$ region has also been reported to overlap with the Shirley background of the O1s signal[112]).

The value found for $V2p_{3/2}$ (in the calcined samples) corresponds to literature values reported for V^{5+}.[104,107,109,174,181] This directly corroborates the data obtained from UV-Vis spectroscopy as well as the proposed conclusions drawn from EPR spectroscopy, *i.e.* when calcined the material gets oxidised from V^{4+} to V^{5+}. Note that this peak does not rule out the presence of V_2O_5 which, being another V^{5+} species, shows a similar or identical signal, and is therefore not distinguishable from framework-incorporated V^{5+} using XPS. No discernible peaks or increased signal intensity is detected at 516 eV, which is where one would expect to find V^{4+}.[107,181] However, as is the case on several reports of vanadium-doped framework species,[35,107,124] the signal is not well-resolved enough to completely exclude the presence of such species. Indeed, as the EPR results do show the presence of a minor portion of V^{4+} after calcination *(v.s.)*, this would seem to be the case.

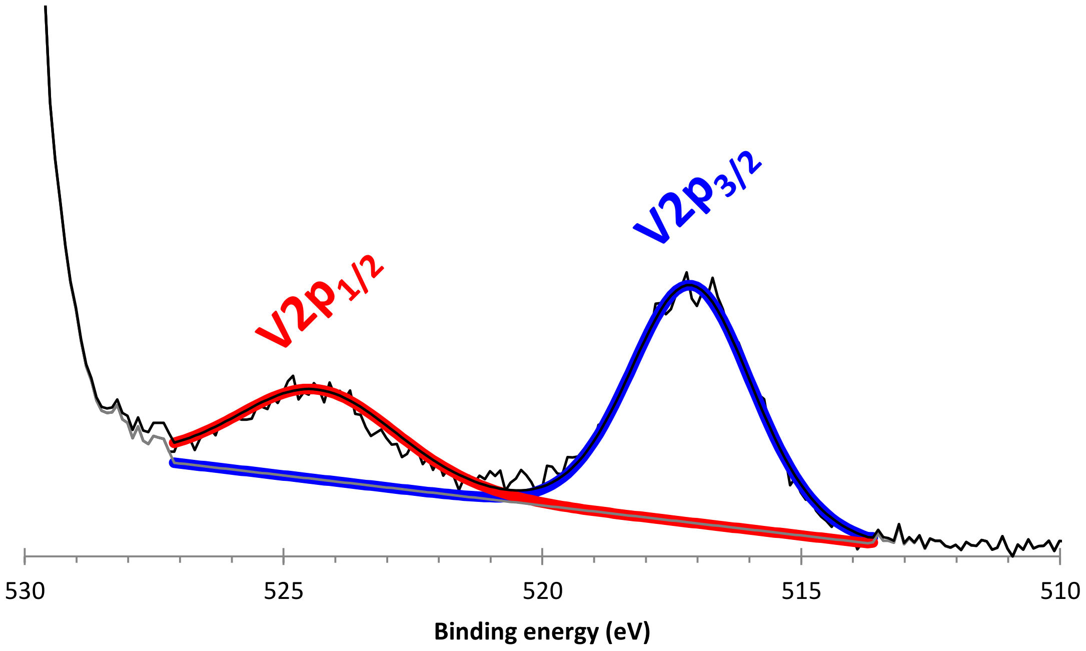

Figure 69: XPS spectrum of 9/1 VTi AlPO-5. Shown in red and blue are the calibrated, refined patterns of the $V2p_{1/2}$ and $V2p_{3/2}$ regions, respectively. The background signal approximation is shown in grey.

The relatively poor resolution of the V2p signal, although more than sufficient to be used for a qualitative analysis, is derived from the extremely low signal intensity. As before, the sample was analysed at lower loadings as well, at which point the signal becomes even weaker. Literature reports on vanadium-doped frameworks have also reported weak signal intensity and poor resolution, which has been attributed to the low amount of metal used as well as its homogeneous distribution over the sample.[35,107,124] Survey spectra of VTi AlPO-5 at 9%, 1% and 0.1% of vanadium are shown in Figure 70. From these spectra, the V2p region is only barely noticeable at 9%, and indistinguishable at 1% and 0.1% except when strong magnification is used.

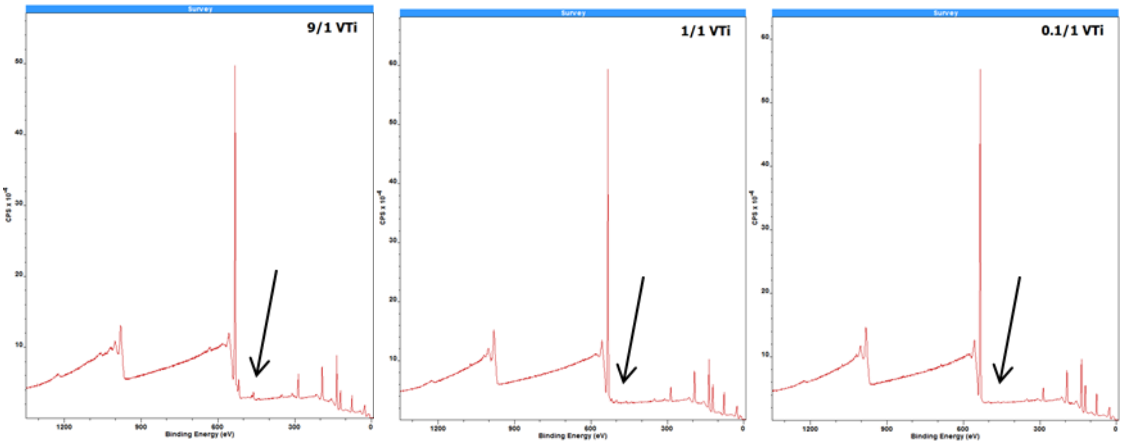

Figure 70: XPS survey spectra of VTi AlPO-5. Left: 9/1 VTi AlPO-5. Centre: 1/1 VTi AlPO-5. Right: 0.1/1 VTi AlPO-5. The V2p region is indicated by a black arrow. Without magnification, it is not distinguishable in any but the highest-loaded sample.

Under magnification, and at 1% vanadium, the signal is still (barely) visible, but presumably due to difficulties with background correction the peak positions are slightly shifted to 516.69 and 524.54. These values are still indicative of V^{5+} as noted before, however. At 0.1% vanadium, no discernible signal is detected at *any* magnification (Figure 71). The strong increase in signal intensity in going from 1% to 9% vanadium might be partially explained (apart from the obvious higher metal loading) by the formation of clustered, extra-framework V_2O_5-like species. This would corroborate the UV-Vis spectroscopy results that show a similar trend *(v.s.).*

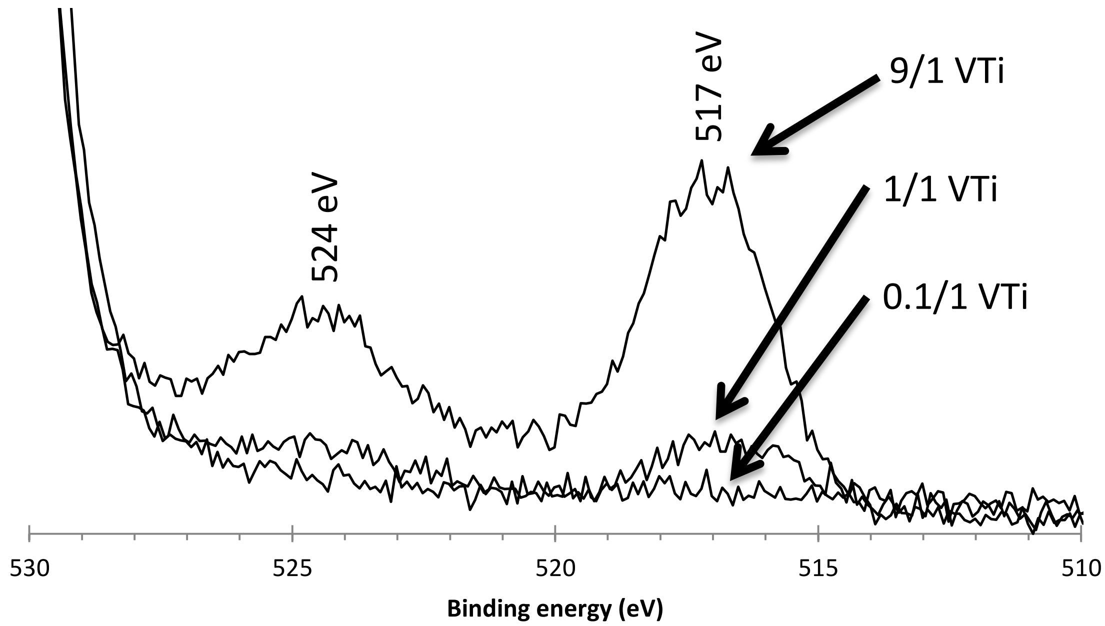

Figure 71: Overlaid XPS spectra of VTi AlPO-5. The spectra are not stacked and therefore the peak height is a directly comparable measure of relative intensity. For ease of viewing, the calibration curves were omitted from this graph.

In order to further back up the data with another bulk-measuring method sensitive to a very wide range of species, solid-state nuclear magnetic resonance (SSNMR) was performed. This method also allows the elucidation of unique spatial and dynamic features as well as detailed information about the electronic and chemical environment of the nuclei under examination. Moreover, this technique allowed investigation of the aluminium and phosphorus centres in detail, which is considerably harder or even unfeasible using the previously mentioned techniques. Therefore, SSNMR spectra were recorded observing the ^{27}Al, ^{31}P and ^{51}V nuclei. Although titanium NMR is technically possible, the very low activity and low abundance of the two NMR-active isotopes, ^{47}Ti and ^{49}Ti (natural abundance 7.3% and 5.5%, respectively), together with their wide shift range, low-resonance frequencies and tendency to appear simultaneously as well as closely together, complicated attempts at measuring these. These factors, combined with the fairly high quadrupole moments and secondary effects associated with titanium NMR as well as the very small, yet extremely similar gyromagnetic ratio values γ of the nuclei (which causes massive line broadening) makes titanium NMR intrinsically very difficult, which is why relatively very few reports on Ti SSNMR exist.[270,271] Preliminary scans were conducted, yet unfortunately, these showed very poor signal quality that was difficult to disentangle or resolve. Therefore, attempts at measuring titanium NMR spectra were abandoned.

Both the ^{27}Al and ^{31}P spectra are relatively straightforward, with a single major peak in each case (at *ca.* 36 and -30 ppm, respectively, Figure 72). The values of these peaks in both ^{31}P and ^{27}Al NMR spectra is quite consistent across all examined loadings of vanadium (1%–12%). The phosphorous spectra all show a single pair of spinning sidebands, while the aluminium spectra show a spectrum-wide series of spinning sidebands. These peaks are typical of tetrahedrally-coordinated framework Al and P in AlPOs, and literature reports also show similar spinning sideband patterns for both nuclei in AlPOs.[104,108,111,129,272,273]

^{27}Al and ^{31}P signals corresponding to impurities containing either element were not present. From ^{27}Al NMR spectra, no signals corresponding to amorphous aluminium phosphate ($AlPO_4$), octahedral aluminium impurities or crystalline tetrahedral aluminium species in domains too small to be visible by XRD are observed.[273] For the ^{31}P spectra, signals showing the presence of vanadyl phosphates or crystalline, non-framework $AlPO_4$ are not present.[108,111,273] The apparent absence of any of these impurities strongly suggests that the synthesis procedure for AlPO-5 was highly successful, with no observable non-framework Al and/or P species present. Keeping the other spectroscopic evidence in mind, this corroborates the SEM and EDX findings, which suggested that the vanadium was present fairly homogeneously throughout the sample, even in small, non-spherical or barrel-shaped particles — if amorphous or otherwise non-AFI impurities were present, one would expect these particles to either contain no vanadium, or clustered vanadium species, however no clustered vanadium species are detected by EPR at low-to-medium metal levels, and all particles examined by EDX contained vanadium.

The aluminium spectra show an additional minor peak around -12 to -16 ppm reported to be caused by coordination of two water ligands to the aluminium, forming an octahedral aqua complex.[111,157,272] Interestingly, this value gradually red-shifts as the vanadium concentration in the sample increases, from -12 ppm for 0.1% V, to -16.4 ppm for 12% V. Presumably this is caused by increasing interaction of the hydrated aluminium species with vanadium sites as the abundance of such sites in the material increases. A signal at 8 ppm, which has been reported to be present very weakly in some

AlPO-5 samples and which has been attributed to penta-coordinate mono-aqua centres, was not observed. Moreover, as only one hydrated Al site is detected, these octahedral water-coordinating sites must be randomly dispersed throughout the material.[157,272]

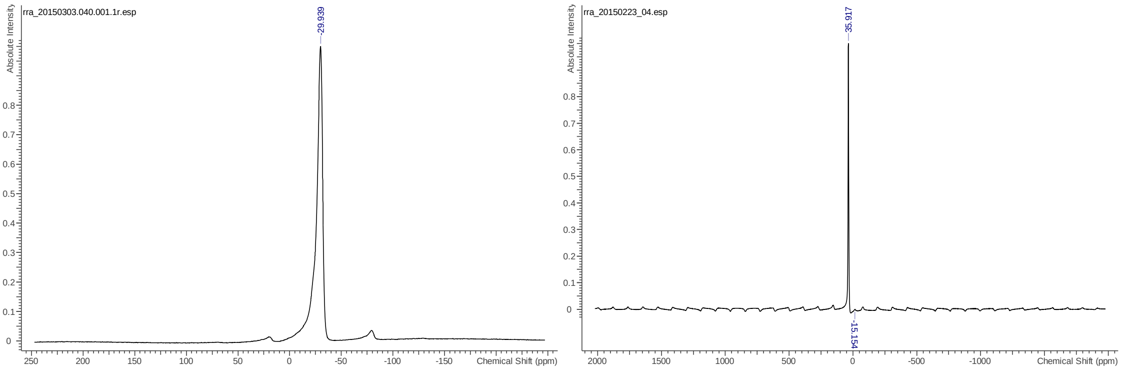

Figure 72: Left: ^{31}P SSNMR spectrum of 9/1 VTi AlPO-5. Right: ^{27}Al SSNMR spectrum of 9/1 VTi AlPO-5. Note the small hydrate peak at -15 ppm.

The ^{51}V spectra show a broad signal with well-resolved spinning sidebands and a very large chemical shift anisotropy. The resolution of these spectra is rather poor, especially at lower loadings, presumably caused by the rather large nuclear electric quadrupolar moment of the ^{51}V nucleus. Indeed, it is well known that ^{51}V-SSNMR spectra have rather large nuclear electric quadrupole moments and high chemical shift anisotropy, which, coupled with second-order quadrupolar effects, can cause considerable line-broadening. The chemical shift anisotropy is considered the dominant effect however, and as a result the absolute values of the chemical shielding anisotropy rather than isotropic shift values are sometimes used to distinguish between various vanadium environments.[111,189,190]

^{51}V VTi AlPO-5 spectra recorded at varying levels of V (0.1–12%) show a clear pattern of spinning sidebands at 12% V, but at 1% V the pattern is quite weak and at 0.1% the signal is noticeable but unworkably poor (Figure 73). Even at 12%, the lines show disorder as well as line broadening. Moreover, it was speculated that, based on analytical results and the presence of slight shoulders on some of the peaks in the high-loaded sample, there are two similar species present in the system that cause slightly offset spectra; the presence of two such signals makes disentangling a spectrum by simulating it as a single signal considerably harder and significant margins of error are to be expected in this case.

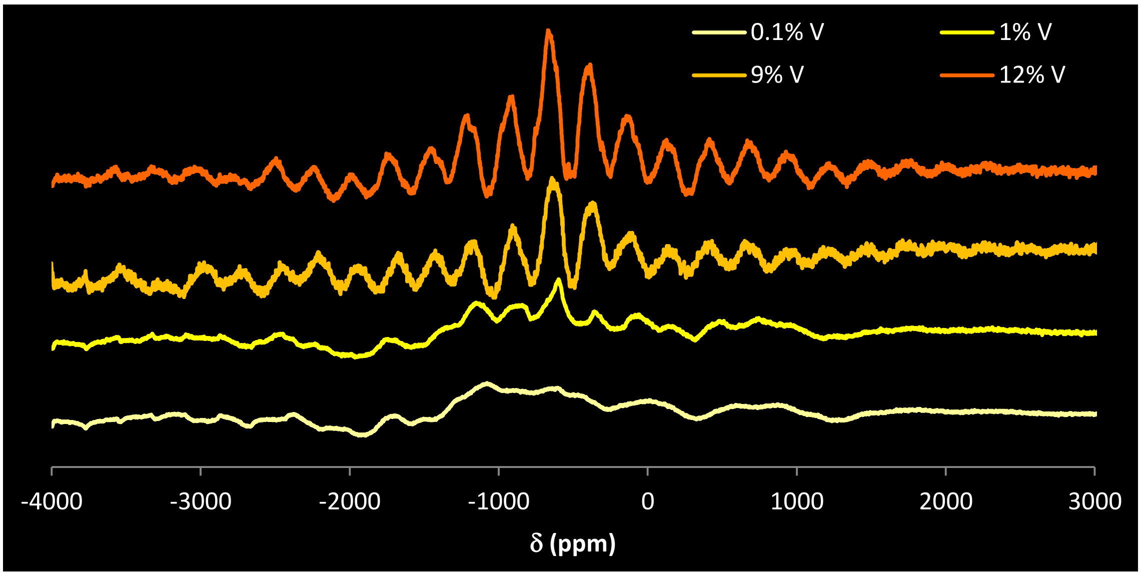

Figure 73: Stacked ^{51}V SSNMR spectra of VTi AlPO-5 at 1% Ti and 0.1% V, 1% V, 9% V and 12% V. All spectra were measured at 35 kHz.

Samples were recorded at different spinning speeds to determine the position of the centreband, which, unlike spinning sidebands, does not move under such variations (Figure 74). Using this data, the isotropic shift was determined to be around *ca.* 660–670 ppm. This is in agreement with previous literature and has been reported to be indicative of $VOPO_4$-like tetrahedrally-coordinated V^{5+}=O species bound to the framework via one to three V–O bonds.[108,273]

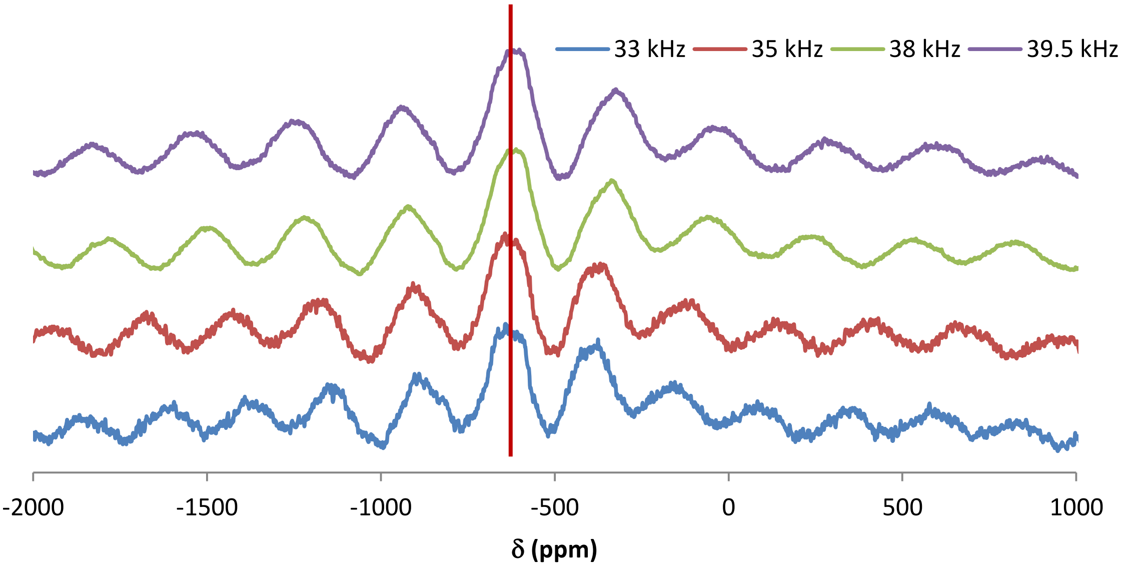

Figure 74: Stacked ^{51}V SSNMR spectra of 12/1 VTi AlPO-5 measured at different sample rotation frequencies. The position of the centreband, which is stationary across spinning speeds, is indicated by a red line. The other peaks, which are spinning sidebands, move linearly inwards as the spinning frequency decreases.

Simulations (Figure 75) were complicated by several factors mentioned above, but show the following parameters (Table 26):

$-\delta_{iso}$	C_Q	η_Q	$-\delta_\sigma$	η_σ	$-\delta_{\parallel}$
625 ppm	3-3.5 MHz	0.7-1.0	350-450 ppm	< 0.3	400-500 ppm

Table 26: Parameters derived from 9/1 VTi AlPO-5 SSNMR spectral fittings and simulations, with δ_{iso} the isotropic chemical shift, C_Q the quadrupolar coupling constant, η_Q the asymmetry parameter, δ_σ the chemical shift anisotropy, η_σ the chemical shift anisotropy asymmetry parameter, and $\delta_{\parallel}$ the perpendicular chemical shift.

Fitted to parameters provided in a study by Lapina *et al.* of a wide variety of vanadium compounds, the results conform closest to a trigonal-pyramidal VO_4 pyramid described as $V{=}O(OR)_3$-like.[191] This supports our UV-Vis observation *(v.s.)* that the calcined material contains oxovanadium species and is present in a tetrahedral-like coordination geometry. The high anisotropy we observed is unsurprising for an oxovanadium species, as the V=O bond in the species would be expected to introduce considerable asymmetry into a system also containing longer V–O bonds. These findings give new, detailed insights into the vanadium environments of calcined VAPOs — which had previously been difficult to assign — constituting a $V{=}O(OT)_3$-like species.

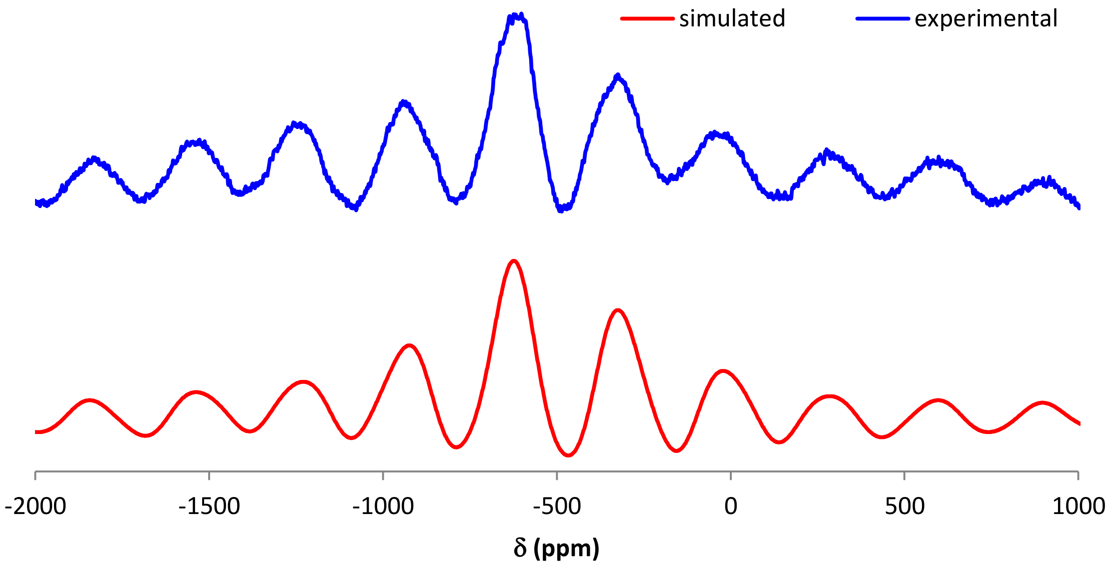

Figure 75: ^{51}V SSNMR spectrum of 12/1 VTi AlPO-5 (red dots) compared to a simulated pattern (blue line).

Interestingly, recalcination of a previously calcined 12% V sample *(i.e.* a twice-calcined single sample) led to the appearance of a second, distinct set of peaks (Figure 76). It was then noticed that this second set of peaks corresponded fairly closely to the positions of the shoulders noticed in the once-calcined sample. The previous analytical results strongly suggested that the 12% V sample included a relatively high amount of impurities, and XRD results show a degradation of the AFI framework of 12/1 VTi AlPO-5 after calcination. This suggests that at these very high V loadings, the material is unstable towards calcination, presumably forming V_2O_5-like or other oxidic, polymeric or oligomeric vanadium species as the framework decomposes. The appearance of this second set of peaks suggests, therefore, that this second set of peaks represents the impurities observed upon calcination of VTi AlPO-5 at very high V loadings.

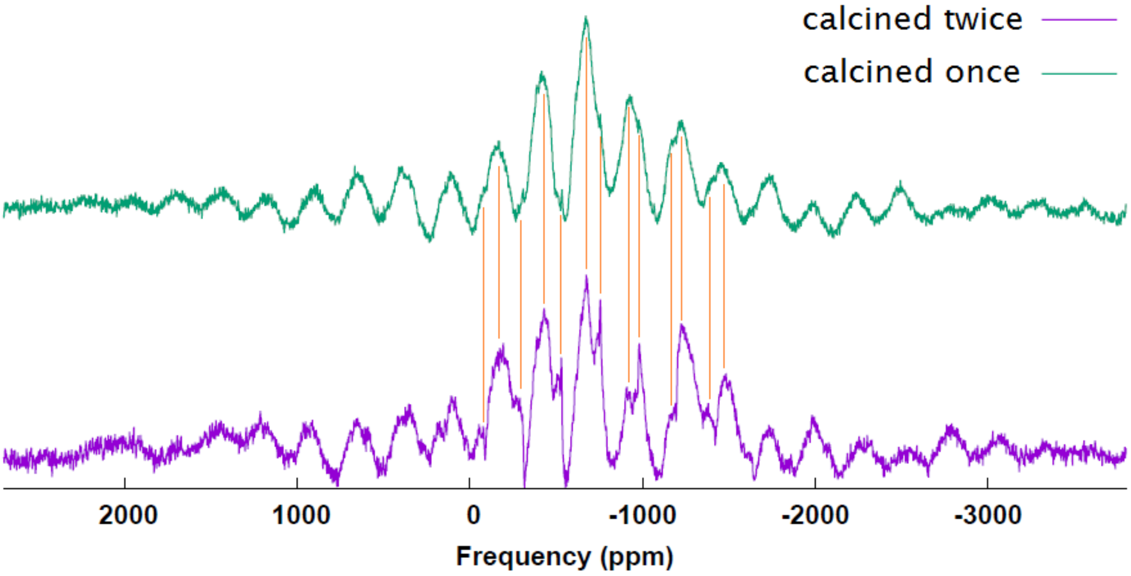

Figure 76: Stacked ^{51}V SSNMR spectra of 12/1 VTi AlPO-5, green; calcined once, purple; calcined twice. Orange lines are drawn to parallelise peak positions between the two scans.

Concluding, SSNMR shows us several things. ^{27}Al and ^{31}P spectra show the only observable Al and P species are AlPO-like and therefore suggest that the synthesis of the AlPO material is highly successful. The presence of hydrated T sites is also established, confirming that the framework contains water due to air exposure. These water sites are highly dispersed and do not form pockets. ^{51}V SSNMR show rather broad spectra, but suggest the presence of a secondary V species in 12/1 VTi AlPO-5, in accordance with previous results. This species becomes considerably more prominent when the material is calcined for a second time. The main species present in the material is a V^{5+} species attributed to oxovanadium(5+) in a tetrahedral environment with three pendant framework V–O bonds.

5.3 Discussion

Based on the evidence presented in section 5.2, the following information has been elucidated about the nature of the V and Ti centres in VTi AlPO-5:

1. Vanadium and titanium were successfully incorporated into the AlPO-5 framework;
2. Vanadium and titanium are present as isolated, single sites in the material;
3. In the as-synthesised sample, vanadium is present as square-pyramidal or tetrahedrally-distorted octahedral vanadyl (V=O^{2+}) sites, likely with four equatorial V–O bonds and one axial V=O bond;
4. When calcined, the vast majority of vanadium sites turn to tetrahedral or tetrahedral-like oxovanadium(5+) (V=O^{3+}) sites bound to the framework by one to three V–O bonds;
5. Titanium is present as tetrahedral Ti^{4+} sites in the material.

Based on these conclusions, it is suggested that the most likely *in situ* species of vanadium and titanium look like this (Figure 77):

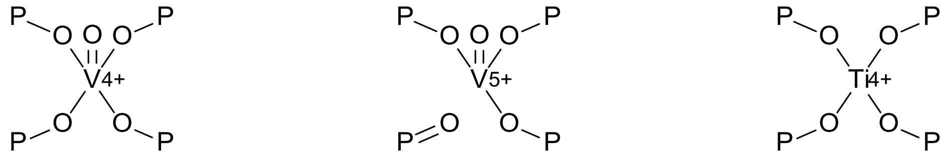

as-synthesised

calcined

as-synthesised
&
calcined

Figure 77: Suggested vanadium and titanium species in VTi AlPO-5.

These findings correspond closely to the vanadium models suggested by Rigutto *et al.*[108] for VAPO-5 (in the case of calcined VAPO-5, with the alternate structure (b) proposed by their group, Figure 78) but are in conflict with the models suggested by Teixeira-Neto *et al.*, Montes *et al.*, Okamoto *et al.*, Hartmann *et al.*, Weckhuysen *et al.* and Prakash *et al.* Below is a further summary of the models suggested by these other groups (Figure 78). The following models were discounted by elimination:

- Teixeira-Neto's, Montes', Okamoto's, Hartmann's and Prakash's models assume substitution of vanadium for phosphorus which is extremely unlikely given the resulting charge imbalance. The V^{5+} ion said by these authors to be produced upon calcination is directly at odds with our UV-

Vis and ^{51}V SSNMR analyses, which indicate the vanadium is present as a $V{=}O^{3+}$ ion. Furthermore, no indication of a $V^{5+}O_4$ ion was observed.

- Rigutto's model (a) for calcined VAPO-5 constitutes a five-coordinate vanadium centre, which would be expected to yield a square-pyramidal or distorted octahedral coordination geometry; our findings indicate it is present as a tetrahedral-like or trigonal pyramidal ion. It is possible that the species we propose can interconvert to or is partly present as this species.
- The models proposed by Teixeira-Neto, Montes and Hartmann for the as-synthesised material are most unlikely as they do not contain four V–O framework bonds and are not square-pyramidal or distorted octahedral, for which we have obtained direct evidence. Moreover, it is proposed that vanadium substitutes for phosphorus instead of aluminium which is most unlikely as stated above.
- Weckhuysen's model for as-synthesised vanadium species does not possess four V–O framework bonds, nor are the ligands located in the equatorial plane, at odds with the evidence we obtained for a square-pyramidal or distorted octahedral environment. It is possible that this structure is the species generated upon hydration of the vanadium, however. Prakash's nearly identical model is discounted for similar reasons, however in this model vanadium substitutes phosphorus which we proved to be highly unlikely.

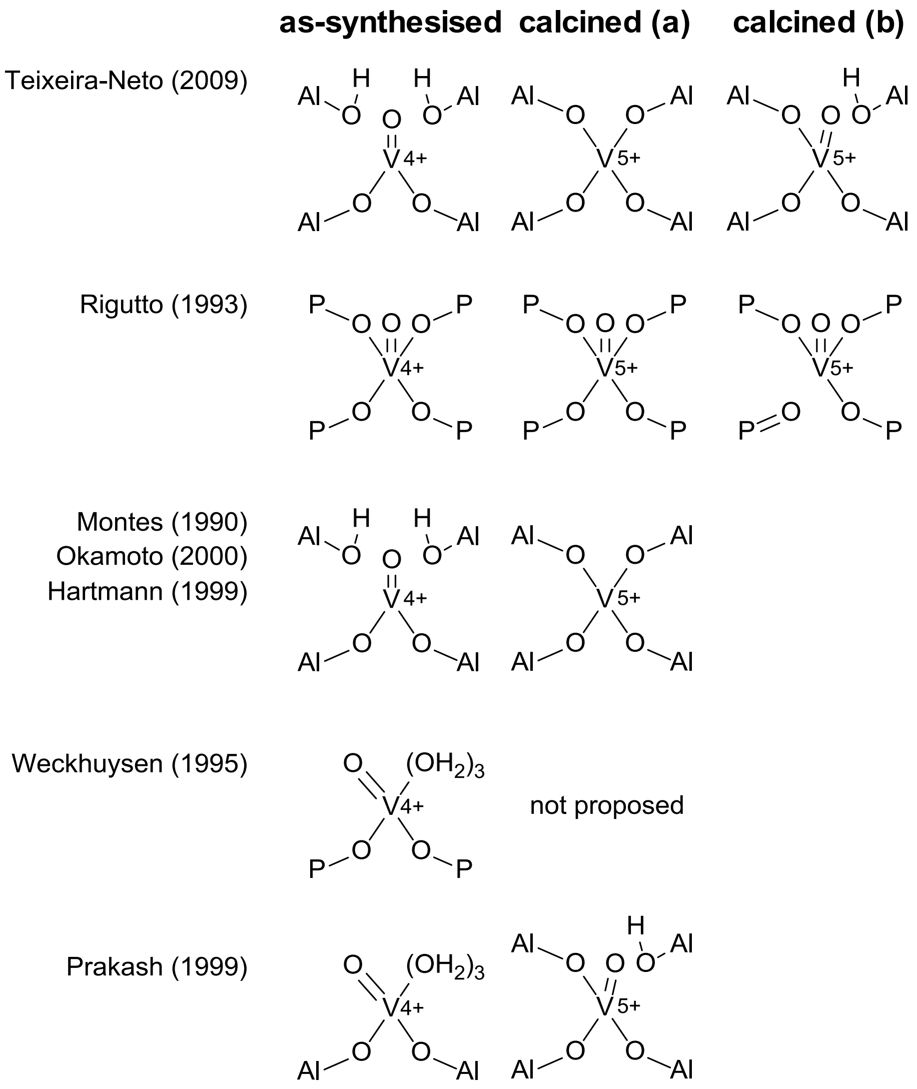
as-synthesised
calcined (a)
calcined (b)
Teixeira-Neto (2009)
Rigutto (1993)
Montes (1990)
Okamoto (2000)
Hartmann (1999)
Weckhuysen (1995)
not proposed
Prakash (1999)

Figure 78: Proposed structures of the in situ vanadium species in VAPO. Shown are as-synthesised and calcined propositions (including alternate possibilities proposed by the authors).[101,104,106,108,172,179,183]

Although mechanistic proposals regarding benzylic oxidation using immobilised vanadium species are scarce in the literature, presumably due to the great difficulty of visualising any of the vanadium intermediates during the reaction, two key processes have been suggested. The first is Rigutto's proposed interaction mechanism of VAPO-5 with TBHP (Scheme 65) while the second is Xia's proposed catalytic cycle for benzylic oxidation of alkylbenzenes using VCp_2Cl_2 (Scheme 66).

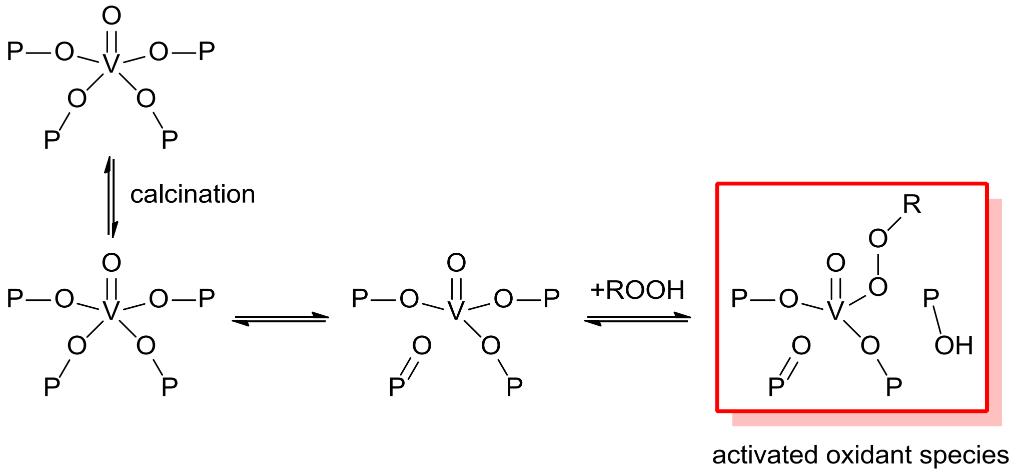

Scheme 65: Postulated interaction mechanism of VAPO-5 with TBHP proposed by Rigutto and Van Bekkum.[108]

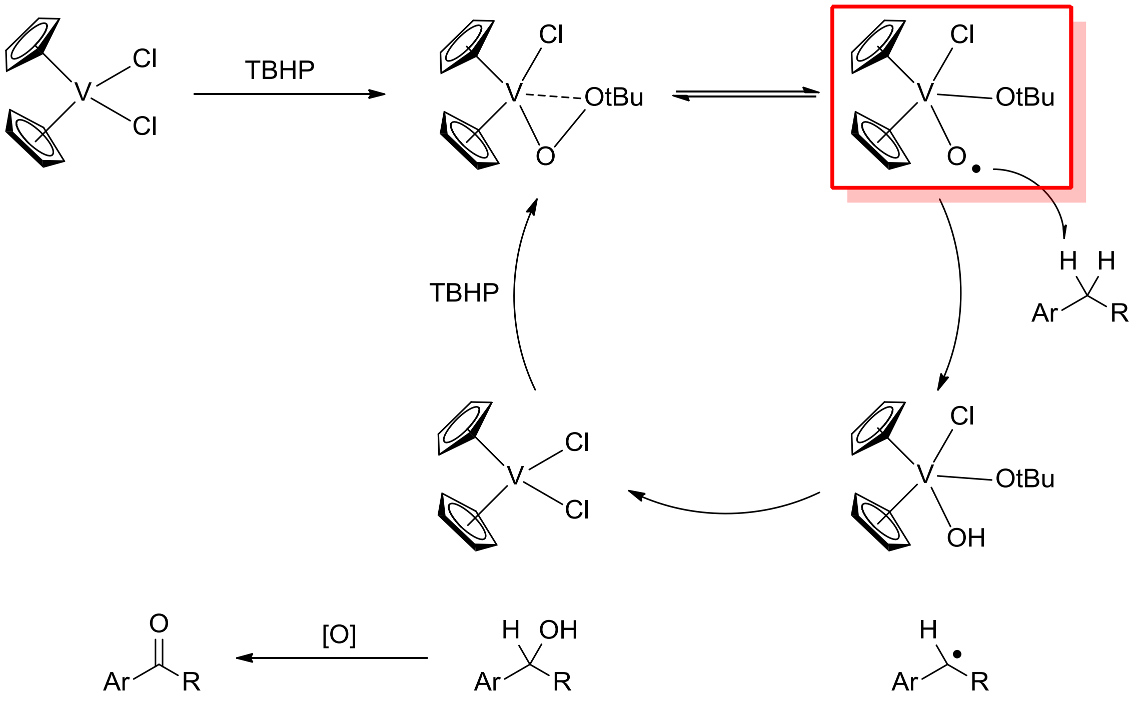

Scheme 66: Proposed catalytic cycle for the benzylic oxidation of alkylbenzenes using vanadocene dichloride postulated by Xia et al.[72]

The two key species in both mechanisms have been highlighted in red above. Starting from these two proposed structures and based on the catalytic and analytical data observed, the following mechanism for the reactions performed with VTi AlPO-5 is tentatively proposed (Scheme 67):

PROPOSED MECHANISM FOR BENZYLIC OXIDATION USING VTi AlPO-5

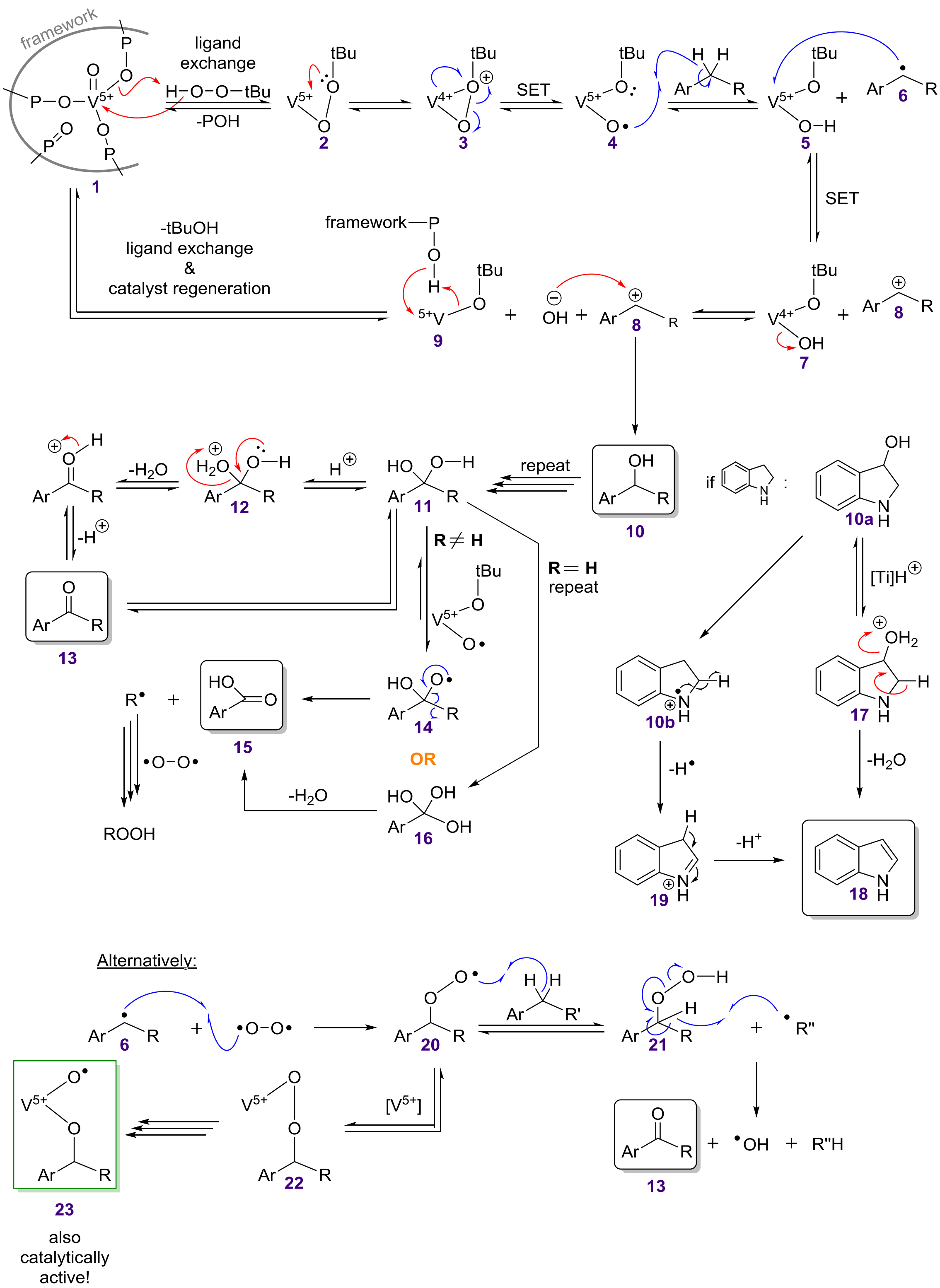
framework
ligand exchange
H–O–O–tBu
-POH
1
2
3
SET
4
5
6
SET
7
8
9
-tBuOH
ligand exchange
&
catalyst regeneration
framework—P
10
if
10a
[Ti]H⊕
10b
17
-H•
-H₂O
19
-H⁺
18
repeat
11
12
-H₂O
13
-H⊕
R ≠ H
R = H
repeat
14
OR
15
16
R•
•O–O•
ROOH
Alternatively:
20
21
[V⁵⁺]
22
13
•OH
R''H
23
also catalytically active!

Scheme 67: Proposed reaction mechanism and catalytic cycle for VTi AlPO-5-catalysed benzylic oxidation using TBHP. Products are indicated with black boxes. A possible secondary pathway is shown at the bottom, with the active intermediate highlighted in green. The indoline pathway is shown on the right.

The mechanism can be described as follows. Starting from the catalytic vanadium species **1**, which we theorised *(v.s.)*, the vanadium up-takes TBHP in a ligand exchange reaction, releasing one of its pendant framework –P–O– bonds. The other framework phosphorous groups are catalytically irrelevant and are therefore omitted for clarity from intermediate **2.** Rearrangement from **2** to the active species **4** proceeds *via* intermediate **3.** With both oxygen atoms of TBHP coordinated to vanadium in **3** (similar to the dative intermediate proposed by Xia et al, *v.s.)*, the O–O bond is weakened and susceptible to homolysis, forming the active species **4.** This species reacts with the substrate by H-atom abstraction at the benzylic position, as these C–H bonds are weakest.

Benzylic radical **6** next engages in SET with the V^{5+} species to form a benzylic carbocation **8** and intermediate **7.** It should be noted at this point that the two crucial SET steps involved in the reaction mechanism show the importance of the presence of a powerful redox-capable metal ion such as V^{5+}. Release of the hydroxyl-ligand formed during the hydrogen abstraction step leading to species **5** and **6** can be released to form V^{5+} intermediate **9**, while the hydroxyl group quickly and irreversibly reacts with carbocation **8** to form the primary product **10** (for propylbenzene; 1-phenyl-1-propanol). Intermediate **9** can then engage in ligand exchange to complete the primary catalytic cycle.

Product **10** itself is susceptible to further reaction. A second oxidation at the benzylic position is expected to be faster than the first as the substitution of a hydrogen atom for a hydroxyl group leads to a weakening of the other benzylic C–H bonds. This explains the low levels of the alcohol product observed in the product mixture. The second oxidation yields a diol **11** which corresponds to the hydrate of a carbonyl compound **13.** For ketone products such as propiophenone, the equilibrium will sit towards the carbonyl compound, with a very small fraction being in the hydrate form (**11**). This is important however as the hydrate is susceptible to hydrogen abstraction by the active oxygen species, leading to **14.**

Collapse of this intermediate to benzoic acid **15** with concomitant release of R· is slow, but thermodynamically favourable, producing the major side-product in alkylbenzene oxidation. In the case of alkylbenzenes, the bond broken is the C–R bond rather than the C–Ar bond, as alkyl radical intermediates are more stable than aryl radical intermediates.

For methylbenzenes, several factors drive this reaction further. First, oxidation leads to an aldehyde (**13**, R=H) rather than a ketone. Its hydration to **11**, catalysed by the acidic sites derived from the titanium incorporation, is more favourable than with ketones. In other words, the combination of vanadium and titanium together within the same catalyst drives the selectivity of the reaction. Moreover, its hydrate reactivity towards active oxygen species **4** favours a third benzylic H-atom abstraction, leading to triol **16** which rapidly dehydrates to carboxylic acid **15.** This explains the high selectivity for methylbenzenes to give carboxylic acid.

In cases where the substrate is a heterocycle like indoline, benzylic oxidation leads to a benzylic alcohol, *e.g.* **10a** that is prone to dehydration in the presence of titanium-derived acidic sites to indole **18.** This explains the absence of any trace of alcohol **10a** in crude product mixtures. Oxidation of **17** to a benzylic ketone is kinetically slow and so does not compete with the dehydration. An alternative pathway, consisting of nitrogen lone pair oxidation to form radical cation **10b** followed by H· elimination to **19** and aromatisation to **18**, is also possible.

After the reaction has been initiated, alternative pathways are possible. For example, generation of benzylic radical **6** could result in facile reaction with oxygen from the atmosphere, generating peroxy radical **20.** This species would be expected to give H-abstraction to form peroxide **21**, which in turn can undergo homolytic cleavage to regenerate the substrate and give ketone **13.** Alternatively, peroxy radical species **20** can engage with V^{5+} species to form **22** and active oxygen species **23**, which is functionally equivalent to **4.** Rearrangement of **22** to **23** proceeds in the same manner as when going from species **2** to **4.**

This mechanism, supported by the catalytic results, shows the benefit of the V and Ti combination of in AFI frameworks, as these provide the means of achieving highly selective reaction outcomes through redox-acid bifunctionality. Potentially, this makes VTi AlPO-5 a very powerful tool for a variety of transformations.

6. Summary & conclusions

Applications of porous materials in industry are plenty, with one of the most important classes being zeolites. These are employed on an enormous scale, to the point where 40% of all industrial, heterogeneous catalysts are zeolite-based. Aluminophosphates (AlPOs) expand on this concept, featuring similar, highly ordered frameworks. However, being more ionic in nature, they are more amenable to isomorphous substitution than zeolites and the inclusion of catalytically active metal ions has proven to be a useful tool in catalysis.

Our goal was to develop an AlPO-based catalyst that would prove useful for a variety of laboratory-scale reactions for the benefit of synthetic chemists. To that end, it was elected to employ a bimetallic AlPO-5 catalyst with a medium-sized pore aperture (ø 7.4 Å) to help control selectivity in the performed reactions by favouring an end-on approach of the substrate towards the active site without compromising too greatly on mass transfer ability. Dispersion of active metal sites with the framework would hopefully create isolated metal centres, which, due to their well-defined nature, would be able to interact with reactants and reagents in a predictable manner, leading to consistent reactivity and high selectivity.

The combination of a redox-active metal oxidant and an accompanying oxophilic centre was chosen as it could result in a catalytic synergy, with the oxophile coordinating the oxidant and activating it towards reaction, while the redox metal would be responsible for facilitating the oxidation step.

To probe the catalytic activity of this system, a substrate was employed that was expected to be susceptible to a variety of reaction outcomes, namely propylbenzene. After an initial screening, it was found that the best choice of AlPO catalyst was vanadium-titanium AlPO-5 when using TBHP as the oxidant. The reaction was selective towards benzylic oxidation, but produced a mixture of oxidation products. The main product was propiophenone, but small amounts of benzoic acid and 1-phenyl-1-propanol were also given (Scheme 68). Tests suggested that the reaction involved radical intermediates, and this leads us to conclude that the first step was a radical-induced hydrogen atom abstraction from the benzylic carbon leading to the formation of an alcohol. As the alcohol moiety activates the remaining benzylic C–H bond towards H-atom abstraction, the alcohol is present in very small quantities in the product mixture. In the case of propylbenzene, the twice-oxidised product is propiophenone which is the major reaction product. Its oxidation to benzoic acid also occurs, but this is a slow process, which explains why it is observed as a side product of the reaction.

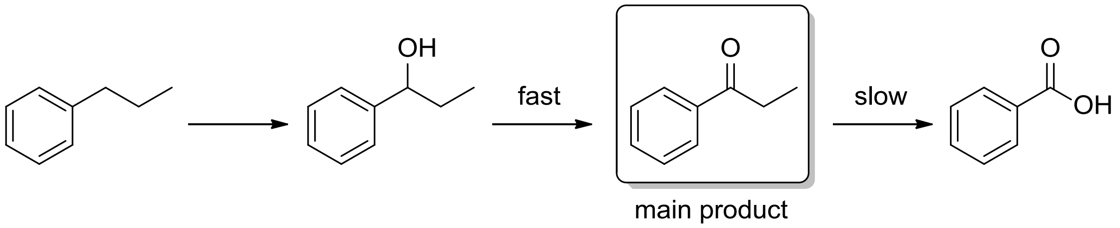

Scheme 68: Sequential oxidation of propylbenzene.

Several different catalyst series were synthesised, with varying amounts of vanadium, various amounts of titanium or similar secondary metals present in the material. After 23 hours, VTi AlPO-5 catalysis with various vanadium and titanium loadings achieved similar conversions, except when no vanadium was added at all, indicating that vanadium was chiefly responsible for catalytic activity. However, when monitored by time, it became apparent that conversion reaches a plateau, and this is reached faster when a high-vanadium sample is used. When monitored after four hours, at which point the reaction is incomplete with all loadings of vanadium, conversion increases as the vanadium loading goes up, albeit with diminishing returns, suggesting that the introduction of more metal may not lead to a proportional uptake of vanadium entering the framework. When low catalyst amounts and low vanadium loadings are used, the reaction is at its most efficient, but conversion drops off. Thus, when going to 0.3 mass% of 0.1 atom% vanadium, turnover numbers soar to over 80 000 due to the high activity of the metal.

VTi AlPO-5 significantly outperforms blanks including undoped AlPO-5, $VOSO_4$, V_2O_5 and the important industrial oxidation catalyst TS-1, proving the uniqueness of the procedure. Although contrary to what was hoped, no significant synergy was noted between V and Ti in terms of oxidation power, but VTi AlPO-5 still outperformed V, VCo, VNi, and VMn AlPO-5. VCr AlPO-5 gave marginally higher conversions but had some undesirable material properties and was therefore considered inferior as well.

Particles of different sizes were synthesised by controlling cooling rates. This allowed access to catalyst particle sizes ranging from 10–30 µm or to 30–

100 μm. However, it was found that this affected aggregate size rather than crystallite size, so this had no noticeable influence on catalytic activity.

Use of different amounts of oxidant was also investigated. Results attained suggest that TBHP is not the only oxidant participating in the reaction. Indeed, as the reaction is radical-based and air-exposed, we suspect that oxygen from the air is the second oxidant.

Recycling tests showed that at 9 atom% V, the catalyst quickly degrades to aluminium phosphates, at which point the activity drops to the level of V_2O_5, which we believe to be the V species formed upon collapse of the framework. When going to lower loadings, such as 1% and 0.1%, conversion remains stable through multiple recycles, and a much smaller amount of degradation of the framework is noted. When AFI decomposition occurs it forms one or more dense aluminium phosphate phases.

Leaching of small amounts of vanadium was noted during reactions, but hot-filtration tests showed an immediate cessation of reactivity when the catalyst was removed from the reaction mixture. This suggests that VTi AlPO-5 is a truly heterogeneous catalyst and that the observed activity is not caused by leached homogeneous vanadium species.

When other types of substrate are used, different reactivities are observed, depending on their nature. For example, when tetralin and indan are used, a much higher selectivity for the ketone product is observed (Scheme 69) together with higher activities and activities at lower temperatures. This is presumably due to the lower bond strength of benzylic C–H bonds in tetralin and indan compared with linear alkylbenzenes, resulting in faster primary oxidation to the alcohol intermediate. The porous nature of the catalyst appears to be of importance. The trapping of catalytic species and substrate in the channels of the catalyst presumably increases exposure of the species to one another, resulting in higher selectivity compared to other systems in literature.

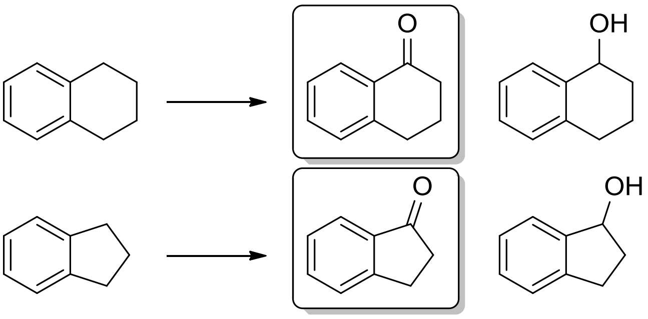

Scheme 69: Oxidation of tetralin and indan.

As with propylbenzene, very high turnover numbers (*ca.* 86 000) can be obtained using low vanadium levels, albeit at the expense of yield. Nonetheless, the activity of the system speaks for itself. Overall, VTi AlPO-5 has proven to be a powerful tool for the facile, selective production of tetralone from tetralin and the oxidation of indan to indanone. Both carry significant value considering the industrial importance of tetralone to chemical industry as well as the significance of the indanone motif in pharmaceutical compounds.

When methylbenzenes are employed, extremely high selectivity towards carboxylic acids is observed (Scheme 70). This makes the system an attractive alternative for the production of the benzoic acid. The selectivity towards benzoic acid rather than the production of mixtures, especially of benzaldehyde, is likely to stem from the combination of vanadium and titanium within the same framework. The inclusion of titanium yields medium-strength Brønsted acid sites, accelerating the formation of the hydrates needed for carboxylic acid formation. As a result, the combination of redox- and acid bifunctionality within the same catalyst drives the high selectivity observed.

When polymethylbenzenes are employed as substrates, *e.g.* xylenes, mesitylene, and durene, VTi AlPO-5 catalyses the selective formation of monocarboxylic acids. This is attributed to a combination of the vanadium and titanium reactivities (Scheme 70, path 1) and a self-limiting mechanism caused by the significant polarity shift in going from the substrate to the product. The formation of large amounts of solid in these reaction mixtures suggests that the acid, once formed, precipitates from the reaction mixture and is not then available for further turnover. It is interesting to note that there are very few literature reports on the selective mono-oxidation of such compounds.

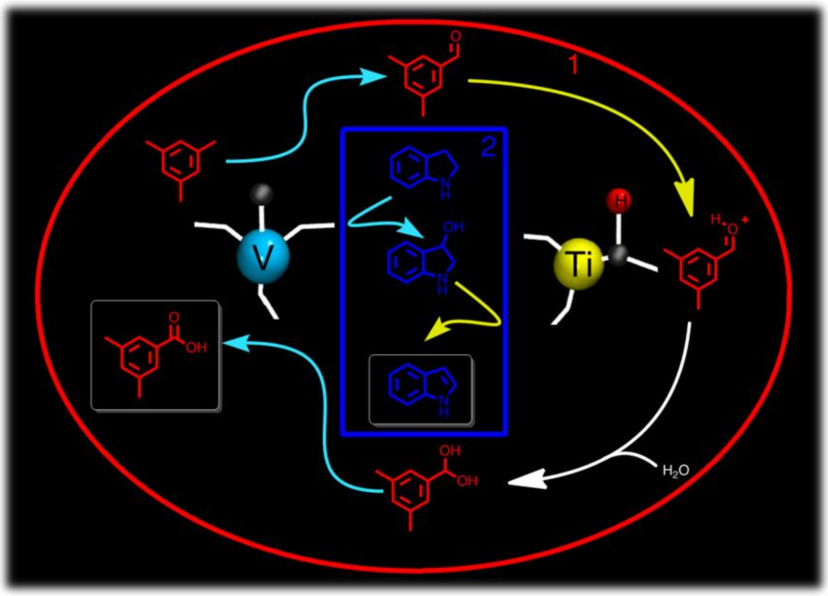

Scheme 70: Oxidation of methylbenzenes (1) and indoline (2), illustrating the role of the vanadium (blue arrows) and titanium (yellow arrows) centres.

The oxidation of indoline affords indole with high selectivity. This is of interest as the production of indole is of industrial significance for the manufacture of indigo dye and various pharmaceuticals. Moreover, the chemistry affords a synthetic pathway for the protection of C3 in indoles towards electrophilic aromatic substitution. The product is formed through vanadium-catalysed oxidation and subsequent acid-catalysed dehydration and so makes use of the catalyst's bifunctional capabilities (Scheme 70, path 2). Again, the combination of vanadium and titanium centres within the material appears to be the driving force behind the selectivity observed. As before, high TONs *(ca.* 82 000) are observed at low vanadium levels. Tetrahydroquinoline also underwent aromatisation to quinoline with very high selectivity. Here, a double oxidation-dehydration sequence is implicated (Scheme 71).

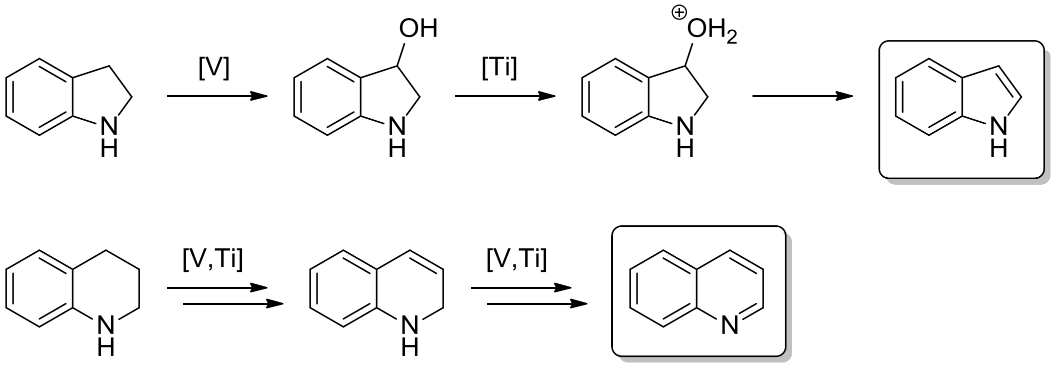

Scheme 71: Bifunctional ODH of indoline and tetrahydroquinoline.

Through virtue of its isolated, single-site metal centres, extremely high activities are noted at low metal loadings and the oxidation procedure involves benign oxidants under mild conditions at atmospheric pressure using easy procedures. The material itself is cheap to produce and does not involve heavy metals or hazardous materials or require the use of solvents. Moreover, it is easily recovered by filtration or dissolved in alkaline aqueous medium making it trivial to separate from the reaction products. Furthermore, the material can be re-used several times without significant drop-off in catalytic activity, as long as low vanadium loadings are employed, and does not require re-activation by calcination to do so.

The material itself is a grey-blue powdery solid that turns bright yellow upon calcination. As more vanadium is added to the sample, the blue/yellow colours become more intense, while adding titanium turns the material green/yellow. The materials are phase-pure AlPO-5 even at very high levels of vanadium, and show little distortion in the unit cell parameters (Figure 79). Synthesis is highly specific towards the AFI framework, with no detectable non-AFI $AlPO_4$ phases present. The powder particles consist of spherical aggregates of roughly 10–30 µm in diameter and are composed of small crystallites (40–60 nm) with surfaces composed of stacked plaquettes. An interparticulate space is present between the crystallites. As more metal is introduced, the aggregates become more barrel-shaped and the interparticulate cavities appear to become less uniform.

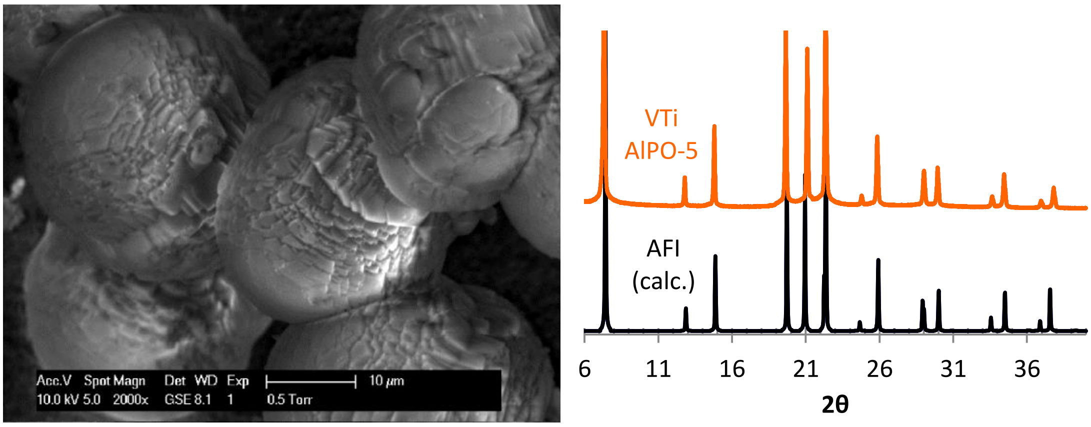

Figure 79: Left; SEM micrograph of VTi AlPO-5. Right: XRD spectrum of VTi AlPO-5 (orange) compared to AFI (black).

The material is not stable towards calcination at very high loadings of vanadium (12%) where decomposition is gradual. Nonetheless, high specificity of the synthetic procedure makes the material more stable towards calcination than other synthetic methods described in the literature.

Compound analyses revealed that the as-synthesised material has vanadium present as a $V{=}O^{2+}$ species in a square pyramidal or distorted octahedral coordination, which upon calcination is oxidised to a $V{=}O^{3+}$ species in a trigonal pyramidal environment with three pendant P–O ligands from the framework. Titanium substitutes as Ti^{4+} in a tetrahedral geometry. Both metals are evenly distributed throughout the material and are successfully incorporated into the framework as isolated single sites. Introduction of more metal into the samples results in the formation of clustered, extra-framework species, likely to be V_2O_5-like, that contribute only marginally to catalytic activity and can hinder diffusion through the material, resulting in catalytic drop-off.

All in all, VTi AlPO-5 has proven to be an interesting and powerful catalyst capable of performing a variety of highly selective oxidative transformations, including one-pot bifunctional acid- and redox-catalysed processes (Figure 80).

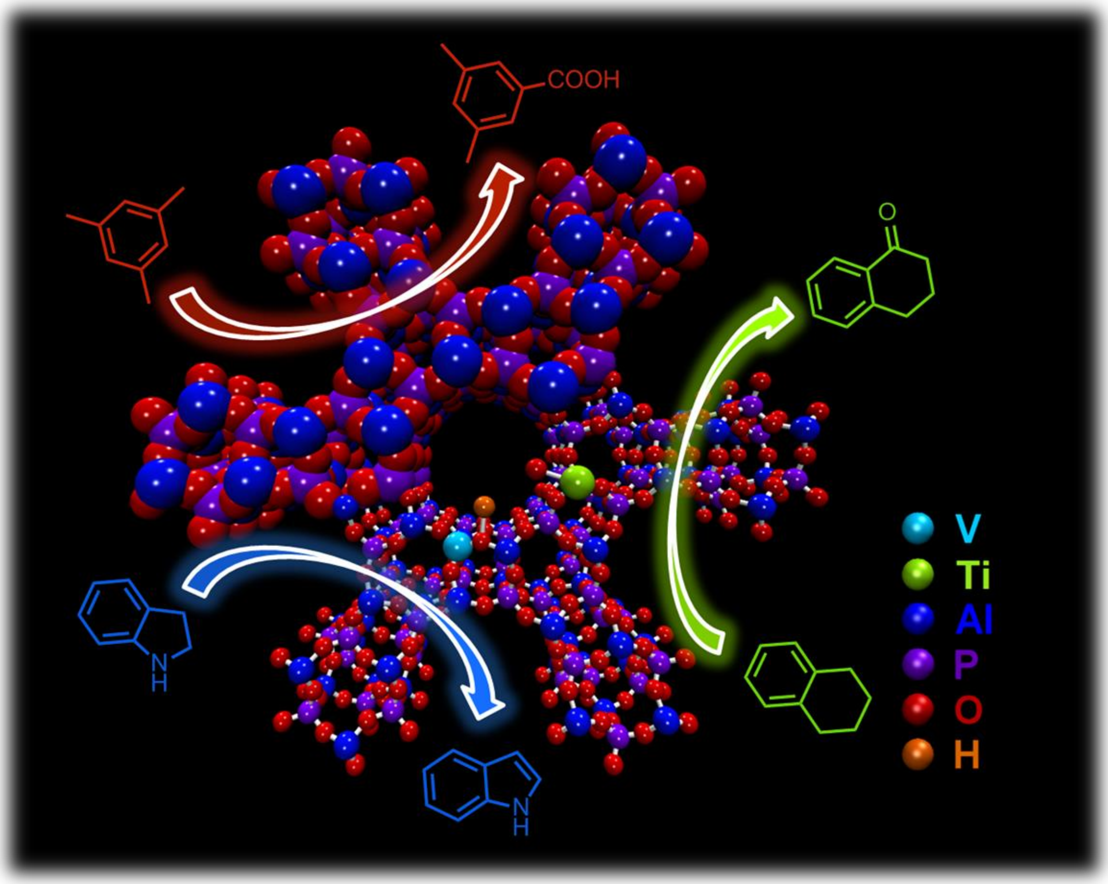

Figure 80: Impression of VTi AlPO-5 showing various reactivities.

7. Future work

Having established several clear trends with regards to the reactivity that can be expected from VTi AlPO-5, and with results showing a high activity and selectivity, several opportunities present themselves for taking advantage of this type of catalyst:

1. Further expansion of the substrate scope. Considering the acid-redox functionalities of the material, a range of oxidation-only, acid-only or acid-redox bifunctional reactions could be explored for a wider range of systems. Ideally, our catalyst could be used as a shelf material to assist in multi-step syntheses as a versatile tool.
2. Use of more or different types of metals. Although VTi acid-redox bifunctional material had successfully been used, inclusion of more or different types of metals, with different characteristics, could possibly be used to afford even more types of reactivity. Using adroitly engineered materials to suit whatever reactivity may be required, expansion of the metal scope of the system could afford a whole range of different catalytic systems.
3. Expanding the framework type to cover a wider range of pore sizes. Use of large-pore analogues could lead to the system's usability on particularly large molecular systems, while small-pore analogues could be explored for imposing size- and shape-selectivity during the reaction, further enhancing the selectivity. Hierarchically porous materials could be used to improve mass transport and speed up the reaction, as well as possibly avoiding pore blockage which might be responsible for the conversion cutoff observed during reactions.
4. Adaptation of the material for flow synthesis. Use in batch synthesis has been successful, and although the reactions have been highly selective, mass-transport and blocking issues appear to limit the yield. When conducted under flow conditions, unreacted starting material could be recovered and fed back, hopefully resulting in a very efficient synthesis.

8. Experimental details

8.1 General methods

All commercial compounds were used without further purification unless noted otherwise.

The solvents used were technical grade and were used without being degassed or dried.

Reaction temperatures refer to the oil bath temperature rather than the *in situ* reaction temperature.

Liquid NMR spectra were recorded at room temperature on a Bruker AV-300 FT-NMR (300 MHz), Bruker AVII400 (400 MHz), Bruker AVIIIHD400 (400 MHz), or Bruker AVIIIHD500 (500 MHz) spectrometer using, unless noted otherwise, dried $CDCl_3$ as solvent.

Vanadium solid-state NMR was performed by Dr Marina Carravetta at 14.1 T on an Agilent DD2 600 MHz spectrometer equipped with a 1.6 mm narrow-bore triple resonance T3 style probe and 1.6 mm rotors using direct acquisition with a small flip angle to excite the NMR signal. The resonance frequency of ^{51}V was referenced to $VOCl_3$. A number of spinning frequencies were used in order to establish the position of the centreband. Simulation and energy minimisation of patterns was also performed by Prof. Carravetta.

Aluminium and phosphorus solid-state NMR was performed at the EPSRC UK National Solid-state NMR Service at Durham using a Varian VNMRS or a Bruker AVIIIHD spectrometer equipped with a 4 mm magic angle spinning probe, using cross-polarisation with a 2 s recycle delay, 3 ms contact time, an ambient probe temperature (~25 °C) and at a sample spin-rate of 10 kHz.

GC data were recorded on a PerkinElmer Clarus 480 Gas Chromatograph using several different programmes.

GCMS data were measured on a Thermoquest trace single quadrupole GCMS at 70 eV with DCM as solvent using various GC programmes.

IR spectra were recorded on a Nicolet 380 FT-IR spectrometer.

Nitrogen adsorption analysis was performed on a Micromeritics Gemini 2375 BET apparatus or a Micromeritics TriStar II 3020.

SEM imaging and EDX analysis were performed on a Philips XL-30 ESEM equipped with Thermo Scientific MagnaRay WDS EDX spectrometer under environmental SEM conditions or a JEOL 7401F field-emission SEM (using an accelerating voltage of 15 kV) equipped with Oxford Inca EDS system.

Powder XRD was performed on a Bruker D2 Phaser or Bruker C2 GADDS diffractometer.

UV-Vis spectroscopy was carried out using a Perkin-Elmer Lambda 750 S NIR/Vis/UV instrument.

EPR spectroscopy was performed on a Bruker EMX MicroX spectrometer. Simulations of obtained patterns were conducted by Stuart Elliott with help from Dr Chris Wedge from the University of Warwick using EasySpin.

ICP-OES was performed by MEDAC Ltd. Samples were digested in a combination of sulfuric and perchloric acids to leave a clear solution for analysis. The resulting solutions were then analysed using a Varian Vista MPX ICP-OES. The calibrations used for the analysis were 1, 2 and 5 ppm standard solutions for vanadium and titanium, and 5, 10 and 20 ppm standard solutions for aluminium and phosphorus analysis.

TLC was performed on pre-coated Merck silica gel F254 plates.

8.2 General procedure for the oxidation of propylbenzene

A mixture of propylbenzene (1.00 g, 8.32 mmol), TBHP (5–6 M in decane, 1.85 mL, 1.35 equiv., or 70% aqueous solution, 1.178 g, 9.15 mmol, 1.1 equiv.) and catalyst (100 mg) was heated in an oil bath at 100 °C for 23 h. The reaction mixture was then cooled to RT and 1,2-dichlorobenzene (0.15 mL, 0.20 g) and 1,2-dichloroethane (0.15 mL, 0.19 g) were added. The reaction products were then analysed by GC and NMR. Reaction parameters such as temperature, catalyst type and amount, reaction duration *etc.* were frequently changed for the various studies described. Spectral data from crude mixtures was ascribed to; 1-propiophenone: ^{1}H-NMR: δ = 8.00–7.93 (2H, m, Ar**H** ortho), 7.55 (1H, m, Ar**H** para), 7.49–7.42 (2H, m, Ar**H** meta), 3.00 (2H, q, J = 7.3, C**H**$_2$Me), 1.23 (3H, t, *J* = 7.3, C**H**$_3$). ^{13}C-NMR: δ = 200.8 (**C**=O), 136.9 (Ar ipso), 132.9 (Ar para), 128.6 (Ar ortho), 128.0 (Ar meta), 31.8 (CO**C**H$_2$), 8.3 (**C**H$_3$). LRMS (EI): m/z = 134 (M), 105 (M–Et), 77 (Ph), 51 (Ph-C_2H_2), 39 (C_3H_3). IR: ν = 3061 (w), 2979 (m), 2873 (m), 1684 (s), 1603 (m), 1582 (m), 1451 (m), 1362 (m), 1280 (m), 1108 (w), 741 (s), 692 (s). 1-Phenyl-1-propanol: ^{1}H-NMR: δ = 7.45–7.25 (5H, m, Ar**H**), 4.60 (1H, td, *J* = 7.6, 3.0, C**H**OH), 2.10 (1H, br. s., O**H**), 1.92-1.70 (2H, m, C**H**$_2$Me), 0.94 (3H, app. t, *J* = 7.5, C**H**$_3$). ^{13}C-NMR: δ = 144.6 (Ar ipso), 128.4 (Ar meta), 127.5 (Ar ortho), 126.0 (Ar para), 76.0 (C**H**OH), 31.9 (C**H**$_2$Me), 10.1 (C**H**$_3$). LRMS (EI): m/z = 136 (M), 107.1 (M–Et), 91 (tropylium), 77 (Ph), 51 (Ph–C_2H_2). Benzoic acid: ^{1}H-NMR: δ = 12.6 (1H, br. s., COO**H**), 8.19–8.13 (2H, m, Ar-**H** ortho), 7.65 (1H, tt, *J* = 7.6, 1.2, Ar-**H** para), 7.51 (2H, app. tt, *J* = 7.8, 1.5, Ar-**H** meta). ^{13}C-NMR: δ = 172.1 (**C**OOH), 133.8 (Ar para), 130.2 (Ar ortho), 129.3 (Ar ipso), 128.5 (Ar meta). LRMS (EI): m/z = 121 (M), 104 (M–OH), 77 (Ph), 51 (Ph–C_2H_2). IR: ν = 2500–3300 (m), 3060 (m), 1684 (s), 1597 (w), 1456 (w), 1322 (m), 710 (s).

8.3 General procedure for the oxidation of tetralin

Tetrahydronaphthalene (1.00 g, 7.56 mmol), TBHP (5–6 M in decane, 1.66 mL, 1.35 equiv.) and the catalyst (100 mg) were heated in an oil bath at 80–100 °C for 23 h. The reaction mixture was then allowed to cool to room temperature and the internal standards were added (1,2-dichlorobenzene, 0.15 m, 0.20 g, and isopropanol, 0.15 mL, 0.12 g). The reaction products were analysed by GC and NMR. Reaction parameters such as temperature and reaction duration were changed for the various studies described. Spectral data from crude mixtures was ascribed to; 1-tetralone: ^{1}H-NMR: δ = 8.05 (1H, d, *J* = 7.8, 0.9, **H9**), 7.48 (1H, td, *J* = 7.5, 1.3, **H7**), 7.32 (1H, t, *J* = 7.4, **H8**), 7.27 (1H, d, *J* = 7.6, **H6**), 2.98 (2H, app. t, *J* = 6.1, **H2**), 2.67 (2H, app. t, *J* = 6.3, **H4**), 2.15 (2H, app. quint, *J* = 6.3, **H3**). ^{13}C-NMR: δ = 198.4 (**C1**), 144.5 (**C5**), 133.4 (**C7**), 132.6 (**C10**), 128.8 (**C9**), 127.2 (**C6**), 126.6 (**C8**), 39.2 (**C2**), 29.7 (**C4**), 23.3 (**C3**). LRMS (EI): m/z = 146 (M), 118 (M–CO), 90 (C_7H_6), 77 (Ph), 51 (Ph-C_2H_2), 39 (C_3H_3). IR: 3069 (w), 2922 (m), 2848 (m), 1684 (s), 1596 (m), 1452 (s), 1321 (m), 1286 (s), 1226 (m), 1285 (s), 1187 (m), 1116 (m), 1029 (m), 907 (w), 761 (s), 729 (s), 654 (m), 548 (m).

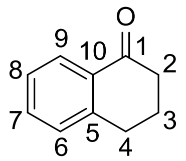

8.4 General procedure for the catalytic oxidation of indan

A mixture of indan (1.00 g, 8.46 mmol), TBHP (5–6 M in decane, 1.86 mL, 1.35 equiv.) and the catalyst (100 mg) was heated at 80–100 ˚C for 23 h. The reaction mixture was then cooled to room temperature and the internal standards were added; bromobenzene (0.15 mL, 0.22 g) and 1,2-dichloroethane (0.15 mL, 0.19 g). Reaction products were analysed by GC and NMR. Reaction parameters such as temperature and reaction duration were changed for the various studies described. Spectral data from crude mixtures was ascribed to; indan-1-one: ^{1}H-NMR: δ = 7.79 (2H, d, *J* = 7.6, **H8**), 7.62 (1H, td, *J* = 7.6, 1.0, **H6**), 7.51 (1H, d, *J* = 7.6, **H5**), 7.40 (1H, t, *J* = 7.6, **H7**), 3.18 (2H, t, *J* = 5.6, **H3**), 2.76–2.68 (2H, m, **H2**). ^{13}C-NMR: δ = 207.1 (**C1**), 155.2 (**C4**), 137.1 (**C9**), 134.6 (**C6**), 127.3 (**C7**), 126.7 (**C5**), 123.8 (**C8**), 36.2 (**C2**), 25.8 (**C3**). LRMS (EI): m/z = 132 (M), 104 (M–CO), 77 (Ph), 51 (Ph–C_2H_2), 39 (C_3H_3). IR: 2927 (m), 2852 (w), 1708 (s), 1601 (m), 1463 (m), 1435 (m), 1333 (m), 1274 (m), 1242 (m), 1199 (m), 1171 (m), 1088 (w), 1037 (m), 820 (w), 753 (s), 560 (m).

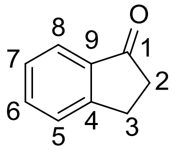

8.5 General procedure for the oxidation of toluene

Toluene (laboratory reagent grade, 1.00 g, 10.8 mmol), TBHP (5–6 M in decane, 2.38 mL, 1.35 equiv.) and the catalyst (100 mg) were heated at 80–100 ˚C for 23 h. The reaction mixture was then cooled to RT and internal standards 1,2-dichlorobenzene (0.15 mL, 0.20 g) and 1,2-dichloroethane (0.15 mL, 0.19 g) were added. The reaction products were analysed by NMR or isolated by extraction from light petroleum ether with 1 M NaOH solution. The aqueous phase was then acidified with H_2SO_4 and extracted three times with DCM. The organic extracts were combined, dried over $MgSO_4$, and concentrated *in vacuo* to afford the product as a colourless solid. Yield: 0.500 g (37.8%). For various studies, reaction parameters such as temperature, duration *etc.* were routinely changed. Benzoic acid: ^{1}H-NMR: δ = 8.05 (2H, d, *J* = 7.3, Ar**H** ortho), 7.55 (1H, t, *J* = 7.3, Ar**H** para), 7.41 (2H, t, *J* = 7.70, Ar**H** meta), COO**H** not observed. ^{13}C-NMR: δ = 171.6 (**C**OOH), 133.7 (Ar para), 130.2 (Ar ortho), 129.3 (Ar ipso), 128.5 (Ar meta). LRMS (EI): m/z = 122 (M), 105 (M–OH), 77 (Ph), 51 (Ph–C_2H_2), 39 (C_3H_3). IR: 3068 (w), 2962 (m), 2922 (m), 2848 (m), 2674 (w), 2556 (w), 1684 (s), 1601 (w), 1585 (w), 1459 (m), 1424 (m), 1329 (m), 1293 (s), 1187 (w), 1072 (w), 1025 (m), 934 (m), 804 (m), 706 (s), 666 (m), 552 (w).

8.6 Oxidation of *o*-xylene

A mixture of *o*-xylene (1.00 g, 9.42 mmol), TBHP (5–6 M in decane, 2.07 mL, 1.35 equiv.) and the catalyst (100 mg) was heated at 100 °C for 23 h. After the reaction, the mixture was cooled to RT and 1,2-dichlorobenzene (0.15 mL, 0.20 g) and 1,2-dichloroethane (0.15 mL, 0.19 g) were added. The reaction products were analysed by NMR or isolated by extraction with 1 M aqueous NaOH from light petroleum ether. The aqueous phase was acidified with H_2SO_4, then extracted three times with DCM. The organic phase was separated off, dried over $MgSO_4$ and concentrated *in vacuo* to afford the product as a colourless solid (0.370 g, 32.5%). 2-Toluic acid: ^{1}H-NMR: δ = 8.09 (1H, dd, *J* = 7.8, 1.2, **H3**), 7.48 (1H, td, *J* = 7.3, 1.0, **H5**), 7.34–7.26 (2H, m, **H6** & **H4**), 2.69 (3H, s, **H8**), COO**H** not observed. ^{13}C-NMR: δ = 172.3 (**C1**), 141.3 (**C7**), 132.9 (**C5**), 131.9 (**C6**), 131.5 (**C3**), 128.3 (**C2**), 125.8 (**C4**), 22.1 (**C8**). LRMS (EI): m/z = 136 (M), 118 (M–H_2O), 105, 91 (tropylium), 77 (Ph), 64, 51, 39 (C_3H_3). IR: 2962 (m), 2925 (m), 2876 (m), 2652 (m), 1683 (s), 1601 (m), 1573 (m), 1487 (m), 1409 (m), 1315 (s), 1299 (s), 1270 (s), 1086 (m), 919 (m), 804 (w), 735 (s), 649 (m), 563 (m), 534 (m), 485 (w).

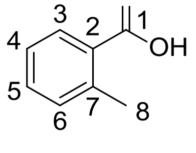

8.7 Oxidation of *p*-xylene

A mixture of *p*-xylene (1.00 g, 9.42 mmol), TBHP (5–6 M in decane, 2.07 mL, 1.35 equiv.), and the catalyst (100 mg) were stirred at 100 °C for 23 h. The mixture was allowed to cool to RT and internal standards 1,2-dichlorobenzene (0.15 mL, 0.20 g) and 1,2-dichloroethane (0.15 mL, 0.19 g) were added. The reaction products were analysed by NMR or isolated by basic extraction with 1 M NaOH from light petroleum ether. The aqueous phase was acidified with H_2SO_4 and extracted three times with DCM. The extracts were dried over $MgSO_4$ and concentrated *in vacuo* to afford a colourless solid (0.309 g, 27.1%). 4-Toluic acid: ^{1}H-NMR: δ = 8.03 (2H, d, *J* = 8.1, C**H**$_2$CCOOH), 7.30 (2H, d, *J* = 8.1, C**H**$_2$CCH$_3$), 2.46 (3H, s, C**H**$_3$), COO**H** not observed. ^{13}C-NMR: δ = 171.9 (**C**OOH), 144.6 (**C**CH$_3$), 130.3 (**C**HCCOOH), 129.2 (**C**HCCH$_3$), 126.6 (**C**COOH), 21.7 (**C**H$_3$). LRMS (EI): m/z = 136 (M), 119 (M–OH), 91 (119–C=O), 77 (Ph), 65 (C_5H_5), 51 (C_4H_3), 39 (C_3H_3) . IR: 2970 (m), 2917 (m), 2672 (m), 2549 (m), 2357 (m), 1683 (s), 1613 (m), 1576 (w), 1515 (w), 1417 (m), 1323 (m), 1286 (s), 1184 (m), 1184 (m), 1151 (w), 1021 (w), 963 (m), 841 (m), 751 (s), 698 (w), 608 (w), 543 (m), 461 (m).

8.8 Oxidation of mesitylene

Mesitylene (1.00 g, 8.32 mmol, Sigma), TBHP (5–6 M in decane, 1.85 mL, 1.35 equiv.) and catalyst (100 mg) were mixed and heated at 100 °C for 23 h. The reaction mixture was then allowed to cool to RT and two internal standards were added; 1,2-dichlorobenzene (0.15 mL, 0.20 g) and 1,2-dichloroethane (0.15 mL, 0.19 g). The products were analysed by NMR or isolated by alkaline extraction with 1 M NaOH from light petroleum ether followed by acidification with H_2SO_4 and subsequent extraction with DCM. The organic extracts were combined, dried with $MgSO_4$, and then concentrated *in vacuo* to afford a colourless powder (0.395 g, 31.5%). 3,5-Dimethylbenzoic acid: ^{1}H-NMR: δ = 7.76 (2H, s, **H3**), 7.28 (1H, s, **H6**), 2.40 (6H, s, **H5**), COO**H** not observed. ^{13}C-NMR: δ = 171.8 (**C1**), 138.2 (**C4**), 135.4 (**C6**), 129.1 (**C2**), 127.9 (**C3**), 21.1 (**C5**). LRMS (EI): m/z = 150 (M), 133 (M–OH), 105 (133–C=O), 91 (tropylium), 77 (Ph), 65 (C_5H_5), 51 (C_4H_3), 39 (C_3H_3). IR: 2970 (m), 2913 (m), 2851 (m), 2712 (m), 2610 (m), 2533 (m), 1687 (s), 1601 (m), 1458 (m), 1421 (m), 1315 (s), 1241 (s), 1119 (w), 1041 (w), 935 (w), 869 (m), 767 (m), 722 (m), 673 (m), 579 (w), 498 (w), 420 (w).

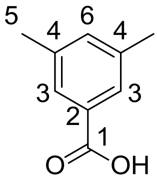

8.9 Oxidation of durene

A mixture of durene (1.00 g, 7.45 mmol), TBHP (5-6 M in decane, 1.64 mL, 1.35 equiv.) and the catalyst was heated at 100 °C for 23 h. After the reaction, this was cooled to RT and the internal standards 1,2-dichlorobenzene (0.15 mL, 0.20 g) and 1,2-dichloroethane (0.15 mL, 0.19 g) were added. The products were analysed by NMR or extracted from light petroleum ether with 1 M NaOH solution. The aqueous extracts were acidified with H_2SO_4 and extracted with DCM. The organic extracts were combined and dried over $MgSO_4$, then concentrated *in vacuo* yielding a colourless powder (0.536 g, 43.1%). Durylic acid: ^{1}H-NMR: δ = 7.77 (1H, s, **H10**), 6.97 (1H, s, **H5**), 2.51 (3H, s, **H4**), 2.21 (3H, s, **H9/7**), 2.20 (3H, s, **H9/7**). ^{13}C-NMR: δ =172.1 (**C1**), 142.3 (**C3**), 138.8 (**C6**), 134.0 (**C8**), 133.3 (**C5**), 132.7 (**C10**), 125.4 (**C2**), 21.5 (**C4**), 19.8 (**C7**), 19.1 (**C9**). LRMS (EI): m/z =164 (M), 146 (M-HOH), 119 (M-COOH), 118 (119-H), 105 (C_8H_9), 91 (tropylium), 77 (Ph), 65 (C_5H_5), 51 (C_4H_3), 39 (C_3H_3). IR: 3019 (m), 2966 (m), 2917 (m), 2864 (m), 2639 (m), 2561 (m), 2357 (w), 1674 (s), 1609 (m), 1552 (m), 1499 (m), 446 (m), 1409 (m), 1311 (m), 1262 (s), 1200 (m), 1156 (m), 1033 (w), 919 (w), 861 (w), 808 (w), 788 (m), 751 (m), 718 (m), 604 (w), 575 (w), 436 (m).

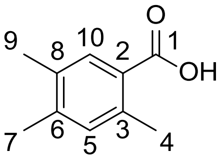

8.10 Oxidation of indoline

Indoline (1.00 g, 8.39 mmol), TBHP (5-6 M in decane, 1.85 mL, 1.35 equiv.) and the catalyst (100 mg) were heated at 100 °C for 23 h. After the reaction, the mixture was cooled to RT. Internal standards 1,2-dichlorobenzene (0.15 mL, 0.20 g) and isopropanol (0.15 mL, 0.12 g) were subsequently added. The reaction products were analysed by GC and NMR. Spectral data from crude mixtures was ascribed to; Indole: ^{1}H-NMR: δ = 8.16 (1H, br. s, N**H**), 7.69 (1H,

dd, *J* = 8.1, 0.7, **H5**), 7.43 (1H, dd, *J* = 8.1, 0.7, **H2**), 7.24 (1H, app. t, *J* = 2.9, **H3**), 7.21 (1H, app. d, *J* = 1.2, **H8**), 7.14 (1H, ddd, *J* = 7.7, 6.9, 1.1, **H4**), 6.59 (1H, ddd, J = 3.1, 2.1, 0.9, **H7**). ^{13}C-NMR: δ = 135.8 (**C1**), 127.9 (**C6**), 124.1 (**C8**), 122.0 (**C4**), 120.7 (**C5**), 119.8 (**C3**), 111.0 (**C2**), 102.7 (**C7**). MS (EI): m/z = 117 (M), 90 (M-C_2H_3), 89 (M-NHCH), 63 (C_5H_3), 58, 39 (C_3H_3). IR: 3412 (m), 3057 (w)m 2962 (w), 2926 (w), 2851 (w), 1656 (w), 1613 (m), 1577 (m), 1510 (w), 1483 (m), 1459 (m), 1412 (m), 1349 (m), 1337 (m), 1250 (w), 1199 (w), 1155 (w), 1128 (w), 1084 (w), 1033 (m), 1005 (w), 895 (m), 737 (s), 658 (m), 603 (m).

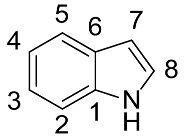

8.11 Oxidation of tetrahydroquinoline

Tetrahydroquinoline (1.00 g, 7.51 mmol), TBHP (5-6 M in decane, 1.82 mL, 1.35 equiv.), and the catalyst (100 mg) were heated at 100 °C for 23 h. The reaction mixture was cooled down to RT and internal standards 1,2-dichlorobenzene (0.15 mL, 0.20 g, BDH) and 1,2-dichloroethane (0.15 mL, 0.19 g) were added. The reaction products were analysed by GC and NMR. Spectral data from crude mixtures was ascribed to; ^{1}H-NMR: δ = 8.93 (1H, dd, *J* = 4.3, 1.7, **H9**), 8.22-8.08 (2H, m, **H2** & **H7**), 7.82 (1H, dd, *J* = 8.1, 0.9, **H5**), 7.73 (1H, ddd, *J* = 8.4, 7.1, 1.3, **H3**), 7.55 (1H, ddd, *J* = 8.1, 7.1, 1.0, **H4**), 7.39 (1H, dd, *J* = 8.3, 4.2, **H8**). ^{13}C-NMR: δ = 150.4 (**C9**), 148.3 (**C1**), 136.0 (**C7**), 129.5 & 129.4 (**C2** & **C3**), 128.3 (**C6**), 127.8 (**C5**), 126.5 (**C4**), 121.0 (**C8**). MS (EI): m/z = 128 (M-H), 102 (M-CHN), 76 (102-C_2H_2), 50 (C_4H_2), 39 (C_3H_3). IR: 3052 (m), 2952 (m), 1679 (m), 1601 (m), 1499 (s), 1454 (w), 1429 (w), 1364 (w), 1307 (s), 1274 (m), 1110 (m), 1033 (m), 1008 (w), 935 (w), 800 (s), 780 (s), 735 (s), 653 (w), 608 (m).

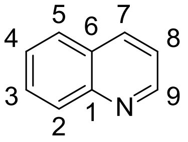

8.12 General procedure for the synthesis of VTi AlPO-5

This procedure was adapted from procedures by Paterson[158] and Leithall.[159] In a Teflon beaker $Al(OH)_3$ (hydrate, 50 mmol – y% ≈ 3.55 g for 9% V) was added portion-wise to H_3PO_4 (1.5 equiv. – x% ≈ 5.1 mL for 1% Ti, 85% in water) in purified water (20 mL). The mixture was stirred for 45 min, then, $Ti(O\textit{i}\text{-}Pr)_4$ (x% ≈ 0.15 mL for 1% Ti) and a solution of $VOSO_4$ (y% ≈ 1.06 g for 9% V) in purified water (20 mL) were added dropwise, simultaneously, colouring the solution a deep blue. The mixture was stirred for one hour, then, Cy_2MeN (8.57 mL, 0.8 equiv.) and purified water (1–3% V: 8.5 mL, 6% V: 15 mL, 7.5% V: 17.5 mL, 9% V: 20 mL, 12% V: 25 mL) were added. After another hour of stirring, the resulting milky light blue suspension was divided equally over two Teflon-lined autoclaves and heated at 180 °C for 2 h in a pre-heated, fan-assisted oven. After this, the autoclaves were quenched in ice and left to cool for at least 15 min (if big particles were desired, the autoclaves were allowed to cool on their own overnight). The resulting grey-green powder was washed with 1 L of purified water and dried overnight at 60 °C. The dried, grey-blue powder was ground using a mortar and pestle, put through a 90 micron sieve, and analysed for phase purity using PXRD. Upon confirmation of AFI phase purity, the sample was calcined in air at 550 °C for 16 h in a tube furnace. This turned the colour a bright golden yellow. A summary of all gel compositions is shown in Table 10.

8.13 General procedure for the synthesis of non-VTi AlPO-5 (bi- and monometallic)

This procedure was adapted from procedures by Paterson[158] and Leithall.[159] To H_3PO_4 (1.5 equiv. – x% ≈ 5.1 mL for 1% Ti, 85% in water) in deionised water (20 mL) in a Teflon beaker was added $Al(OH)_3$ (hydrate, 50 mmol – y% ≈ 3.55 g for 9% V) portionwise. After 45 min of stirring, metal salts or solutions thereof for whatever dopants were desired were added (vanadium: $VOSO_4$, titanium: $Ti(O\textit{i}\text{-}Pr)_4$, cobalt: $Co(OAc)_2$, chromium: $Cr(NO_3)_3$, manganese: $Mn(OAc)_2$, nickel: $Ni(OAc)_2$) along with or in deionised water (20 mL) were added dropwise (simultaneously, if using multiple dopants), generally changing the colour of the solution except when using only titanium. After an hour of stirring, Cy_2MeN (8.57 mL, 0.8 equiv.) and deionised water were added (the volume depending on the amount and type of dopants employed). After another hour of stirring, the resulting suspension was divided equally over two Teflon-lined autoclaves and heated at 180 ˚C for 2 h in a pre-heated, fan-assisted oven. After this, the autoclaves were quenched in ice and left to cool for at least 15 min (if big particles were desired, the autoclaves were allowed to cool down on their own overnight). The resulting solid was washed with 1 L of deionised water and dried overnight at 60 ˚C (for colours, see below). The dried powder was ground using a mortar and pestle, put through a 90 micron sieve, and analysed for phase purity using PXRD. Upon confirmation of AFI phase purity, the sample was calcined in air at 550 ˚C for 16 h in a tube furnace (for colours, see below). Sample colours: V AlPO-5: grey-blue (dried), bright yellow (calcined). Ti AlPO-5: white (dried), white to light yellow (calcined). Co and CoTi AlPO-5; deep blue (dried), green (calcined). VCo AlPO-5: dark blue (dried), yellow-brown (calcined). VCr AlPO-5: dark green (dried), brown (calcined). VMn AlPO-5: grey-green (dried), gold (calcined). VNi AlPO-5: grey-green (dried), bright yellow (calcined).

8.14 Procedure for recycling study 1

Propylbenzene (1.00 g, 8.32 mmol, Sigma), TBHP (5–6 M in decane, 1.85 mL, 1.35 equiv.) and catalyst (9/1 VTi AlPO-5, 100 mg) were heated in a 100 ˚C oil bath for 23 h. The mixture was cooled to RT and then the liquids were siphoned off using a syringe. To the siphoned liquids were added 1,2-dichlorobenzene (0.75 mL, 0.98 g) and 1,2-dichloroethane (0.15 mL, 0.19 g) prior analysis by GC and NMR. The reaction was rerun three more times using the same catalyst and procedure. After the third rerun (fourth run), the solids were recovered from the flask and washed with acetone and DCM, and analysed using PXRD.

8.15 Procedure for recycling study 2

Propylbenzene (2.00 g, 16.64 mmol), TBHP (5–6 M in decane, 3.70 mL, 1.35 equiv.) and the catalyst (9/1 VTi AlPO-5, 200 mg) were heated in a 100 ˚C oil bath for 23 h, after which the reaction mixture was cooled to RT. 1,2-dichlorobenzene (0.75 mL, 0.98 g) and 1,2-dichloroethane (0.15 mL, 0.19 g) were then added. The reaction mixture was filtered and analysed by GC and NMR. The remaining solids were washed with acetone and DCM, dried, recalcined in air at 550 ˚C for 16 h and examined by PXRD. The whole procedure was repeated two more times, scaling down the amount of oxidant and substrate according to the amount of catalyst recovered after every recalcination step.

8.16 Procedure for recycling study 3

A mixture of propylbenzene (2.00 g, 16.64 mmol), TBHP (5–6 M in decane, 3.70 mL, 1.35 equiv.) and catalyst (1/1 VTi AlPO-5, 200 mg) was heated in a 100 °C oil bath for 23 h. The reaction mixture was then cooled to RT and 1,2-dichlorobenzene (0.75 mL, 0.98 g) and 1,2-dichloroethane (0.15 mL. 0.19 g). The mixture was filtered and analysed by GC and NMR. The remaining solids were washed with acetone and DCM, dried, and analysed by PXRD. After this, the sample was recalcined in air at 550 °C for 16 h, and analysed by PXRD again. The procedure was repeated two more times, scaling down the amount of oxidant and substrate according to the amount of catalyst recovered after every recalcination step.

8.17 Procedure for recycling study 4

Propylbenzene (1.00 g, 8.32 mmol), TBHP (5–6 M in decane, 1.85 mL, 1.35 equiv.) and catalyst (9/1, 1/1 or 0.1/1 VTi AlPO-5, 100 mg) were heated in an oil bath at 100 °C for 23 h. The mixture was then cooled to RT and the liquids were siphoned off using a syringe. To the siphoned liquids were added 1,2-dichlorobenzene (0.75 mL,0.98 g) and 1,2-dichloroethane (0.15 mL, 0.19 g). The mixture was analysed by GC and NMR and the reaction was rerun three more times using the same catalyst and procedure.

8.18 Hot-filtration study

A mixture of propylbenzene (1.00 g, 8.32 mmol), TBHP (5–6 M in decane, 1.85 mL, 1.35 equiv.) and catalyst (9/1 or 1/1 VTi AlPO-5, 100 mg) was heated in an oil bath at 100 °C. After 4 hours, the reaction mixture was taken up in a syringe using a screw-on syringe filter and transferred to a new flask. The reaction mixture was then re-heated at 100 °C for another 19 hours and subsequently cooled down to RT. 1,2-dichlorobenzene (0.15 mL, 0.20 g) and 1,2-dichloroethane (0.15 mL, 0.19 g) were added prior to analysis by GC and NMR.

8.19 Leaching study

A mixture of propylbenzene (typically 1.00 g, 8.32 mmol), TBHP (5–6 M in decane, 1.85 mL, 1.35 equiv.) and catalyst (9/1 or 1/1 VTi AlPO-5, 100 mg) was heated in an oil bath at 100 °C. After 23 h, the reaction mixture was filtered using a screw-on syringe filter, and the filtrate was analysed by ICP-OES analysis.

8.20 Synthesis of APB

To AcOOH (32% in H_2O, 4 mL) was added $Na_2B_4O_7$ (2.00 g, 10.0 mmol) slowly. The mixture was gently stirred over two to four days, until the mixture had turned solid. The solids were transferred to a Petri dish and dried overnight at 60 °C. The resulting dried flakes were ground in a mortar and pestle and its peroxide content assayed by iodometric titration *in triplo*. Typical peroxide content: 20–25%.

9. Appendix

9.1 Calibration of GC response factors

To determine the amounts of individual compounds in the reaction mixture using gas chromatography, one can use the signal-to-signal ratio of these compounds to an internal or external standard. However, as the detector responds with varying intensity to each compound, it is necessary to calibrate the response intensity of these compounds to the standard. The factor by which these relate is called the response factor. To determine this factor, one should correlate the signal-to-signal ratio of a compound to the standard using known amounts of both entities. This should preferably be done at several compound-to-standard ratios (to ascertain a linear correlation – if this was not the case, a calibration would only work within the span of compound-to-standard ratios calibrated for).

To ensure applicability and accuracy of the response factor, a series of six samples, measured in triplicate in random order, was run for the starting material (propylbenzene) as well as the three main reaction products (propiophenone, 1-phenyl-1-propanol, and benzoic acid). The results are outlined below. The inclination of trendline to the plots below shows the response factor of that compound to the standard, while the R^2-factor shows the accuracy of the fit.

Note that for ^{1}H-NMR, no response factor to the internal standard was calculated, as by definition nuclei of the same type resonate with equal intensity with only minor skewing across a spectrum. Although for some types of nuclei the signal-to-noise ratio disqualifies quantification using integration of NMR signals, ^{1}H-NMR is among the most sensitive and noiseless types of NMR, making quantification quite facile in the absence of overlapping signals. Nonetheless, for certain experiments, relative per-peak response rates were determined using standards to verify this.

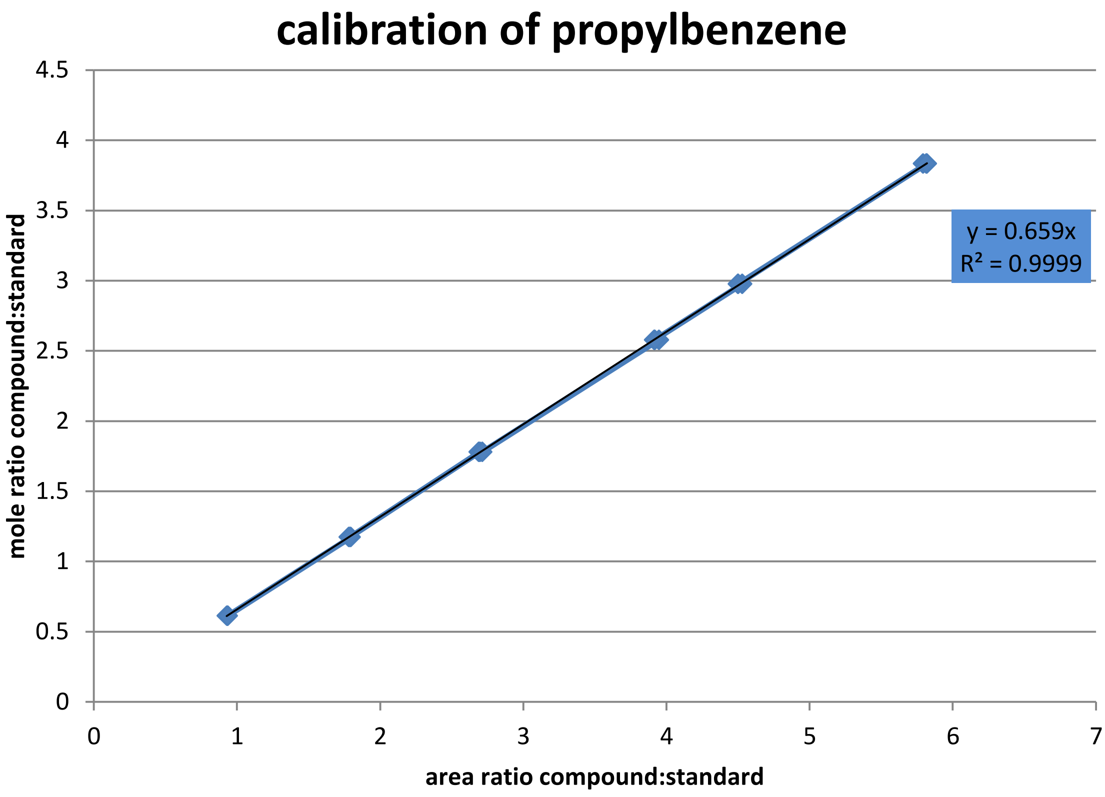

Figure 81: GC calibration series of propylbenzene relative to 1,2-dichlorobenzene.

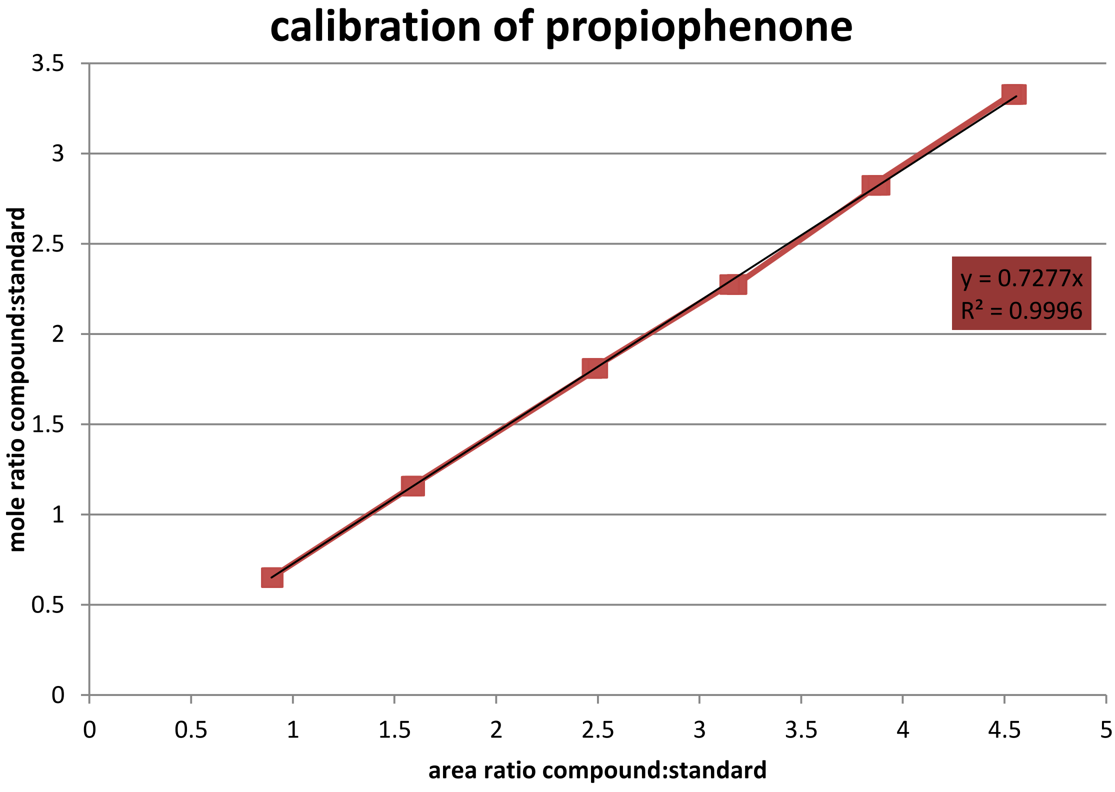

Figure 82: GC calibration series of propiophenone relative to 1,2-dichlorobenzene.

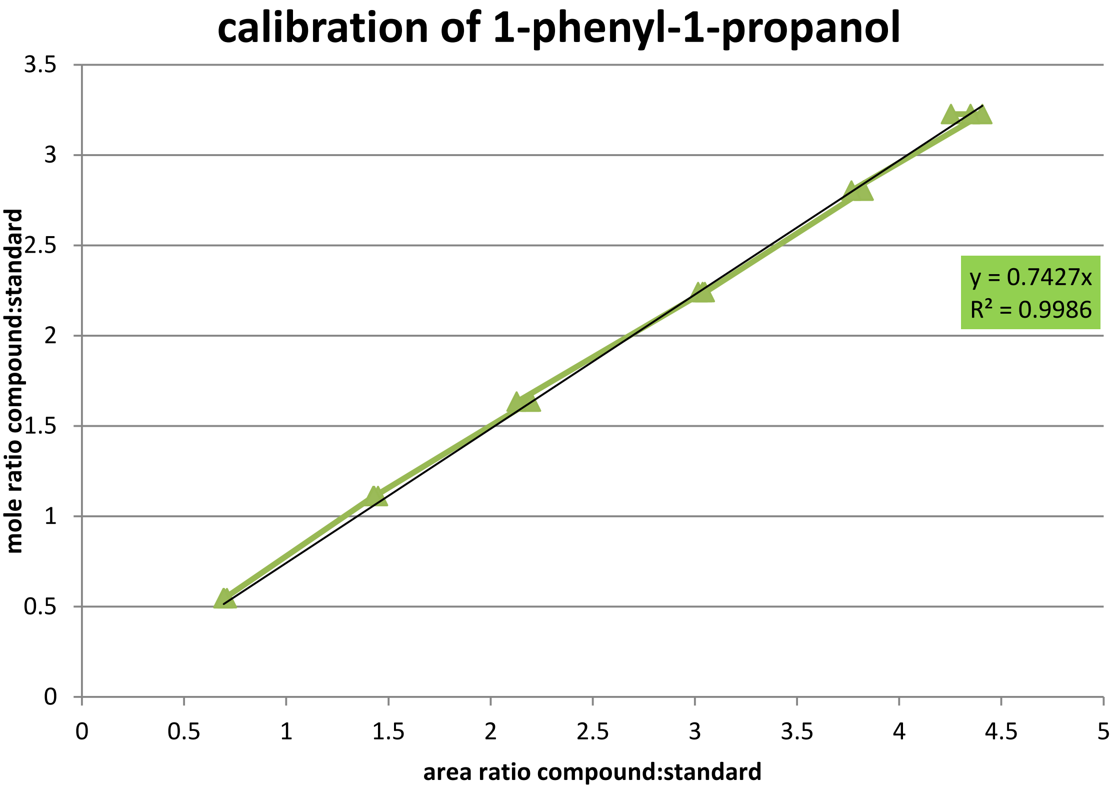

Figure 83: GC calibration series of 1-phenyl-1-propanol relative to 1,2-dichlorobenzene.

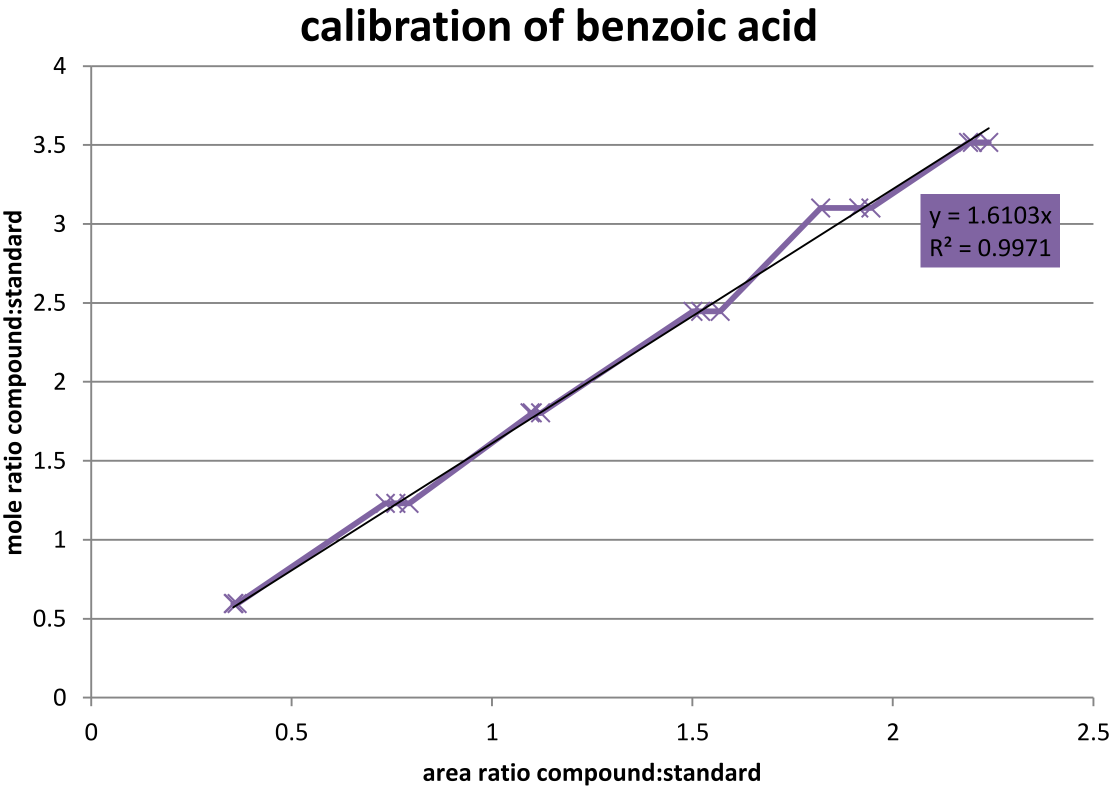

Figure 84: GC calibration series of benzoic acid relative to 1,2-dichlorobenzene.

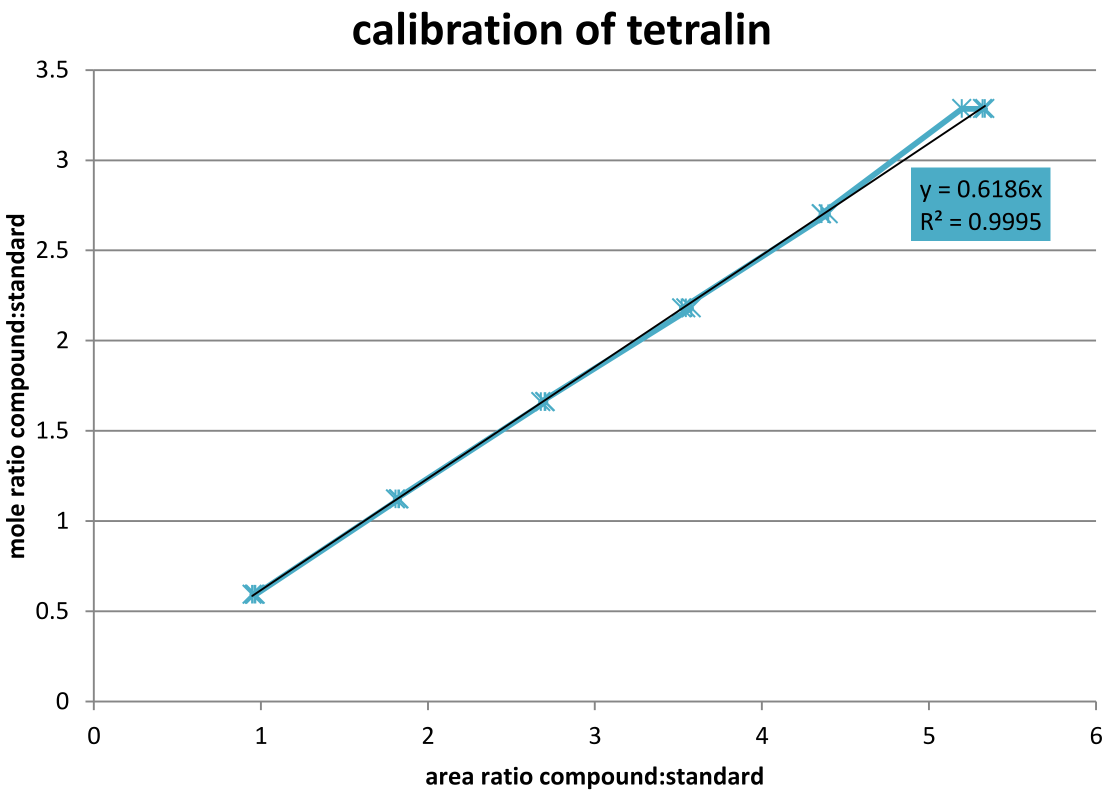

Figure 85: GC calibration series of tetralin relative to 1,2-dichlorobenzene.

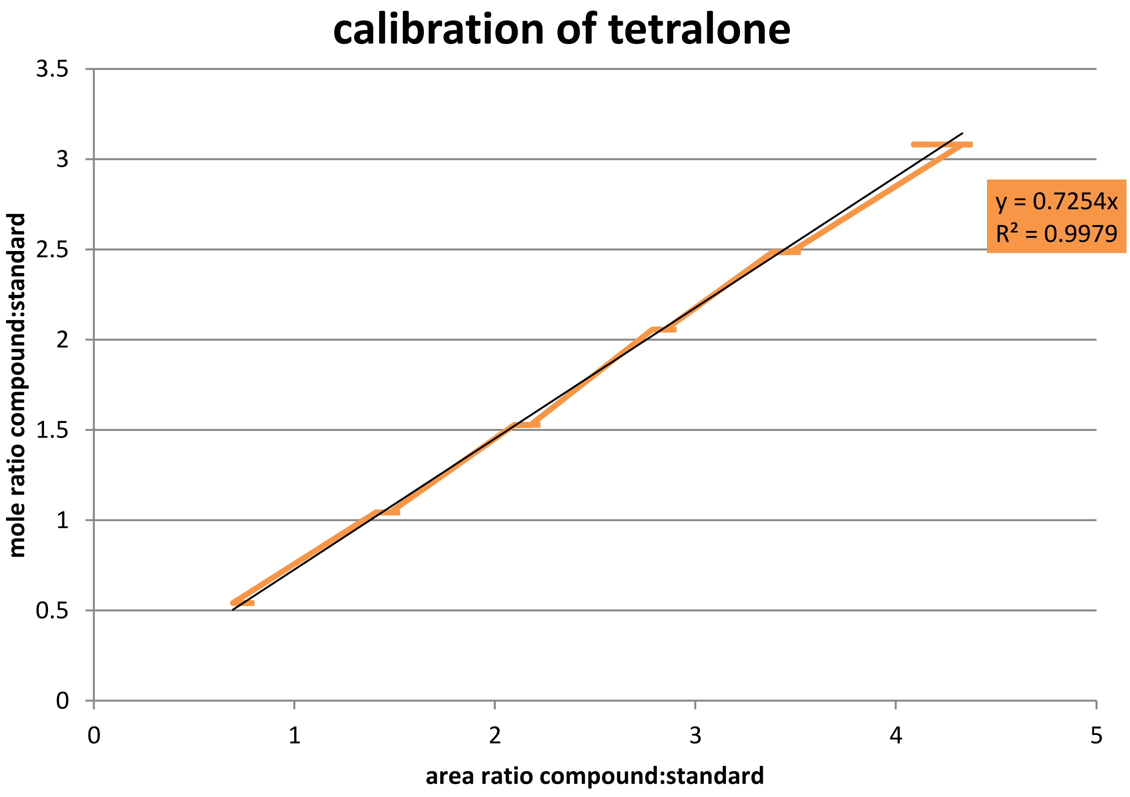

Figure 86: GC calibration series of 1-tetralone relative to 1,2-dichlorobenzene.

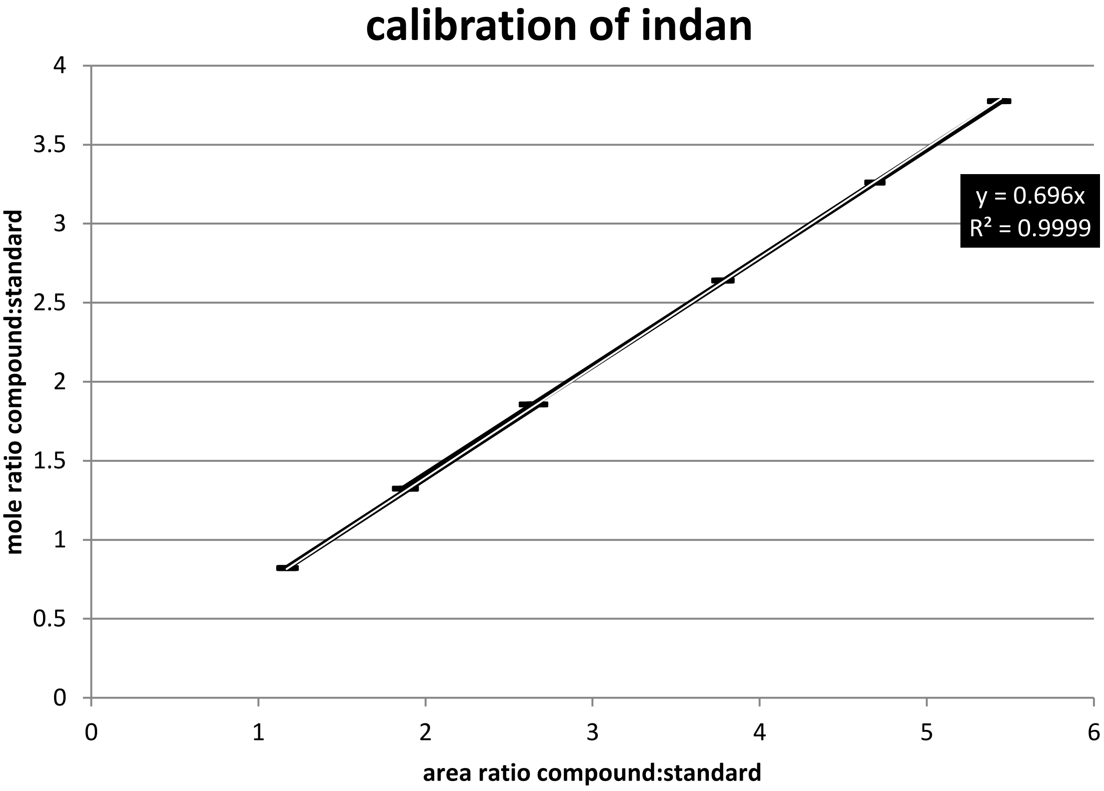

Figure 87: GC calibration series of indan relative to bromobenzene.

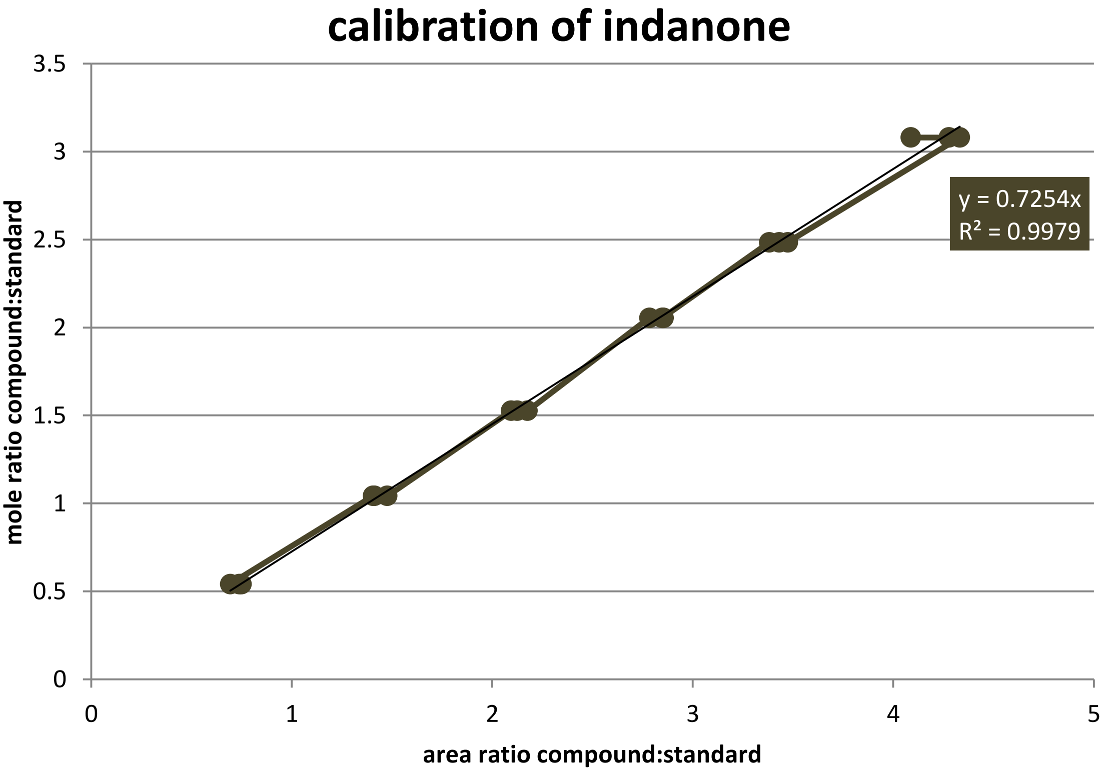

Figure 88: GC calibration series of 1-indanone relative to bromobenzene.

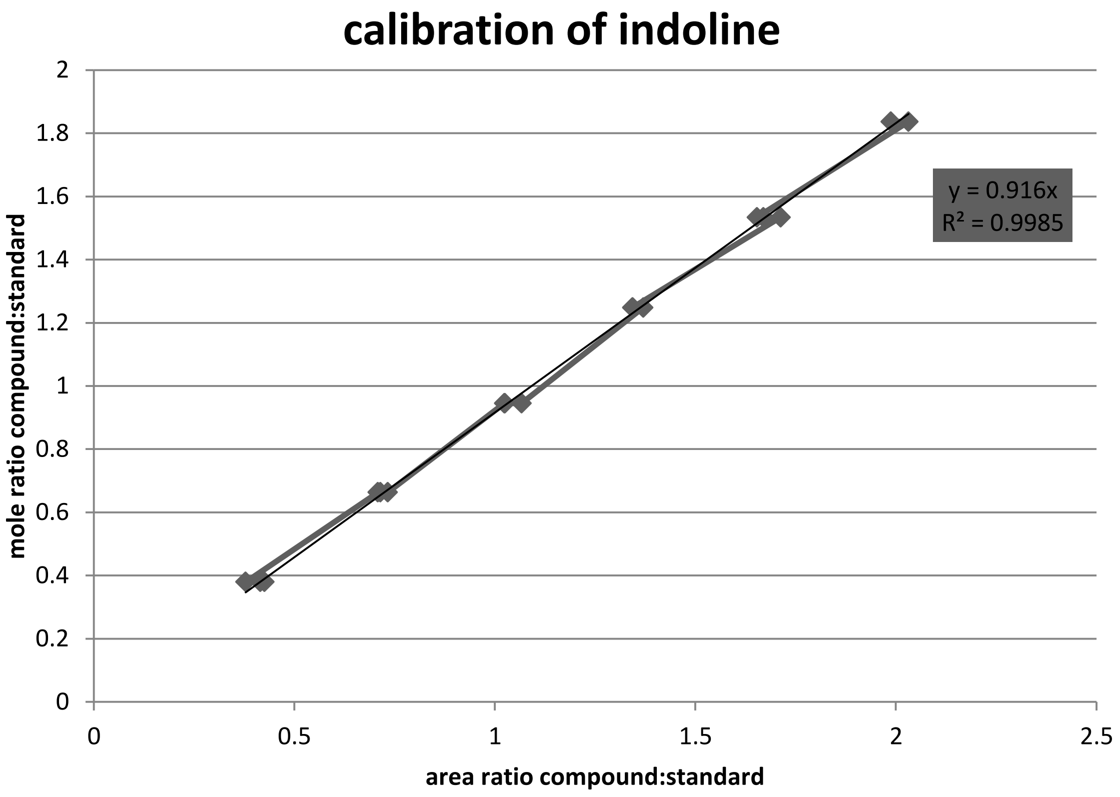

Figure 89: GC calibration series of indoline relative to 1,2-dichlorobenzene.

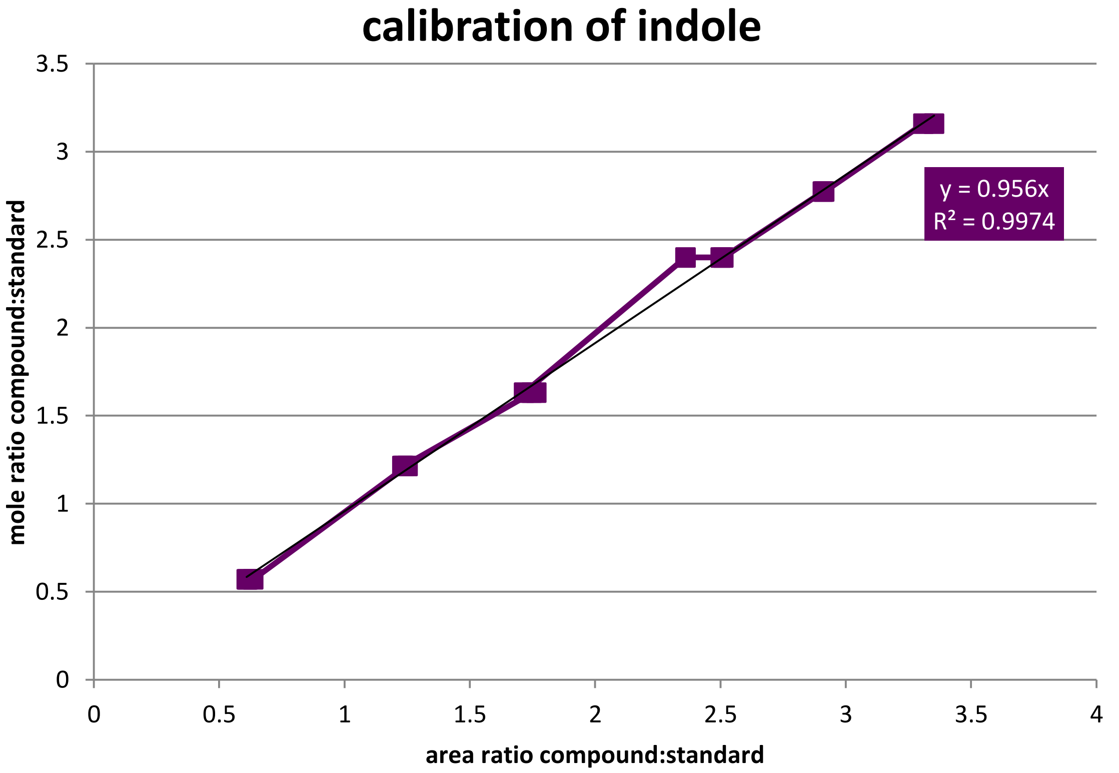

Figure 90: GC calibration series of indole relative to 1,2-dichlorobenzene.

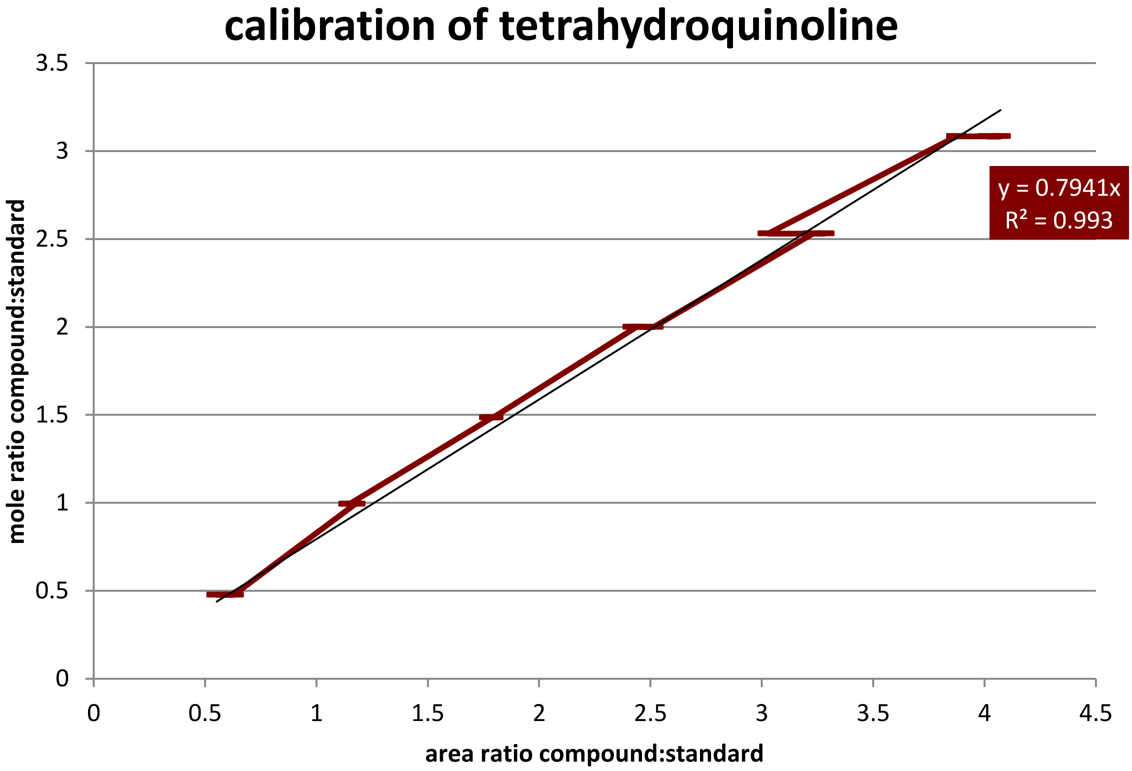

Figure 91: GC calibration series of tetrahydroquinoline relative to 1,2-dichlorobenzene.

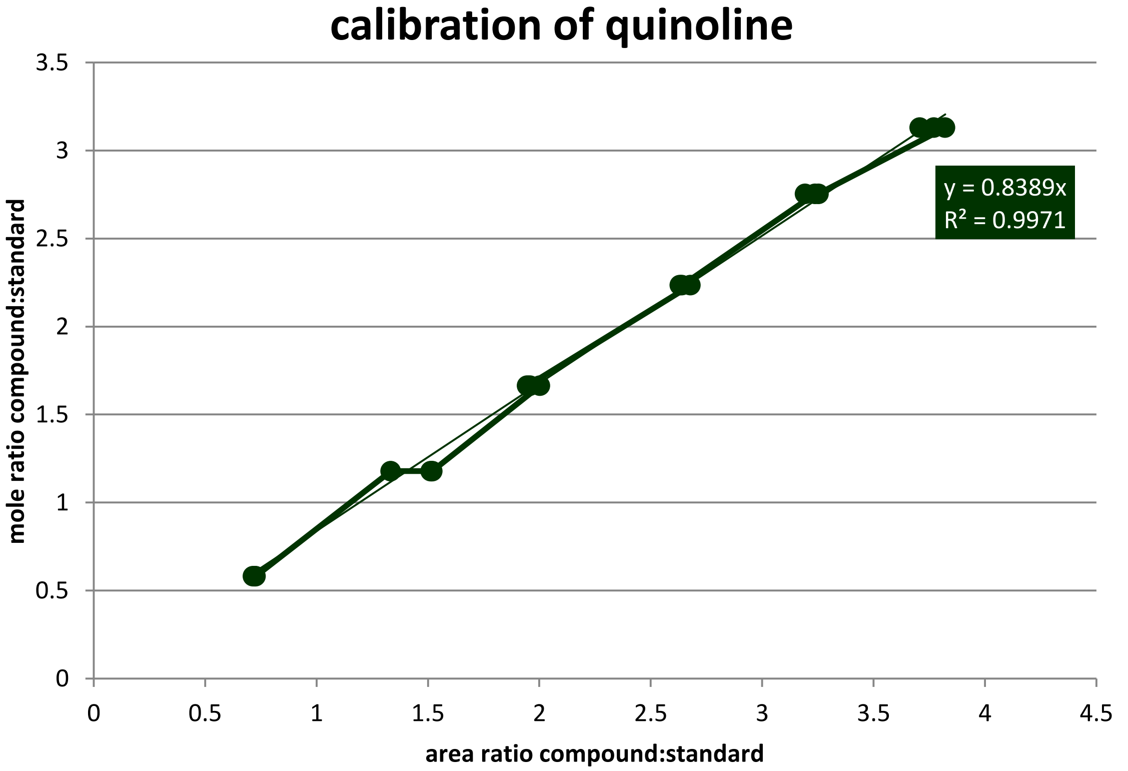

Figure 92: GC calibration series of quinoline relative to 1,2-dichlorobenzene.

9.2 Formulae used for reaction analysis

In order to determine the conversion, selectivity and yield of each reaction, GC and NMR data were used and averaged. The individual entities were determined as outlined in the paragraphs below.

9.2.1 GC determination of moles of compound

To determine the amount of moles of a given compound using GC, the following formula was used:

$$n_x = \left(\frac{A_x}{A_{IS}} \cdot RF_x\right)\left(\frac{m_{IS}}{MW_{IS}}\right)$$

With *n* the amount of moles, *A* the GC area, *RF* response factor, *m* mass, and *MW* molecular weight. Suffixes *x* and *IS* signify compound x and the internal standard, respectively.

9.2.2 NMR determination of moles of compound

To determine the amount of moles of a given compound using NMR, the following formula was used:

$$n_x = \left(\frac{I_x/P_x}{I_{IS}/P_{IS}}\right)\left(\frac{m_{IS}}{MW_{IS}}\right)$$

With *n* the amount of moles, *I* the relative NMR signal integral area of a signature peak, *P* amount of protons of the signature peak, *m* mass, and *MW* molecular weight. Suffixes *x* and *IS* signify compound x and the internal standard, respectively.

9.2.3 Determination of conversion, selectivity, yield and mass balance

Using the amount of moles obtained from both methods, the conversions, selectivity, yield and mass balance were determined separately for NMR and GC, then averaged afterwards. The following formula was used to determine conversion:

$$Conversion\ (\%) = 1 - \frac{n_{SM,t}}{n_{SM,0}}$$

With $n_{SM,t}$ the amount of moles of the starting material at time t (typically the end of the reaction), and $n_{SM,0}$ the amount of moles of the starting material at t = 0. Normalisation of conversion was performed by deducting the loss in mass balance as follows:

$$Normalised\ conversion\ (\%) = C - (1 - MB)$$

With *C* the conversion and *MB* the mass balance.

The following formula was used to determine selectivity:

$$Selectivity\ (\%) = \frac{n_{x,t}}{n_{x,t} + n_{y,t} + n_{z,t}}$$

With $n_{x,t}$ the amount of moles of product x at time t, $n_{y,t}$ the amount of moles of product y at time t, *etc.*

The following formula was used to determine the yield of a given compound:

$$Yield\ (\%) = \frac{n_{x,t}}{n_{SM,0}}$$

The mass balance of a reaction was determined as follows:

$$Mass\ balance = \frac{n_{SM,t} + n_{x,t} + n_{y,t} + n_{z,t}}{n_{SM,0}}$$

With $n_{x,t}$, $n_{y,t}$, and $n_{z,t}$ the amount of moles of all quantified reaction products. Note: in the traditional sense, the term “mass balance” is based on reaction mass rather than moles, however, in this work, a balance based on moles was deemed much more instructive.

The following formula was used to determine turnover numbers (TON):

$$Turnover\ number = \frac{n_{SM,0} - n_{SM,t}}{(m_{cat} \times m\%_V)/MW_V}$$

With m_{cat} the mass of the catalyst in the reaction, $m\%_V$ the mass percentage of vanadium within the catalyst as determined by ICP-OES, and MW_V the molecular weight of vanadium. TONs were normalised by multiplication by mass balance.

9.3 Titration procedure for TBHP

All titrations were performed iodometrically. However, as TBHP is not reactive enough to spontaneously react quantitatively with the reagent, a procedure was developed to correct for this. Below the general procedure used for titrations of TBHP is outlined.

Aiming for *ca.* 0.3 mmol of peroxide per sample, five samples were prepared in screw-cap vials. To each sample, 5 mL of a 0.6 M solution of KI in purified water (9.96 g in 100 mL) was added along with 1 mL of a 20 V% solution of concentrated HCl in purified water (colouring the solution a dark brown) as well as a 10 mm crosshead stirrer. The sample vials were closed, carefully agitated, wrapped in aluminium foil and left to develop overnight in a fridge. After developing the samples, they were sequentially titrated against a 0.1 M solution of $Na_2S_2O_3$ in purified water (2.482 g per 100 mL). When the colour of the sample reached a pale yellow, a few drops of a 1.0 M solution of starch in water were added, changing the colour to dark blue. Titration was continued until the sample was colourless. After all samples were titrated, they were stirred vigorously for 10 min to develop any final remains of peroxide, then titrated again if their colour changed back from colourless. Moles count for the analyte was calculated from the titre used and averaged across the five samples to determine peroxide content.

9.4 Determination of crystallite size

Crystallite size was determined using the Scherrer equation, using the largest peak in the spectrum:

$$\tau = \frac{K \cdot \lambda}{FWHM \cdot \cos\theta}$$

With τ the crystallite size, *K* the “shape factor” of the material (a dimensionless constant generally set to 0.9), λ the wavelength of the X-rays used, *FWHM* the full width of the peak at half maximum, and θ the Bragg angle of the peak.

9.5 Powder diffractograms of V-heterometal series

The following is a collection of powder diffractograms of the V-heterometal series presented in Chapter 3, compared to a calculated AlPO-5 pattern. The background hump indicated by white arrows is a scattering event from the sample holder (this background is absent from other spectra as a background-silent sample holder was used for those experiments instead).

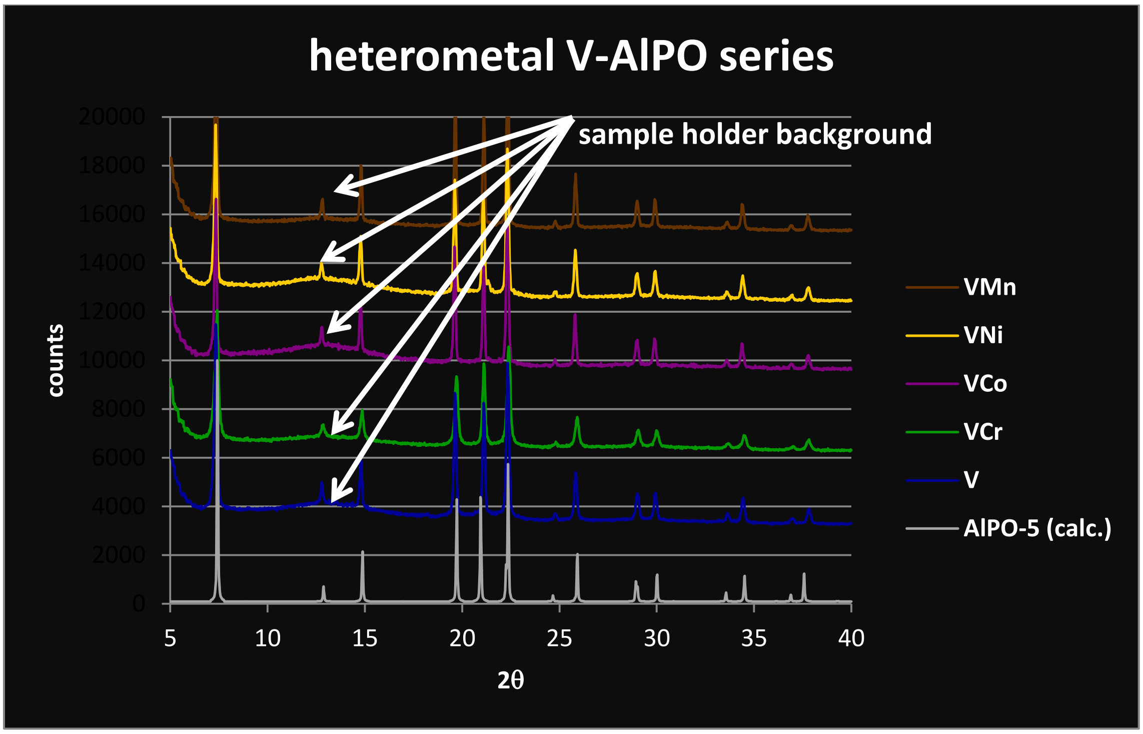

Figure 93: XRD patterns of VAPO-5, VCr AlPO-5, VCo AlPO-5, VNi AlPO-5, and VMn AlPO-5.

9.6 Compound spectra and chromatograms

9.6.1 **Propylbenzene**

Propylbenzene mixture

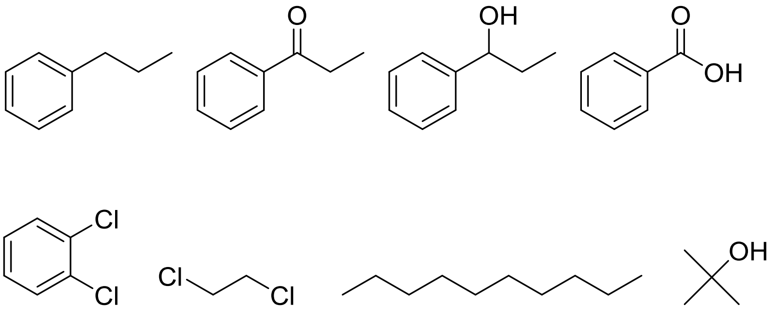
O
OH
O
OH
Cl
Cl
Cl
Cl
OH

9. Appendix

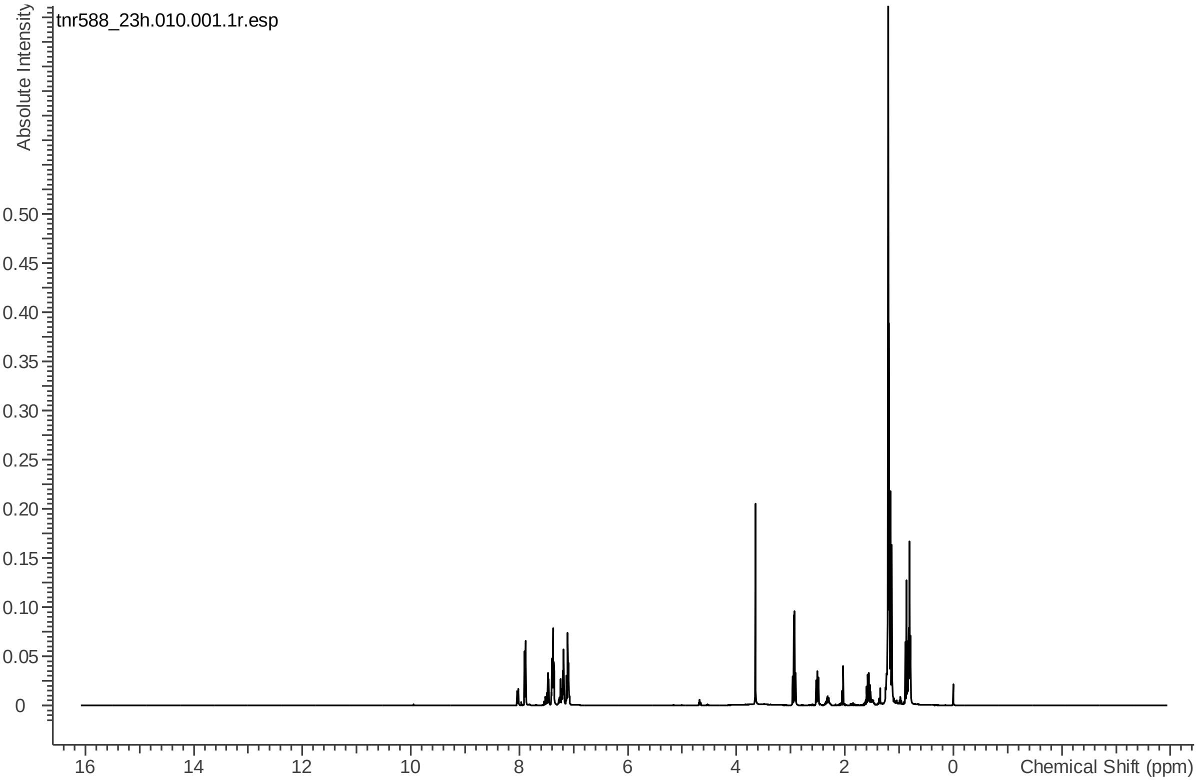
tnr588_23h.010.001.1r.esp
Absolute Intensity
0.50
0.45
0.40
0.35
0.30
0.25
0.20
0.15
0.10
0.05
0
16
14
12
10
8
6
4
2
0
Chemical Shift (ppm)

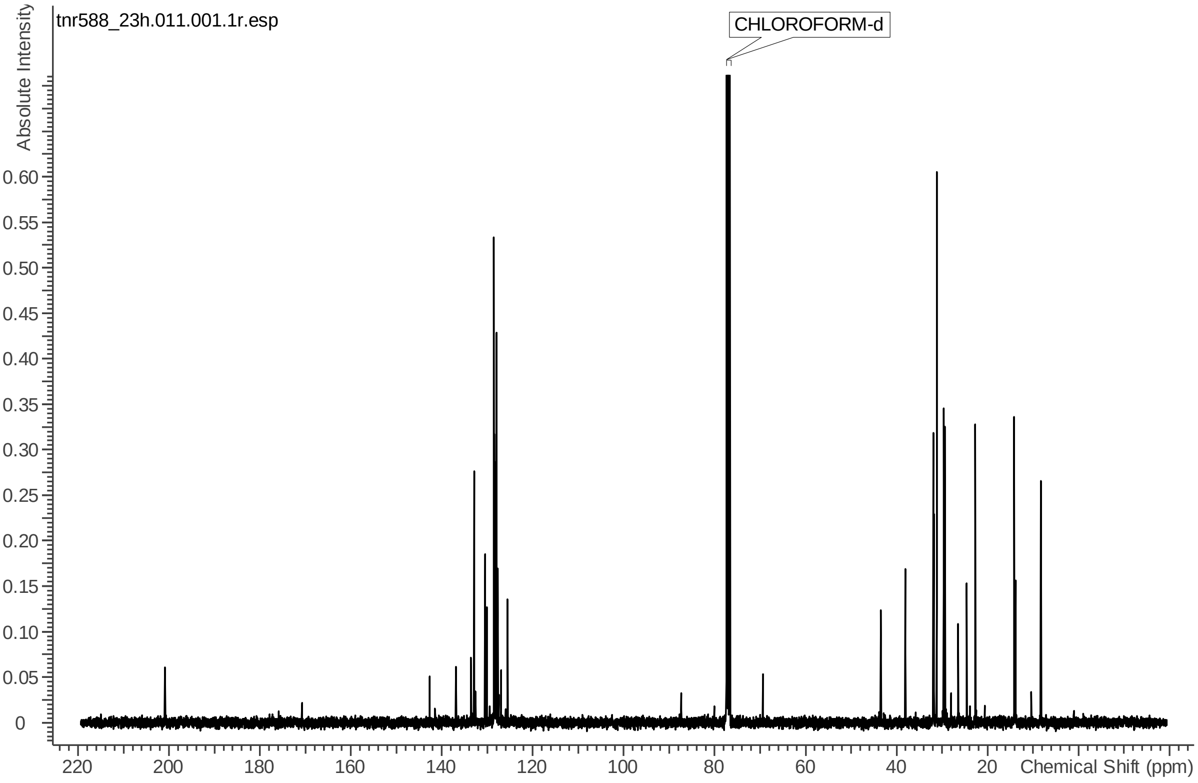
tnr588_23h.011.001.1r.esp
CHLOROFORM-d
Absolute Intensity
0.60
0.55
0.50
0.45
0.40
0.35
0.30
0.25
0.20
0.15
0.10
0.05
0
220
200
180
160
140
120
100
80
60
40
20
Chemical Shift (ppm)

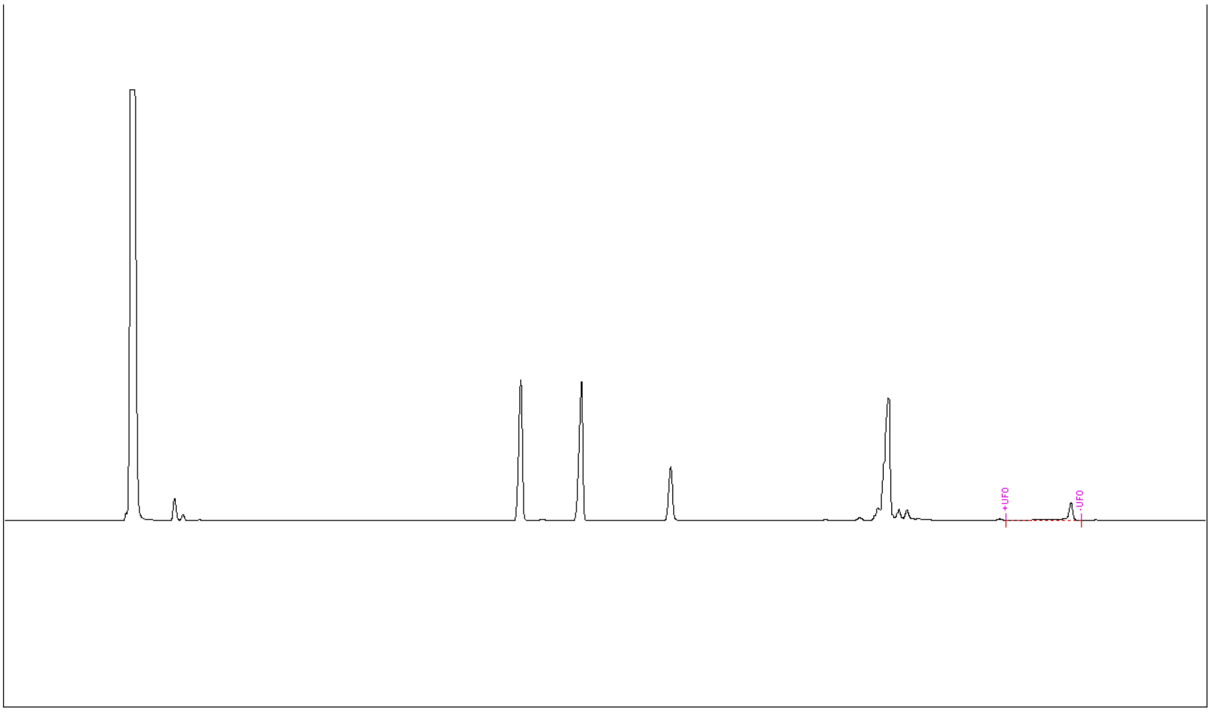
+UFO
-UFO

9. Appendix

9.6.2 **Tetralin**

Tetralin mixture

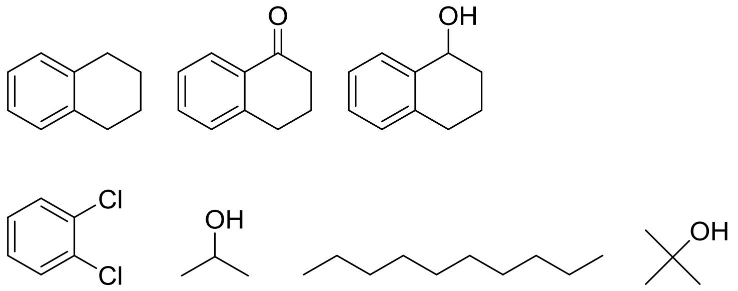
O
OH
OH
Cl
Cl
OH
OH

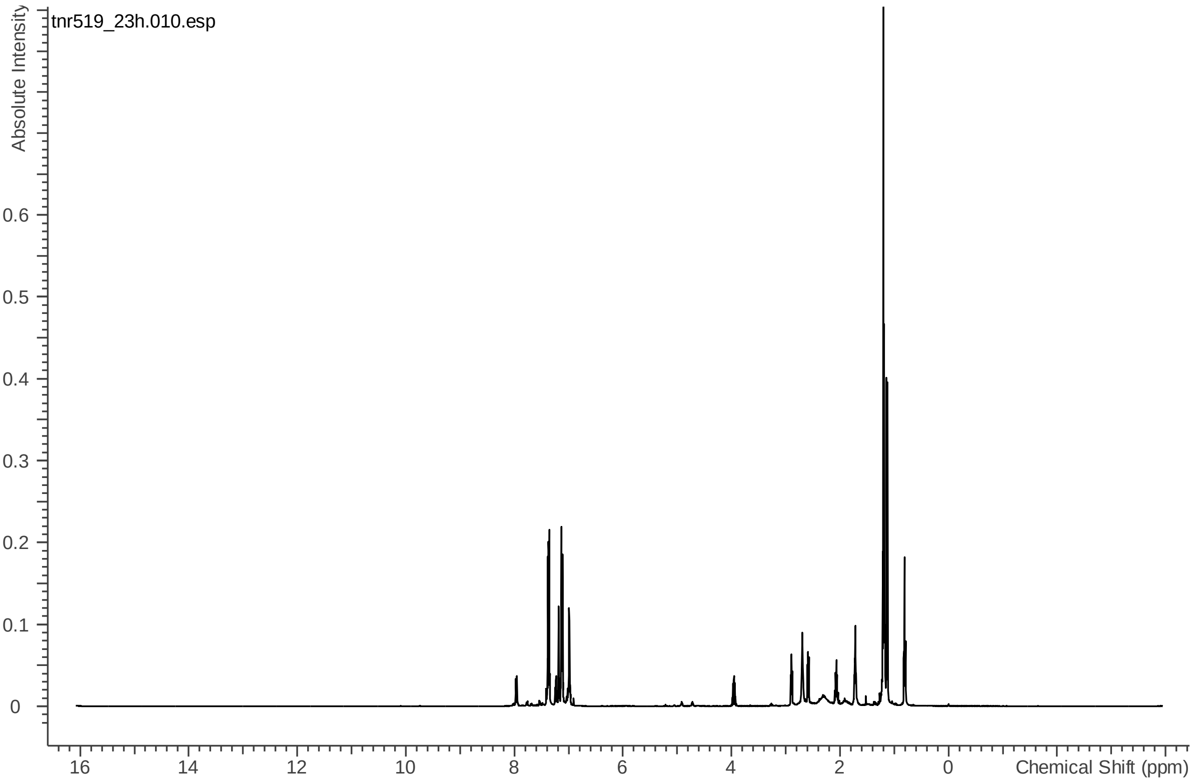

9. Appendix

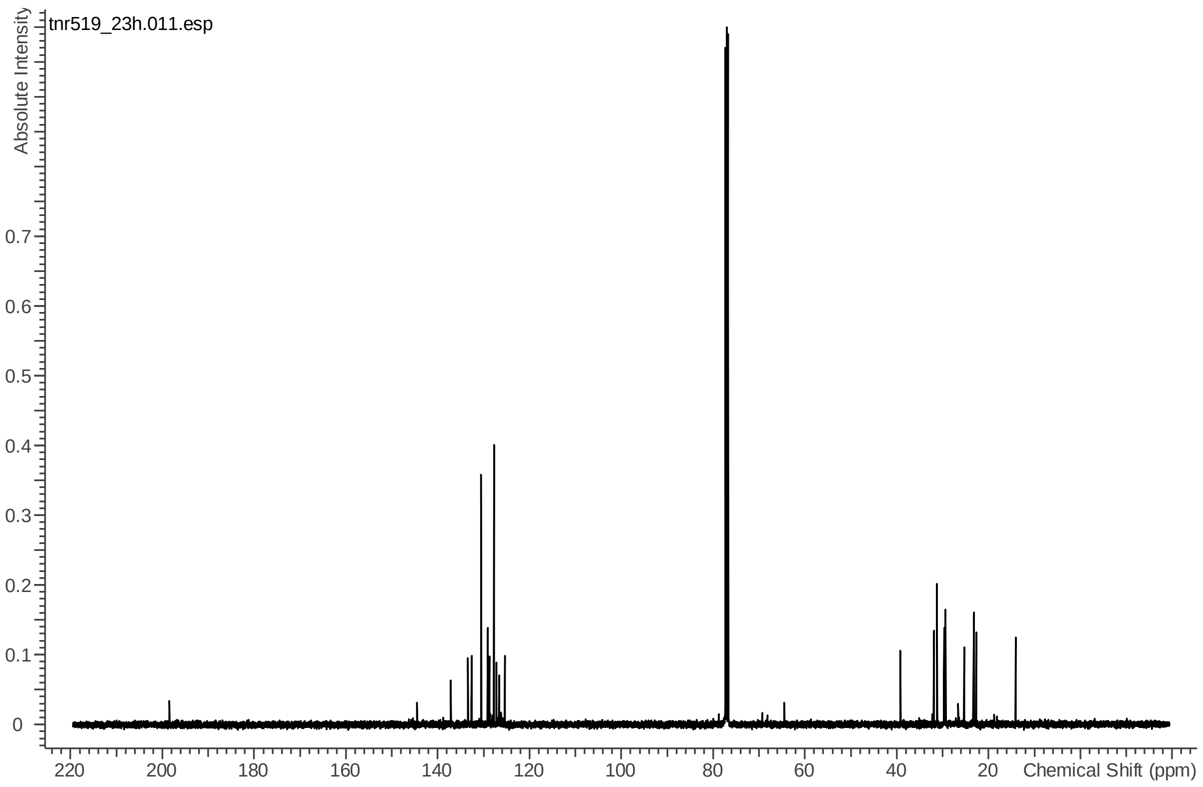
tnr519_23h.011.esp
Absolute Intensity
0.7
0.6
0.5
0.4
0.3
0.2
0.1
0
220
200
180
160
140
120
100
80
60
40
20
Chemical Shift (ppm)

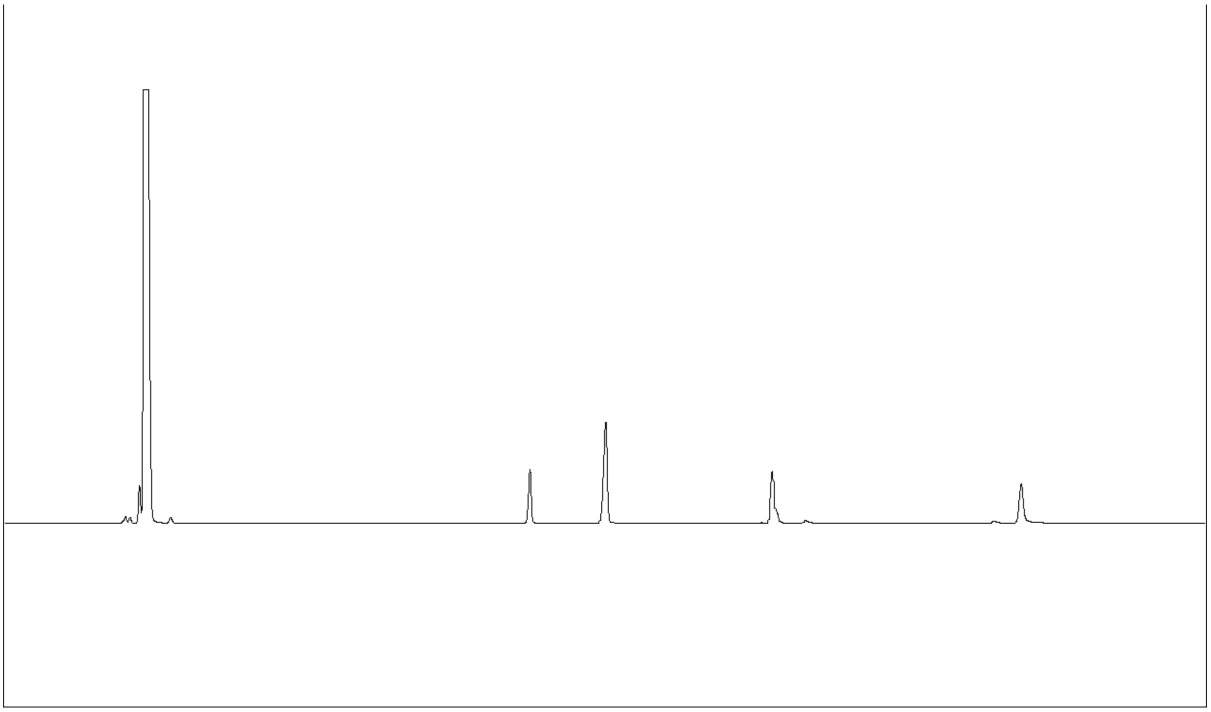

9.6.3 **Indan**

Indan mixture

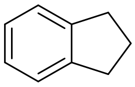

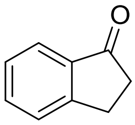

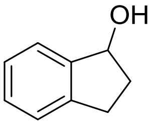

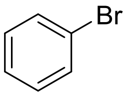

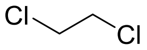

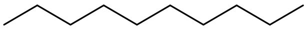

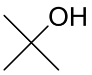

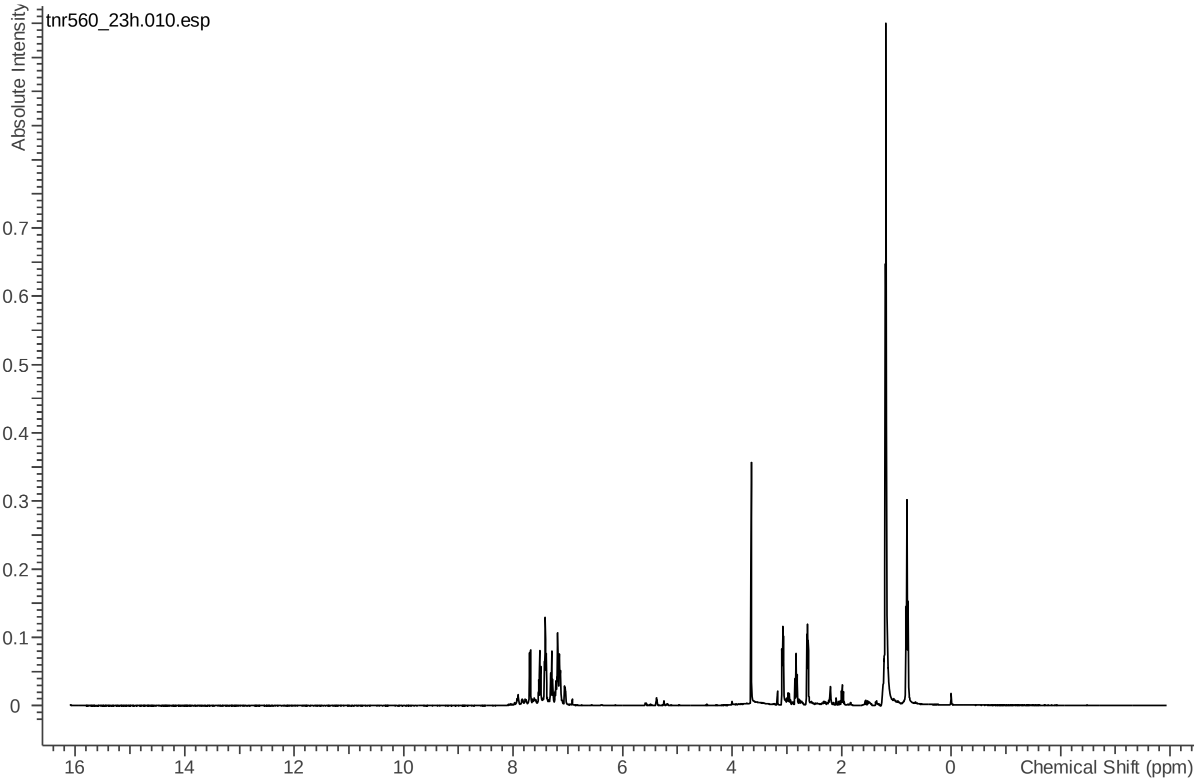

9. Appendix

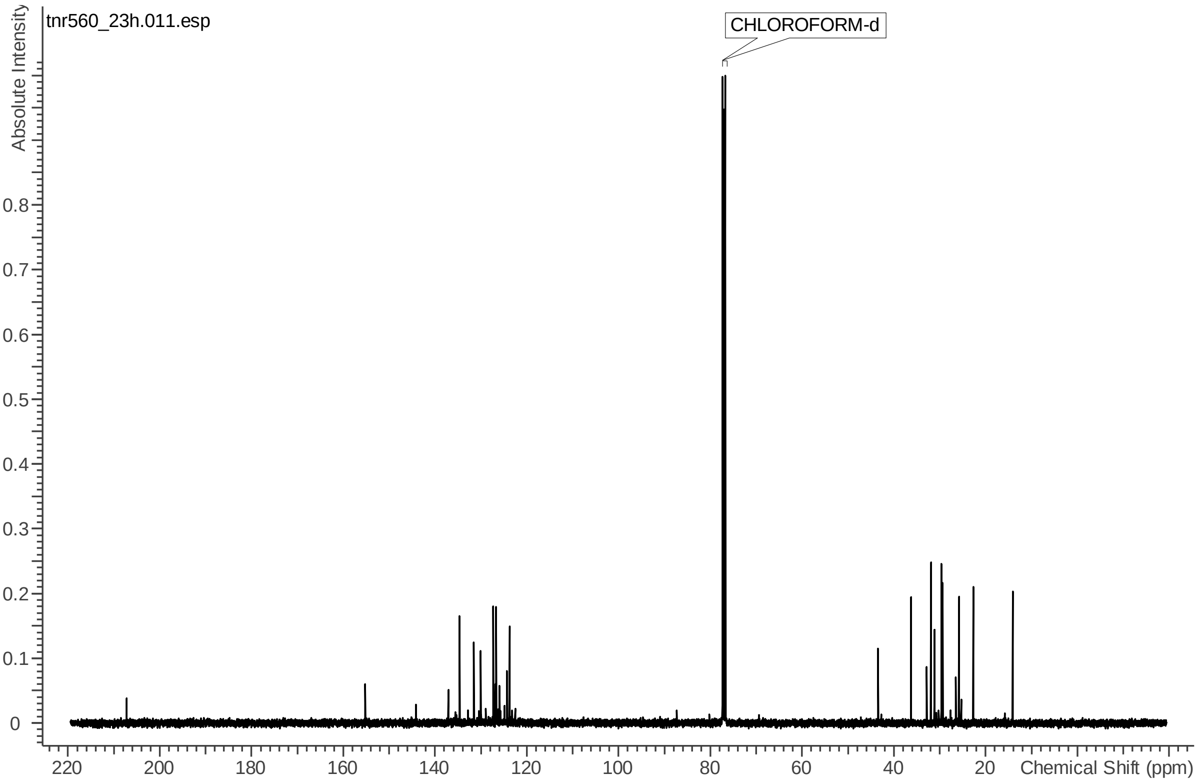
tnr560_23h.011.esp
CHLOROFORM-d
Absolute Intensity
0.8
0.7
0.6
0.5
0.4
0.3
0.2
0.1
0
220
200
180
160
140
120
100
80
60
40
20
Chemical Shift (ppm)

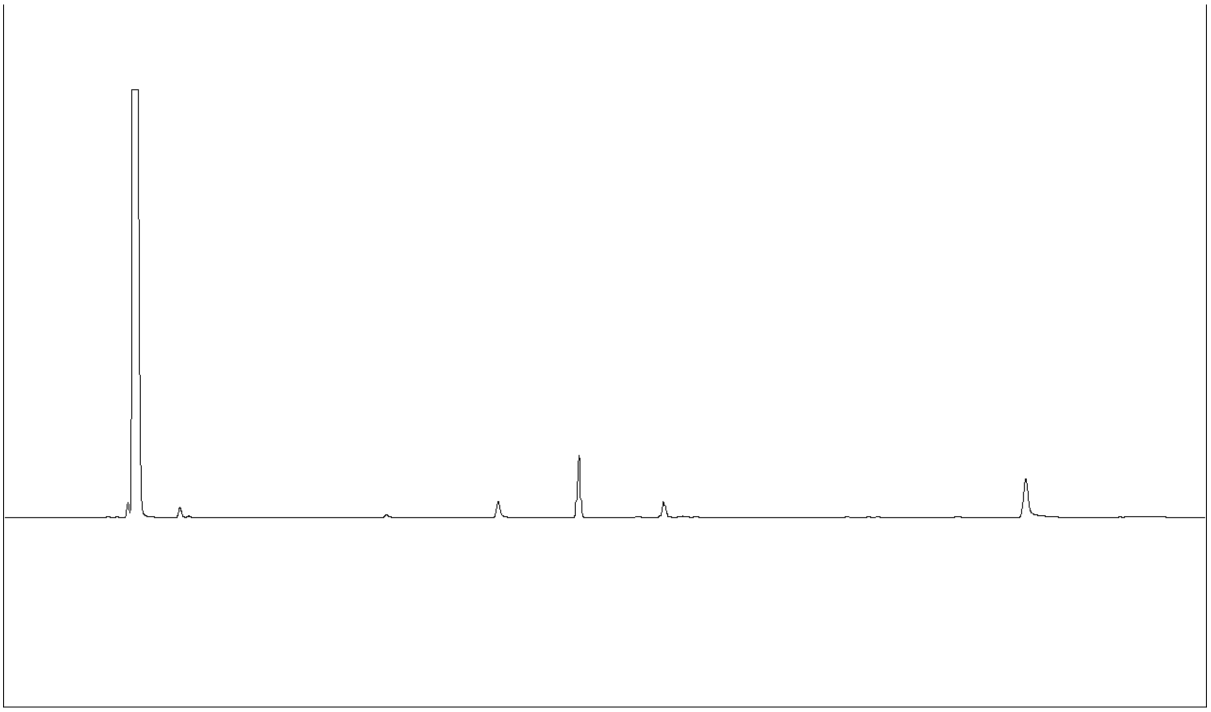

9.6.4 **Toluene**

Toluene mixture

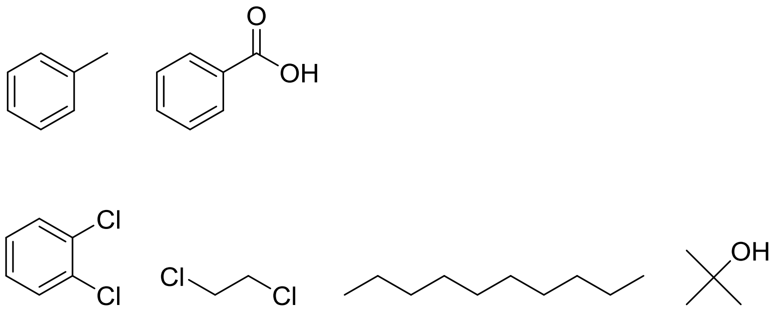
O
OH
Cl
Cl
Cl
Cl
OH

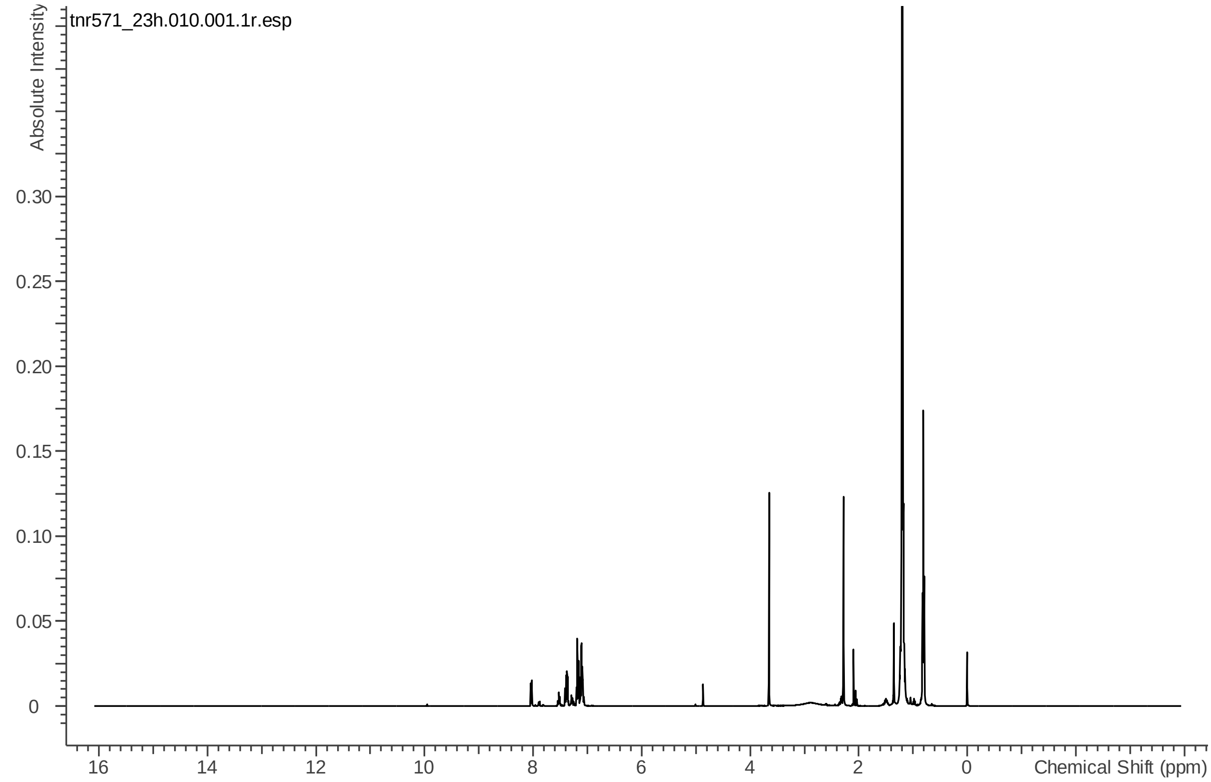

9. Appendix

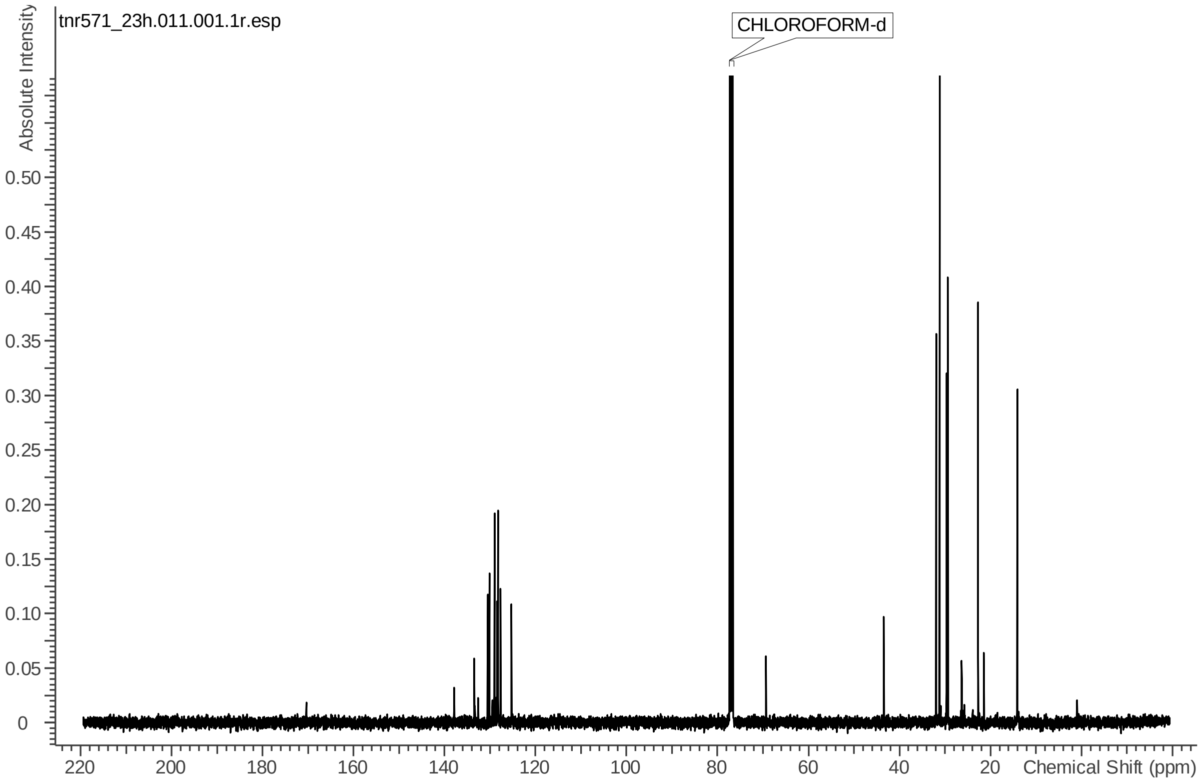

tnr571_23h.011.001.1r.esp
CHLOROFORM-d
Absolute Intensity
0.50
0.45
0.40
0.35
0.30
0.25
0.20
0.15
0.10
0.05
0
220
200
180
160
140
120
100
80
60
40
20
Chemical Shift (ppm)

Toluene extracted

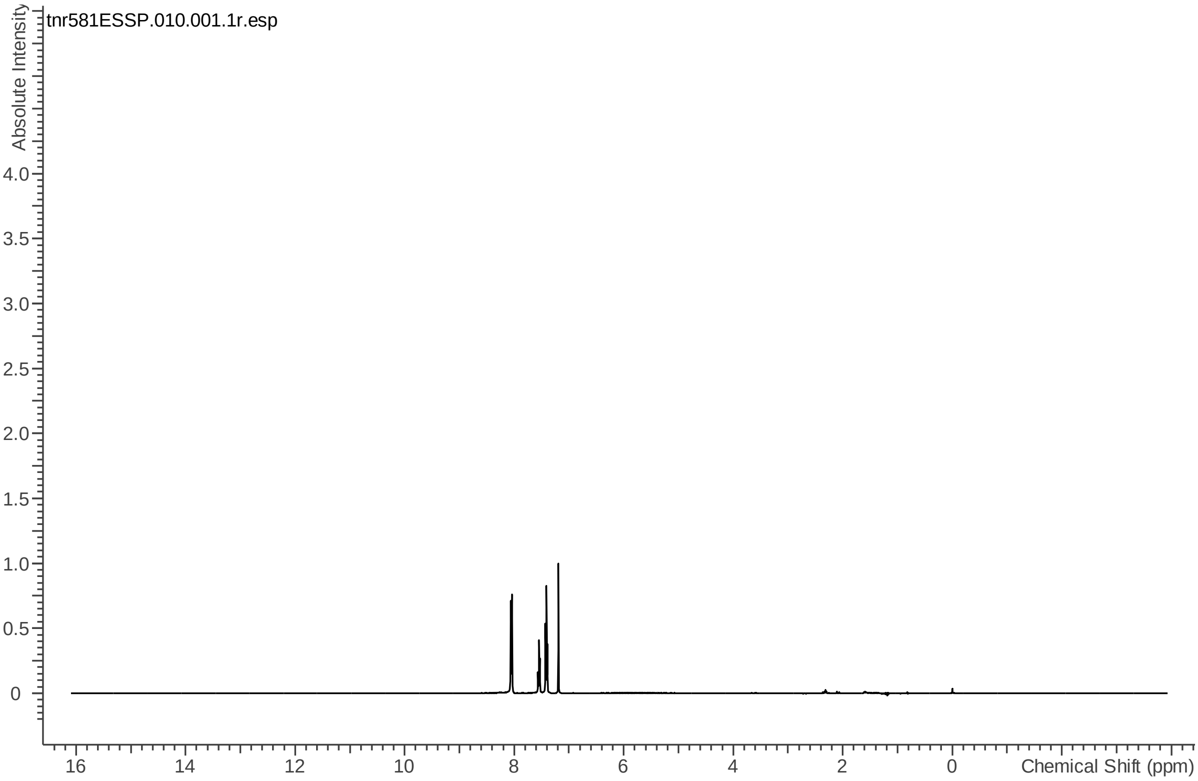

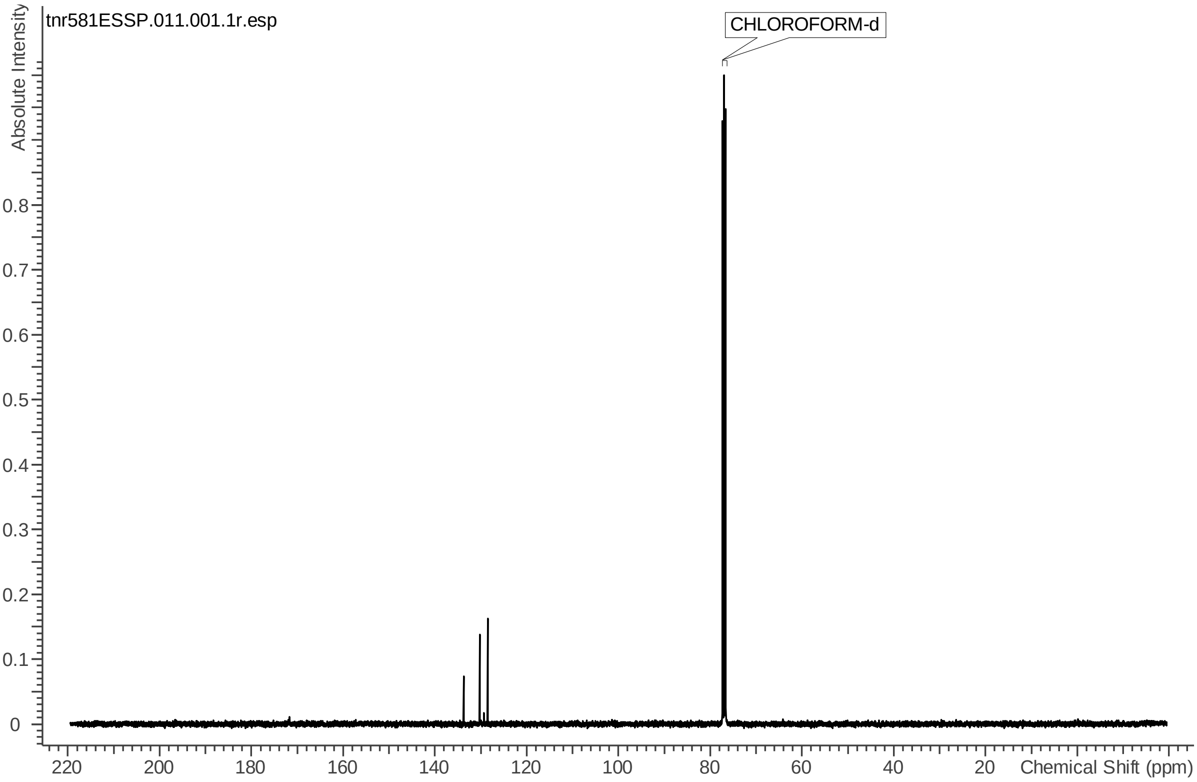

9.6.5 ***o*-Xylene**

O-xylene mixture

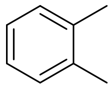

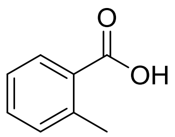

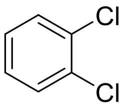

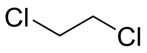

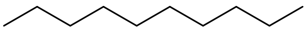

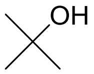

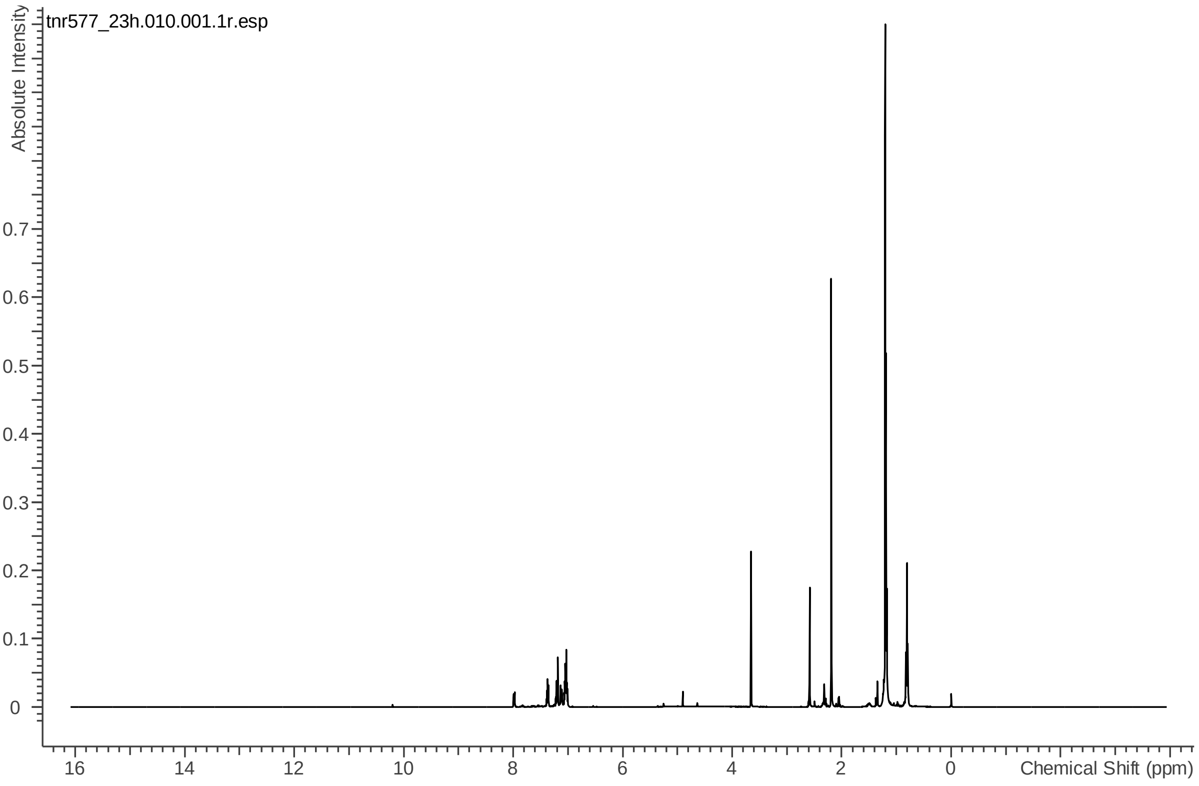

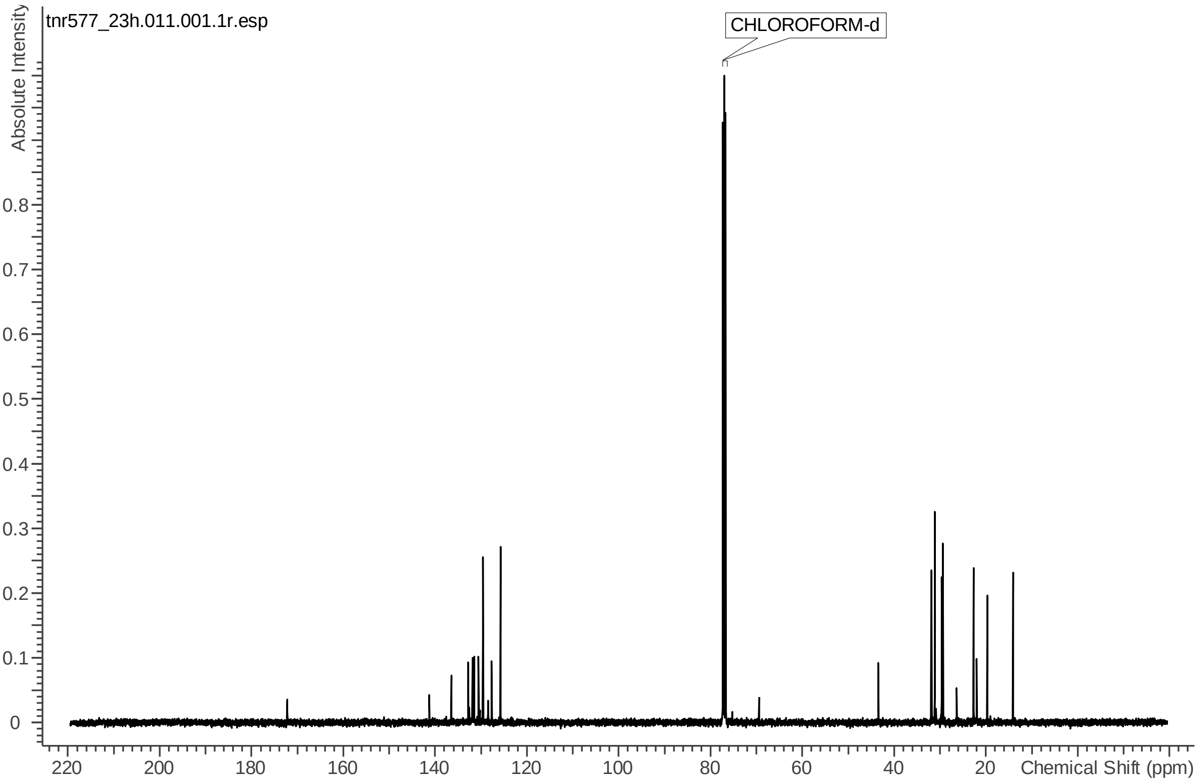
tnr577_23h.011.001.1r.esp
CHLOROFORM-d
Absolute Intensity
0.8
0.7
0.6
0.5
0.4
0.3
0.2
0.1
0
220
200
180
160
140
120
100
80
60
40
20
Chemical Shift (ppm)

9. Appendix

O-xylene extracted

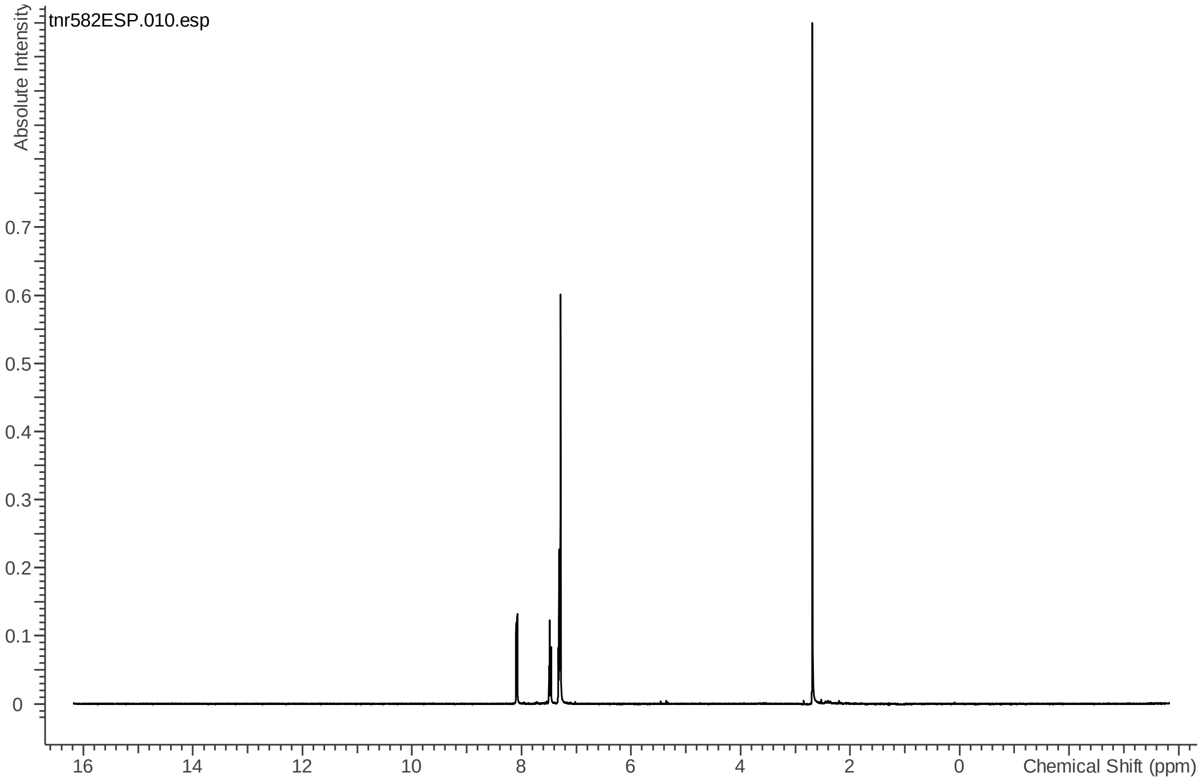

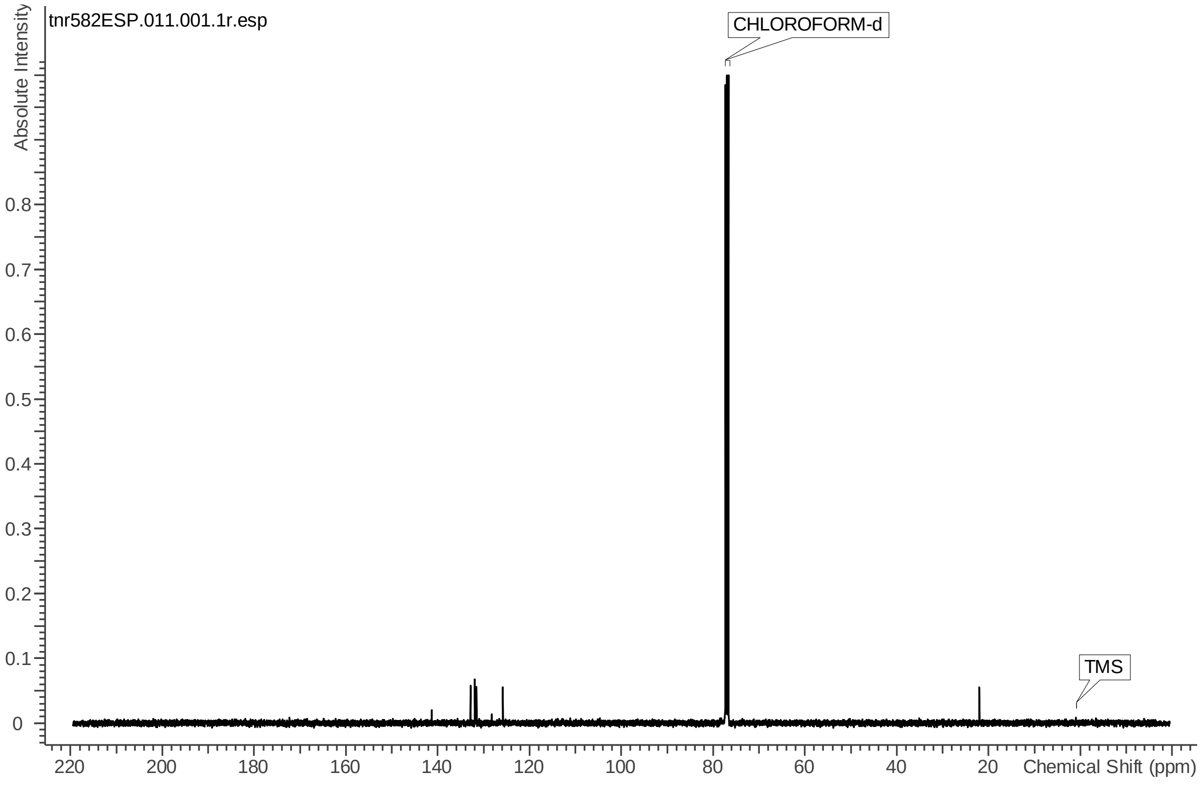

9.6.6 ***p*-Xylene**

P-xylene mixture

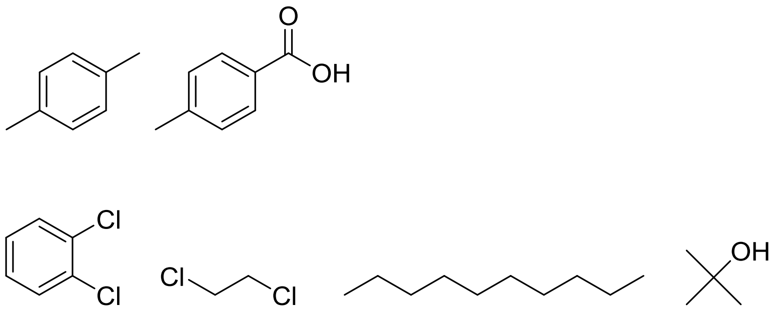
O
OH
Cl
Cl
Cl
Cl
OH

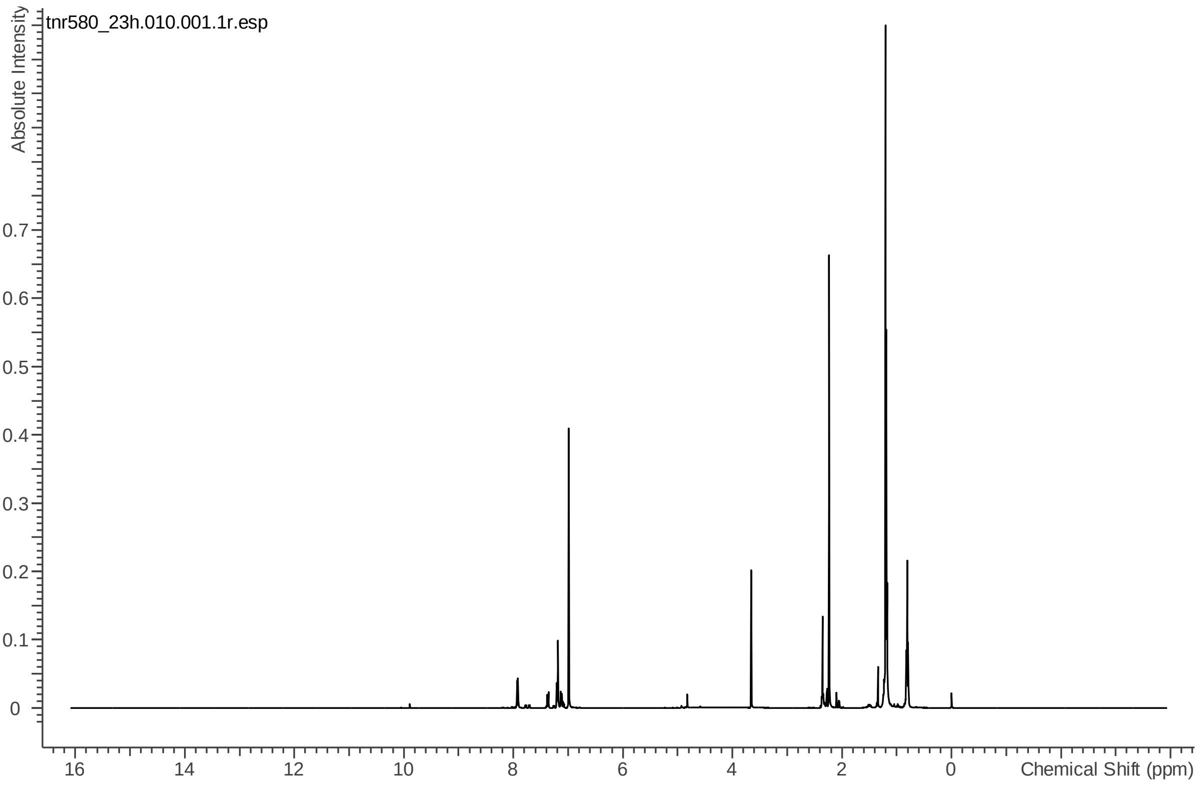

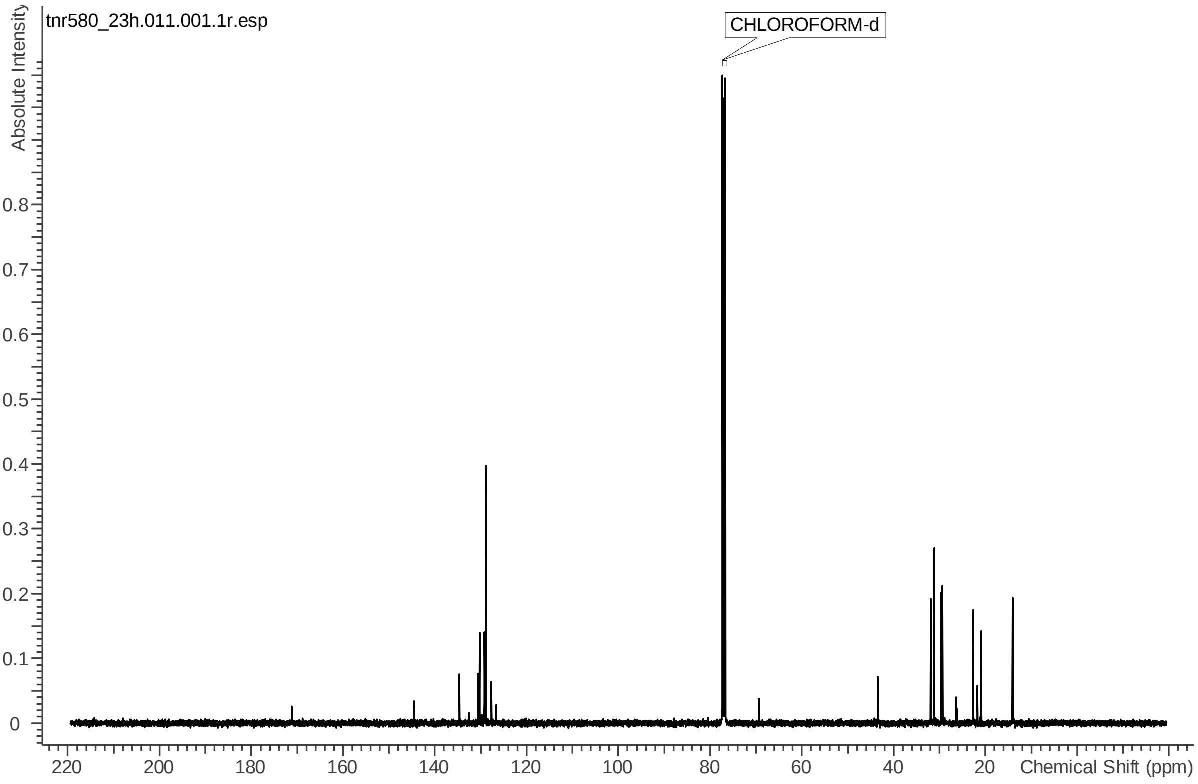
tnr580_23h.011.001.1r.esp
CHLOROFORM-d
Absolute Intensity
0.8
0.7
0.6
0.5
0.4
0.3
0.2
0.1
0
220
200
180
160
140
120
100
80
60
40
20
Chemical Shift (ppm)

P-xylene extracted

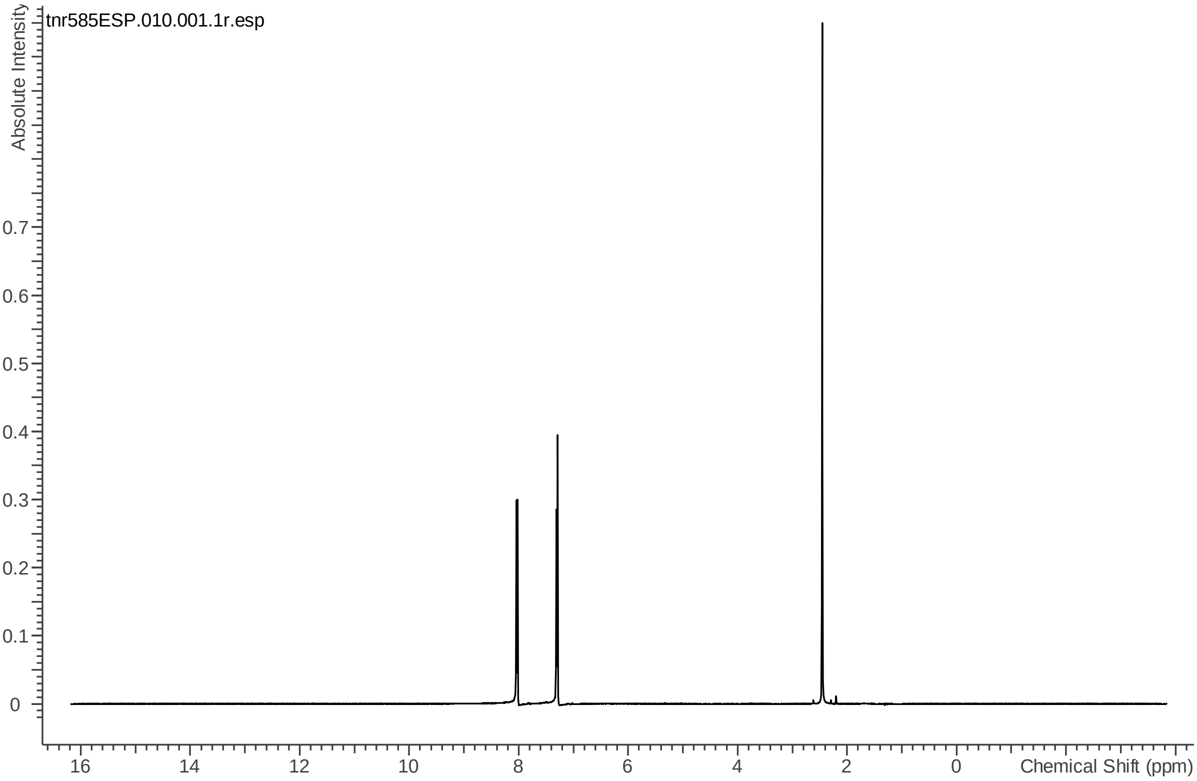

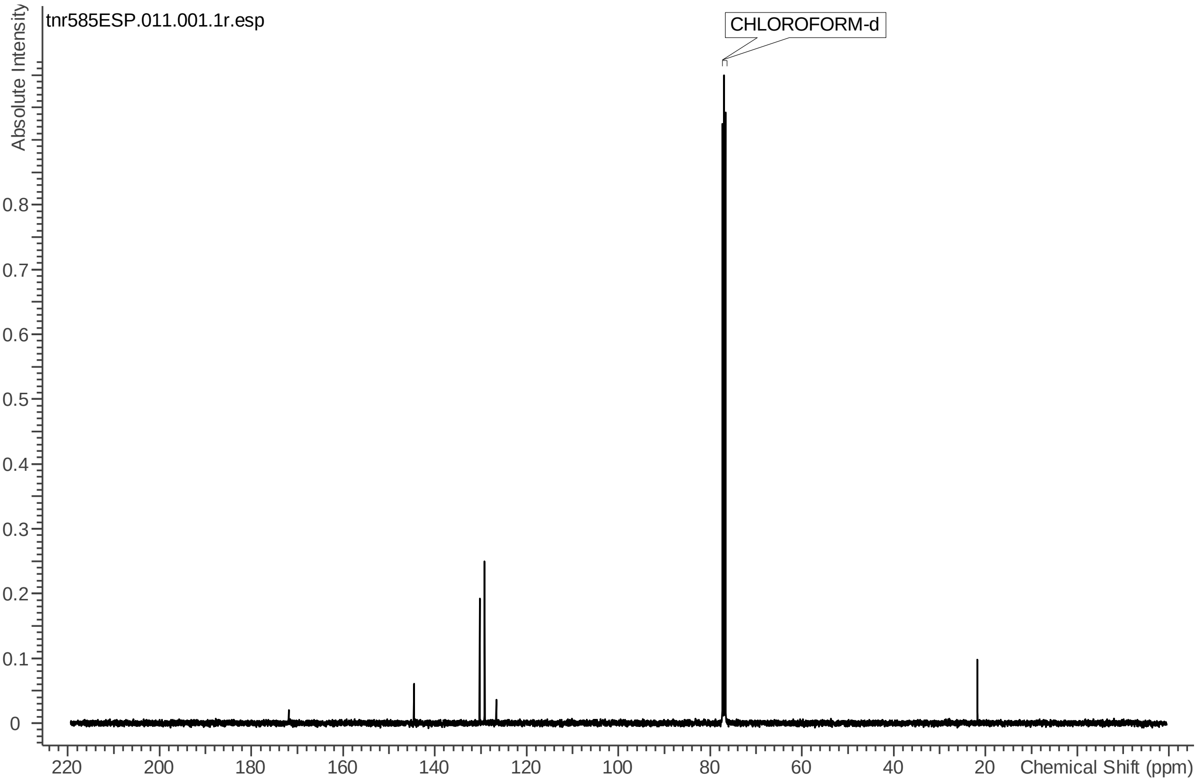

9.6.7 **Mesitylene**

Mesitylene mixture

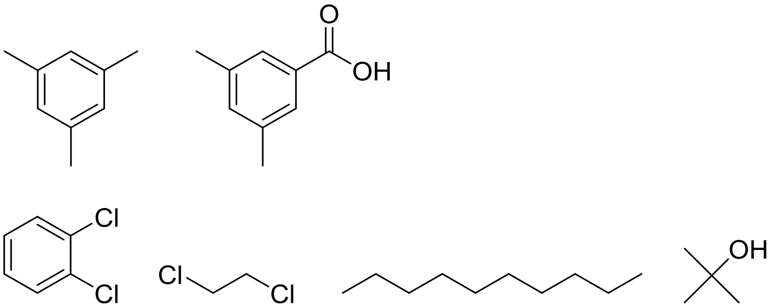
O
OH
Cl
Cl
Cl
Cl
OH

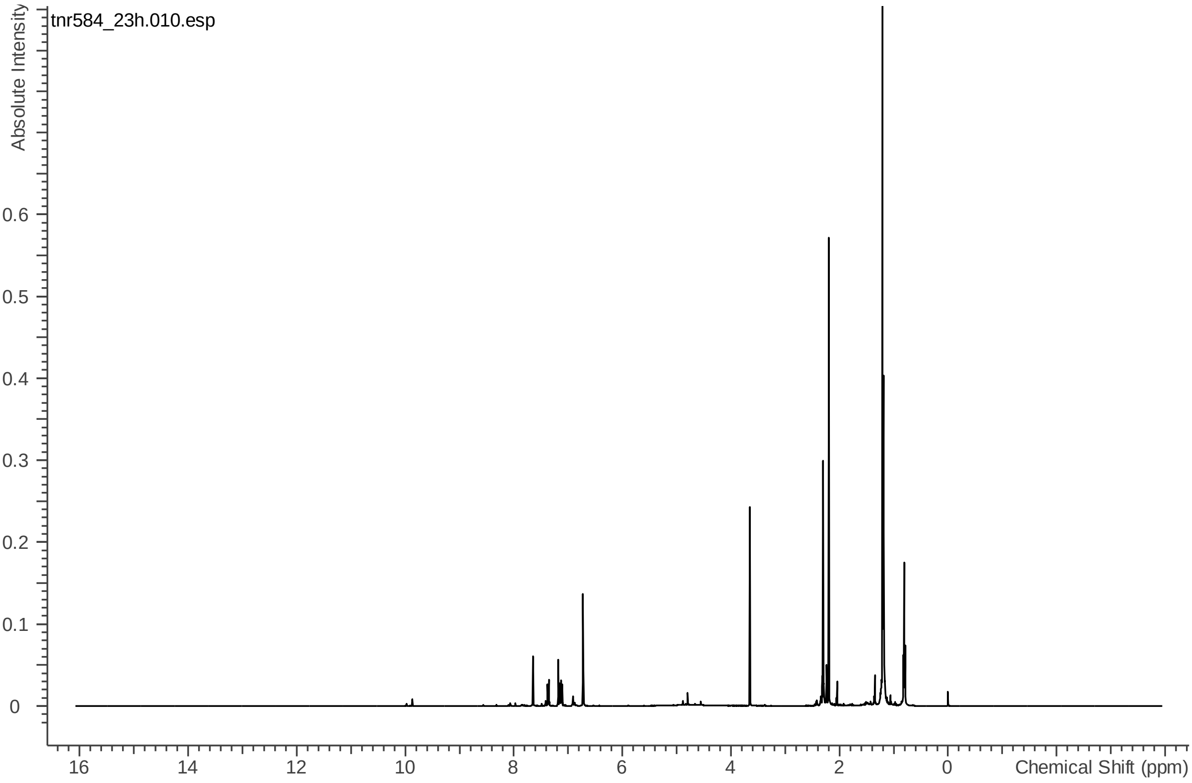

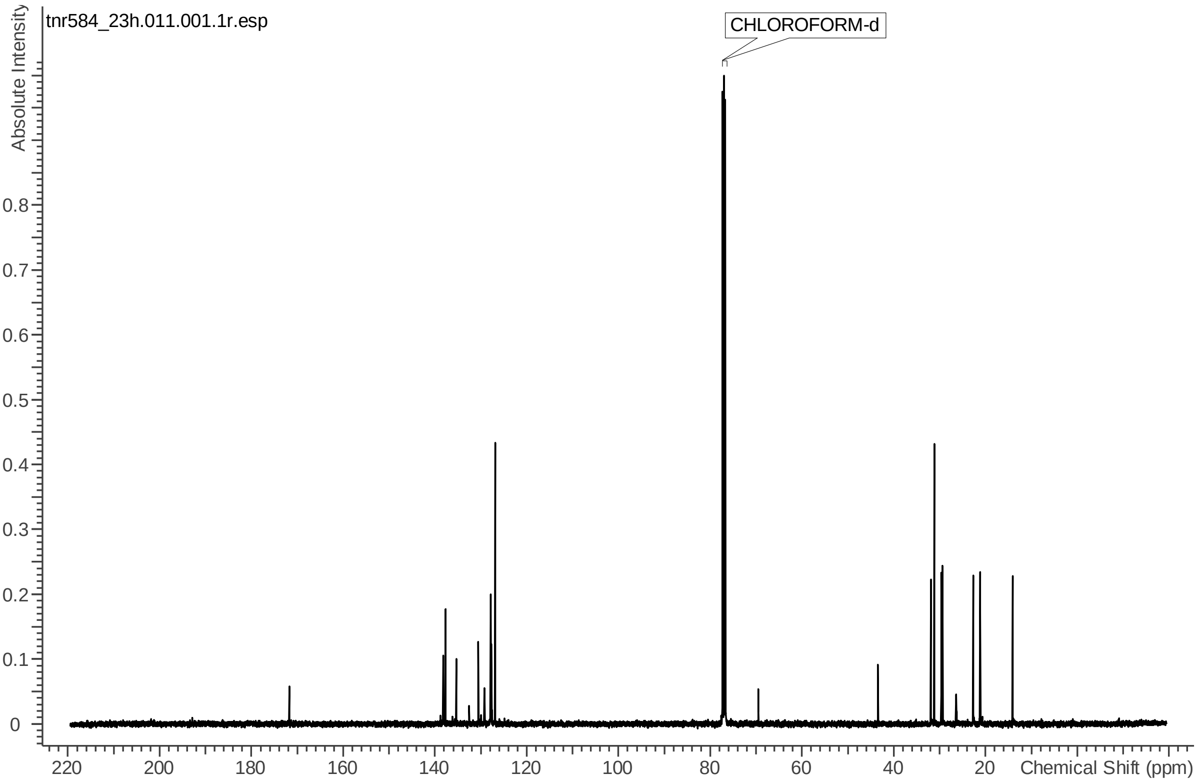
tnr584_23h.011.001.1r.esp
CHLOROFORM-d
Absolute Intensity
0.8
0.7
0.6
0.5
0.4
0.3
0.2
0.1
0
220
200
180
160
140
120
100
80
60
40
20
Chemical Shift (ppm)

9. Appendix

Mesitylene extracted

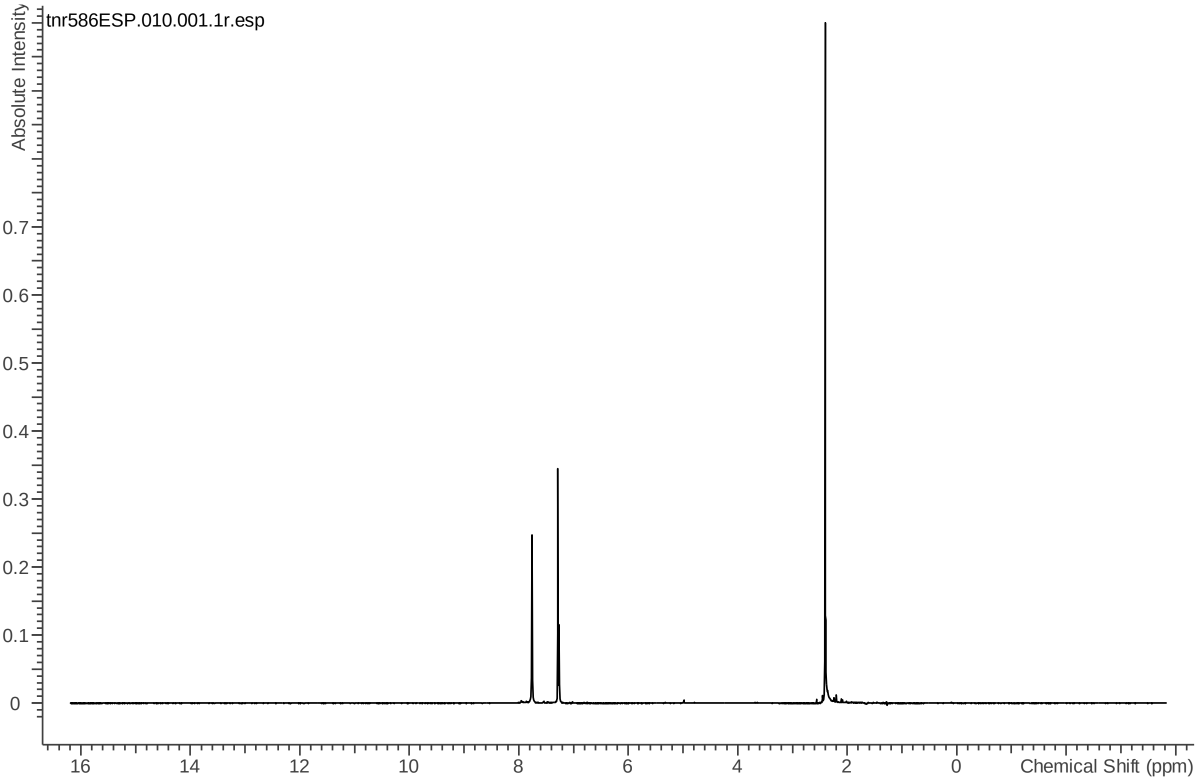

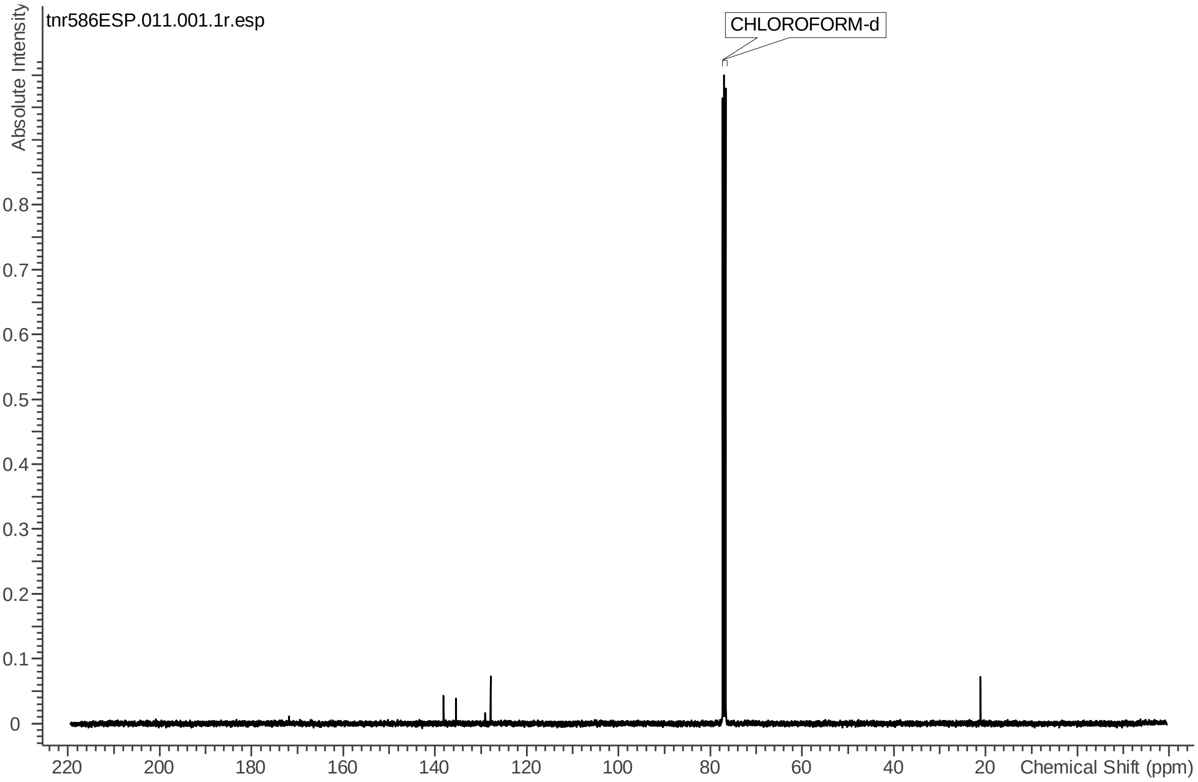

9.6.8 **Durene**

Durene mixture

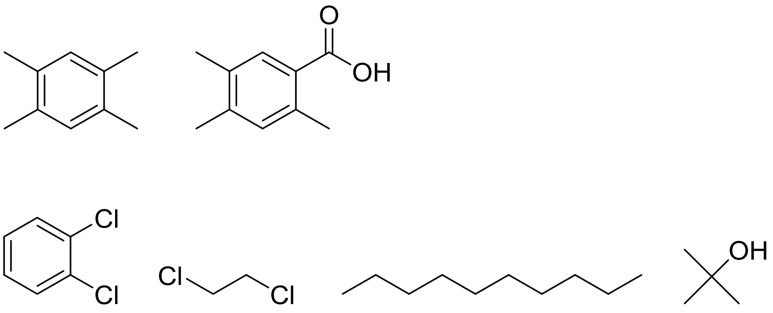
O
OH
Cl
Cl
Cl
Cl
OH

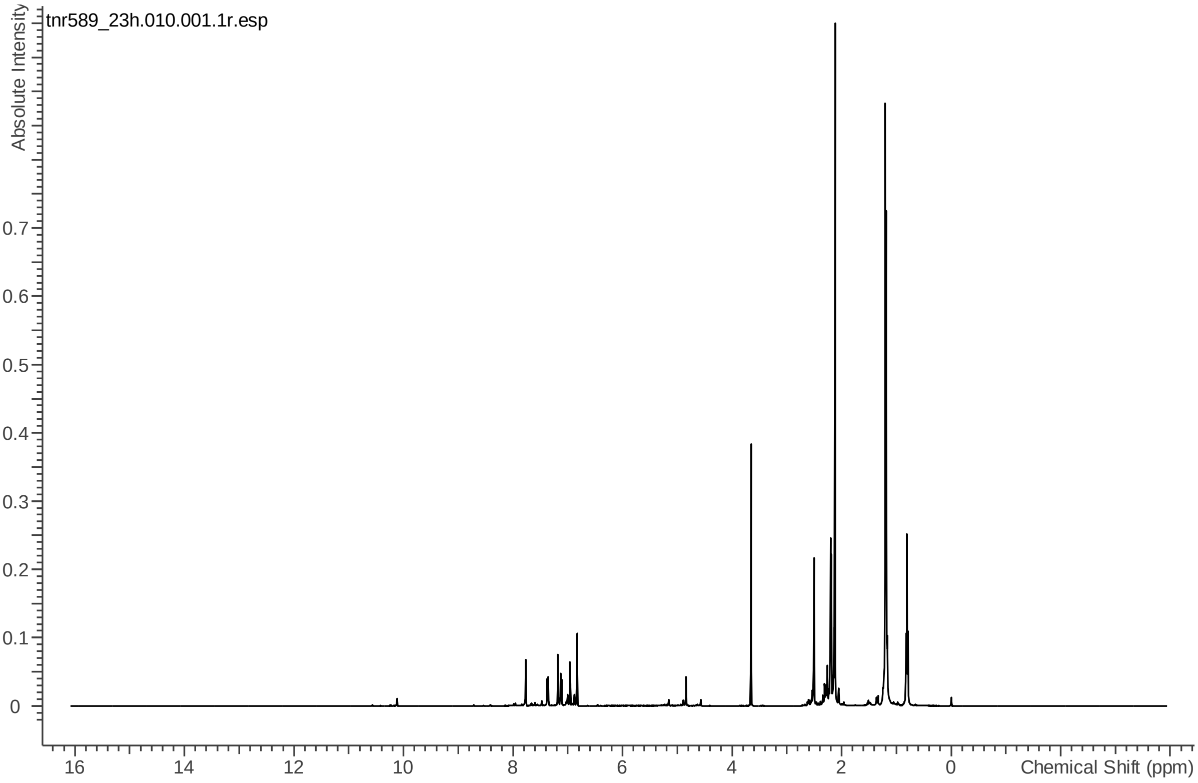

9. Appendix

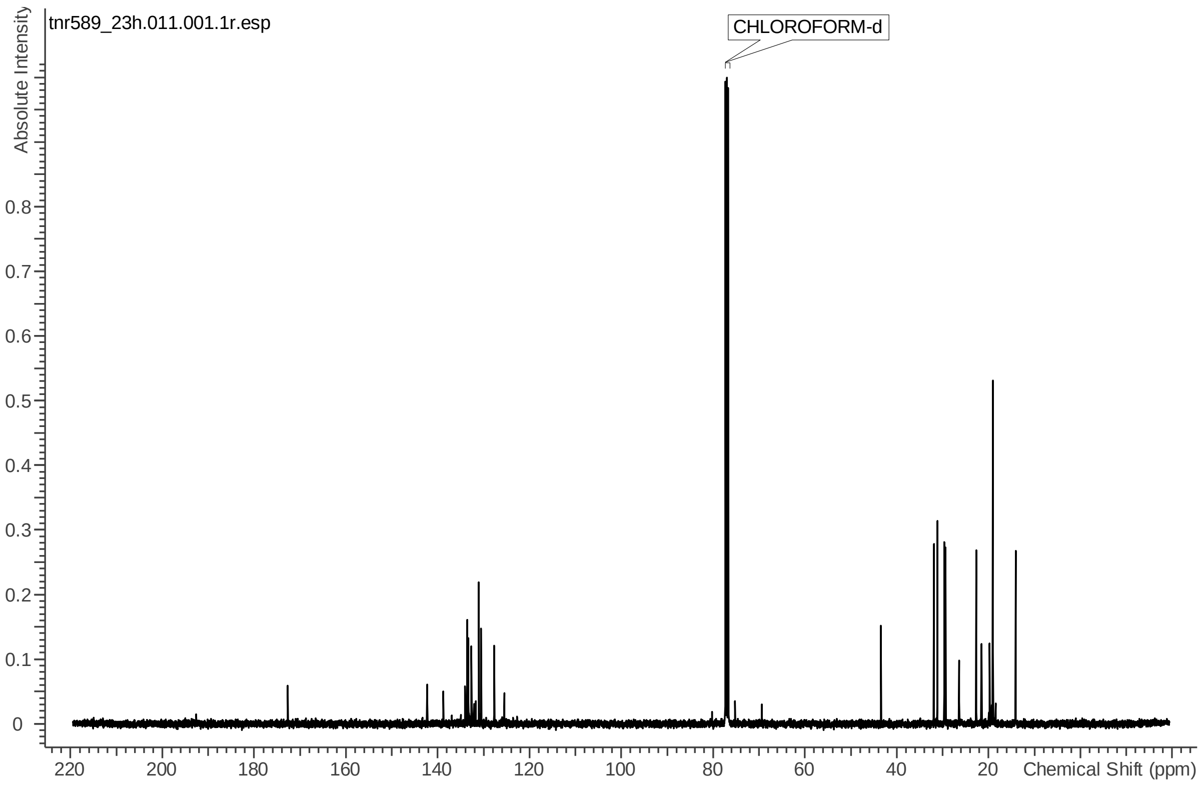
tnr589_23h.011.001.1r.esp
CHLOROFORM-d
Absolute Intensity
0.8
0.7
0.6
0.5
0.4
0.3
0.2
0.1
0
220
200
180
160
140
120
100
80
60
40
20
Chemical Shift (ppm)

Durene extracted

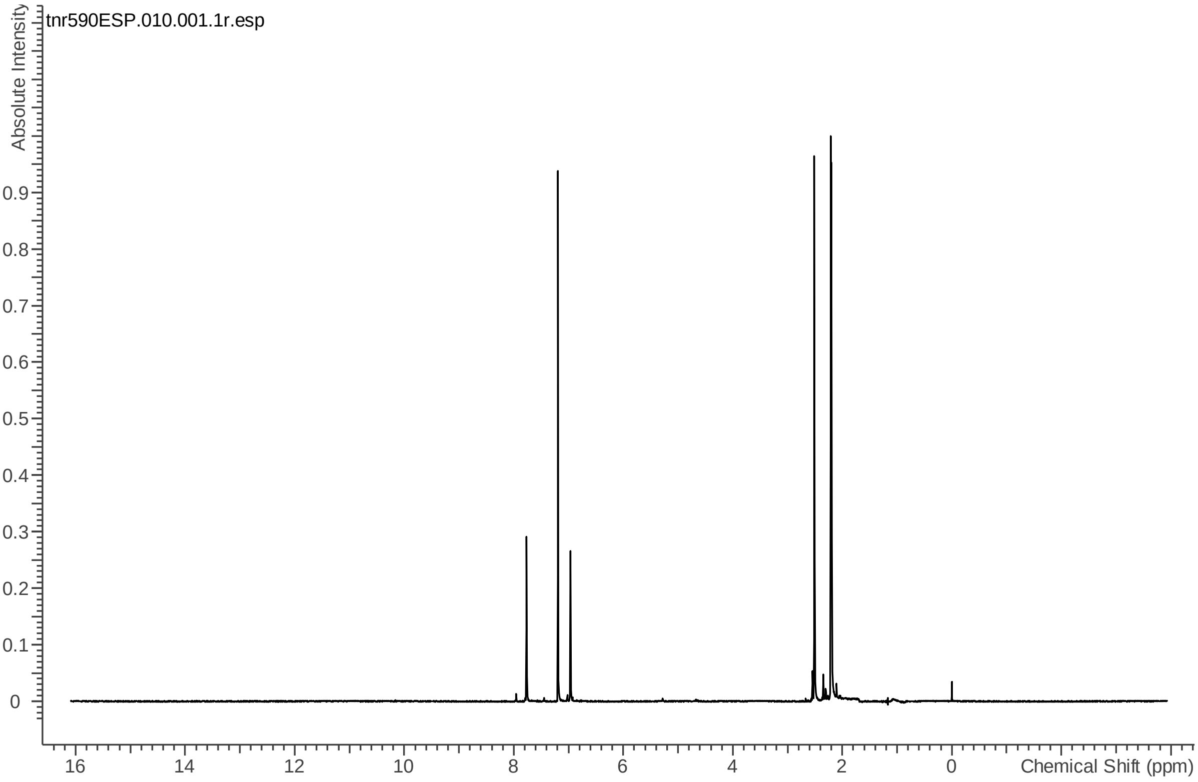

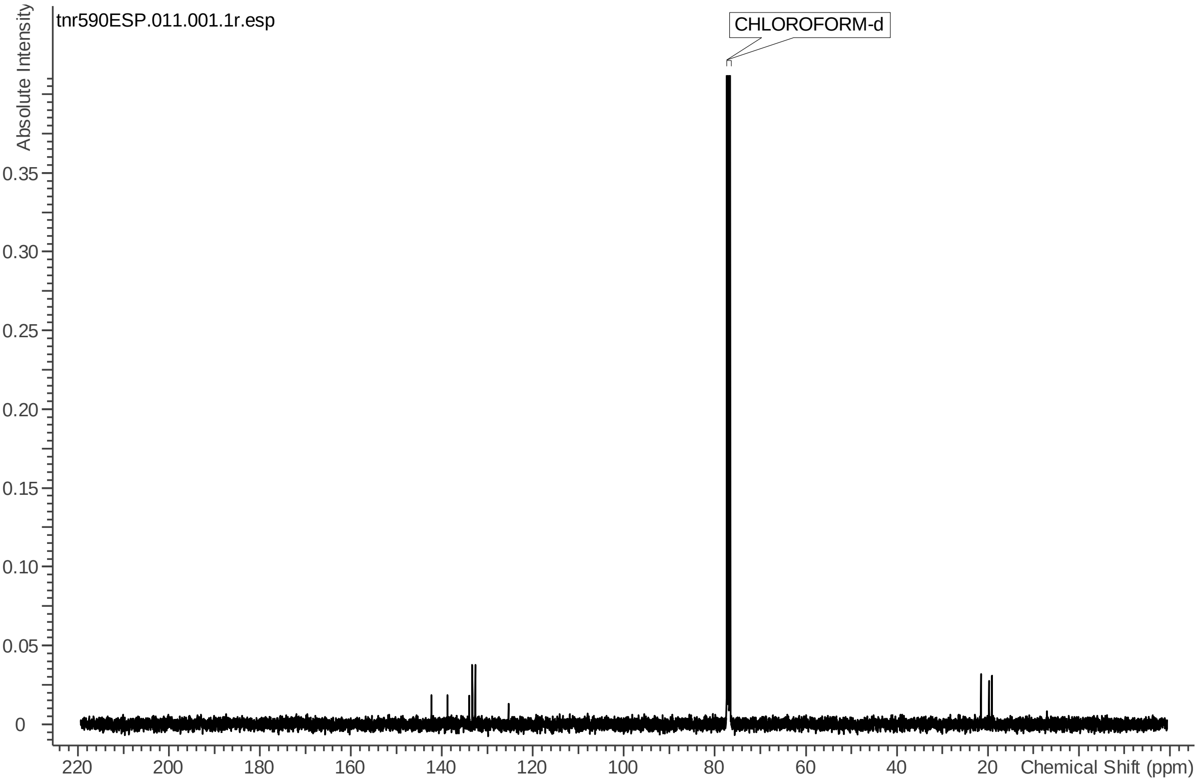

9.6.9 **Indoline**

Indoline mixture

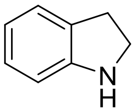

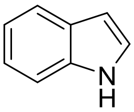

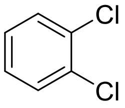

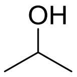

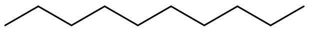

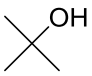

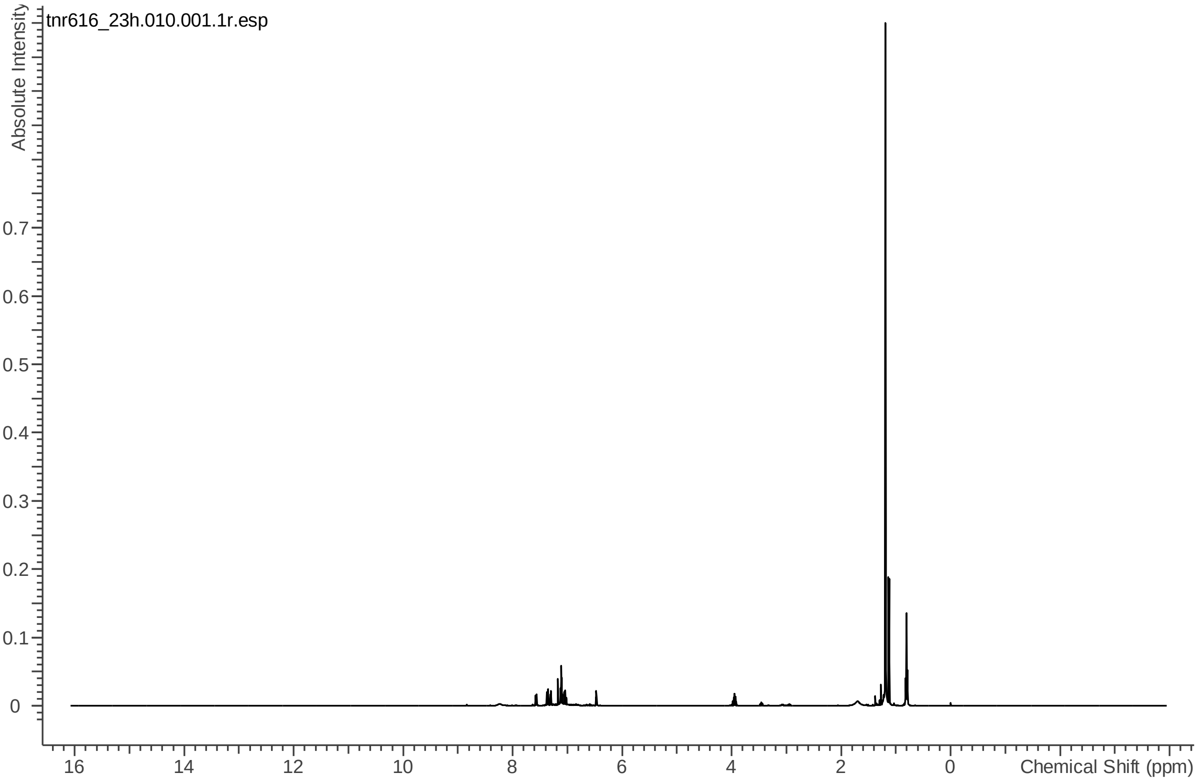

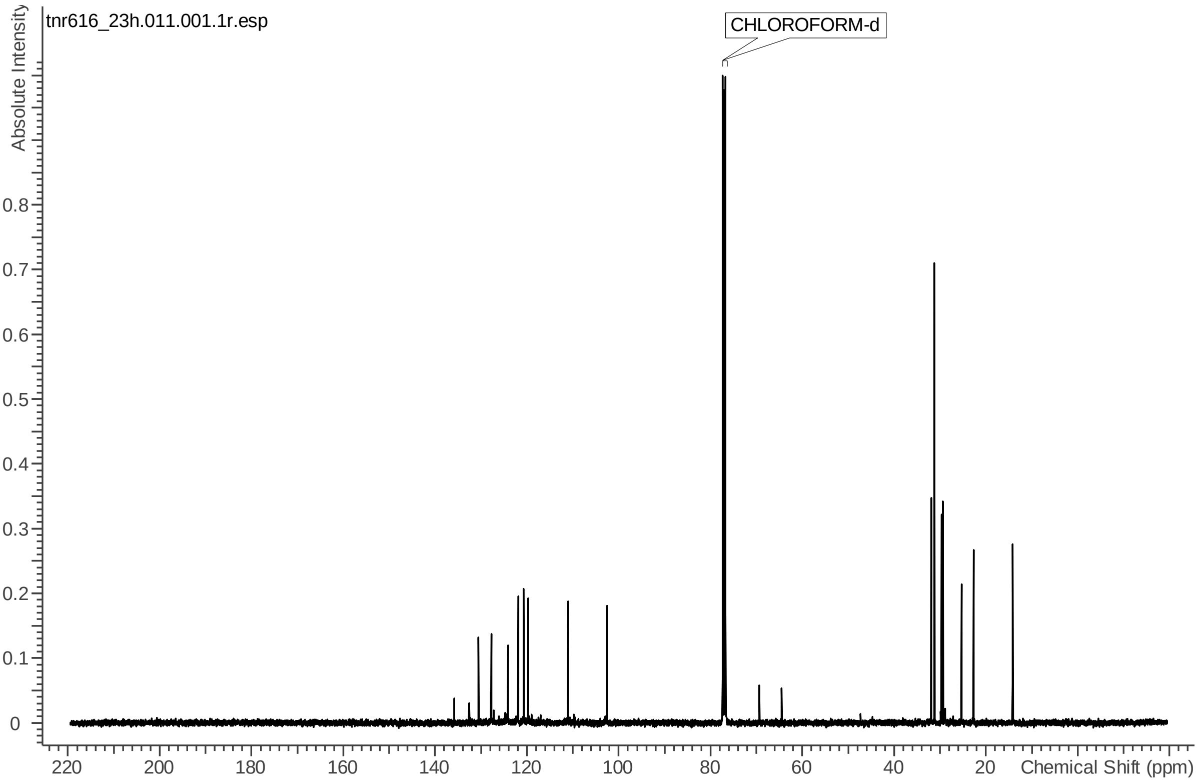
tnr616_23h.011.001.1r.esp
CHLOROFORM-d
Absolute Intensity
0.8
0.7
0.6
0.5
0.4
0.3
0.2
0.1
0
220
200
180
160
140
120
100
80
60
40
20
Chemical Shift (ppm)

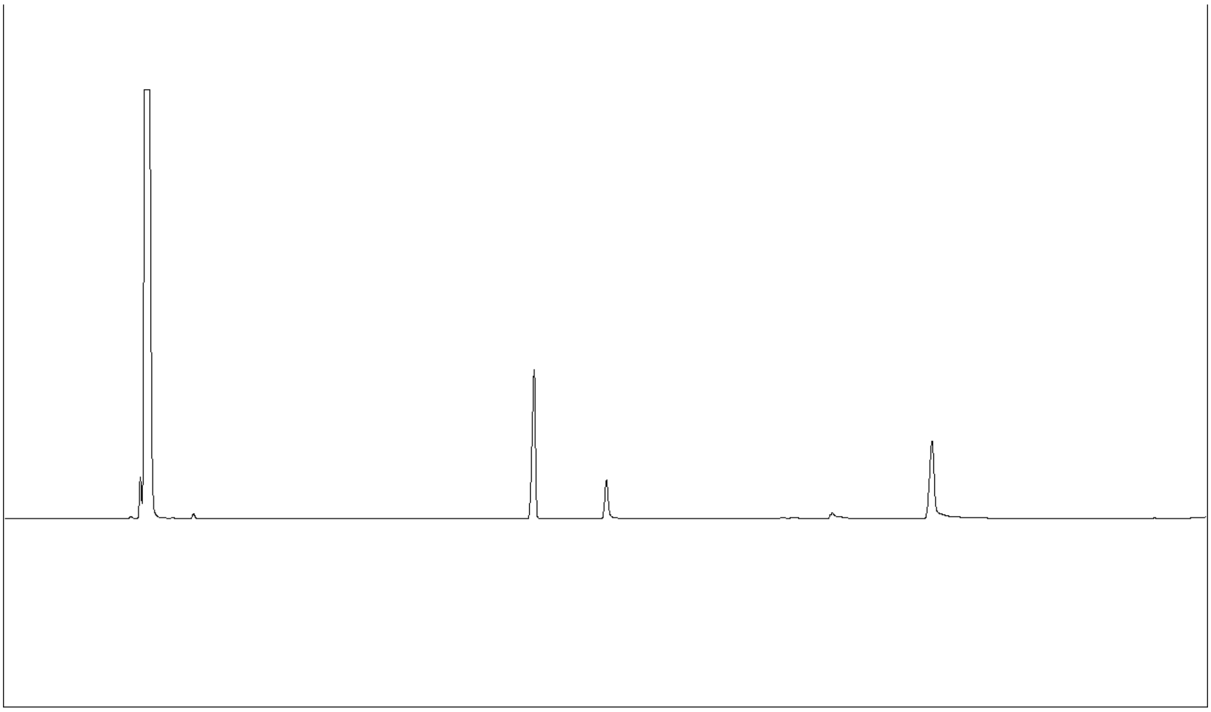

9.6.10 **Tetrahydroquinoline**

Tetrahydroquinoline mixture

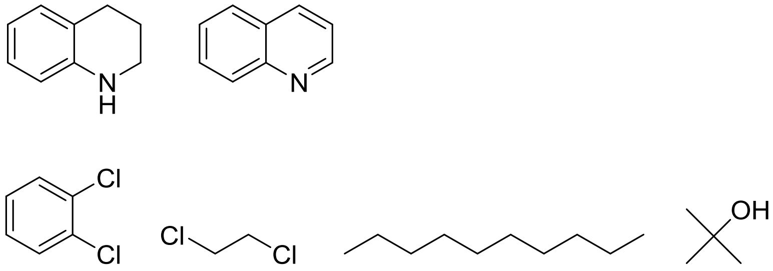
N
H
N
Cl
Cl
Cl
Cl
OH

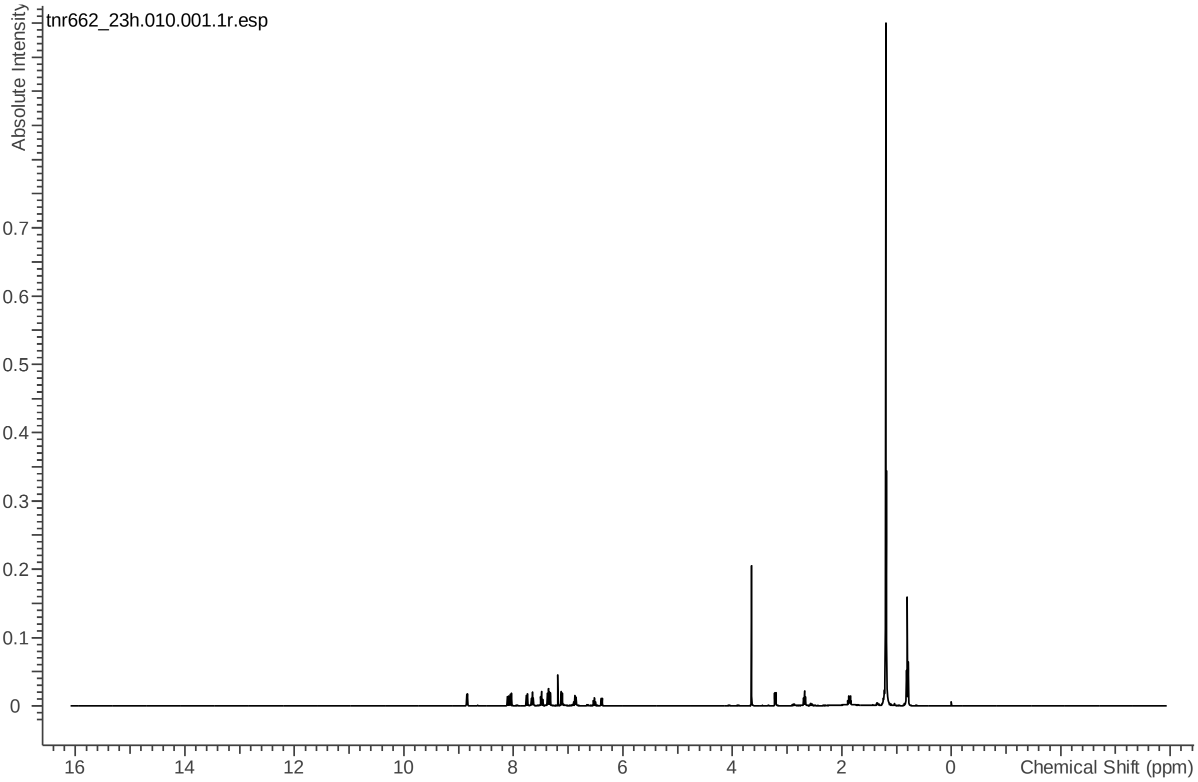

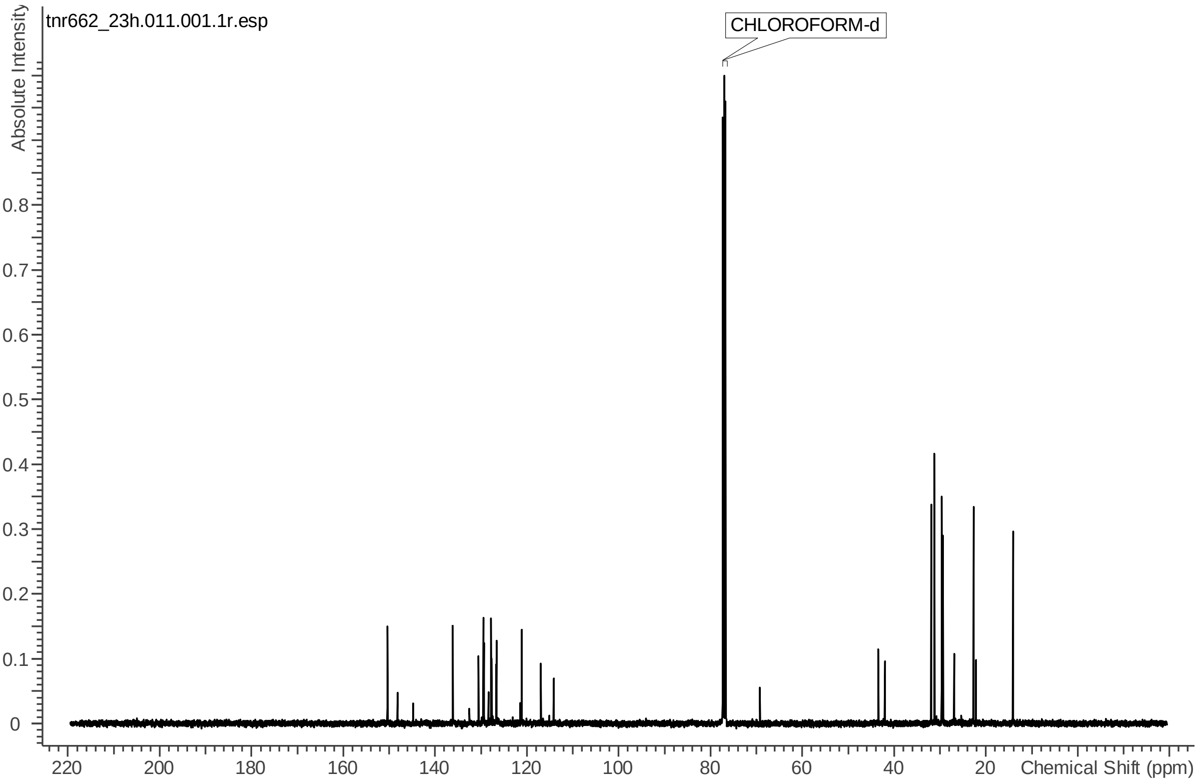
tnr662_23h.011.001.1r.esp
CHLOROFORM-d
Absolute Intensity
0.8
0.7
0.6
0.5
0.4
0.3
0.2
0.1
0
220
200
180
160
140
120
100
80
60
40
20
Chemical Shift (ppm)

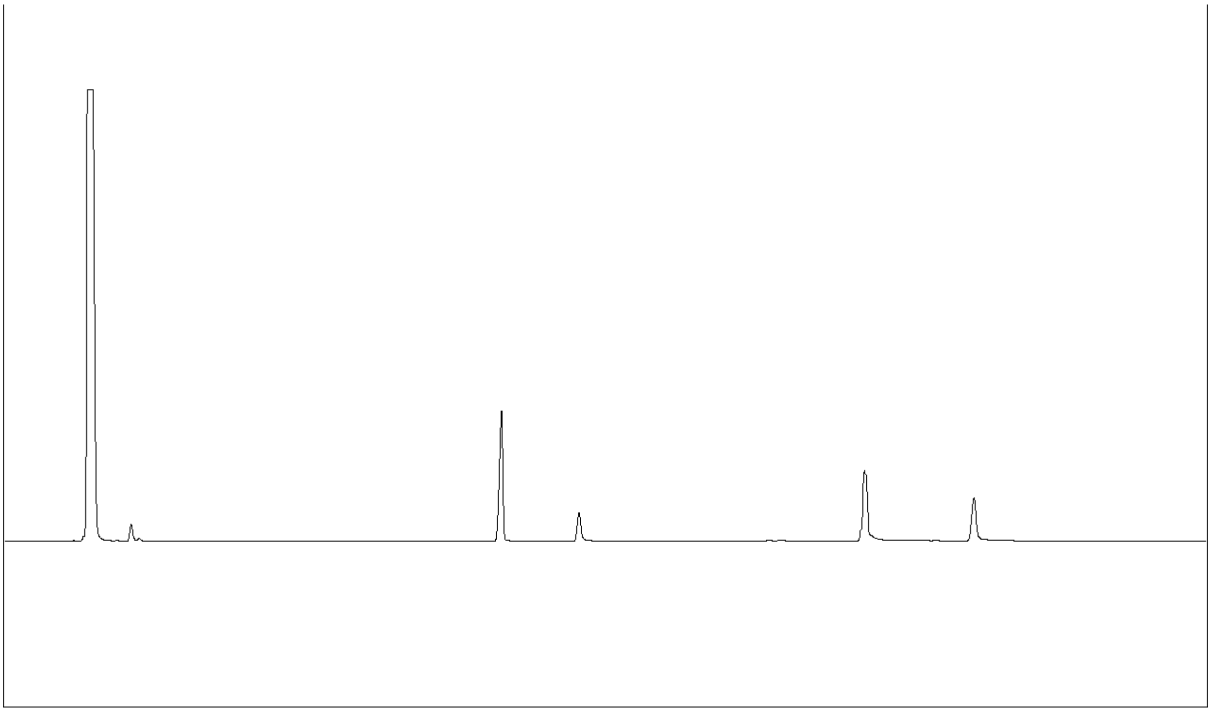

9.6.11 **Tetrahydroisoquinoline**

Tetrahydroisoquinoline mixture

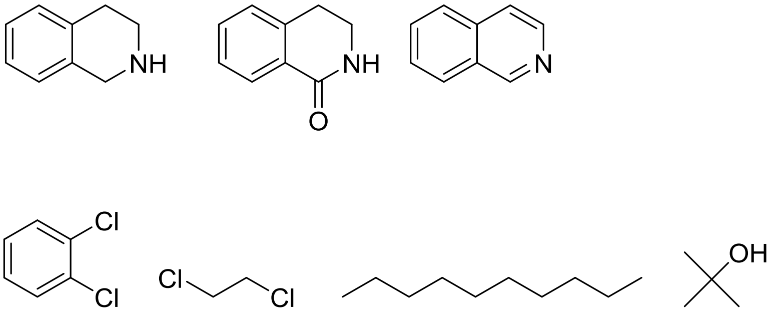
NH
NH
O
N
Cl
Cl
Cl
Cl
OH

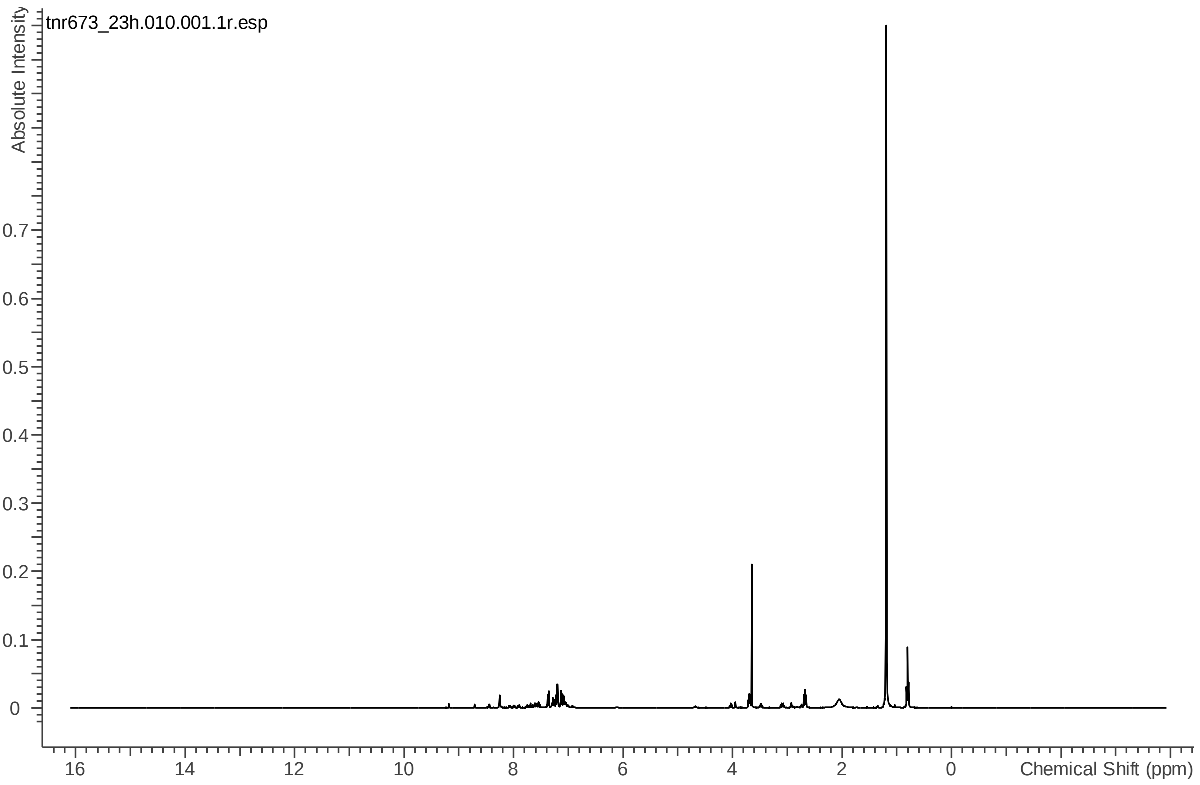

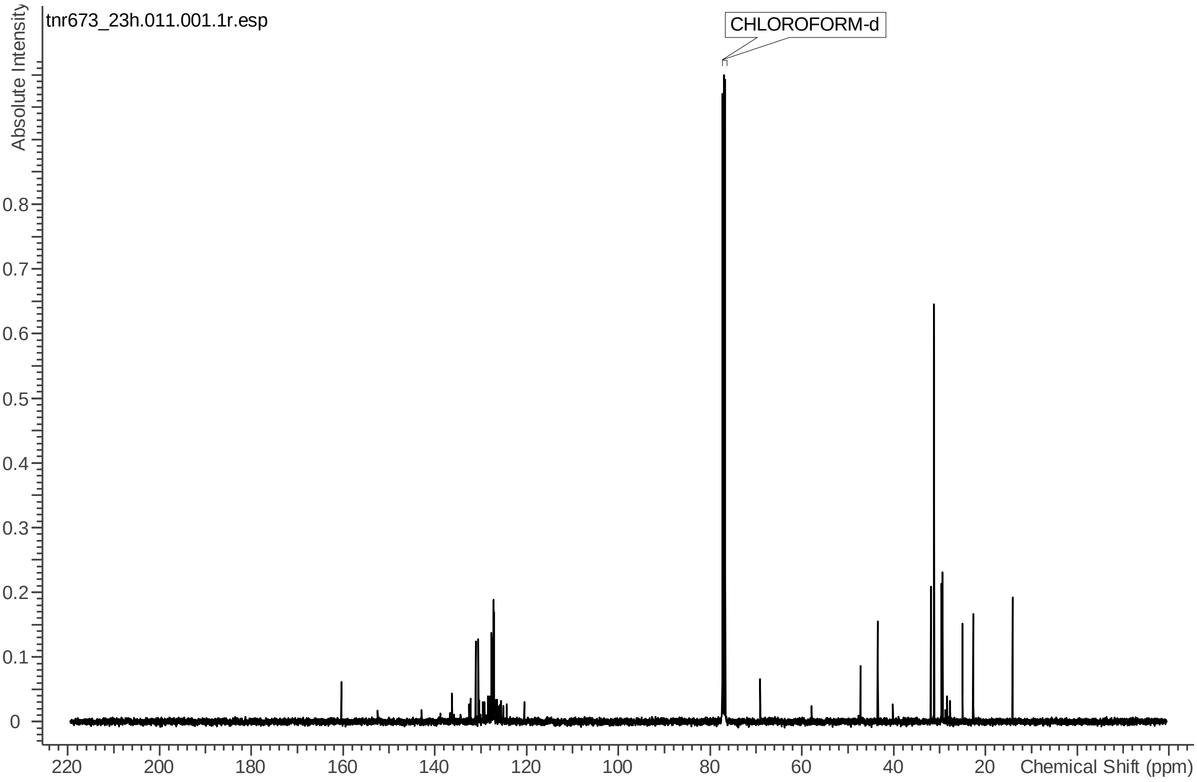
tnr673_23h.011.001.1r.esp
CHLOROFORM-d
Absolute Intensity
0.8
0.7
0.6
0.5
0.4
0.3
0.2
0.1
0
220
200
180
160
140
120
100
80
60
40
20
Chemical Shift (ppm)

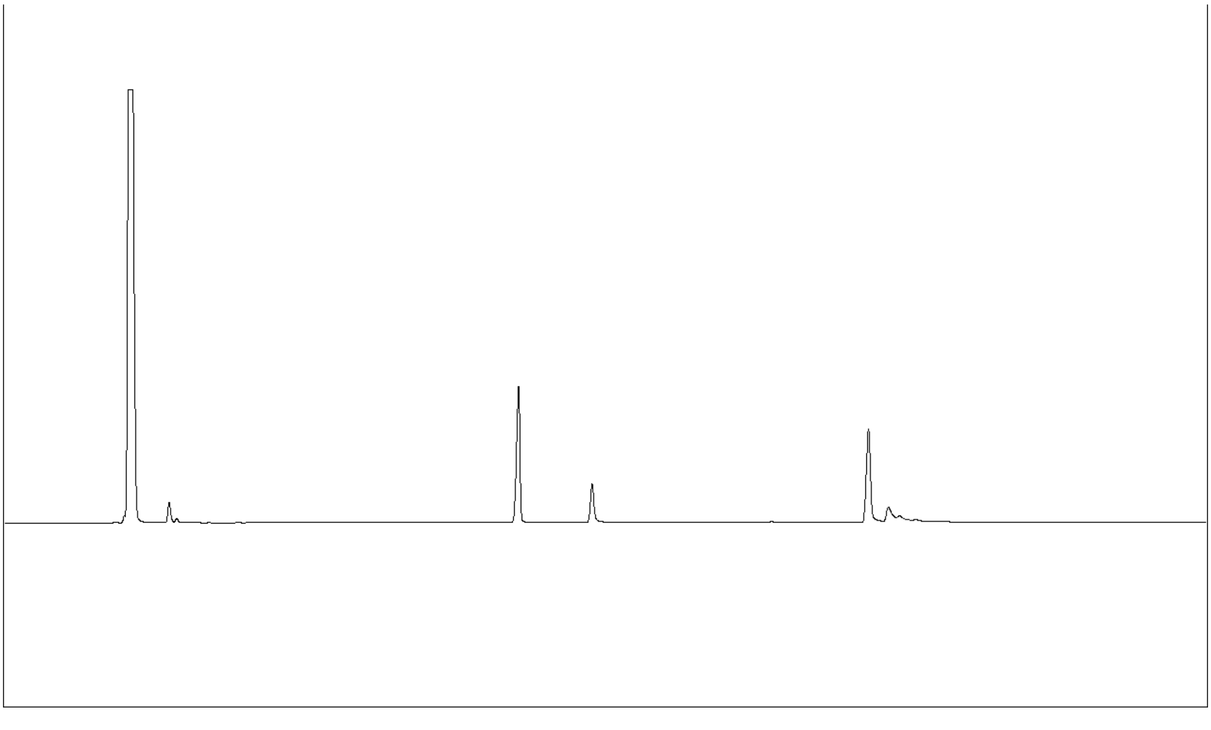

9.6.12 **Dihydrobenzofuran**

Dihydrobenzofuran mixture

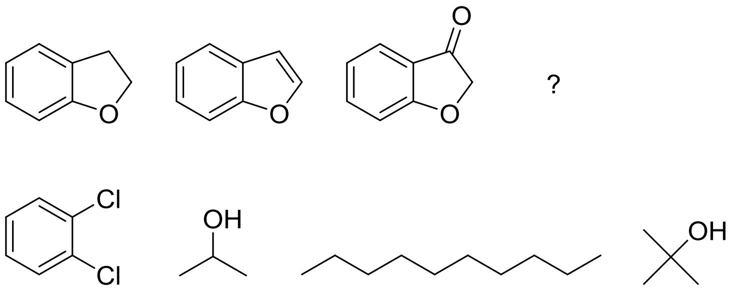

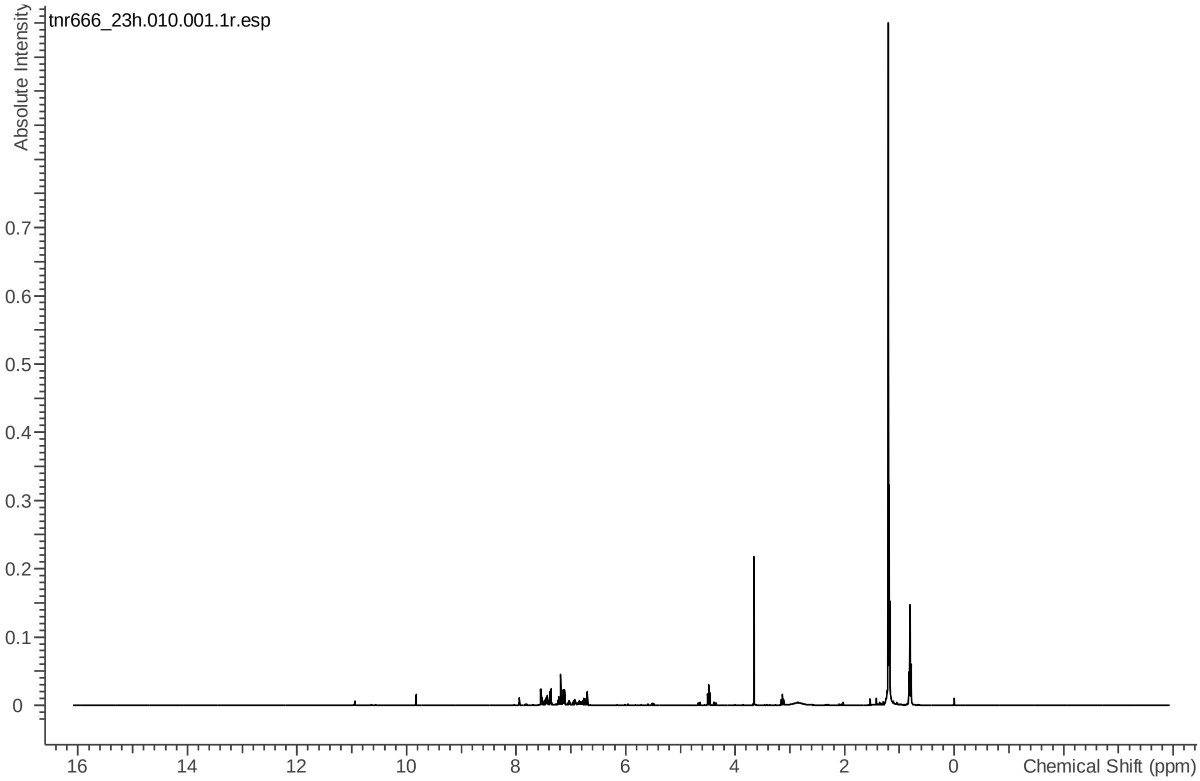

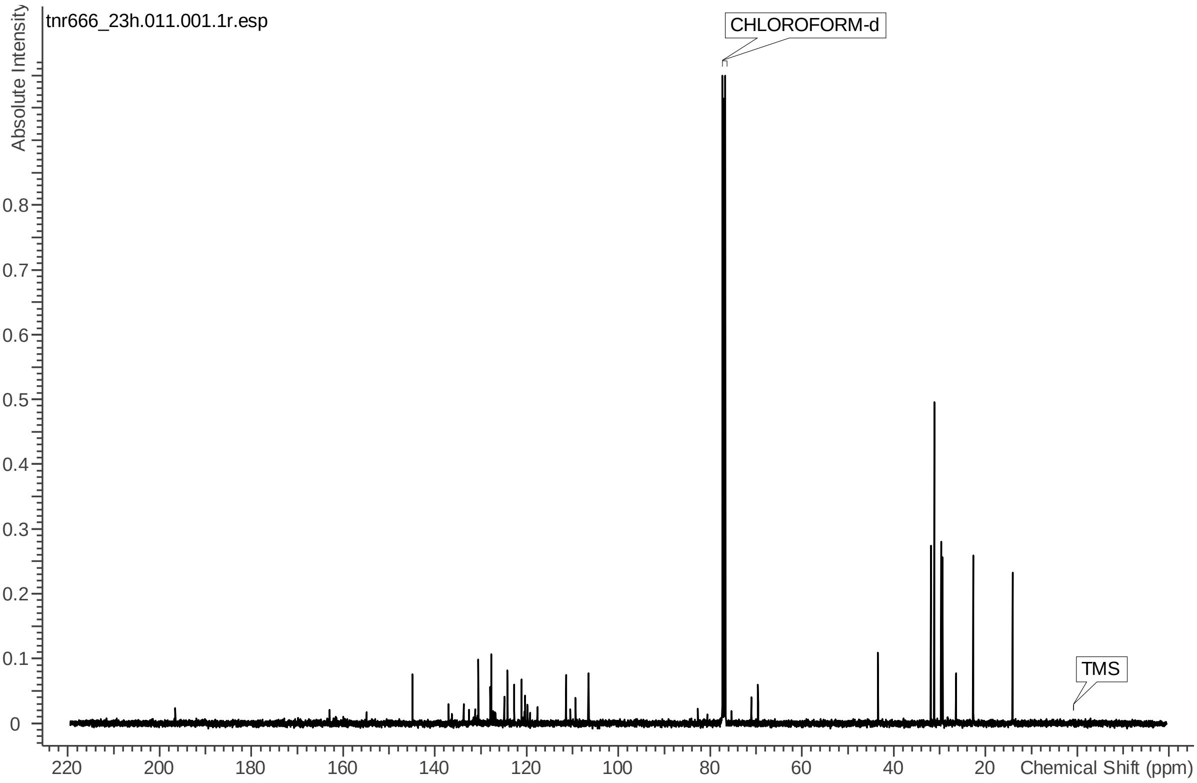
tnr666_23h.011.001.1r.esp
CHLOROFORM-d
TMS
Absolute Intensity
0.8
0.7
0.6
0.5
0.4
0.3
0.2
0.1
0
220
200
180
160
140
120
100
80
60
40
20
Chemical Shift (ppm)

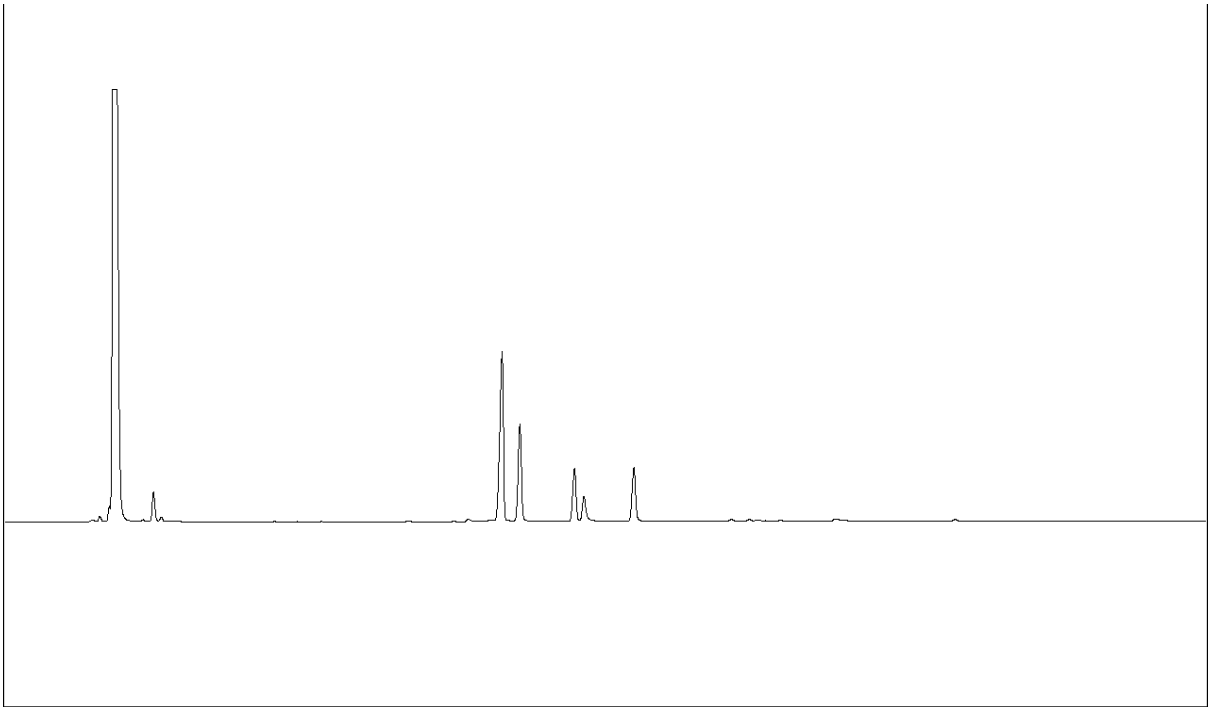

Bibliography

(1) Berzelius, J. J. *Jahres-Bericht* **1836**, *15*, 237-245.

(2) Berzelius, J. J. *Ann. Chim.* **1836**, *61*, 146-151.

(3) *Compendium of Chemical Terminology Gold Book*; International Union for Pure and Applied Chemistry, 2012. Available online at goldbook.iupac.org

(4) Grasselli, R. K. *Top. Catal.* **2002**, *21*, 79-88.

(5) Deutschmann, O.; Knözinger, H.; Kochloefl, K.; Turek, T. *Heterogeneous Catalysis and Solid Catalysts*; Wiley, 2009.

(6) Mars, P.; van Krevelen, D. W. *Chem. Eng. Sci.* **1954**, *3*, 41-59.

(7) Mckay, D.; Gregory, D. H.; Hargreaves, J. S. J.; Hunter, S. M.; Sun, X. L. *Chem. Commun.* **2007**, 3051-3053.

(8) Arends, I. W. C. E.; Sheldon, R. A.; Wallau, M.; Schuchardt, U. *Angew. Chem. Int. Ed.* **1997**, *36*, 1144-1163.

(9) McBain, J. W. *The Sorption of Gases and Vapours by Solids*; Rutledge, 1932.

(10) Gallo, E.; Piovano, A.; Marini, C.; Mathon, O.; Pascarelli, S.; Glatzel, P.; Lamberti, C.; Berlier, G. *J. Phys. Chem. C* **2014**, *118*, 11745-11751.

(11) Perego, C.; Carati, A.; Ingallina, P.; Mantegazza, M. A.; Bellussi, G. *Appl. Catal. A: Gen.* **2001**, *221*, 63-72.

(12) Loewenstein, W. *Am. Mineral.* **1954**, *39*, 92-96.

(13) *International Zeolite Association, www.iza-online.org*

(14) Breck, D. W.; Eversole, W. G.; Milton, R. M.; Reed, T. B.; Thomas, T. L. *J. Am. Chem. Soc.* **1956**, *78*, 5963-5972.

(15) Flanigen, E. M.; Lok, B. M.; Patton, R. L.; Wilson, S. T. *Pure Appl. Chem.* **1986**, *58*, 1351-1358.

(16) Xu, R.; Pang, W.; Yu, J.; Huo, Q.; Chen, J. *Chemistry of Zeolites and Related Porous Materials: Synthesis and Structure*; Wiley, 2007.

(17) Milton, R. M. US2882243, 1959.

(18) Breck, D. W. US3130007, 1964.

(19) Sand, L. B. US3436174, 1969.

(20) Wadlinger, R. L.; Kerr, G. T.; Rosinski, E. J. US3308069, 1967.

(21) Argauer, R. J.; Landolt, G. R. US307886, 1972.

(22) Grose, R. W.; Flanigen, E. M. US4061724, 1977.

(23) Wilson, S. T.; Lok, B. M.; Messina, C. A.; Cannan, T. R.; Flanigen, E. M. *J. Am. Chem. Soc.* **1982**, *104*, 1146-1147.

(24) Smith, J. V. *Am. Mineral.* **1978**, *63*, 960-969.

(25) Martens, J.; Jacobs, P. *Stud. Surf. Sci. Catal.* **1994**, *85*, 653-685.

(26) Yu, J. H.; Xu, R. R. *Chem. Soc. Rev.* **2006**, *35*, 593-604.

(27) Lok, B. M.; Messina, C. A.; Patton, R. L.; Gajek, R. T.; Cannan, T. R.; Flanigen, E. M. *J. Am. Chem. Soc.* **1984**, *106*, 6092-6093.

(28) Weckhuysen, B. M.; Rao, R. R.; Martens, J. A.; Schoonheydt, R. A. *Eur. j. inorg. chem.* **1999**, *1999*, 565-577.

(29) Frache, A.; Gianotti, E.; Marchese, L. *Catal. Today* **2003**, *77*, 371-384.

(30) Corà, F.; Catlow, C. R. A.; Civalleri, B.; Orlando, R. *J. Phys. Chem. B* **2003**, *107*, 11866-11870.

(31) Elanany, M.; Vercauteren, D. P.; Kubo, M.; Miyamoto, A. *J. Mol. Catal. A: Chem.* **2006**, *248*, 181-184.

(32) Nur, H.; Hamdan, H. *Mater. Res. Bull.* **2001**, *36*, 315-322.

(33) Elanany, M.; Koyama, M.; Kubo, M.; Selvam, P.; Miyamoto, A. *Microporous Mesoporous Mater.* **2004**, *71*, 51-56.

(34) Saadoune, I.; Corà, F.; Catlow, C. R. A. *J. Phys. Chem. B* **2003**, *107*, 3003-3011.

(35) Blasco, T.; Concepcion, P.; Grotz, P.; Nieto, J. M. L.; Martinez-Arias, A. *J. Mol. Catal. A: Chem.* **2000**, *162*, 267-273.

(36) Thomas, J. M.; Raja, R.; Sankar, G.; Bell, R. G. *Nature* **1999**, *398*, 227-230.

(37) Thomas, J. M.; Raja, R. *Top. Catal.* **2006**, *40*, 3-17.

(38) Thomas, J. M. *Top. Catal.* **2006**, *38*, 3-5.

(39) Thomas, J. M.; Raja, R.; Lewis, D. W. *Angew. Chem. Inter. Ed.* **2005**, *44*, 6456-6482.

(40) Wulff, H. P. GP1249079, 1971.

(41) Sheldon, R. A. *J. Mol. Catal.* **1980**, *7*, 107-126.

(42) Abbenhuis, H. L.; van Santen, R. *Chem. Commun.* **1997**, 331-332.

(43) Romanovsky, B. V.; Gabrielov, A. G. *J. Mol. Catal.* **1992**, *74*, 293-303.

(44) Balkus Jr, K. J.; Eissa, M.; Levado, R. *J. Am. Chem. Soc.* **1995**, *117*, 10753-10754.

(45) Herron, N.; Tolman, C. A. *J. Am. Chem. Soc.* **1987**, *109*, 2837-2839.

(46) Corbin, D. R.; Herron, N. *J. Mol. Catal.* **1994**, *86*, 343-369.

(47) Parton, R. F.; Vankelecom, I. F. J.; Casselman, M. J. A.; Bezoukhanova, C. P.; Uytterhoeven, J. B.; Jacobs, P. A. *Nature* **1994**, *370,* 541-544.

(48) Parton, R. F.; Uytterhoeven, L.; Jacobs, P. A. *Stud. Surf. Sci. Catal.* **1991**, *59*, 395-403.

(49) Herron, N.; Stucky, G. D.; Tolman, C. A. *J. Chem. Soc. Chem. Comm.* **1986**, 1521-1522.

(50) Shilov, A. E.; Shul'pin, G. B. *Chem. Rev.* **1997**, *97*, 2879-2932.

(51) Newhouse, T.; Baran, P. S. *Angew. Chem. Int. Ed.* **2011**, *50*, 3362-3374.

(52) Thomas, J. M.; Raja, R.; Sankar, G.; Bell, R. G. *Acc. Chem. Res.* **2001**, *34*, 191-200.

(53) Borovik, A. S. *Chem. Soc. Rev.* **2011**, *40*, 1870-1874.

(54) Raja, R.; Sankar, G.; Thomas, J. M. *Angew. Chem. Int. Ed.* **2000**, *39*, 2313-2316.

(55) Lounis, Z.; Riahi, A.; Djafri, F.; Muzart, J. *Appl. Catal. A: Gen.* **2006**, *309*, 270-272.

(56) Xu, Y.; Yang, Z.; Hu, J.; Yan, J. *Synthesis* **2013**, *45*, 370-374.

(57) Xu, Y.; Hu, J. T.; Yan, J. *Chin. Chem. Lett.* **2012**, *23*, 891-894.

(58) Clayden, J.; Greeves, N.; Warren, S.; Wothers, P. *Organic Chemistry*; Oxford University Press, 2001.

(59) Lazlo, P. *Organic Reactions: Simplicity and Logic*; Wiley, 1995.

(60) Fieser, L. F. *Organic Chemistry*; Reinhold, 1956.

(61) Weissermel, K.; Arpe, H.-J. *Industrial Organic Chemistry*; Wiley, 2008.

(62) Zhou, M.; Hintermair, U.; Hashiguchi, B. G.; Parent, A. R.; Hashmi, S. M.; Elimelech, M.; Periana, R. A.; Brudvig, G. W.; Crabtree, R. H. *Organometallics* **2013**, *32*, 957-965.

(63) Yamazaki, S. *Org. Lett.* **1999**, *1*, 2129-2132.

(64) Modica, E.; Bombieri, G.; Colombo, D.; Marchini, N.; Ronchetti, F.; Scala, A.; Toma, L. *Eur. J. Org. Chem.* **2003**, *2003*, 2964-2971.

(65) Choudary, B. M.; Prasad, A. D.; Bhuma, V.; Swapna, V. *J. Org. Chem.* **1992**, *57*, 5841-5844.
(66) Hsu, S. F.; Plietker, B. *ChemCatChem* **2013**, *5*, 126-129.
(67) Nikalje, M. D.; Sudalai, A. *Tetrahedron* **1999**, *55*, 5903-5908.
(68) Wusiman, A.; Tusun, X.; Lu, C. D. *Eur. J. Org. Chem.* **2012**, *2012*, 3088-3092.
(69) Catino, A. J.; Nichols, J. M.; Choi, H.; Gottipamula, S.; Doyle, M. P. *Org. Lett.* **2005**, *7*, 5167-5170.
(70) Wu, X.-F. *Tetrahedron Lett.* **2012**, *53*, 6123-6126.
(71) Bonvin, Y.; Callens, E.; Larrosa, I.; Henderson, D. A.; Oldham, J.; Burton, A. J.; Barrett, A. G. M. *Org. Lett.* **2005**, *7*, 4549-4552.
(72) Xia, J. B.; Cormier, K. W.; Chen, C. *Chem. Sci.* **2012**, *3*, 2240-2245.
(73) Bollinger, J. M.; Broderick, J. B. *Curr. Opn. Chem. Biol.* **2009**, *13*, 51-57.
(74) Thomas, J. M.; Raja, R. *Catal. Today* **2006**, *117*, 22-31.
(75) Moden, B.; Zhan, B. Z.; Dakka, J.; Santiesteban, J. G.; Iglesia, E. *J. Phys. Chem. C* **2007**, *111*, 1402-1411.
(76) Paterson, J.; Potter, M.; Gianotti, E.; Raja, R. *Chem. Commun.* **2011**, *47*, 517-519.
(77) Raja, R.; Lee, S. O.; Sanchez-Sanchez, M.; Sankar, G.; Harris, K. D. M.; Johnson, B. F. G.; Thomas, J. M. *Top. Catal.* **2002**, *20*, 85-88.
(78) Raja, R.; Thomas, J. M.; Xu, M. C.; Harris, K. D. M.; Greenhill-Hooper, M.; Quill, K. *Chem. Commun.* **2006**, 448-450.
(79) Raja, R.; Thomas, J. M.; Greenhill-Hooper, M.; Doukova, V. *Chem. Commun.* **2007**, 1924-1926.
(80) Kent, J. A. *Kent and Riegel's Handbook of Industrial Chemistry and Biotechnology*; Springer-Verlag, 2007.
(81) Cornils, B.; Herrmann, W. A. *Applied Homogeneous Catalysis with Organometallic Compounds*; Wiley-VCH Verlag, 2002.
(82) *Ullmann's Encyclopedia of Industrial Chemistry*; Wiley-VCH Verlag, 2011.
(83) Candela, L. M.; Cochran, R. N.; Sandler, S. H. US4950794, 1990.
(84) Wittcoff, H. A.; Reuben, B. G.; Plotkin, J. S. *Industrial Organic Chemicals, 3rd Edition*; Wiley, 2013.
(85) Clerici, M. G.; Kholdeeva, O. A. *Liquid Phase Oxidation via Heterogeneous Catalysis: Organic Synthesis and Industrial Applications*; Wiley, 2013.
(86) Kollar, J. US3351635, 1967.
(87) Lemoine, R. O., PhD Thesis, University of Pittsburgh, 2005.
(88) Morimoto, T.; Ogata, Y. *J. Chem. Soc. B: Phys. Org.* **1967**, 62-66.
(89) Thomas, J. M.; Raja, R.; Johnson, B. F. G.; Sankar, G.; Bell, R. G. *Russ. Chem. B+* **2001**, *50*, 2010-2014.
(90) Thomas, J. M.; Raja, R.; Sankar, G.; Johnson, B. F. G.; Lewis, D. W. *Chem. Eur. J.* **2001**, *7*, 2973-2978.
(91) Raja, R.; Thomas, J. M. *J. Mol. Catal. A: Chem.* **2002**, *181*, 3-14.
(92) Raja, R.; Thomas, J. M.; Sankar, G. *Chem. Commun.* **1999**, 525-526.
(93) Raja, R.; Thomas, J. M.; Dreyer, V. *Catal. Lett.* **2006**, *110*, 179-183.
(94) Dugal, M.; Sankar, G.; Raja, R.; Thomas, J. M. *Angew. Chem. Int. Ed.* **2000**, *39*, 2310-2313.
(95) Chang, C. D.; Silvestri, A. J. *J. Catal.* **1977**, *47*, 249-259.
(96) Dai, W.; Wu, G.; Li, L.; Guan, N.; Hunger, M. *ACS Catal.* **2013**, *3*, 588-596.
(97) Tian, P.; Wei, Y.; Ye, M.; Liu, Z. *ACS Catal.* **2015**, *5*, 1922-1938.

(98) Dahl, I. M.; Kolboe, S. *Catal. Lett.* **1993**, *20*, 329-336.

(99) Wilson, S.; Barger, P. *Microporous Mesoporous Mater.* **1999**, *29*, 117-126.

(100)Arstad, B.; Kolboe, S. *J. Am. Chem. Soc.* **2001**, *123*, 8137-8138.

(101)Hartmann, M.; Kevan, L. *Chem. Rev.* **1999**, *99*, 635-663.

(102)Flanigen, E. M.; Lok, B. M. T.; Patton, R. L.; Wilson, S. T. 1985.

(103)Miyamoto, A.; Iwamoto, Y.; Matsuda, H.; Inui, T. *Stud. Surf. Sci. Catal.* **1989**, *49*, 1233-1242.

(104)Montes, C.; Davis, M. E.; Murray, B.; Narayana, M. *J. Phys. Chem.* **1990**, *94*, 6431-6435.

(105)Eichele, K.; Grimmer, A.-R. *Can. J. Chem.* **2011**, *89*, 870-884.

(106)Teixeira-Neto, Â. A.; Marchese, L.; Pastore, H. O. *Quím. Nova* **2009**, *32*, 463-468.

(107)Zahedi-Niaki, M. H.; Zaidi, S. M. J.; Kaliaguine, S. *Appl. Catal. A: Gen.* **2000**, *196*, 9-24.

(108)Rigutto, M. S.; Van Bekkum, H. *J. Mol. Catal.* **1993**, *81*, 77-98.

(109)Mendialdua, J.; Casanova, R.; Barbaux, Y. *J. Electron Spectrosc. Relat. Phenom.* **1995**, *71*, 249-261.

(110)Punniyamurthy, T.; Velusamy, S.; Iqbal, J. *Chem. Rev.* **2005**, *105*, 2329-2364.

(111)Blasco, T.; Concepcion, P.; Nieto, J. M. L.; Perezpariente, J. *J. Catal.* **1995**, *152*, 1-17.

(112)Silversmit, G.; Depla, D.; Poelman, H.; Marin, G. B.; De Gryse, R. *J. Electron Spectrosc. Relat. Phenom.* **2004**, *135*, 167-175.

(113)Corma, A.; Nieto, J. M. L.; Paredes, N. *J. Catal.* **1993**, *144*, 425-438.

(114)Centi, G.; Trifirò, F.; Ebner, J.; Gleaves, J. *Faraday Discuss. Chem. Soc.* **1989**, *87*, 215-225.

(115)Centi, G.; Trifiro, F.; Ebner, J. R.; Franchetti, V. M. *Chem. Rev.* **1988**, *88*, 55-80.

(116)Thorn, D. L.; Harlow, R. L.; Herron, N. *Inorg. Chem.* **1996**, *35*, 547-548.

(117)Chen, B.; Munson, E. J. *J. Am. Chem. Soc.* **2002**, *124*, 1638-1652.

(118)Hodnett, B. K. *Catal. Rev. Sci. and Eng.* **1985**, *27*, 373-424.

(119)Ballarini, N.; Cavani, F.; Cortelli, C.; Ligi, S.; Pierelli, F.; Trifiro, F.; Fumagalli, C.; Mazzoni, G.; Monti, T. *Top. Catal.* **2006**, *38*, 147-156.

(120)Pyke, D. R.; Whitney, P.; Houghton, H. *Appl. Catal.* **1985**, *18*, 173-190.

(121)Venkatathri, N.; Hegde, S. G.; Sivasanker, S. *J. Chem. Soc. Chem. Comm.* **1995**, 151-152.

(122)Venkatathri, N. *Appl. Catal. A: Gen.* **2003**, *242*, 393-401.

(123)Concepción, P.; Blasco, T.; Nieto, J. M. L.; Vidal-Moya, A.; Martínez-Arias, A. *Microporous Mesoporous Mater.* **2004**, *67*, 215-227.

(124)Centi, G.; Perathoner, S.; Trifiro, F.; Aboukais, A.; Aissi, C. F.; Guelton, M. *J. Phys. Chem.* **1992**, *96*, 2617-2629.

(125)Concepción, P.; Nieto, J. M. L.; Pérez-Pariente, J. *J. Mol. Catal. A: Chem.* **1995**, *97*, 173-182.

(126)Kraushaar, B.; Van Hooff, J. H. C. *Catal. Lett.* **1988**, *1*, 81-84.

(127)Maurelli, S.; Vishnuvarthan, M.; Berlier, G.; Chiesa, M. *Phys. Chem. Chem. Phys.* **2012**, *14*, 987-995.

(128)Prakash, A. M.; Kurshev, V.; Kevan, L. *J. Phys. Chem. B* **1997**, *101*, 9794-9799.

(129)Ulagappan, N.; Krishnasamy, V. *J. Chem. Society Chem. Commun.* **1995**, 373-374.

(130)Taramasso, M.; Perego, G.; Notari, B. US4410501A, 1983.

(131)Jones, C. W. *Applications of Hydrogen Peroxide and Derivatives*; The Royal Society of Chemistry, 1999.

(132)Jackson, S. D.; Hargreaves, J. S. J. *Metal Oxide Catalysis*; Wiley, 2009.

(133)Serrano, D.; Sanz, R.; Pizarro, P.; Moreno, I. *Chem. Commun.* **2009**, 1407-1409.

(134)Blasco, T.; Corma, A.; Navarro, M. T.; Pariente, J. P. *J. Catal.* **1995**, *156*, 65-74.

(135)Corma, A.; Navarro, M. T.; Pariente, J. P. *J. Chem. Soc. Chem. Commun.* **1994**, 147-148.

(136)Corma, A. *Chem. Rev.* **1997**, *97*, 2373-2420.

(137)Corma, A.; Domine, M.; Gaona, J. A.; Jordá, J. L.; Navarro, M. T.; Rey, F.; Pérez-Pariente, J.; Tsuji, J.; McCulloch, B.; Nemeth, L. T. *Chem. Commun.* **1998**, 2211-2212.

(138)Tanev, P. T.; Chibwe, M.; Pinnavaia, T. J. *Nature* **1994**, *368,* 321-323.

(139)Leithall, R. M.; Shetti, V. N.; Maurelli, S.; Chiesa, M.; Gianotti, E.; Raja, R. *J. Am. Chem. Soc.* **2013**, *135*, 2915-2918.

(140)Wang, Y.; Wang, G.; Yang, M.; Tan, L.; Dong, W.; Luck, R. *J. Colloid Interface Sci.* **2011**, *353*, 519-523.

(141)Jarupatrakorn, J.; Tilley, T. D. *J. Am. Chem. Soc.* **2002**, *124*, 8380-8388.

(142)Oldroyd, R. D.; Thomas, J. M.; Maschmeyer, T.; MacFaul, P. A.; Snelgrove, D. W.; Ingold, K. U.; Wayner, D. D. M. *Angew. Chem. Int. Ed.* **1996**, *35*, 2787-2790.

(143)Thomas, J. M.; Sankar, G. *Acc. Chem. Res.* **2001**, *34*, 571-581.

(144)Zecchina, A.; Bordiga, S.; Lamberti, C.; Ricchiardi, G.; Scarano, D.; Petrini, G.; Leofanti, G.; Mantegazza, M. *Catal. Today.* **1996**, *32*, 97-106.

(145)Lee, S. O.; Raja, R.; Harris, K. D. M.; Thomas, J. M.; Johnson, B. F. G.; Sankar, G. *Angew. Chem.* **2003**, *115*, 1558-1561.

(146)Schuchardt, U.; Cardoso, D.; Sercheli, R.; Pereira, R.; Da Cruz, R. S.; Guerreiro, M. C.; Mandelli, D.; Spinacé, E. V.; Pires, E. L. *Appl. Catal. A: Gen.* **2001**, *211*, 1-17.

(147)Zahedi-Niaki, M. H.; Zaidi, S. M. J.; Kaliaguine, S. *Microporous Mesoporous Mater.* **1999**, *32*, 251-255.

(148)Kikhtyanin, O. V.; Mastikhin, V. M.; Ione, K. G. *Appl. Catal.* **1988**, *42*, 1-13.

(149)Roesler, R.; Schelle, S.; Gnann, M.; Zeiss, W. US5462692A, 1995.

(150)Thomas, J. M.; Hernandez-Garrido, J. C.; Raja, R.; Bell, R. G. *Phys. Chem. Chem. Phys.* **2009**, *11*, 2799-2825.

(151)Zhou, L.; Xu, J.; Chen, C.; Wang, F.; Li, X. *J. Porous Mater.* **2008**, *15*, 7-12.

(152)Zhou, L.; Xu, J.; Miao, H.; Li, X.; Wang, F. *Catal. Lett.* **2005**, *99*, 231-234.

(153)Cora, F.; Catlow, C. R. A. *J. Phys. Chem. B* **2001**, *105*, 10278-10281.

(154)Cora, F.; Saadoune, I.; Catlow, C. R. A. *Angew. Chem. Int. Ed.* **2002**, *41*, 4677-4680.

(155)Cora, F.; Alfredsson, M.; Barker, C. M.; Bell, R. G.; Foster, M. D.; Saadoune, I.; Simperler, A.; Catlow, C. R. A. *J. Solid. State. Chem.* **2003**, *176*, 496-529.

(156)Li, J. Y.; Yu, J. H.; Xu, R. R. *P. Roy. Soc. A-Math. Phys.* **2012**, *468*, 1955-1967.

(157)Meinhold, R. H.; Tapp, N. J. *J. Chem. Soc. Chem. Commun.* **1990**, 219-220.

(158)Paterson, A. J. P., PhD Thesis, University of Southampton, 2011.

(159)Leithall, R. M., PhD Thesis, University of Southampton, 2013.

(160)Simmance, K. PhD Thesis, University College London, 2011.

(161)Baerns, M. *Basic Principles in Applied Catalysis*; Springer-Verlag, 2004.

(162)Wright, P. A. *Microporous Framework Solids*; The Royal Society of Chemistry, 2008.

(163)Middelkoop, V.; Jacques, S. D. M.; O'Brien, M. G.; Beale, A. M.; Barnes, P. *J. Mater. Sci.* **2008**, *43*, 2222-2228.

(164)Fan, F. T.; Feng, Z. C.; Sun, K. J.; Guo, M. L.; Guo, Q.; Song, Y.; Li, W. X.; Li, C. *Angew. Chem. Int. Ed.* **2009**, *48*, 8743-8747.

(165)Grandjean, D.; Beale, A. M.; Petukhov, A. V.; Weckhuysen, B. M. *J. Am. Chem. Soc.* **2005**, *127*, 14454-14465.

(166)Norby, P.; Hanson, J. C. *Catal. Today.* **1998**, *39*, 301-309.

(167)Oliver, S.; Kuperman, A.; Ozin, G. A. *Angew. Chem. Int. Ed.* **1998**, *37*, 47-62.

(168)Hooper, D.; Barnes, P.; Cockcroft, J. K.; Jupe, A. C.; Jacques, S. D. M.; Bailey, S. P.; Lupo, F.; Vickers, M.; Hanfland, M. *Phys. Chem. Chem. Phys.* **2003**, *5*, 4946-4950.

(169)Barrett, P. A.; Sankar, G.; Catlow, C. R. A.; Thomas, J. M. *J. Phys. Chem.* **1996**, *100*, 8977-8985.

(170)Haanepen, M. J.; ElemansMehring, A. M.; vanHooff, J. H. C. *Appl. Catal. A: Gen.* **1997**, *152*, 203-219.

(171)Shannon, R. D.; Prewitt, C. T. *Acta Crystallogr., Sect. B: Struct. Sci.* **1970**, *B 26*, 1046-1048.

(172)Prakash, A. M.; Kevan, L. *J. Phys. Chem. B* **1999**, *103*, 2214-2222.

(173)Maurelli, S.; Berlier, G.; Chiesa, M.; Musso, F.; Corà, F. *J. Phys. Chem. C* **2014**, *118*, 19879-19888.

(174)Jhung, S. H.; Uh, Y. S.; Chon, H. *Appl. Catal.* **1990**, *62*, 61-72.

(175)Morris, R. E.; Weigel, S. J. *Chem. Soc. Rev.* **1997**, *26*, 309-317.

(176)Ng, E. P.; Delmotte, L.; Mintova, S. *Green Chem.* **2008**, *10*, 1043-1048.

(177)Gulin-Gonzalez, J.; Alcaz, J. D.; Nieto, J. M. L.; de las Pozas, C. *J. Mater. Chem.* **2000**, *10*, 2597-2602.

(178)Kumar, A.; Srinivas, D.; Ratnasamy, P. *Chem. Commun.* **2009**, 6484-6486.

(179)Okamoto, M.; Luo, L.; Labinger, J. A.; Davis, M. E. *J. Catal.* **2000**, *192*, 128-136.

(180)Vishnuvarthan, M.; Paterson, A. J.; Raja, R.; Piovano, A.; Bonino, F.; Gianotti, E.; Berlier, G. *Microporous Mesoporous Mater.* **2011**, *138*, 167-175.

(181)Subrahmanyam, C.; Louis, B.; Viswanathan, B.; Renken, A.; Varadarajan, T. K. *Appl. Catal. A: Gen.***2005**, *282*, 67-71.

(182)Lakshmi, L. J.; Srinivas, S. T.; Rao, P. K.; Nosov, A. V.; Lapina, O. B.; Mastikhin, V. M. *Solid State Nucl. Magn. Reson.* **1995**, *4*, 59-64.

(183)Weckhuysen, B. M.; Vannijvel, I. P.; Schoonheydt, R. A. *Zeolites* **1995**, *15*, 482-489.

(184)Maurelli, S.; Vishnuvarthan, M.; Chiesa, M.; Berlier, G.; Van Doorslaer, S. *J. Am. Chem. Soc.***2011**, *133*, 7340-7343.

(185)WCASLAB (www.wcaslab.com)

(186)Dal Pozzo, L.; Fornasari, G.; Monti, T. *Catal. Commun.* **2002**, *3*, 369-375.

(187)Boccuti, M. R.; Rao, K. M.; Zecchina, A.; Leofanti, G.; Petrini, G. *Stud. Surf. Sci. Catal.***1989**, *48*, 133-144.

(188)Arena, F.; Frusteri, F.; Martra, G.; Coluccia, S.; Parmaliana, A. *J. Chem. Soc. Faraday Trans.* **1997**, *93*, 3849-3854.

(189)Eckert, H.; Wachs, I. E. *J. Phys. Chem.* **1989**, *93*, 6796-6805.

(190)Gee, B. A. *Solid State Nucl. Magn. Reson.* **2006**, *30*, 171-181.

(191)Lapina, O. B.; Khabibulin, D. F.; Shubin, A. A.; Terskikh, V. V. *Prog. Nucl. Magn. Reson. Spectrosc.* **2008**, *53*, 128-191.

(192)CasaXPS Online Manual (www.casaxps.com)

(193)Schwartz, H. E.; Miller, J. T.; Henley, B. J.; Huff, G. A. US20070049780A1, 2007.

(194)Aborways, M. M.; Moran, W. J. *Tetrahedron Lett.* **2016**, *57*, 983-985.

(195)Rylander, P. N.; Meyerson, S. *J. Am. Chem. Soc.* **1956**, *78*, 5799-5802.

(196)Hua, G.; Henry, J. B.; Li, Y.; Mount, A. R.; Slawin, A. M. Z.; Woollins, J. D. *Org. Biomol. Chem.* **2010**, *8*, 1655-1660.

(197)Boyd, D. R.; Sharma, N. D.; Bowers, N. I.; Duffy, J.; Harrison, J. S.; Dalton, H. *J. Chem. Soc. Perkin Trans. 1* **2000**, 1345-1350.

(198)Suhana, H.; Srinivasan, P. C. *Synth. Commun.* **2003**, *33*, 3097-3102.

(199)Bond, S.; Draffan, A. G.; Fenner, J. E.; Lambert, J.; Lim, C. Y.; Lin, B.; Luttick, A.; Mitchell, J. P.; Morton, C. J.; Nearn, R. H. *Bioorg. Med. Chem. Lett.* **2015**, *25*, 969-975.

(200)Shaabani, A.; Teimouri, F.; Lee, D. G. *Synth. Commun.* **2003**, *33*, 1057-1065.

(201)Sreekumar, R.; Padmakumar, R. *Tetrahedron Lett.* **1997**, *38*, 5143-5146.

(202)Shaabani, A.; Soleimani, K.; Bazgir, A. *Synthetic Commun.* **2004**, *34*, 3303-3315.

(203)Pritzkow, W.; Thomas, G.; Willecke, L. *J. Prak. Chem.* **1985**, *327*, 945-952.

(204)Whitehouse, C. J. C.; Bell, S. G.; Wong, L. L. *Chem. Eur. J.* **2008**, *14*, 10905-10908.

(205)D'Auria, M.; Ferri, T.; Mauriello, G. *Gazz. Chim. Ital.* **1996**, *126*.

(206)Sugai, T.; Itoh, A. *Tetrahedron Lett.* **2007**, *48*, 2931-2934.

(207)Yi, C. S.; Kwon, K.-H.; Lee, D. W. *Org. Lett.* **2009**, *11*, 1567-1569.

(208)Biradar, A. V.; Asefa, T. *Appl. Catal. A: Gen.* **2012**, *435*, 19-26.

(209)Tandon, P. K.; Srivastava, M.; Singh, S. B.; Singh, S. *Synth. Commun.* **2008**, *38*, 2125-2137.

(210)Miller, W. V.; Rohde, G. *Ber. Dtsch. Chem. Ges.* **1890**, *23*, 1070-1079.

(211)Crites, C.-O. L.; Netto-Ferreira, J. C.; Hallett-Tapley, G. L.; Scaiano, J. C. *J. Braz. Chem. Soc.* **2016**, *27*, 334-340.

(212)Gudiyella, S.; Brezinsky, K. *Combust. Flame* **2012**, *159*, 940-958.

(213)Hronec, M.; Holotík, Š.; Ilavský, J. *Collect. Czech. Chem. Commun.* **1980**, *45*, 880-887.

(214)Earle, M.; Katdare, S. US20040015009A1, 2004.

(215)Dapurkar, S. E.; Shervani, Z.; Yokoyama, T.; Ikushima, Y.; Kawanami, H. *Catal. Lett.* **2009**, *130*, 42-47.

(216)Foote, C. S.; Valentine, J. S.; Greenberg, A.; Liebman, J. F. *Active Oxygen in Chemistry*; Chapman & Hall, 1995.

(217)Johnson, R. M.; Siddiqi, I. W. *The Determination of Organic Peroxides*; Pergamon, 1970.

(218)Bach, R. D.; Ayala, P. Y.; Schlegel, H. B. *J. Am. Chem. Soc.* **1996**, *118*, 12758-12765.

(219)Walling, C.; Heaton, L. *J. Am. Chem. Soc.* **1965**, *87*, 38-47.

(220)Cheng, H.; Yang, E.; Chao, K.; Wei, A.; Liu, P. H. *J. Phys. Chem. B* **2000**, *104*, 10293-10297.

(221)Sheldon, R. A.; Wallau, M.; Arends, I. W. C. E.; Schuchardt, U. *Acc. Chem. Res.* **1998**, *31*, 485-493.

(222)Franck, H.-G.; Stadelhofer, J. W. *Industrial Aromatic Chemistry*; Springer, 1988.

(223)Stohandl, J.; Frantisek, J.; Zapadlo, Z.; Stohandlova, M. 2003.

(224)Quallich, G. H. US006593496B1, 2003.

(225)Šunjic, V.; Parnham, M. J. *Signposts to Chiral Drugs*; Springer, 2011.

(226)Grayson, M. *Kirk–Othmer Encyclopedia of Chemical Technology*; Wiley, 1981.

(227)Deshpande, M. N.; Cain, M. H.; Patel, S. R.; Singam, P. R.; Brown, D.; Gupta, A.; Barkalow, J.; Callen, G.; Patel, K.; Koops, R. *Org. Proc. Res. Dev.* **1998**, *2*, 351-356.

(228)Arora, S.; Pareek, A.; Agrawal, N.; Nagori, B. P. Int. *J. Res. Pharm. Chem.* **2013**, *3,* 797-802.

(229)Holden, M. S.; Crouch, R. D.; Barker, K. A. *J. Chem. Educ.* **2005**, *82*, 934.

(230)Kletz, T. *Process Plants: A Handbook For Inherently Safer Design*; Taylor & Francis, 1998.

(231)Li, J. J. *Name Reactions: A Collection of Detailed Reaction Mechanisms*; Springer-Verlag, 2003.

(232)Haworth, R. D. *J. Chem. Soc.* **1932**, 1125-1133.

(233)Szmant, H. H. *Organic Building Blocks of the Chemical Industry*; Wiley, 1989.

(234)Coon, R. W.; US4473711, 1984.

(235)Iton, L. E.; Choi, I.; Desjardins, J. A.; Maroni, V. A. *Zeolites* **1989**, *9*, 535-538.

(236)Muzart, J. *Tetrahedron Lett.* **1987**, *28*, 2131-2132.

(237)Pan, J.-F.; Chen, K. *J. Mol. Catal. A: Chem.* **2001**, *176*, 19-22.

(238)Nechab, M.; Einhorn, C.; Einhorn, J. *Chem. Commun.* **2004**, 1500-1501.

(239)Tong, X.; Xu, J.; Miao, H.; Gao, J. *Tetrahedron Lett.* **2006**, *47*, 1763-1766.

(240)Shaabani, A.; Bazgir, A.; Teimouri, F.; Lee, D. G. *Tetrahedron Lett.* **2002**, *43*, 5165-5167.

(241)Small, R. J.; US4960944, 1990.

(242)Kim, J.; Bhattacharjee, S.; Jeong, K.-E.; Jeong, S.-Y.; Ahn, W.-S. *Chem. Commun.* **2009**, 3904-3906.

(243)Dapurkar, S. E.; Kawanami, H.; Yokoyama, T.; Ikushima, Y. *New J. of Chem.* **2009**, *33*, 538-544.

(244)Razi, R.; Abedini, M.; Kharat, A. N.; Amini, M. M. *Catal. Commun.* **2008**, *9*, 245-249.

(245)Martan, M.; Manassen, J.; Vofsi, D. *Tetrahedron* **1970**, *26*, 3815-3827.

(246)Erker, G.; Stephan, D. W. *Petroleum Biotechnology: Developments and Perspectives*; Elsevier, 2004.

(247)Laarhoven, L. J. J.; Mulder, P. *J. Phys. Chem. B* **1997**, *101*, 73-77.

(248)Billings, R. E.; Sullivan, H. R.; McMahon, R. E. *Biochemistry* **1970**, *9*, 1256-1260.

(249)Guo, C.-C.; Liu, Q.; Wang, X.-T.; Hu, H.-Y. *Appl. Catal. A: Gen.* **2005**, *282*, 55-59.

(250)Ibusuki, T.; Takeuchi, K. *Atmos. Environ.* **1986**, *20*, 1711-1715.

(251)Kesavan, L.; Tiruvalam, R.; Ab Rahim, M. H.; bin Saiman, M. I.; Enache, D. I.; Jenkins, R. L.; Dimitratos, N.; Lopez-Sanchez, J. A.; Taylor, S. H.; Knight, D. W. *Science* **2011**, *331*, 195-199.

(252)Lechner, R.; Kümmel, S.; König, B. *Photochem. Photobiol. Sci.* **2010**, *9*, 1367-1377.

(253)Mukherjee, A. *Chem. Commun.* **1999**, 1627-1628.

(254)Okada, T.; Kamiya, Y. *Bull. Chem. Soc. Jpn.* **1981**, *54*, 2724-2727.

(255)Huuhtanen, J.; Sanati, M.; Andersson, A.; Andersson, S. L. T. *Appl. Catal. A: Gen.***1993**, *97*, 197-221.

(256)Bulushev, D. A.; Kiwi-Minsker, L.; Zaikovskii, V. I.; Renken, A. .*J Catal.* **2000**, *193*, 145-153.

(257)Grabowski, R.; Grzybowska, B.; Haber, J.; Słoczynski, J. *React. Kinet. Catal. Lett.* **1975**, *2*, 81-87.

(258)Brunton, G.; Griller, D.; Barclay, L. R. C.; Ingold, K. U. *J. Am. Chem. Soc.* **1976**, *98*, 6803-6811.

(259)Porter, R. J.; Mulder, R. T.; Joyce, P. R.; Luty, S. E. *J. Affective Disord.* **2005**, *86*, 129-134.

(260)Shasaltaneh, M. D.; Fooladi, J.; Moosavi-Nejad, S. Z. *J. Paramed. Sci.***2010**, *1*.

(261)Heaton, C. A. *The Chemical Industry*; Springer, 1994.

(262)Makiguchi, N.; Fukuhara, N.; Shimada, M.; Asai, Y.; Nakamura, T.; Soda, K. *Biochemistry of Vitamin B6*; Springer, 1987.

(263)Schaefer, B. *Natural Products in the Chemical Industry*; Springer, 2014.

(264)Sanchez-Sanchez, M.; Sankar, G.; Simperler, A.; Bell, R. G.; Catlow, C. R. A.; Thomas, J. M. *Catal. Lett.* **2003**, *88*, 163-167.

(265)Wang, W.; Liu, P.; Zhang, M.; Hu, J.; Xing, F. *Open J. Compos. Mater.* **2012,** *2,* 104-112.

(266)Anpo, M.; Zhang, S. G.; Higashimoto, S.; Matsuoka, M.; Yamashita, H.; Ichihashi, Y.; Matsumura, Y.; Souma, Y. *J. Phys. Chem. B* **1999**, *103*, 9295-9301.

(267)Whittington, B. I.; Anderson, J. R. *J. Phys. Chem.* **1993**, *97*, 1032-1041.

(268)Liu, Z.; Davis, R. J. *J. Phys. Chem.* **1994**, *98*, 1253-1261.

(269)Klein, S.; Weckhuysen, B. M.; Martens, J. A.; Maier, W. F.; Jacobs, P. A. *J. Catal.* **1996**, *163*, 489-491.

(270)Bräuniger, T.; Madhu, P. K.; Pampel, A.; Reichert, D. *Solid. State Nucl. Magn. Reson.* **2004**, *26*, 114-120.

(271)Padro, D.; Jennings, V.; Smith, M. E.; Hoppe, R.; Thomas, P. A.; Dupree, R. *J. Phys. Chem. B* **2002**, *106*, 13176-13185.

(272)Fyfe, C. A.; Wong-Moon, K. C.; Huang, Y. *Zeolites* **1996**, *16*, 50-55.

(273)Gougeon, R. D.; Bodart, P. R.; Harris, R. K.; Kolonia, D. M.; Petrakis, D. E.; Pomonis, P. J. *Phys. Chem. Chem. Phys.* **2000**, *2*, 5286-5292.